Technische Universität München
TUM School of Life Sciences

TLⲘ

Mitochondrial function in the regulation of epithelial cell homeostasis – impact on intestinal pathologies

Elisabeth Urbauer

Vollständiger Abdruck der von der TUM School of Life Sciences der Technischen Universität München zur Erlangung einer

Doktorin der Naturwissenschaften (Dr. rer. nat)

genehmigten Dissertation.

Vorsitz: Prof. Dr. Martin Klingenspor

Prüfende der Dissertation:

1.   Prof. Dr. Dirk Haller
2.   apl. Prof. Dr. Klaus-Peter Janssen
3.   Prof. Dr. Stephan Rosshart

Die Dissertation wurde am 02.08.2023 bei der Technischen Universität München eingereicht und durch die TUM School of Life Sciences am 11.03.2024 angenommen.

Zusammenfassung

Das intestinale Epithel ist eine essentielle Schnittstelle zwischen dem mikrobiellen Ökosystem und der darunterliegenden Schleimhaut, und führt sowohl immun-vermittelte als auch metabolische Funktionen aus. Die Signalübertragung und Funktion von Mitochondrien kontrollieren dabei sowohl den Phänotyp als auch die Funktion der intestinalen Epithelzellen. Interessanterweise ist eine mitochondriale Störung mit chronischer Entzündung assoziiert. Es wurde daher die Hypothese aufgestellt, dass eine Störung der mikrobiell-metabolischen Kreisläufe und ein Versagen der Mitochondrien-Funktion zu Gewebeverletzung und chronischer Entzündung beiträgt.

Konditionale Deletion des mitochondrialen „heat shock protein 60" (Hsp60) im intestinalen Epithel (Hsp60$^{\Delta/\Delta IEC}$) induziert eine „mitochondrial unfolded protein response" (MT-UPR). Dieser mitochondriale Stress führt zu Veränderungen im zellulären Metabolismus, was eine irreguläre Krypt-Architektur hervorruft, die wiederum eine transiente Gewebeverletzung (metabolische Verletzung genannt) induziert. Während Hsp60^{+}, verletzungs-assoziierte regenerative Stammzellen die Erneuerung des Gewebes koordinieren, ist dieser Prozess in Abwesenheit des Interleukin 10 (Hsp60$^{\Delta/\Delta IEC}$;$Il10^{-/-}$) gestört, was bedeutet, dass eine metabolische Verletzung die Entzündung in einem anfälligen Wirt beschleunigt. Im Gegensatz dazu entwickelt der proximale Kolon von keimfreien (KF) Hsp60$^{\Delta/\Delta IEC}$ Mäusen eine milde und der distale Kolon keine metabolische Verletzung, was die Hypothese unterstützt, dass Bakterien direkt in die Regulierung von Gewebeverletzung und Heilung involviert sind. Darüber hinaus ist die metabolische Verletzung mit einer Reduktion des Artenreichtums und Veränderungen in der Zusammensetzung der Mikrobiota in Hsp60$^{\Delta/\Delta IEC}$ Mäusen assoziiert. *Bacteroides* spp. und nah verwandte *Phocaeicola* spp. zählen zu den signifikant angereicherten Genera, und „shallow shotgun" Sequenzierung identifizierte *B. uniformis*, *B. caecimuris* und *Phocaeicola vulgatus.* Interessanterweise bleiben die dysbiotischen Veränderungen der intestinalen Mikrobiota in Hsp60$^{\Delta/\Delta IEC}$;$Il10^{-/-}$ Mäusen bestehen. Eine selektive Monokolonisierung von KF Hsp60$^{\Delta/\Delta IEC}$ Mäusen mit *B. caecimuris* induziert erneut Gewebeaberration, und sowohl Bakterien-produzierte Indole als auch Wirt-produzierte Tryptophan Metabolite amplifizieren die MT-UPR Signalübertragung *in vitro*. Dies führt zu der Annahme, dass Veränderungen im Tryptophan Metabolismus zur metabolischen Verletzung beitragen. Zusammenfassend unterstützen diese Daten das neuartige Konzept, dass mikrobiell-metabolische Kreisläufe die intestinale Gewebehomöostase kontrollieren. Die Mitochondrien treten dabei als wichtige Integratoren von Signalen aus dem intestinalen Milieu auf, und unbewältigte metabolische Verletzungen stellen ein neuartiges Konzept in der Pathogenese von intestinaler Entzündung dar.

Abstract

The intestinal epithelium is an essential interface between the microbial ecosystem and the underlying mucosa, orchestrating immune-mediated and metabolic functions. Mitochondrial signaling and metabolism control the phenotype and function of intestinal epithelial cells, and mitochondrial perturbation is associated with chronic inflammation. Considering the metabolic requirements of the epithelial interface, it was hypothesized that disruption of microbial-metabolic circuits and failure of mitochondrial functionality at the intestinal interface contribute to the initiation and progression of tissue injury and chronic inflammation.

Conditional deletion of mitochondrial heat shock protein 60 (Hsp60) in the intestinal epithelium (Hsp60$^{\Delta/\Delta IEC}$) induces mitochondrial unfolded protein response (MT-UPR). Mitochondrial stress-induced dysfunction is accompanied by alterations in the cellular metabolism leading to irregular crypt architecture, causing transient tissue injury (referred to as metabolic injury). Epithelial renewal is orchestrated by Hsp60^{+} injury-associated regenerative stem cells and is disrupted in the absence of interleukin 10 (Hsp60$^{\Delta/\Delta IEC}$;$Il10^{-/-}$), demonstrating that metabolic injury accelerates inflammation in a susceptible host. In contrast, tissue aberration is mildly present in the proximal colon and absent in the distal colon of germfree Hsp60$^{\Delta/\Delta IEC}$ mice, supporting the hypothesis that bacteria are directly involved in regulating tissue injury and regeneration. Metabolic injury is associated with a rapid drop in species richness and changes in the bacterial community profile of Hsp60$^{\Delta/\Delta IEC}$ mice. Significantly enriched genera include *Bacteroides* spp. and closely related *Phocaeicola* spp., and shallow metagenomics further identified *B. uniformis*, *B. caecimuris,* and *Phocaeicola vulgatus.* Interestingly, dysbiotic changes of the intestinal microbiota persist in Hsp60$^{\Delta/\Delta IEC}$;$Il10^{-/-}$ mice. Selective mono-colonization of germfree Hsp60$^{\Delta/\Delta IEC}$ mice with *B. caecimuris* triggers tissue aberration and specific bacterial-derived indoles as well as host-derived tryptophan metabolites amplify MT-UPR signaling *in vitro*, suggesting that changes in tryptophan metabolism might contribute to metabolic injury.

In conclusion, these experimental data support the novel concept that microbial-metabolic circuits control intestinal tissue homeostasis. Mitochondria are emerging as the intriguing interceptors of milieu signals in the intestine, and unresolved metabolic injury is a novel concept in the pathogenesis of intestinal inflammation.

Table of contents

1. Introduction

The human gastrointestinal tract is a complex organ harboring a functionally diverse milieu of dietary factors, digestive mediators, and a dense microbial ecosystem close to the intestinal epithelium [1]. Both luminal factors and the underlying lamina propria are essential regulators of intestinal epithelial cell (IEC) homeostasis. Hence, alterations in the microbial milieu [2, 3], as well as genetic alterations [4], can contribute to gastrointestinal diseases, including inflammatory bowel diseases (IBD) and colorectal cancer (CRC). Emerging evidence implicates the influence of mitochondrial function and metabolism on IBD pathogenesis [5]. Since mitochondria are essential in sensing host and microbial-derived signals [6, 7], they emerge as pivotal players in intestinal tissue homeostasis and disease pathogenesis (Figure 1). Addressing the functional consequences of mitochondrial dysfunction in microbe-host mutualism will increase the understanding of gastrointestinal diseases and yield new therapeutic approaches.
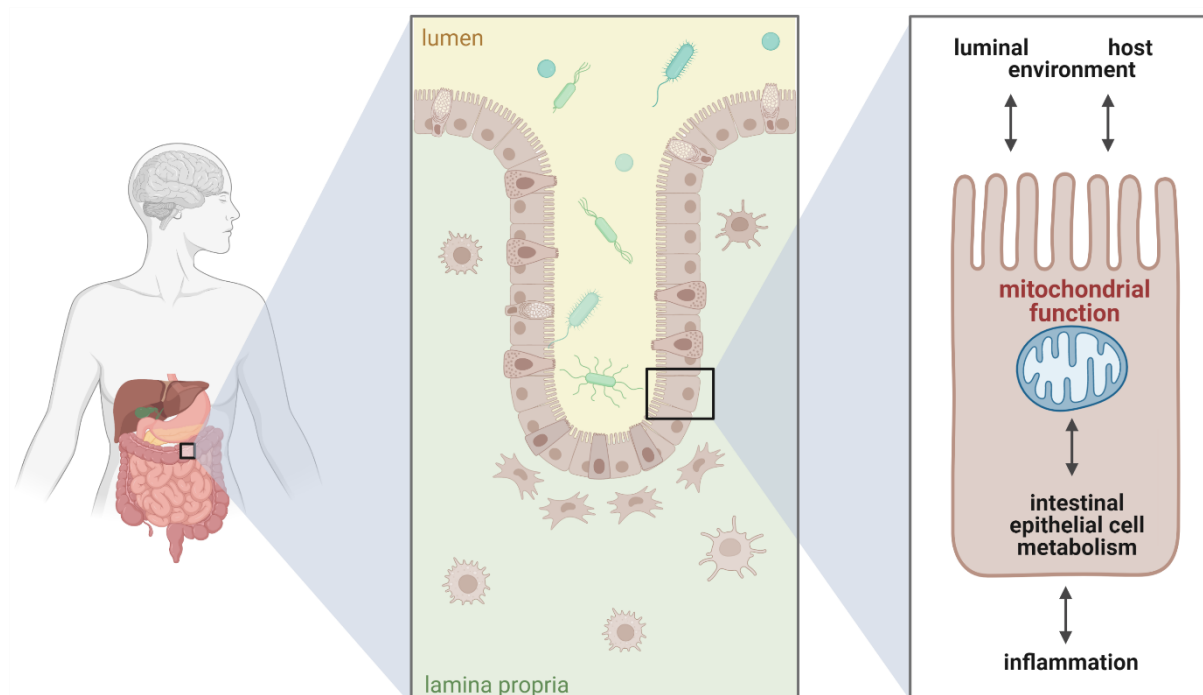
Figure 1: Mitochondrial function contributes to the homeostasis of the gastrointestinal tract.
The intestinal interface separates the gut lumen and host and is pivotal for maintaining tissue homeostasis. Both microbe-host interactions and the cellular tissue environment impact mitochondrial function and intestinal epithelial metabolism and hence tissue health and disease.

1.1. Intestinal epithelial anatomy and function

The gastrointestinal architecture consists of a small intestinal (duodenum, jejunum, ileum) and a large intestinal segment, whose primary function is the digestion and absorption of food [8]. The intestinal epithelium is crucial for digestive processes and forms a physical and immune-mediated barrier for host defense [9]. IECs are an integral part of the mucosal immune system, constituting a dynamic interface between the host and a complex microbial ecosystem with spatially adapted, often mutualistic mechanisms to acquire homeostasis towards the luminal milieu. Although the epithelium of the small and large intestine share a similar basic anatomical architecture, their biological functions and tertiary architecture are noticeably different. The small intestine is characterized by crypt and villus structures, providing a large resorptive surface, while longer crypts build the colonic architecture [6]. With estimated 1.400 cells being shed from a single villus tip per day (in the mouse), this single-layered interface (30-40 m^2) shows the highest turnover rate of any fixed-cell population in the body [10]. The complete cell layer is renewed every 3-5 days, most likely as a protective mechanism against injuries and infections [11]. Both self-renewal under homeostatic conditions and regeneration in response to injury are organized in the stem cell niche. Constantly dividing crypt-based columnar stem cells expressing the leucine-rich repeat-containing G protein-coupled receptor 5 (Lgr5) reside at the crypt base and give rise to progenitors feeding the transit-amplifying zone to terminally differentiate into mature secretory (Paneth cells, goblet cells, enteroendocrine cells, Tuft cells, and M cells) and absorptive cells (enterocytes) (Figure 2) [12]. Paneth cells contribute to stem cell homeostasis and anti-microbial defense in the small intestine. Goblet cells are spread throughout the entire epithelial lining of the digestive tract, specifically the colon, where the cells produce a thick and well-structured mucus layer responsible for the sequestration of bacteria from the host [13]. In addition to actively dividing intestinal stem cells (ISCs), a population of quiescent stem cells (+4 ISCs or reserve ISCs) is located at the +4 position above the crypt base. It is characterized by the expression of maker genes, including *Hopx, Bmi1, Tert,* and *Lrig1* [14-17]. These slow-cycling ISCs are less vulnerable to genotoxic stress and replace damaged crypt-based columnar stem cells in response to epithelial injury, ensuring tissue regeneration [15, 18]. The self-renewal capacity of ISCs plays a pivotal role in regulating healing processes upon tissue injury. In addition to ISC proliferation, IEC maturation and differentiation are essential for self-renewal and tissue healing. Hence, the balance between ISC quiescence, renewal, proliferation, and differentiation is pivotal in regulating intestinal homeostasis and is precisely controlled by several external and internal signals [6], including mesenchymal cells, fibroblasts, nerve and immune cells of the underlying tissue, as well as the microbial milieu [13, 19, 20].
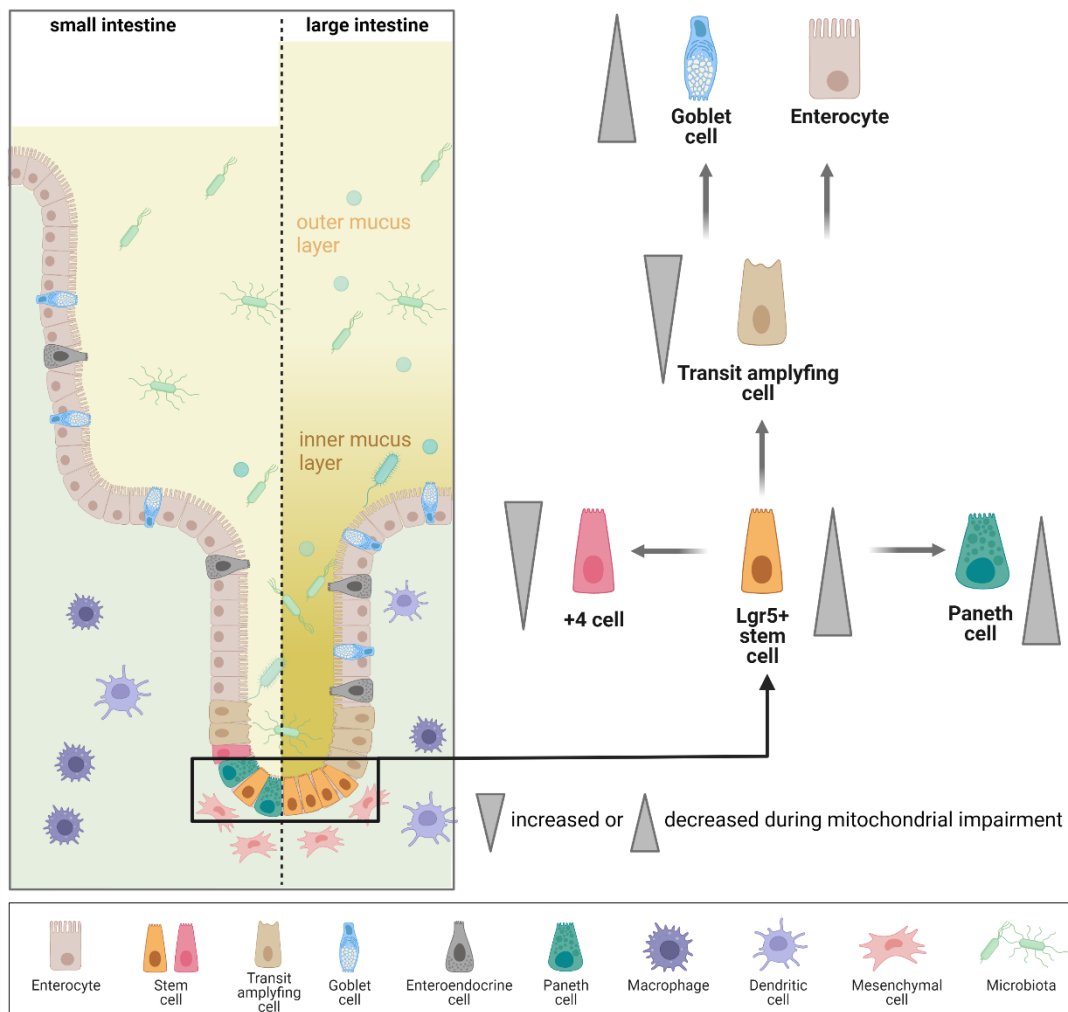
Figure 2: Overview of the different intestinal epithelial cell subpopulations.
The small and large intestine are organized as a monolayer of specialized epithelial cells. Lgr5+ intestinal stem cells are found at the crypt base, giving rise to transit-amplifying cells. These cells are highly proliferative and terminally differentiate into mature secretory and absorptive cells. During mitochondrial impairment, the balance of intestinal epithelial proliferation and differentiation is skewed (adapted from [21]).

1.2. Mitochondrial function and metabolism

Mitochondria are unique organelles that arose from endosymbiosis and comprise an outer and inner mitochondrial membrane, separating the intermembrane space and enclosing the inner matrix. Referred to as the 'powerhouse of the cell', mitochondria have long been reduced to their function in ATP generation. Nevertheless, beyond energy generation through oxidative phosphorylation (OXPHOS), tricarboxylic acid cycle (TCA), and fatty acid oxidation, they contribute, i.a., to reactive oxygen species (ROS) production, apoptosis, and immune responses and, hence, constitute a cellular signaling platform coordinating stress signaling pathways [21, 22]. Mitochondria are dynamic organelles organized in networks physically and functionally interacting with other cellular compartments, such as the endoplasmic reticulum

and peroxisomes. The function and morphology of mitochondria are linked and regulated through fusion and fission, and dysfunctional mitochondria producing high levels of ROS are removed via mitochondria-specific autophagy (mitophagy) [23]. Proliferation and differentiation of stem cells are thought to boost the demand for oxygen along with mitochondrial biogenesis due to increased requirements for energy and biosynthetic processes. Cytosolic glycolysis yields pyruvate, which can be (inter)converted to lactate or be used to generate acetyl-CoA, the initial molecule fueling the TCA cycle. The TCA cycle produces substrates for OXPHOS and metabolites serving as biosynthetic precursors and signaling molecules, controlling chromatin modifications and DNA methylation, responses to hypoxia, and immune functions [24]. Interestingly, Lgr5+ crypt-based columnar stem cells show a higher mitochondrial OXPHOS activity compared to other differentiated epithelial cells, and metabolic cooperation supporting stemness has been proposed between glycolytic Paneth cells and Lgr5+ crypt-based columnar stem cells that use Paneth cell-derived lactate to fuel their high demand for OXPHOS [25]. This metabolic compartmentalization is reflected by mitochondrial morphology, with Lgr5+ crypt-based columnar stem cells featuring fragmented and fused mitochondria and Paneth cells showing diminished mitochondrial numbers and lacking fused structures [26].

1.2.1. Mitochondrial unfolded protein response (MT-UPR)

Mitochondrial proteostasis is essential to coordinate cellular metabolism, including OXPHOS, TCA cycle, and fatty acid biosynthesis. Notably, mitochondrial metabolic activity affects epithelial cell fate and phenotype [21]. The mitochondrial unfolded protein response (MT-UPR) is a set of conserved signaling pathways from yeast to mammals. It is initiated in response to protein aggregation or misfolding in the mitochondrial matrix [27] (Figure 3). This autoregulatory mechanism adapts mitochondrial function to cellular demand, including self-renewal and differentiation, which determines epithelial homeostasis or skews the balance to the development of intestinal pathologies.

The central transcription factor C/EBP homologous protein (Chop) [28, 29] induces with its cofactor C/EBPß via c-Jun-N-terminal protein kinase 2 (Jnk2) retrograde signaling to the nucleus. Targets of the MT-UPR retrograde signaling include a set of chaperones and proteases located in the mitochondrial matrix, such as the evolutionary conserved heat shock protein 60 (Hsp60) and the caseinolytic mitochondrial matrix peptidase (ClpP). An additional branch of the MT-UPR signaling pathway includes ROS-mediated activation of the protein kinase B (Akt), which in turn phosphorylates estrogen receptor-α (ERα), leading to the transcription of mitochondrial regulator nuclear respiratory factor 1 (Nrf1) and the intermembrane-localized serine protease Htra2 [21]. Moreover, activation of the NAD-

dependent protein deacetylase sirtuin 3 (Sirt3) induces forkhead box transcription factor 3 (Foxo3) accumulation in the nucleus and subsequent transcriptions of mitophagy genes and the ROS detoxification enzyme superoxide dismutase 2 (Sod2) [21]. The activating transcription factor 5 (Atf5) constitutes an additional key regulator of the MT-UPR pathway and is a mammalian homolog of the well-described stress-activated transcription factor (atfs-1) in *Caenorhabditis elegans*. Under homeostatic conditions, Atf5 is imported into mitochondria via its N-terminal mitochondrial targeting sequence and degraded by the mitochondrial Lon protease. However, Atf5 traffics to the nucleus during mitochondrial stress via its C-terminal nuclear localization sequence, where it activates MT-UPR target genes, including mitochondrial chaperones, proteases, and respiration and proliferation-related genes [21, 30]. Collectively, mitochondrial signaling pathways are essential in maintaining cellular function and metabolism [31] to ensure intestinal epithelial integrity.
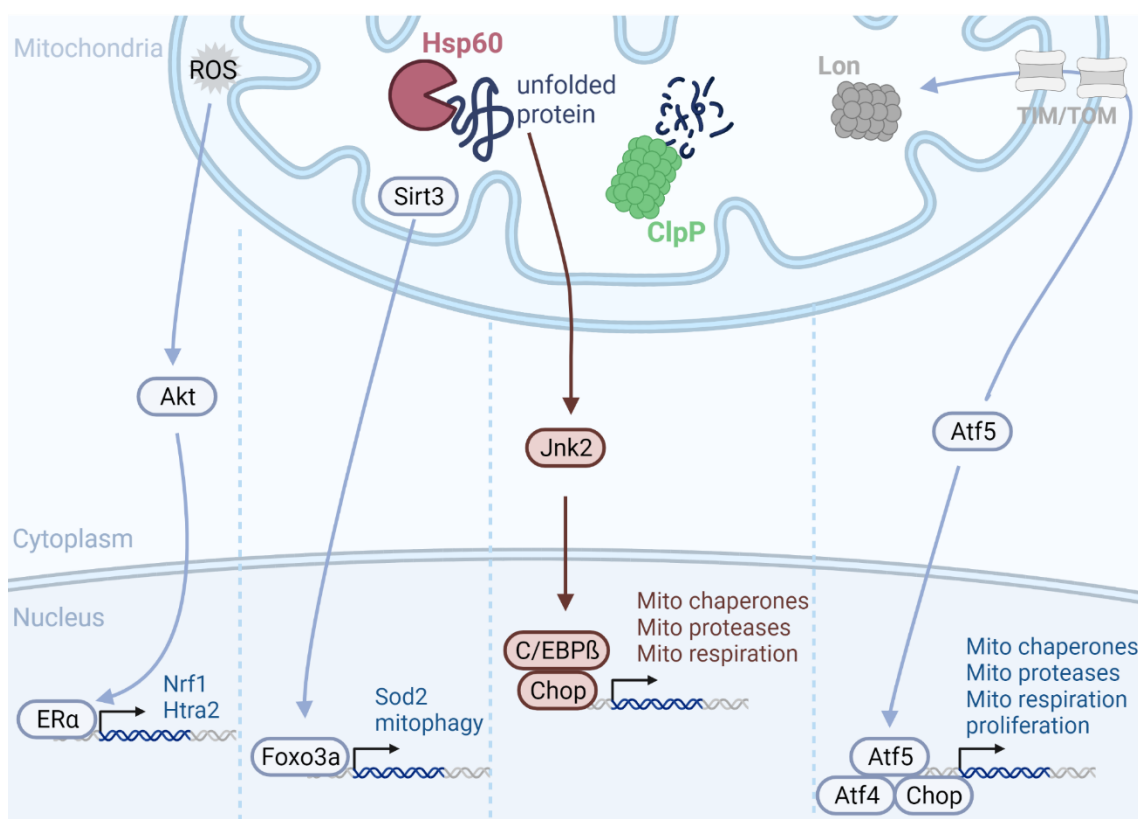
Figure 3: Overview of the different MT-UPR retrograde signaling pathways.
Accumulation of unfolded or misfolded proteins in the mitochondrial matrix induces mitochondrial perturbations. The mammalian MT-UPR pathway (constituting several distinct signaling pathways) is activated to restore protein homeostasis. Accumulation of unfolded proteins in the mitochondrial matrix under stress conditions leads to activation of transcriptions factors, including C/EBP homologous protein (Chop) and activating transcription factor (Atf) 4 and Atf5, resulting in transcription of genes involved in mitochondrial proteostasis (mitochondria-specific chaperones and proteases) as well as genes regulating mitochondrial respiration and other aspects of cellular metabolism. Abbreviations: Hsp60: heat shock protein 60; ClpP: caseinolytic mitochondrial matrix peptidase; Chop: C/EBP homologous protein; Jnk2: c-Jun-N-terminal protein kinase 2; ROS: reactive oxygen species; Sirt3: sirtuin 3; Akt: protein kinase B; ERα: estrogen receptor-α; Nrf1: nuclear respiratory factor 1; Foxo3: forkhead box transcription factor 3; Sod2: superoxide dismutase 2; Atf4/5: activating transcription factor 4/5. (adapted from [21]).

1.3. Mitochondrial dysfunction in the etiology of chronic intestinal diseases

Mitochondria emerge as critical players in intestinal homeostasis, and mitochondrial dysfunction is associated with many cellular diseases. For instance, reprogramming of mitochondrial metabolism is a hallmark of cancer, and several mitochondrial genes are associated with a poor CRC prognosis [32]. In addition, ~5% of IBD susceptibility genes regulate mitochondrial homeostasis [33], indicating an essential role of mitochondrial dysfunction in the pathogenesis of IBD. IBD are lifelong, chronic disorders with accelerating incidence and prevalence in industrialized countries [34-36], including the two main idiopathic pathologies Crohn's disease (CD) and ulcerative colitis (UC). While the mucosal inflammation in UC is restricted to the colon, CD predominantly affects the terminal ileum and is characterized by transmural inflammation [37, 38]. The current paradigm for the pathogenesis of these multifactorial diseases comprises host genetic susceptibility, environmental triggers, microbial challenges, and a dysregulated immune response [39] (Figure 4). Genome-wide association studies identified more than 240 target regions for IBD susceptibility [40-42], which regulate several critical biological functions, including mucosal barrier integrity [43], organelle stress, and immune defense, as well as immunoregulation [44, 45]. Prominent genes implicated are nucleotide-binding oligomerization domain-containing protein 2 (*NOD2*) [46, 47] and autophagy-related 16 like 1 (*ATG16L1*) [48, 49]. The inflamed tissue is characterized by increased recruitment of macrophages, neutrophils, and T-cells, which elevate the production of pro-inflammatory cytokines and chemokines [50, 51].
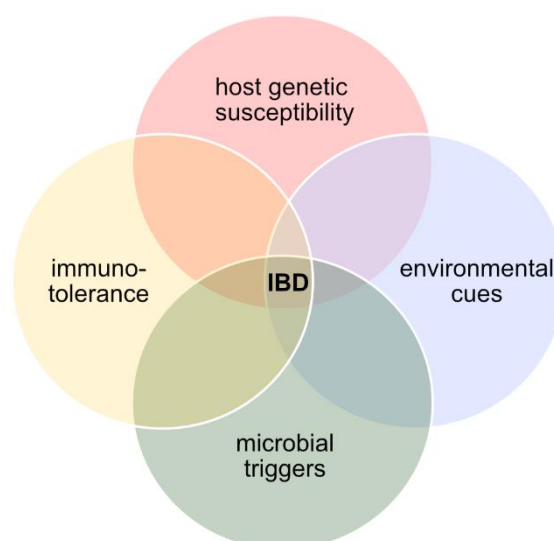
Figure 4: IBD is a multifactorial disease with distinct, interacting contributors.
Host genetic susceptibility, environmental cues, a dysregulated immune system and microbial triggers interact and impact IBD pathophysiology. Abbreviation: IBD: inflammatory bowel diseases.

The onset and recurrence of disease are most likely triggered by unknown environmental agents, such as smoking [52] or microbial factors [53]. Evidence suggests that loss of oral tolerance towards the commensal microbiota [54] and invasion of specific pathogens, including the most prominent adherent-invasive *Escherichia coli* [55], *Bacteroides fragilis* [56] and *Ruminococcus gnavus* [57], influences inflammation. In line with the high energy demand of the inflamed mucosa, loss of metabolic circuits between microbiota and host, including butyrate [58], carnitine [59], purine [60], and tryptophan [61] metabolism, are involved in the development of chronic inflammation. Colonizing germfree rodent models with disease-relevant bacteria and fecal material from patients re-establishes chronic intestinal inflammation [62, 63], substantiating the microbiome's causal role in IBD's pathogenesis.

CD and UC are associated with an increased risk for colitis-associated colon cancer (CAC) [64]. CAC and sporadic colon cancer are two forms of CRC with distinct disease phenotypes and immune profiles [65]. While sporadic CRC develops from the adenoma-carcinoma pathway, CAC arises from flat dysplastic mucosa following the inflammation-dysplasia carcinoma pathway [66], is diagnosed at a younger age (~ 20 years earlier than the average of 70 years) and shows poorer survival [67].

The intestinal epithelium represents the frontline in the pathogenesis of IBD and is challenged by recurrent cycles of tissue injury followed by (incomplete) healing processes. Distinctive changes of IECs in IBD pathophysiology include loss of Lgr5+ ISCs [68] and increased transit-amplifying compartment, a feature characteristic for reduced differentiation. In line, a reduction in Paneth cell numbers [68, 69] and loss of mucin-producing goblet cells [70] is an early event in intestinal inflammation. The associated decrease of the colonic mucus barrier and bacterial penetration into the inner mucus layer predisposes the host to colonic inflammation and CRC pathogenesis [6, 70-72].

1.3.1. Metabolic injury as a novel concept in IBD

Previously published data showed sustained expression of Hsp60 in small intestinal and colonic epithelial cells in IBD patients [73]. Moreover, histological analysis of inflamed tissue from IBD patients revealed an increase in Atf5 (unpublished data), suggesting persistent activated MT-UPR signaling throughout the intestinal epithelium under conditions of chronic inflammation. Transient and cell-specific induction of these MT-UPR mediators reflects homeostatic responses to cellular demand. At the same time, sustained and uncontrolled activation of MT-UPR disrupts the structural and functional organization of the epithelium and is associated with chronically progressing pathologies, such as IBD [21].

In line, overexpression of the mitochondrial chaperone prohibitin 1 [74] or its nanoparticle-based therapeutic delivery [75] reduces the severity of DSS-induced colitis in mice, and prohibitin 1 deletion in Paneth cells induces ileitis [76]. Moreover, it was shown that the postoperative recurrence risk of patients with Crohn's disease is linked to mitochondrial dysfunction in the small intestinal stem cell niche [68]. In addition, mitochondrial stress induced by a conditional Hsp60 deficiency in the small intestinal epithelium of mice demonstrated that impaired mitochondrial function initiated stem cell loss, followed by the subsequent appearance of a regenerative crypt architecture characteristic for intestinal injury responses [77]. Interestingly, liver-specific Hsp60 deficiency resulted in cholangiocellular tumor formation induced by the paracrine release of inflammatory and proliferative mediators, suggesting that metabolic injury leads to severe pathologies in the context of other highly regenerative organs [78].
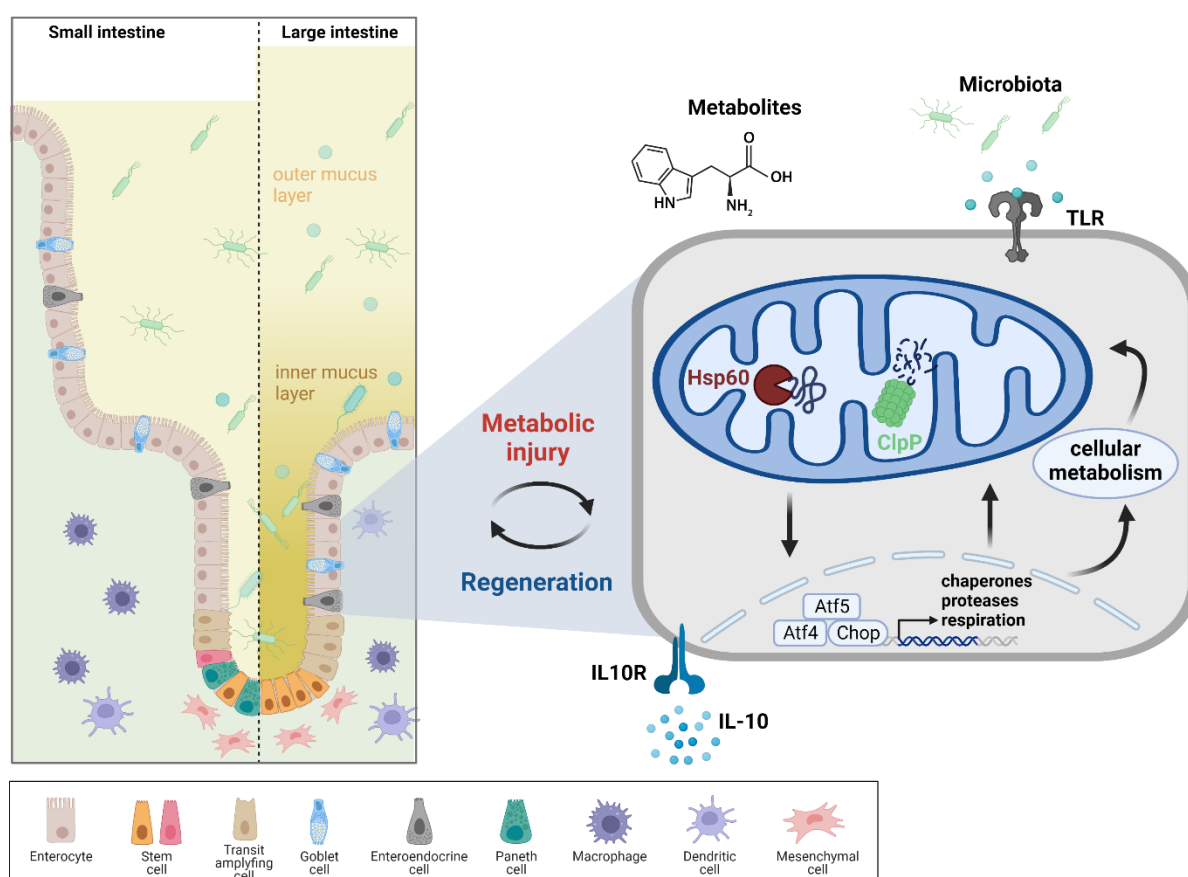
Figure 5: Mitochondria-related mechanisms of the MT-UPR regulate epithelial cell functions during tissue homeostasis and are disrupted during chronic inflammation.

In intestinal crypts, MT-UPR and mitochondrial metabolism control the self-renewal and proliferative capacity of the stem cell compartment and the transit-amplifying zone. Thus, the metabolic plasticity of IECs likely determines the ability for tissue reconstitution after metabolic injury. The epithelial tissue environment also interacts with and impacts IEC mitochondrial function, regulating regenerative tissue responses. Interleukin (IL)-10, modulating inflammatory and wound healing processes might directly target mitochondrial metabolism and MT-UPR-related mechanisms to confer their functions on epithelial reconstitution. Abbreviations: TLR: Toll like receptor; Atf4/5: activating transcription factor 4/5; Hsp60: heat shock protein 60; ClpP: caseinolytic mitochondrial matrix peptidase; Chop: C/EBP homologous protein; IL-10: interleukin 10; IL10R: interleukin 10 receptor. (adapted from [6]).

Considering the epithelial interface's metabolic requirements, especially under chronic inflammation conditions, it was hypothesized that mitochondrial perturbation of the epithelium is an underlying or at least strongly contributing mechanism in inflammation-associated tissue injury. This process is referred to as metabolic injury, defined as disturbances of the cellular metabolism causing tissue wounding, supporting the idea that mitochondrial exhaustion contributes to functional perturbation in IBD. This hypothesis backs the notion that the impaired metabolic flexibility of IECs impacts the regenerative capacity of the intestinal mucosa and renders the epithelium susceptible to inflammatory cues (Figure 5) [79].

1.4. Intestinal tissue environment in regulating metabolic injury

Both radiation and inflammation-induced intestinal injury are characterized by a loss of ISCs in the crypt base, eventually leading to apoptosis of the intestinal epithelium [68, 80]. Tissue regeneration upon injury is essential to restore mucosal homeostasis, requiring a tight regulation of epithelial renewal, proliferation, and (de)differentiation. The self-renewal of Lgr5+ ISCs in the crypt base is pivotal in re-gaining a normally functioning epithelium. Upon injury-mediated ablation of Lgr5+ ISCs, reserve ISCs [14-17] or de-differentiated Paneth cells [81, 82] reconstitute the epithelium. Of note, augmented intestinal stemness caused by genetic alterations demonstrated a protective effect of T-cell-mediated [83] and chemically induced colitis [84], providing a proof-of-concept for targeting the ISC niche to prevent inflammation [6]. Further, monitoring the proliferative capacity plays a pivotal role, as increasing proliferation depicts a hallmark in inflammation-associated tissue injury and neoplastic changes [85].

It was proposed that intrinsic defects in cellular metabolism (= metabolic injury) cause epithelial dysfunction, evoking attempts of the ISC niche to reconstitute standard tissue architecture and function [79]. Vice versa, functional adaptations of the ISC niche are initiated by extrinsic signals, including the microbial milieu and tissue-related factors [6].

The lamina propria is a connective tissue comprising intestinal immune cells, endothelial cells, neurons, mesenchymal cells, fibroblasts, and myofibroblasts. Next to integrating microbial signals, mediators from immune and mesenchymal cells converge at the intestinal interface [9], influencing the ISC niche during wound healing and tissue regeneration (Figure 6).
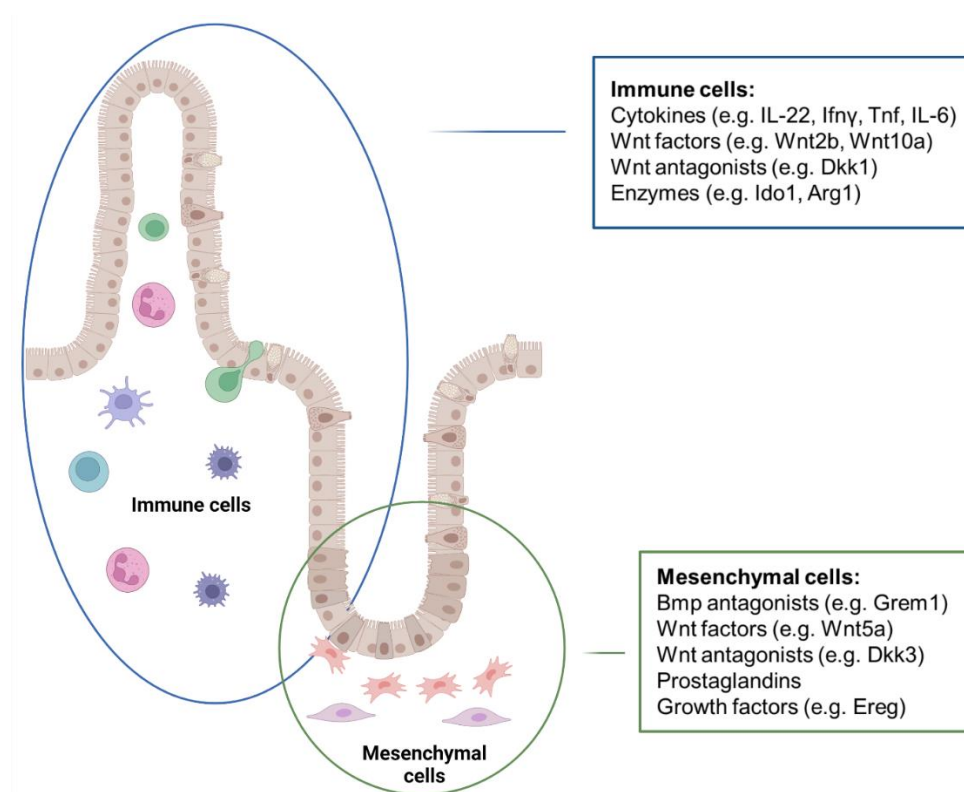
Figure 6: Microenvironment signals influence the intestinal stem cell niche during tissue injury and regeneration.
Immune cells and mesenchymal cells produce a diverse range of cytokines, chemokines, growth factors, wingless (Wnt) factors and antagonists, BMP antagonists, and growth factors, mediating crucial cross-talk between different cell types to orchestrate tissue homeostasis and repair following injury.

1.4.1. Immune cells and cytokines

Intestinal inflammatory processes and tissue healing depend on immune cells and their secreted factors [86]. Innate lymphoid cells, T-cells, dendritic cells, neutrophils, macrophages, and intraepithelial lymphocytes reside close to IECs and communicate via enzymes, cytokines, and a diverse range of wingless (Wnt) and growth factors. For instance, myeloid-derived suppressor cells, neutrophils, and regulatory macrophages express the enzyme arginase 1 (Arg1), leading to a depletion of the amino acid L-arginine, a well-known immunoregulatory mechanism [87, 88]. Arginase represents a conserved enzyme involved in the final step of the urea cycle and is involved in IL-10-mediated metabolic regulation [89] and wound healing [90]. Another crucial enzyme in immune-epithelial cross-talk is the inducible nitric oxide synthase 2 (Nos2), which converts arginine to citrulline and nitric oxide and is predominantly produced by macrophages [91].

Next to these enzymes, resident immune cells, infiltrating inflammatory cells, and IECs produce diverse cytokines and chemokines, influencing IEC proliferation, apoptosis, and permeability [92, 93]. For instance, the pro-inflammatory cytokines tumor necrosis factor (Tnf),

IL-6, and IL-17 play an integral role in the pathogenesis of IBD [94] and impact both injured IECs and their proliferative response [95-97] as well as mitochondrial metabolism [6, 98]. The anti-inflammatory cytokine IL-10, on the other hand, is crucial in maintaining immune homeostasis and promoting tissue healing in IBD pathology [99]. It is predominantly produced by T-cells and macrophages [100] during the acute phase of injury, but also IECs, suggesting both paracrine and autocrine roles in regulating tissue homeostasis [100, 101]. While IL-10 stimulates IEC proliferation and augments barrier integrity [102, 103], loss-of-function mutations of *IL10* and *IL10RA1* are associated with IBD pathogenesis [104]. Interestingly, IL-10 reprograms the cellular metabolism of activated macrophages by inhibiting glucose uptake and glycolysis, promoting OXPHOS and suppressing mammalian target of rapamycin (mTOR) activity, consequently enhancing the elimination of dysfunctional mitochondria by mitophagy [105]. In addition, IL-10 inhibits activating transcription factor 6 (Atf6)-mediated UPR as one of three conserved arms of the endoplasmic reticulum stress machinery, providing first evidence for the relevance of IL-10 family members to modulate organelle-related UPR in the epithelium [106]. In summary, disruption of the IL-10 signaling axis contributes to the pathogenesis of IBD, especially early-onset disease, and the risk of developing CAC.

1.4.2. Mesenchymal cells

Besides epithelial-immune cell cross-talk, epithelial-mesenchymal cell and epithelial-epithelial communication are pivotal players in maintaining tissue homeostasis. Wnt signaling through a diverse range of Wnt ligands and antagonists produced by Paneth cells and surrounding stromal cells crucially determines crypt niche function by regulating ISC proliferation [107]. While Paneth cells support ISCs via secretion of Wnt3, Wnt6, and Wnt9b [108, 109], mesenchymal cells produce Wnt2b, Wnt4, and Wnt5a [108, 110]. In line, depletion of the Wnt antagonist Dickkopf 1 (Dkk1) increases a proliferative response during wound repair after colitis [111]. Furthermore, hyperactivation of the Wnt pathway is believed to be an initiating and driving event in CRC pathogenesis [112]. The subepithelial mesenchyme further provides bone morphogenetic protein (Bmp) antagonists, such as gremlin 1 (Grem1) and noggin, to suppress BMP-driven terminal differentiation of ISCs [113], in turn regulating ISC homeostasis and repair after injury [114]. Epidermal growth factor (Egf) ligands, including neuregulin 1 (Nrg1) [115] and epiregulin (Ereg) [116], display another group of mesenchymal-secreted molecules controlling tissue homeostasis.

1.5. The human intestinal microbiota

The digestive tract harbors a complex and dynamic array of microorganisms, comprising bacteria, archaea, viruses, and fungi [1], collectively termed intestinal microbiota. Bacterial colonization gradually increases from the proximal to the distal part of the intestine, reaching the highest density of 10^{12} colony-forming units per gram of luminal content in the colon [117]. Here the microbiota is dominated by the two major phyla *Bacillota* (previously renamed; old name: *Firmicutes*) and *Bacteroidota* (previously renamed; old name: *Bacteroidetes*) [118, 119]. Colonic motility is substantially slower than motility of the small intestine, leading to prolonged retention of luminal content (20-50 hours) and the accumulation of biologically active metabolites [120]. The host shapes the niche for commensal microbiota and responds to non-pathogenic bacteria and infections [121]. The relationship between host and microbes is mutualistic, with microbes regulating and maintaining intestinal tissue homeostasis via microbial metabolites, such as short-chain fatty acids and conjugated bile acids. Disruption of this microbiome-host symbiosis contributes to the initiation and progression of diseases. Examples include immune and metabolic pathologies, such as IBD [122], graft-versus-host disease [123], and type 2 diabetes [124]. Interestingly, these pathologies correlate with compositional shifts in the intestinal microbiome, referred to as dysbiosis [125].

1.5.1. Mitochondria as metabolic integrators of microbial signals

The intestinal interface's functional plasticity and barrier integrity depend on host-related factors' coordinated contribution and the microbial milieu [7]. Specific pathogens are reported to interact with mitochondria to impact IEC homeostasis. For instance, infection with *Listeria monocytogenes* causes mitochondrial network fragmentation in a human IEC line, consistent with Helicobacter pylori vacuolating cytotoxin A inducing mitochondrial fragmentation in gastric epithelial cells [126]. Of note, *Helicobacter pylori*-infected patients display enhanced expression of the stem cell marker olfactomedin 4 (Olfm4) [127], substantiating the interrelation of microbial signaling, mitochondrial activity, and ISC niche.

Additionally, the intestinal microbiota modulates epithelial metabolic function through direct contact or release of products/metabolites [128-130] that emerge as essential players in tissue healing [5]. Examples: For instance, SCFAs promote the growth of intestinal organoids and regulate genes involved in energy metabolism and mitochondrial biogenesis [131, 132]. Moreover, differentiated colonocytes metabolize butyrate, preventing ISCs from butyrate exposure, and thus, the colonic crypt architecture has been suggested to form a metabolic barrier [133]. In line, studies in germfree mice demonstrate a profound effect of the microbiota

on IEC maturation and differentiation [134], with goblet cell numbers significantly increased in colonized mice [135]. Notably, the microbiota composition and functions differ along the gastrointestinal tract, and IECs are extensively adapted to their specific microbial milieu.

1.5.2. Tryptophan metabolism

In addition to innate immune mechanisms integrating microbial signals, IECs are equipped with various sensors, receptors, and transceptors, like purinergic receptors (ATP receptors), chemosensitive receptors (aryl hydrocarbon receptor (AhR)) and olfactory receptors [136-139], to surveil the cellular environment and adapt the metabolic state accordingly. For instance, specific olfactory receptors respond to microbial metabolites, including SCFAs, affecting whole-body metabolism by activating the release of incretin hormones from enteroendocrine cells [140] and modulating tissue responses to colitogenic stimuli [139]. In line, Ahr signaling is a well-described pathway modulated by endogenous and microbiota-derived compounds such as butyrate and derivatives of tryptophan (indoles and kynurenines) [138, 141]. Ahr is a ligand-activated transcription factor in the cytosol and inner mitochondrial membrane [142], impacting mitochondrial function and mucosal healing processes [141, 142]. In particular, host-derived kynurenines can alter cellular respiration and metabolic pathways [143], and by maintaining ISC homeostasis and modulating Notch signaling, Ahr has been shown to enhance epithelial barrier function and protect from inflammatory damage [144, 145]. Concomitantly, microbial-derived Ahr ligands induce immunoregulatory T-cells [146], regulate IL-10 receptor expression in IECs [147] and maintain an IL-22 mucosal response via innate lymphoid cells [148-150].

The microbiota can degrade the essential amino acid tryptophan via the indole pathway or the host via the kynurenine and serotonin pathways (Figure 7). The host's rate-limiting enzyme indolamine 2,3-dioxygenase 1 (*Ido1*) catabolizes most luminal tryptophan. It is expressed by a specific subset of dendritic cells [151] but also epithelial cells [152] and tumor cells [153]. Interestingly, the downstream-produced kynurenines are sensed by IECs via AhR, regulating epithelial IL10R1 expression and promoting wound healing [147]. Ido1 fosters immune tolerance by limiting activated T-cell response and promoting regulatory T-cell activity [154], diminishing colonic inflammation and reducing disease severity [7]. Conversely, *IDO1* expression, tryptophan depletion, and elevated kynurenine levels positively correlate with graft versus host disease severity [155] and IBD activity [156, 157]. The microbiota converts ~5% of luminal tryptophan to indole and several downstream metabolites, including tryptamine, indole-3-acetic acid (IAA), and indole-3-propionic acid (IPA), directly via the enzyme tryptophanase or indirectly via several other enzymes [158]. Increasing evidence suggests an

interaction of bacterial tryptophan metabolites with the host, including functions as antimicrobial agents, signaling molecules, AhR ligands, regulators of barrier function, and gut hormone secretion [158]. For instance, mice fed a tryptophan-deficient diet exhibit altered microbial composition and increased inflammatory response [159]. In line, dextran sulfate sodium (DSS)-induced colitis is ameliorated through supplementation with dietary tryptophan [160] or indole derivatives [161].
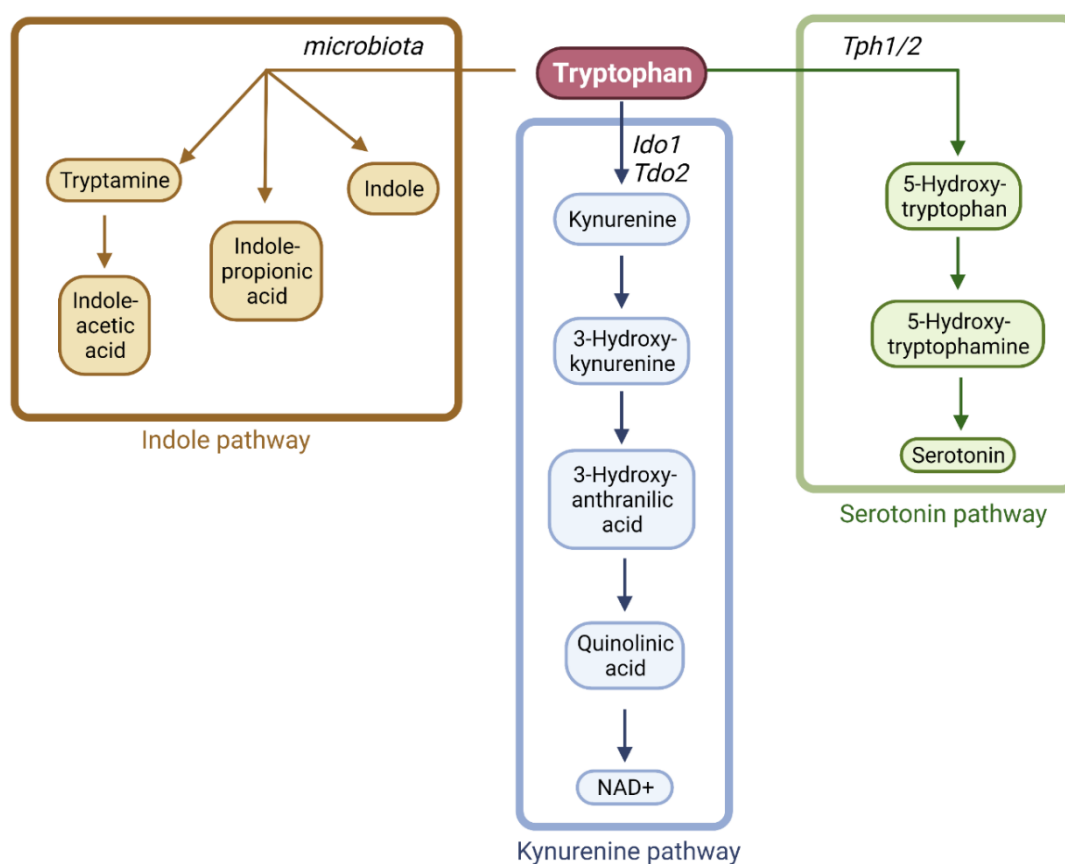
Figure 7: The different pathways of tryptophan metabolism.
The host converts dietary-derived luminal tryptophan via the kynurenine and serotonin pathway. Ido1 is a key enzyme generating kynurenines, similar to Tph1/2 in serotonin production. In addition, the microbiota catabolizes tryptophan to indole and several indole metabolites via the indole pathway. Abbreviations: *Tph1/2*: tryptophan hydroxylase 1; *Ido1*: indolamine 2,3-dioxygenase 1; *Tdo2*: tryptophan-2,3-dioxygenase 2.

In summary, metabolites derived from intestinal microbes and IECs under homeostasis and stress conditions might act to shape intestinal immune responses and epithelial cell metabolism [6], underlining the hypothesis that microbe-host interactions are pivotal to intestinal health [162].

2. Aim of the work

The intestinal epithelium is the most regenerative tissue in the human body, located near a dense and functionally diverse microbial milieu. Next to luminal factors, IECs integrate mediators from immune and mesenchymal cells to ensure the intestinal interface's functional plasticity and barrier integrity. Mitochondrial signaling and metabolism control the phenotype and function of IECs, and mitochondrial perturbation is associated with chronic inflammation [21]. Considering the metabolic requirements of the epithelial interface, especially under conditions of chronic inflammation, it is assumed that disruption of microbe-host interactions and failure of mitochondrial functionality at the intestinal interface contributes to the initiation and progression of tissue injury and chronic inflammation. To date, scant attention has been paid to the connection between microbiota, mitochondria, and disease development. The present work aims to investigate the role of Hsp60 deficiency-induced metabolic injury on tissue regeneration under homeostatic and pathological conditions. Thus, the impact of an IEC-specific Hsp60 deficiency (Hsp60$^{\Delta/\Delta IEC}$) was analyzed on the colonic phenotype with respect to proliferation, stemness, and microbial composition. It is already known that Hsp60 deletion induces MT-UPR signaling and hyperproliferative crypts in the small intestine [77]. In parallel, IEC-specific ClpP deficiency (ClpP$^{\Delta/\Delta IEC}$) was investigated using comparable readouts. A particular focus was on tissue injury and resolution under cancerogenic and inflammatory conditions. Therefore, Hsp60$^{\Delta/\Delta IEC}$ mice were treated with the chemical carcinogen azoxymethane (AOM) to generate a pro-cancer background or crossed with IL-10 deficient mice to induce a pro-inflammatory environment. Phenotypic characterization, analysis of tissue architecture, and microbial composition during tissue healing after injury were central matters of investigation. Moreover, *ex vivo* intestinal organoid cultures from the respective mouse models were generated to decipher cellular and molecular mechanisms, and co-culture systems with intestinal mesenchymal cells and macrophages were established to dissect paracrine signaling mechanisms and model cellular communication. To clarify the role of the microbiota on metabolic injury in response to mitochondrial perturbation, germfree Hsp60$^{\Delta/\Delta IEC}$ mice were generated and analyzed. The findings were elaborated by specific colonization with the Oligo-Mouse-Microbiota (OMM^{12}) synthetic bacterial community, *Bacteroides caecimuris*, a combination of *Bacteroides caecimuris* and *Akkermansia muciniphila* or *Limosilactobacillurs reuteri*. Further, the role of bacterial-derived indoles was analyzed *in vitro* using organoid cultures.

In summary, the role of mitochondria as intriguing receptors of milieu signals in the intestine was addressed using a mouse model for metabolic injury and mitochondrial UPR under homeostatic and pathological conditions.

3. Material and Methods

3.1. Animal experiments

3.1.1. Ethics statement

All animal experiments, as well as maintenance and breeding of mouse lines, were approved by the Committee on Animal Health Care and Use of the state of Upper Bavaria (Regierung von Oberbayern; AZ ROB-55.2-2532.Vet_02-14-217, AZ ROB-55.2-2532.Vet_02-20-58, AZ ROB-55.2-2532.Vet_02-18-37) and performed in strict compliance with the EEC recommendations for the care and use of laboratory animals (European Communities Council Directive of November 24, 1986 (86/609/EEC)).

3.1.2. Mouse models and animal housing

Mice with a conditional deletion of *Hsp60* or *ClpP* in intestinal epithelial cells are models for metabolic injury or mitochondrial impairment. Hsp60$^{flox/flox}$ and ClpP$^{flox/flox}$ mice were crossed with Cre transgenic *Villin*CreER^{T2-Tg} mice (C57Bl/6N) to induce epithelial cell-specific *Hsp60* knockout (Hsp60$^{\Delta/\Delta IEC}$) or *ClpP* knockout (ClpP$^{\Delta/\Delta IEC}$) mice. *Villin*CreER^{T2-Tg} mice (C57Bl/6N) were provided by Klaus-Peter Janssen (Klinikum Rechts der Isar, TU München). In addition, both Hsp60$^{\Delta/\Delta IEC}$ and ClpP$^{\Delta/\Delta IEC}$ mice were crossed with entire-body IL-10 protein knockout (*Il10$^{-/-}$*) mice (C57Bl/6J), a widely used model for chronic enterocolitis [163], to generate Hsp60$^{\Delta/\Delta IEC}$;*Il10$^{-/-}$* and ClpP$^{\Delta/\Delta IEC}$;*Il10$^{-/-}$* mice. Table 1 summarizes all mouse breedings.

Table 1: Mouse lines and characteristics.

Mouse line		Characteristics	Mode	Hygiene status
Hsp60$^{\Delta/\Delta IEC}$ (Hsp60$^{flox/flox}$ x *Villin*CreER^{T2-Tg})		Villin-based deletion of Hsp60	tamoxifen-inducible recombination of Hsp60 in IECs	SPF, GF
	x *Il10$^{-/-}$*	+ whole-body knockout of IL-10	+ constitutive IL-10 deficiency	SPF
ClpP$^{\Delta/\Delta IEC}$ (ClpP$^{flox/flox}$ x *Villin*CreER^{T2-Tg})		Villin-based deletion of ClpP	tamoxifen-inducible recombination of ClpP in IECs	SPF
	x *Il10$^{-/-}$*	+ whole-body knockout of IL-10	+ constitutive IL-10 deficiency	SPF

Mice were housed under specific pathogen-free (SPF) or germfree (GF) conditions according to the criteria of the Federation for Laboratory Animal Science Associations (FELASA) (12 h light/dark cycles at 24–26°C). All mice received a standard diet (autoclaved V1124-300, Ssniff, Soest, Germany) *ad libitum*, autoclaved water and were sacrificed by CO_2, isoflurane, or cervical dislocation. Mice were monitored and aborted when a combined score considering weight loss, changes in stool consistency, general behavior, and general state of health was attained. Germfree status was controlled by the cultivation of feces in Wilkins-Chalgren Anaerobe (WCA) broth (Oxoid Limited, Hampshire, UK) before the start of the experiments and at sampling time.

3.1.3. Mouse experiments

3.1.3.1. Induction of postnatal genomic recombination

For conditional *Hsp60* or *ClpP* deletion, male mice from all lines listed in Table 1 and their appropriate controls were kept on a phytoestrogen-reduced diet (V1154-300, Ssniff, Soest, Germany) for four weeks starting from the age of 6 weeks. At the age of 10 weeks, mice were put on tamoxifen (4-OHT)-diet (CreActive T400 (10 mm, Rad), Genobios, Laval, France) *ad libitum* for seven days. After the induction phase, the feed was switched back to the phytoestrogen-reduced diet. During and after the induction phase, body weight was monitored daily. Body weight, general condition, behavior, and intestinal symptoms were assessed using a score according to the respective approved application for animal experiments. Mice were sampled on days 0, 4, 8, 11, and 14 after the end of the induction phase.

3.1.3.2. AOM treatment

Hsp60$^{\Delta/\Delta IEC}$ mice were subjected to two doses of the chemical cancerogen azoxymethane (AOM; Sigma- Aldrich, Taufkirchen, Germany). The mutagenic agent AOM facilitates base mispairings by alkylation of DNA, leading to spontaneous colonic tumor development [164]. Mice were intraperitoneally (i.p.) injected with 10mg/kg bodyweight AOM on day 4 and day 11 after the tamoxifen induction phase (treatment scheme Figure 17). Three consecutive days after i.p. injection, body weight, general condition, behavior and intestinal symptoms were assessed using a score according to the respective approved application for animal experiments. Mice were sampled at an early (day 18) and a late (day 70) time point.

3.1.3.3. Selective colonizations

For selective colonizations, GF Hsp60$^{flox/flox}$ x *Villin*CreER^{T2-Tg} and Hsp60$^{flox/flox}$ x *Villin*CreER^{T2-Tg} x IL10$^{-/-}$ mice, and their appropriate control mice were rectally gavaged (two times) using 20 Gauge gavage needles (Fine Science Tools, Heidelberg, Germany) at the age of 6 weeks with

the Oligo-Mouse-Microbiota (OMM[12]) synthetic bacterial community [165], *Limosilactobacillus reuteri* I49 (DSM 32035) or *Bacteroides caecimuris* I48 (DSM 26085) alone or in combination with *Akkermansia mucinicphila* YL44 (DSM 26127). After the 2nd gavage, induction of postnatal genomic recombination was performed as described before. For preparation of the gavages, each bacteria was grown in Hungate tubes in Akkermansia medium [166] (AAM) for 24-48h under anaerobic conditions. Bacterial growth was assessed using OD600, adjusted to mix the same amount of each bacteria needed with a density of at least $3x10^7$ bacteria/ml, and glycerol was added (20% v/v final concentration). The gavages were sealed with a rubber septum in N_2 gased tubes and stored at -80°C until their transfer to the gnotobiotic facility.

3.2. Histological methods

3.2.1. Tissue processing

Small intestinal and colonic tissues were removed immediately after euthanization and dissected from adjacent tissue. The different parts of the gastrointestinal tract were cut open longitudinally, the content was removed, and the tissue was processed as swiss rolls. Swiss rolls were cut in half and fixed in 4% phosphate-buffered formalin for 48h, dehydrated (Leica TP1020, Table 2), and embedded in melted paraffin (FFPE; VWR, Ismaning, Germany; Leica EG1150C) or embedded in optical cutting temperature (OCT) medium without fixation (Richard-Allan Scientific™ Neg-50™; Thermo Fisher Scientific GmbH, Dreieich, Germany).

Table 2: Dehydration of paraffin embedding of FFPE tissue.

Step	Reagent	Time (min)	Step	Reagent	Time (min)
1	70% EtOH	60	7	100% EtOH	60
2	70% EtOH	60	8	100% EtOH	60
3	80% EtOH	60	9	Xylene	60
4	96% EtOH	60	10	Xylene	60
5	96% EtOH	60	11	Paraffin	60
6	100% EtOH	60	12	Paraffin	60

3.2.2. Histology and tissue staining

3.2.2.1. H&E staining

For H&E staining, FFPE sections were cut (5µm, Leica RM2255, Soest, Germany) and deparaffinized and rehydrated automated (Table 3; Leica ST5020, Soest, Germany). Staining was performed using hematoxylin Mayer (Medite, Burgdorf, Germany), bluing reagent (Fisher, Dreieich, Germany), and 0.2% eosin (Medite, Burgdorf, Germany). Slides were mounted with DPX new (Merck KGaA, Darmstadt, Germany) and covered with a glass slip (VWR, Ismaning, Germany).

Table 3: Deparaffinization and H&E staining.

Deparaffinization and Rehydration		
Step	**Reagent**	**Time**
1	Xylene	5 min
2	Xylene	5 min
3	100% EtOH	5 min
4	100% EtOH	5 min
5	96% EtOH	2 min
6	96% EtOH	2 min
7	70% EtOH	2 min
8	70% EtOH	2 min
9	dH_2O	30 sec
H&E staining		
Step	**Reagent**	**Time**
1	Hematoxylin	2 min
2	Tab H_2O	15 sec
3	Bluing reagent	30 sec
4	dH_2O	30 sec
5	96% EtOH	30 sec
6	Eosin	2 min
7	96% EtOH	30 sec

8	96% EtOH	30 sec
9	100% EtOH	30 sec
10	100% EtOH	30 sec
11	Xylene	1.5 min
12	Xylene	1.5 min

3.2.2.2. Histopathological analysis

For histopathological evaluation, a molecular pathologist (Dr. Marianne Reiser/Dr. Katja Steiger, Institute of Pathology, TUM, Germany) blindly scored ileal and colonic sections stained with H&E. Two scores were obtained, one for inflammation (tissue pathology index) and one for aberrant epithelial architecture. The latter includes crypt architectural distortion (crypt hyperplasia, shifted nucleus-plasma relations, enlarged nuclei, nucleoli, apical shifted mitoses) in a score from 0 (regular crypts) to 4 (highly aberrant crypts). The tissue pathology index infiltration of mononuclear cells into the individual wall layers (mucosa, submucosa and muscularis), hyperplasia and atypia of the crypts, depletion of goblet cells and epithelial damage, resulting in a score from 0 (non-inflamed) to 12 (severely inflamed) [167]. Images were acquired by a PreciPoint M8 microscope (Precipoint, Freising, Germany).

3.2.2.3. Immunohistochemical / -fluorescent staining

For immunohistochemical (IHC) and immunofluorescence (IF) stainings, FFPE tissue sections of intestinal swiss rolls (5µM) mounted on Superfrost Plus slides (VWR, Ismaning, Germany) were deparaffinized and rehydrated in an automated manner (Table 3; Leica ST5020, Soest, Germany). After heat-mediated antigen retrieval with 10mM citrate buffer (pH=6; 23 min; 900 watt; Table 4) or tris-EDTA buffer (pH=9; 30 min; 900 watt; Table 4), tissue sections were equilibrated in PBS. Only pStat3 antigen retrieval was performed using a tris-EDTA puffer. For IHC staining, endogenous peroxidase quenching was conducted for 10 min with 3% H_2O_2 (Sigma- Aldrich, Taufkirchen, Germany). Sections were blocked with a blocking buffer (Table 4) according to the secondary antibody species and incubated overnight at 4°C with the primary antibody. Antibodies and concentrations used are depicted in Table 5. After three washing steps with PBS, sections were incubated with the secondary antibody (fluorochrome or HRP coupled) for 1h at RT (Table 5). In the case of IF staining, Dapi (Sigma- Aldrich, Taufkirchen, Germany) was used for nuclei staining and was added to the secondary antibody solution. Sections were mounted with Aquatex (Merck KGaA, Darmstadt, Germany), and signal visualization was performed via a Fluoview FV10i microscope (Olympus, Shinjuku, Japan). In the case of IHC staining, antigen detection was performed by DAB/metal

concentrate (Fisher, Dreieich, Germany), nuclei counterstained with hematoxylin, and tissue sections dehydrated and mounted with DPX new (Merck KGaA, Darmstadt, Germany). Slides were scanned and further analyzed via a PreciPoint M8 microscope (Precipoint, Freising, Germany). For both IF and IHC stainings, antibodies were dissolved in antibody dilution buffer (Table 4).

Table 4: Buffers and solutions used for IHC / IF staining.

Buffers and Solutions	Preparation
10mM Citrate buffer	2.94g sodium citrate tribasic dehydrate (Sigma- Aldrich, Taufkirchen, Germany) dH$_2$O up to 1L pH = 6
Tris-EDTA buffer	1.21g tris base (Sigma- Aldrich, Taufkirchen, Germany) 2ml ethylenediamine tetraaceticacid (EDTA; Fisher, Dreieich, Germany) dH$_2$O up to 1L pH = 9
Phosphate-buffered saline (10x)	20 tablets of PBS (Life Technologies, Carlsbad, CA) dH$_2$O up to 1L
Blocking buffer	2.5ml 10x PBS 1.25ml serum of the same species as the secondary antibody 21.25ml dH$_2$O 75µl Triton X-100 (100%) (Sigma- Aldrich, Taufkirchen, Germany)
Antibody dilution buffer	4ml 10x PBS 36ml dH$_2$O 0.4g BSA (Sigma- Aldrich, Taufkirchen, Germany) 120µl Triton X-100 (100%) (Sigma- Aldrich, Taufkirchen, Germany)

Table 5: Primary and secondary antibodies used for IHC / IF staining.

Primary antibody	Species	Manufacturer	Dilution
Anti-Hsp60 (IF)	Goat	Enzo, New York, USA	1:150
Anti-Hsp60 (IHC)	Rabbit	Cell Signaling Technology, Danvers, USA	1:400
Anti-Ido1	Rat	Enzo, New York, USA	1:200
Anti-Ki67	Rabbit	Cell Signaling Technology, Danvers, USA	1:300
Anti-Mmp7	Rabbit	Cell Signaling Technology, Danvers, USA	1:100

Anti-Muc2	Rabbit	Bio-Techne GmbH, Novus, Wiesbaden, Germany	1:100
Anti-pStat3	Rabbit	Cell Signaling Technology, Danvers, USA	1:100
Anti-Wnt10a	Rabbit	Abcam, Cambridge, UK	1:100
Secondary antibody		**Manufacturer**	**Dilution**
Alexa Fluor donkey anti-goat 488		Life Technologies, Carlsbad, CA	1:200
Alexa Fluor donkey anti-rat 594		Life Technologies, Carlsbad, CA	1:200
Alexa Fluor donkey anti-rabbit 647		Life Technologies, Carlsbad, CA	1:200
Donkey anti-rabbit HRP		Dianova, Hamburg, Germany	1:300

3.2.2.4. Alcian blue / Periodicacid-Schiff (PAS-AB) staining

FFPE tissue sections were deparaffinized, rehydrated, and stained with alcian blue (Fisher, Dreieich, Germany) for detection of acidic mucins (0.5% v/v in 3% acetic acid, pH=2.5, 5 min) in goblet cells. Sections were then treated with periodic acid (0.5% v/v, 10 min) and co-stained with Schiff's reagent (Sigma- Aldrich, Taufkirchen, Germany) for neutral mucins (15 min). Nuclei were counterstained with hematoxylin, and tissue sections were dehydrated and mounted with DPX new (Merck KGaA, Darmstadt, Germany). Slides were scanned and further analyzed using a PreciPoint M8 microscope (Precipoint, Freising, Germany).

3.2.3. *In-situ* hybridization

In-situ hybridization for murine *Lgr5* and *HopX* was performed in colonic FFPE tissue (5µM) using the RNAscope-2.5 HD *in situ* assay Kit-Brown (ACD, Bio-Techne GmbH, Wiesbaden, Germany) based on the manufacturer's instructions. Briefly, the endogenous peroxides were blocked with H_2O_2 for 10 min, and antigen retrieval was performed using the provided retrieval buffer. Sections were treated with ProteasePlus for 30 min at 40°C, followed by incubation with the desired probe (RNAscope Probe-Mm-Lgr5; RNAscope Probe-Mm-Hopx) for 2h at 40°C. Six amplification steps achieved signal amplification, and signal detection was performed using DAB solution for 10 min. Sections were counterstained with hematoxylin, dipped in ammonium hydroxide solution (0.02% v/v), and mounted with DPX new (Merck KGaA, Darmstadt, Germany). Slides were scanned and further analyzed using a PreciPoint M8 microscope (Precipoint, Freising, Germany).

3.2.4. Quantifications of tissue sections

All quantifications were performed in a blinded manner to histological scoring and genotypes.

3.2.4.1. Quantification of *Lgr5+* ISCs

Lgr5+ transcripts were quantified based on *Lgr5 in situ* hybridization staining of colonic tissue sections. To determine *Lgr5+* crypts, Fifty well-oriented crypts were categorized as positive or negative for *Lgr5* expression. Crypts with at least one *Lgr5* transcript (each dot represents one transcript) counted as positive. The number of *Lgr5+* crypts was calculated as a percentage of all crypts.

3.2.4.2. Quantification of *HopX* expression

Determination of *HopX* expression was performed based on *HopX in situ* hybridization staining of colonic tissue sections. Fifty well oriented crypts in 100x images were analyzed using the ImageJ software. The positive area was quantified within the selected IEC area based on the best-fitting threshold. Briefly, the intensity threshold that covered the entire positive signal in the selected crypt area was identified. The chosen threshold remained unchanged for all samples during the whole quantification. The amount of *HopX* expression was calculated as *HopX+* area per crypt.

3.2.4.3. Quantification of Hsp60 expression

Hsp60 expression was quantified in Hsp60 IHC stainings of colonic tissue sections. To determine Hsp60+ crypts, 50 well-oriented crypts were categorized as positive, half-positive, or negative for Hsp60 expression. Half-positive crypts were crypts with a positive signal in only the left or right side of the crypt.

3.2.4.4. Quantification of Ki67+ cells

IEC positive for Ki67 were quantified based on Ki67 IHC stainings of colonic tissue sections. To determine Ki67+ crypts, Fifty well-oriented crypts were categorized as positive or negative for Ki67 expression, and the number of Ki67+ cells was calculated per crypt.

3.2.4.5. Quantification of goblet cells

The number of goblet cells was counted based on Alcian blue/Periodicacid-Schiff (PAS-AB) staining. Fifty well-oriented crypts were selected, and PAS+ cells were counted. The number of PAS+ cells was calculated as a total number per 100 μm^2.

3.2.4.6. Quantification of crypt depth

The crypt depth and number of crypts per area were analyzed in H&E stainings of colonic tissue sections. In fifty well-oriented crypts, the length from the crypt base to the crypt top was measured using the ViewPoint Light software, and the average length was calculated for each

section. To determine the number of crypts per area, the area of fifty well oriented crypts was measured, and the number of crypts inside the area was calculated using the ViewPoint Light software.

3.3. Molecular biological methods

3.3.1. Genotyping

Tail cuts or ear punches were lysed in 10mM Tris-HCl buffer (pH=8.3) containing 50mM KCl, 0.45% Nonidet P40, 0.45% Tween 20, and 0.5mg/mL Proteinase K overnight (O.N.) at 65°C and inactivated at 80°C for 20 min. DNA was extracted using the NucleoSpin RNAII kit (Macherey-Nagel, Düren, Germany) according to the manufacturer's instructions for separate genotyping of colonic tissue samples. 1µl of the supernatant (tail cuts or ear punches) or 100ng eluted DNA (colonic tissue) was mixed with 10µl 2x Onetaq DNA polymerase (NEB, Frankfurt, Germany) or 2x FastGene® Optima HotStart Ready Mix (Nippon, Düren, Germany; only for the IL10$^{-/-}$ PCR). The respective quantity and combination of primers are specified in Table 6 for the different genotyping PCRs in a final volume of 20µl (Primer sequence given in Table 7). The various PCR programs for genotyping are defined in Table 8. The PCRs were designed to detect both Wild-type (Wt) sequences and knockout (KO)/ transgenic (Tg)/ modified (mod) locus.

Table 6: Primer combinations and PCR product sizes for genotyping.

PCR	Hsp60 (Rosa26)	ClpP (Rosa26)	Villin-CreER^{T2}	IL10$^{-/-}$
Primers (nM)	#1117 (200) #1118 (200) #1724 (200) #1725 (200)	#2139 (200) #2140 (200) #2142 (200)	#1484 (200) #1485 (200) #1119 (400) #1120 (400)	#2762 (500) #2763 (500) #2764 (500)
Product size [bp]	Wt: 193 mod: 353 KO: 178	Wt: 218 mod: 337 KO: 250	DNA: 585 Tg: 318	Wt: 137 KO: 312

Table 7: Sequences of genotyping primers.

Primer number	5´ - 3´ Sequence	Primer number	5´ - 3´ Sequence
#1117	ACCAAGACCCTGTACTCTTAACC	#1725	ACCAGAACAACCTCAGGCCTCAA
#1118	AACTTGACCTAGATGTTGTGTGG	#2139	TCCATCGTCCTGCCATAGC
#1119	CCTTCAGCAAGAGCTGGG	#2140	CCCTGGGTTTAAGCACTGC
#1120	GAGACTCTGGCTACTCATCCAGC	#2142	GGTGCTAGGAATCATGTCTGG
#1484	GACCATATCCACCGAGTCC	#2762	CTTGCACTACCAAAGCCACA
#1485	AGGAATGCGATGAAGTAGAGC	#2763	CCACACGCGTCACCTTAATA
#1724	TCTGCCTGCTTCTTCTGCCTTCA	#2764	GTTATTGTCTTCCCGGCTGT

Table 8: PCR program for genotyping.

Temp (°C) / Time (sec)		Hsp60 (Rosa26)	ClpP (Rosa26)	Villin-CreER^{T2}	IL10$^{-/-}$
Initial Denaturation		94/60	94/60	94/60	94/120
Denaturation		94/20	94/20	94/20	94/15
Annealing		58/20	60/20	58/20	60/15
Extension		68/20	68/30	68/30	72/15
Final extension		68/60	68/60	68/60	72/30
Cooling		4/∞	4/∞	4/∞	4/∞

3.3.2. Gene expression analysis

mRNA of total colonic tissue or small and large intestinal organoids was isolated according to the manufacturer's instructions (NucleoSpin RNAII kit; Macherey-Nagel GmbH, Düren, Germany). mRNA was eluted in 60µl (tissue) or 40µl (organoids) RNase-free water (Macherey-Nagel, Düren, Germany) and measured by Nanodrop ND-1000 spectrophotometer or Implen™ NanoPhotometer™ N60. Complementary DNA was synthesized from 100-1000ng mRNA using random hexamers and Moloney murine leukemia virus (M-MLV) reverse transcriptase Point Mutant Synthesis System (Promega, Mannheim, Germany).

To analyze relative gene transcript amounts of specific genes of interest, quantitative real-time PCR (qRT-PCR) was performed using the Universal Probe Library System (Roche, Mannheim, Germany) and 1µl cDNA according to the manufacturer's instructions in a Light Cycler ® 480 system (Roche, Mannheim, Germany). Relative induction of gene mRNA expression was calculated by the 2-ΔΔCt method [168] using the expression of the housekeeper *Hprt* for normalization. Primer sequences and respective probes are listed in Table 9.

Table 9: Primer sequences and UPL probe numbers used for qRT-PCR analysis.

Target gene	Forward primer (L)	Reverse primer (R)	UPL probe #
Alpi	CATCTCCAACATGGACATTGA	GGTTCCAGACTGGTTACTGTCA	109
Arg1	GAATCTGCATGGGCAACC	GAATCCTGGTACATCTGGGAAC	2
Arg2	CATTTGATCGGCTGATTGG	CTGGAGCCAGTTTAGGGTCA	13
Atf4	ATGATGGCTTGGCCAGTG	CCATTTTCTCCAACATCCAATC	88
Atf5	TTTTTATGAAGAGGAATAAGATGAGGT	GGAGGCTGCACCAACAAT	16
Chac1	GGTGACCCTCCTTGAAGACC	AGGTACTTCAGGGCCTCGTT	32
ChgA	GGAGGCTGTGGCTACACACA	CCATCCACTGCCTGAGAGTC	89
Chop	GCGACAGAGCCAGAATAACA	GATGCACTTCCTTCTGGAACA	91
Cox-I	CAGACCGCAACCTAAACACA	TTCTGGGTGCCCAAAGAAT	25
ClpP	GCAACAAGAAGCCCATTCAT	GTACTGCATTGTGTCGTAGATGG	26
Ereg	TTGACGCTGCTTTGTCTAGG	GGATCACGGTTGTGCTGAT	96
Grem1	ACCCACGGAAGTGACAGAAT	CCCTCAGCTGTTGGCAGTAG	63
Hk2	TTCACCTTCTCCTTCCCTTG	CCCTTTGTCCACTTGAGGAG	64
Hif1α	GCACTAGACAAAGTTCACCTGAGA	CGCTATCCACATCAAAGCAA	95
Hprt	TCCTCCTCAGACCGCTTTT	CCTGGTTCATCATCGCTAATC	95
Hsp60	TCTTCAGGTTGTGGCAGTCA	CCCCTCTTCTCCAAACACTG	1
Ido1	GGGCTTCTTCCTCGTCTCTC	TGGATACAGTGGGGATTGCT	2
Ifnγ	GGAGGAACTGGCAAAAGGAT	TTCAAGACTTCAAAGAGTCTGAGG	21
Il1ß	TGTAATGAAAGACGGCACACC	TCTTCTTTGGGTATTGCTTGG	78
Il10	CAGAGCCACATGCTCCTAGA	TGTCCAGCTGGTCCTTTGTT	41

Il22	GTGACGACCAGAACATCCAG	GATCTCTCCACTCTCTCCAAGC	94
Il22ra1	TGCTCTGTTATCTGGGCTACAA	TCAGGACACGTTGGACGTT	9
Irf8	AGTGTGGCCGCTCAGAGA	GGCTCCTCTTGGTCATACCC	17
Ki67	GCTGTCCTCAAGACAATCATCA	GGCGTTATCCCAGGAGACT	80
KC/IL8	AGACTCCAGCCACACTCCAA	TGACAGCGCAGCTCATTG	83
Lgr5	CTTCACTCGGTGCAGTGCT	CAGCCAGCTACCAAATAGGTG	60
Muc2	GGCAGTACAAGAACCGGAGT	GGTCTGGCAGTCCTCGAA	66
Nos2	GGGCTGTCACGGAGATCA	CCATGATGGTCACATTCTGC	76
Pdk4	CGCTTAGTGAACACTCCTTCG	CTTCTGGGCTCTTCTCATGG	22
Pgc1α	GAGCGAACCTTAAGTGTGGAA	TCTTGGTTGGCTTTATGAGGA	52
Ptgs2	GATGCTCTTCCGAGCTGTG	GGATTGGAACAGCAAGGATTT	45
Prom1	CAGCGGCAGAAGCAGAAT	TGGTTAGCCACAAAGCCATA	69
Rspo1	CGACATGAACAAATGCATCA	CTCCTGACACTTGGTGCAGA	5
Saa3	ATGCTCGGGGGAACTATGAT	ACAGCCTCTCTGGCATCG	26
Tnf	TGCCTATGTCTCAGCCTCTTC	GAGGCCATTTGGGAACTTCT	49
Trb3	GTCGCTTTGTCTTCAGCAACT	TCATCTGATCCAGTCATCACG	67
Wnt2b	CCGGGACCACACTGTCTTT	GCTGACGAGATAGCATAGACGA	16
Wnt3	CTCGCTGGCTACCCAATTT	GAGGCCAGAGATGTGTACTGC	81
Wnt4	ACTGGACTCCCTCCCTGTCT	TGCCCTTGTCACTGCAAA	62
Wnt5b	AGCACCGTGGACAACACAT	AAGGCAGTCTCTCGGCTACC	53
Wnt9a	CGAGTGGACTTCCACAACAA	GGCATTTGCAAGTGGTTTC	19
Wnt9b	CCAAGAGAGGAAGCAAGGAC	TCTCAGGCCGCTCTTCAC	105
Wnt10a	GGCGCTCCTGTTCTTCCTA	GTCGTTGGGTGCTGACCT	71

3.3.3. Quantitative qPCR of bacterial 16S rRNA genes

Quantitative PCR of the twelve different bacteria from the OMM[12] consortium was performed using 10ng gDNA as a template. Strain-specific 16S rRNA primers and hydrolysis probes were used for amplification [166]. For duplex qPCR assays, hydrolysis probes were 5′-labelled with either 6-carboxyfluorescein (FAM) or 6-carboxyhexafluorescein (HEX). qPCR standard curves were determined using linearized plasmids as DNA templates and run on a Light Cycler 480

system (Roche Diagnostics) in duplicates. A standard curve was then used for absolute quantification of 16S rRNA gene copy numbers of individual strains.

3.3.4. Microbiota profiling

3.3.4.1. 16S amplicon sequencing

gDNA isolation, 16S rRNA high-throughput sequencing, and downstream analysis of murine colonic content were conducted as previously described [169]. Briefly, cells were mechanically lysed, and DNA was purified using a column-based procedure (NucleoSpin gDNA CleanUp kit; Macherey-Nagel GmbH, Düren, Germany). Amplicon libraries (V3/V4 region) were amplified by PCR (25 cycles), purified using the AMPure XP system (Beckmann, Krefeld, Germany), pooled in an equimolar amount, and sequenced in paired-end mode (PE275) using a MiSeq system (Illumina, Inc., San Diego, USA) according to the manufacturer's instructions and 25% (v/v) PhiX standard library. Data were analyzed as described previously [170]. Raw sequences were processed using IMNGS based on the UPARSE approach [171]. Sequences were demultiplexed, trimmed to the first base with a quality score <3 and then paired. Sequences with less than 300 and more than 600 nucleotides and paired reads with an expected error >3 were excluded from the analysis. The remaining reads were trimmed by 5 nucleotides on each end to avoid GC bias and nonrandom base composition. The presence of chimeras was tested using UCHIME [172]. Clustering of zero-radius operational taxonomic units (zOTUs) was done at 97% sequence similarity. Taxonomic binning was assigned at an 80% confidence level using the RDP classifier [173] and compared to the SILVA ribosomal RNA gene database project [174]. Analysis was performed using R-package Rhea [175]. In brief, rarefaction curves were used to assess sequencing depth and eliminate low-quality reads. zOTU counts were normalized, and percentage relative abundance was computed. Beta-diversity analysis was used to determine the diversity between groups based on generalized UniFrac distances. Alpha-diversity within species was calculated based on species richness and Shannon effective number of species. EvolView v2 was used to visualize phylogenetic trees [176].

3.3.4.2. Shallow shotgun metagenomics

Shallow shotgun metagenomic sequencing was performed on a NovaSeq machine (1G raw data with paired-end 150bp) as previously described [177] using gDNA isolated from murine colonic content. After demultiplexing the data, adapters were trimmed from the raw sequencing reads using Trim Galore (https://github.com/FelixKrueger/TrimGalore). Reads were processed with the KneadData quality control pipeline to remove low-quality read bases and murine contamination (https://bitbucket.org/biobakery/kneaddata/wiki/Home). Taxonomic profiling

was performed using the MetaPhlAn3.0.13 classifier [178], which unambiguously classifies metagenomic reads to taxonomies based on a database of clade-specific marker genes derived from 17,000 microbial genomes (~13,500 bacterial and archaeal, ~3,500 viral, and ~110 eukaryotic). Species-level assignments were extracted, data was centered log ratio scaled and used for subsequent analysis.

3.3.5. NanoString analysis

Multiplexed gene expression of a panel of 768 metabolic genes was analyzed using the nCounter® Metabolic Pathway Panel (NanoString, Seattle, USA) according to the manufacturer's instructions. In brief, 125ng isolated RNA of total colonic tissue underwent code set hybridization and was processed using a nCounter® MAX/FLEX system (NanoString, Seattle, USA). Raw data were subjected to quality control, followed by normalization and further analysis applying the nSolver Analysis Software (NanoString, Seattle, USA). Further KEGG pathway analysis was conducted using the DAVID tool [179, 180].

3.3.6. Western Blot analysis

According to the manufacturer's instructions, the total protein concentration of colonic tissue samples lysed in urea-containing protein lysis buffer was assessed by Pierce 660nm Protein Assay (Thermo Fisher Scientific GmbH, Dreieich, Germany). Lysates were diluted with 4x NuPage™ LDS Sample Buffer (Thermo Fisher Scientific GmbH, Dreieich, Germany) and incubated at 70°C for 5 min. Samples were separated by reducing sodium dodecyl sulfate-polyacrylamide gel electrophoresis (SDS-PAGE) and transferred on polyvinylidene difluoride membranes (Immobilon-P Membrane, Merck-Millipore, Darmstadt, Germany) by semi-dry blotting using a semi-dry blotting chamber (Peqlab, Erlangen, Germany). After blocking with 2% ECL Prime Blocking Reagent (Amersham; Cytiva, Freiburg, Germany) in 1xTBS/0.1% Tween-20 (TBST) for 1h at RT, membranes were incubated in primary antibody diluted in blocking buffer ON at 4°C (Table 10). After three washes with TBST, membranes were incubated in a blocking buffer with a secondary antibody (Table 10) for 1h at RT, followed by three washes with TBST. Direct NIR detection was performed using an Odyssey imaging system (LI-COR Biosciences, Lincoln, USA), and Western blots were quantified using Image Studio Lite Version 5.2 (LI-COR Biosciences, Lincoln, USA).

Table 10: Primary and secondary antibodies for Western Blot.

Primary antibodies				Secondary antibodies		
Antigen	Manufacturer	Dilution	Species	Species	Manufacturer	Dilution
Hsp60 XP	Cell Signaling	1:10000	Rabbit	Goat anti-rabbit CW800	LI-COR	1:10000
ß-actin	Invitrogen	1:25000	mouse	Goat anti-mouse GF680	Biotium	1:10000

3.3.7. Co-Immunoprecipitation MS/MS analysis

Co-Immunoprecipitation (Co-IP) was performed according to the protocol provided by Cell Signaling. Briefly, ModeK or PTK6 cells were lysed in 1x RIPA buffer (Thermo Fisher Scientific GmbH, Dreieich, Germany) supplemented with 1µM PMS, sonicated and centrifuged to remove cell debris. SureBeads™ Magnetic Beads (Bio-Rad, Feldkirchen, Germany) were coated with anti-Hsp60 (Proteintech Europe, Manchester, UK) or control IgG antibody (Santa Cruz, Heidelberg, Germany) and incubated with cell lysate at 4°C O.N. at 1500rpm. Protein was eluted from magnetic beads with 4x NuPage™ LDS Sample Buffer (Thermo Fisher Scientific GmbH, Dreieich, Germany) and incubated at 70°C for 5 min for Coomassie staining and MS/MS analysis. For Coomassie staining, half of the eluted protein was separated on an SDS-PAGE and incubated with Roti® Blue (Carl Roth, Karlsruhe, Germany) until bands were visible to validate the Co-IP. With the other half of the eluted protein, LC-MS/MS analysis was performed by BayBioMS (Bavarian Center for Biomolecular Mass Spectrometry; Dr. Christina Ludwig and Dr. Chen Meng). In brief, samples were reduced with 10mM DTT, alkylated with 55mM 2-chloroacetamide, diluted 1:4 in 50mM ammonium bicarbonate, and digested with trypsin. The reaction was stopped with 1% formic acid, the peptides were purified, eluted, dried, and resuspended in washing solution shortly before MS measurement. Generated peptides were analyzed on a Dionex Ultimate 3000 RSLCnano system coupled to an Orbitrap Fusion Lumos Tribrid Mass Spectrometer (Thermo Fisher Scientific, Bremen, Germany). Downstream analysis was performed using the software MaxQuant (version 1.6.3.4) to generate a list of Hsp60-bound proteins, and further analysis was conducted using the PANTHER tool [181].

3.4. Cell and organoid culture

3.4.1. Cell culture

The small intestinal epithelial cell line ModeK [182] and the large intestinal cell line PTK6 [183] were grown in a humidified 5% CO_2 atmosphere at 37°C to confluency in 12 well tissue plates (Eppendorf, Hamburg, Germany). The respective cell culture media is listed in Table 11.

Table 11: Cell culture medium.

ModeK cell medium	Concentration	Manufacturer
DMEM	-	Sigma- Aldrich, Taufkirchen, Germany
FCS	10% (w/v)	Thermo Fisher, Dreieich, Germany
Antibiotic Antimycotic	1x	Sigma- Aldrich, Taufkirchen, Germany
PTK6 cell medium	**Concentration**	**Manufacturer**
RPMI-1640	-	Sigma- Aldrich, Taufkirchen, Germany
FCS	5% (w/v)	Thermo Fisher, Dreieich, Germany
Antibiotic Antimycotic	1x	Sigma- Aldrich, Taufkirchen, Germany
Insulin-transferrin-selenium A	1% (w/v)	Thermo Fisher, Dreieich, Germany

3.4.2. Small intestinal and colonic organoid culture

Small intestinal and colonic organoids were generated from mice (jejunum and colon), as described previously [184, 185]. In brief, intestinal tissue (6-10 cm) was inverted, digested for 30 min (small intestine) or 2h (colon) with EDTA at 4°C, and mechanically dissociated. The supernatant was filtered via a 70µm cell strainer, pelleted by centrifugation, and embedded in Matrigel (BD Biosciences, Franklin Lakes, NJ, USA). 25µl Matrigel-organoid suspension was plated in 48 well plates (Eppendorf, Hamburg, Germany) and incubated in IntestiCult™ Organoid Growth Medium (STEMCELL Technologies, Vancouver, Canada) in a humidified 5% CO_2 atmosphere at 37°C. For subsequent passaging every 7-10 days, organoids were mechanically disrupted using a 1ml syringe with a 20G needle, pelleted by centrifugation, and embedded in fresh Matrigel. During experimental procedures, organoids were passaged three days before the start of the experiment and cultivated on a self-made crypt culture medium (CCM; Table 12).

Table 12: Organoid crypt culture media.

	Component	Concentration	Manufacturer
Basic culture medium (BCM)	Advanced DMEM/F12	-	Gibco life technologies, Waltham, USA
	GlutaMax	1x	Sigma- Aldrich, Taufkirchen, Germany
	HEPES	1x	Sigma- Aldrich, Taufkirchen, Germany
	Antibiotic Antimycotic	1x	Sigma- Aldrich, Taufkirchen, Germany
Crypt culture medium (CCM)	N2 Supplement	1x	Gibco life technologies, Waltham, USA
	B27 Supplement	1x	Gibco life technologies, Waltham, USA
	N-Acetylcysteine	1mM	Sigma- Aldrich, Taufkirchen, Germany
	Recombinant murine EGF dissolved in 0.1% BSA/PBS	50ng/ml	ImmunoTools GmbH, Friesoythe, Germany
	Murine Noggin dissolved in 0.1% BSA/PBS	100ng/ml	PeproTech, Rocky Hill, USA
	Recombinant human R-Spondin1 dissolved in 0.1% BSA/PBS	0.5µg/ml	PeproTech, Rocky Hill, USA

3.4.2.1. Induction of *ex vivo* recombination

Ex vivo induction of *Hsp60* and *ClpP* deletion was achieved by adding 500nM (Z)-4-hydroxytamoxifen (4-OHT; LKT, St Paul, MN, USA) to the culture medium. After 24h, organoid culture media was changed to fresh CCM.

3.4.2.2. Quantification of size, *de novo* crypt formation and crypt length

Essential readouts are organoid growth patterns comprising increased *de novo* crypt formation (buds), increased growth, elongated buds, skewed cell composition, and cystic growth (Figure 8). Growth patterns can be linked to specific cellular functions with *de novo* crypt formation

indicating the abundance of Lgr5+ ISC-related stemness, length of crypt-like domains, and organoid area reflecting transit amplifying zone activity and proliferative capacity.
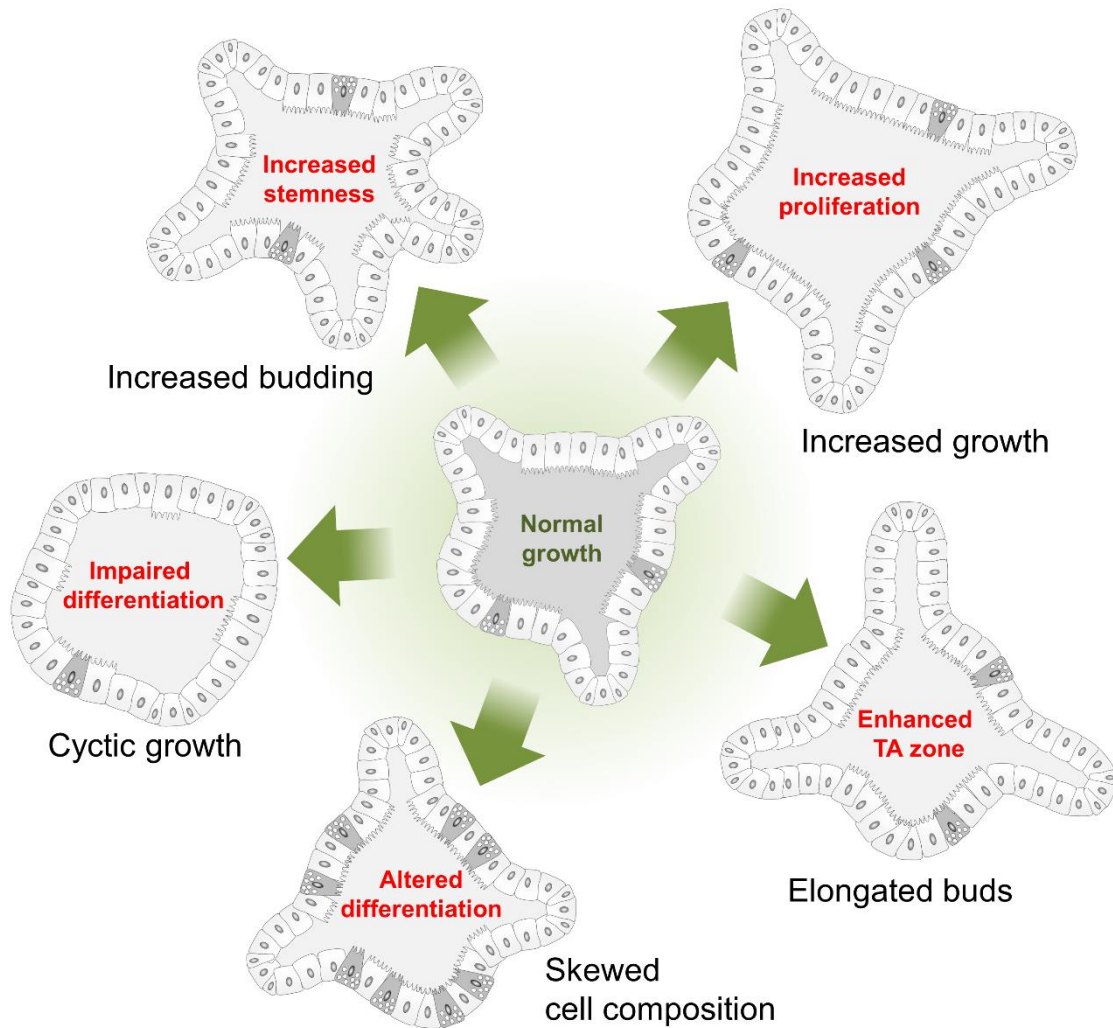

Figure 8: Distinct intestinal organoid growth pattern and their cellular function *ex vivo.*
The different growth patterns of intestinal organoids can be linked to specific cellular functions. For instance, *de novo* crypt formation indicates an abundance of Lgr5 ISC-related stemness, and the organoid area reflects transit-amplifying zone activity and proliferative capacity. Figure generated by Dr. Eva Rath.

Videos of organoids were generated using an Olympus CK X 41 microscope and Olympus cellSens Entry software. For *de novo* crypt formation, numbers of buds (0, 1, 2, 3, >4) were counted in 120 organoids (in 4-6 wells) per group at the desired time point. Percentages were calculated based on the total number of organoids. The area of organoids and crypt length were measured using the ImageJ software and normalized to the control group.

3.4.3. Intestinal mesenchymal culture

For the isolation of intestinal mesenchymal cells (IMCs), small intestinal tissue (6-10 cm; jejunum) was inverted, cut into 0.5 – 1 cm pieces, and digested with 5mM EDTA and 1mM DTT at 37°C for 30 min at 200rpm. After several washing steps (until a clear supernatant was generated), tissues pieces were enzymatically digested with collagenase XI (3000U; Sigma-Aldrich, Taufkirchen, Germany) and Dispase II (0.8U; Roche Diagnostics, Mannheim, Germany) at 37°C for 40 min at 200rpm. The supernatant was vigorously shaken to become cloudy, filtered via a 70µm cell strainer, pelleted by centrifugation, and resuspended in IMC culture medium (Table 13). IMCs were cultured in 6 well plates (Eppendorf, Hamburg, Germany) in a humidified 5% CO_2 atmosphere at 37°C.

Table 13: Intestinal mesenchymal cell (IMC) culture medium.

IMC medium	Concentration	Manufacturer
DMEM	-	Sigma- Aldrich, Taufkirchen, Germany
FCS	10% (w/v)	Thermo Fisher, Dreieich, Germany
Antibiotic Antimycotic	1x	Sigma- Aldrich, Taufkirchen, Germany
L-Glutamine	1x	Sigma- Aldrich, Taufkirchen, Germany
Non-essential amino acids	1x	Sigma- Aldrich, Taufkirchen, Germany

3.4.4. Macrophage culture

For primary macrophage culture, hematopoietic stem cells were isolated from murine femurs and differentiated into macrophages (MΦ). In brief, both femurs were removed from mice, and bone marrow was flushed out using a 26G needle and RPMI medium supplemented with 10% FCS. After centrifugation and washing, the supernatant was filtered via a 100µM cell strainer, layered onto Histopaque®-1083 (Ficoll, density: 1.083; Sigma- Aldrich, Taufkirchen, Germany), and centrifuged according to manufacturer's instructions. The cell layer of interest was removed, washed, and resuspended in MΦ media (Table 14). Isolated bone-marrow-derived hematopoietic stem cells were cultured in 10 cm Petri dishes (Eppendorf, Hamburg, Germany) in a humidified 5% CO2 atmosphere at 37°C. Four days after isolation and cultivation on MΦ media, cells were completely differentiated into macrophages and could enter an experiment. During experimental procedures, macrophages were seeded with a density of 2×10^5 cells/ml to reach confluency after 4 days.

Table 14: Macrophage culture media.

MΦ medium	Concentration	Manufacturer
RPMI-1640	-	Sigma- Aldrich, Taufkirchen, Germany
FCS	10% (w/v)	Thermo Fisher, Dreieich, Germany
Antibiotic Antimycotic	1x	Sigma- Aldrich, Taufkirchen, Germany
ß-mercaptoethanol	0.1% (w/v)	Sigma- Aldrich, Taufkirchen, Germany
M-CSF	20ng/µl	PeproTech, Rocky Hill, USA

3.5. Statistical analysis

Statistical analyses were performed with GraphPad Prism (V.8.0; GraphPad, La Jolla, CA) using unpaired two-tailed T-test, analysis of variance (ANOVA) followed by pairwise comparison testing (Tukey, Bonferroni correction), by Kruskal-Wallis test followed by Dunn`s multiple comparisons or Mann-Whitney test. Unless otherwise stated, data are presented as mean ± SD, and p-values below 0.05 were considered statistically significant (p<0.05: *; p<0.01: **; p<0.001: ***; p<0.0001: ***;).

4. Results

4.1. Loss of Hsp60 in the intestinal epithelium induces MT-UPR signaling

MT-UPR signaling plays a vital role in maintaining intestinal epithelial cell homeostasis, and dysregulation can skew the balance toward intestinal pathologies such as inflammation. To investigate the contribution of mitochondria on intestinal tissue homeostasis, a previously generated conditional knockout model of the mitochondrial chaperone Hsp60 was used. Hsp60 loss induced mitochondrial dysfunction in small intestinal epithelial cells, reducing proliferation and stemness [77]. Following these observations, the aim was to characterize the colonic phenotype in this mouse model. Inducible Cre-mediated recombination is required to cause conditional deletion of Hsp60, specifically in IECs after feeding tamoxifen-containing diet for one week (Hsp60$^{\Delta/\Delta IEC}$ mice, Ctrl: Hsp60$^{fl/fl}$).

To reveal the impact of Hsp60 deficiency on colonocytes, Hsp60$^{\Delta/\Delta IEC}$ mice were analyzed at five different time points (D0, D4, D8, D11, D14) after the end of tamoxifen treatment and complete *Hsp60* deletion (Figure 9A). DNA isolated from mouse tail or colonic tissue was used to detect the presence or absence of *Villin*CreER^{T2} and the Hsp60 flox or KO allele (Figure 9B). Weight curves showed a significantly reduced weight in Hsp60$^{\Delta/\Delta IEC}$ mice compared to Hsp60$^{fl/fl}$ mice from day 0 to day 14, with a general increase of weight in both genotypes starting from D1 due to a switch back to soy-free diet (Figure 9C). The length of all intestinal segments (duodenum, jejunum, ileum and colon) as well as the weight of all organs (cecum, stomach, pancreas, spleen, thymus, liver, kidney, muscle) except mesenteric lymph nodes (MLNs) did not differ (Supplementary figure 1). To confirm the deletion of Hsp60, colonic tissue was processed for qRT-PCR and Western Blot analysis (Figure 9D,E). These data demonstrate that Hsp60 is deleted in colonocytes, confirming that the mouse model works.

Next to a complete *Hsp60* deletion at day 0, a transiently activated MT-UPR signaling was confirmed. The MT-UPR transcription factor *Chop* was increased at day 0, along with the downstream MT-UPR target genes tribbles homolog 3 (*Trb3)* and cation transport regulator-like protein 1 (*Chac1)*. While the transcription factor *Atf4* was also elevated at day 0, the transcription factor *Atf5* was unchanged at the analyzed time points (Figure 9F-H).
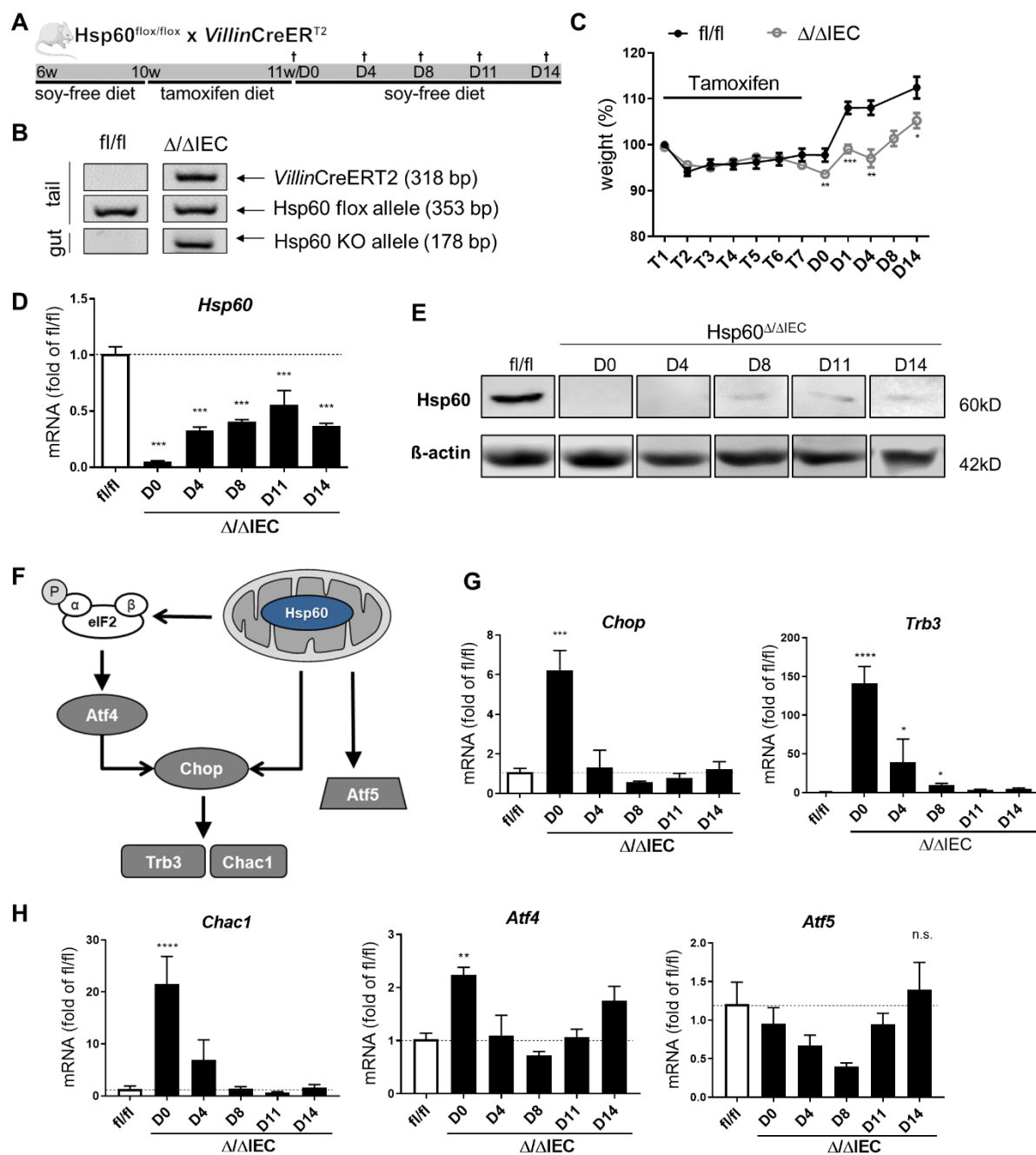
Figure 9: Deletion of Hsp60 in colonic IECs induces MT-UPR signaling.
(A) Experimental setup illustrating the IEC-specific deletion of Hsp60 in mice (Hsp60$^{\Delta/\Delta IEC}$ mice, Ctrl: Hsp60$^{fl/fl}$) by oral feeding with tamoxifen-supplemented food. Mice were sacrificed at day (D) 0, 4, 8, 11, and 14 after the end of tamoxifen treatment and full Hsp60 deletion. **(B)** Agarose gels depicting genotyping results for the CreERT2 transgene and Hsp60 flox allele in tails and Hsp60 KO specifically in the gut. **(C)** Weight curves of Hsp60$^{\Delta/\Delta IEC}$ and Hsp60$^{fl/fl}$ mice from the start of tamoxifen feeding until D14. **(D)** mRNA levels of colonic tissue for *Hsp60* expression. **(E)** Western Blots of colonic IECs for Hsp60. ß-Actin served as loading control. **(F)** Illustration of MT-UPR signaling and the relevant marker genes. **(G,H)** mRNA expression levels of colonic tissue for MT-UPR relevant *genes Chop, Trb3, Chac1, Atf4,* and *Atf5*. Statistics: (C) Multiple t-tests using the Two-stage linear step-up procedure of Benjamini, Krieger and Yekutieli. (D,G,H) ANOVA followed by pairwise comparison testing (Tukey). Mean ± SD, n=6. Asterisks indicate significant differences *P<0.05, **P<0.01, ***P<0.001; ****P<0.0001.

4.2. MT-UPR signaling is induced *in vitro* in intestinal organoids

To dissect the molecular mechanisms involved in the loss of Hsp60 *in vitro,* intestinal organoid cultures were generated. They closely reflect crypt physiology and Cre-mediated recombination is achieved by adding tamoxifen to the organoid medium.

For the metabolic injury mouse model (Hsp60$^{\Delta/\Delta IEC}$), protocols for targeted gene deletion *ex vivo* were established, and organoid responses in both small intestinal and colonic organoids were characterized (Figure 10A,B). Previous studies show that it takes 4 days until Hsp60 is entirely deleted on protein level. In line, loss of Hsp60 expression resulted in activation of MT-UPR signaling (*Chop, Trb3*) from day 4 on and caused a rapid decrease in the expression of the stem cell marker *Lgr5* and an increase in the enterocyte marker intestinal alkaline phosphatase (*Alpi)* (Figure 10C). The transit-amplifying zone marker prominin1 (*Prom1)* was slightly decreased in small intestinal organoids but increased in colonic organoids. In general, effects on day 4 were more pronounced in colonic organoids. However, SI organoids showed more robust signaling on day 6 (data not shown). Unfortunately, colonic organoids were not viable in culture until day 6.

The profound impact of Hsp60 deletion is reflected by organoid growth patterns, comprising reduced growth and diminished *de novo* crypt formation (budding) (Figure 10D,E). Furthermore, reduced ATP levels were demonstrated (Figure 10F), suggesting a reduced mitochondrial respiratory capacity.

Together, these data implicate an overall reduction in the proliferation and differentiation of IECs upon mitochondrial stress, making intestinal organoids a great tool to study the molecular mechanisms underlying mitochondrial impairment.
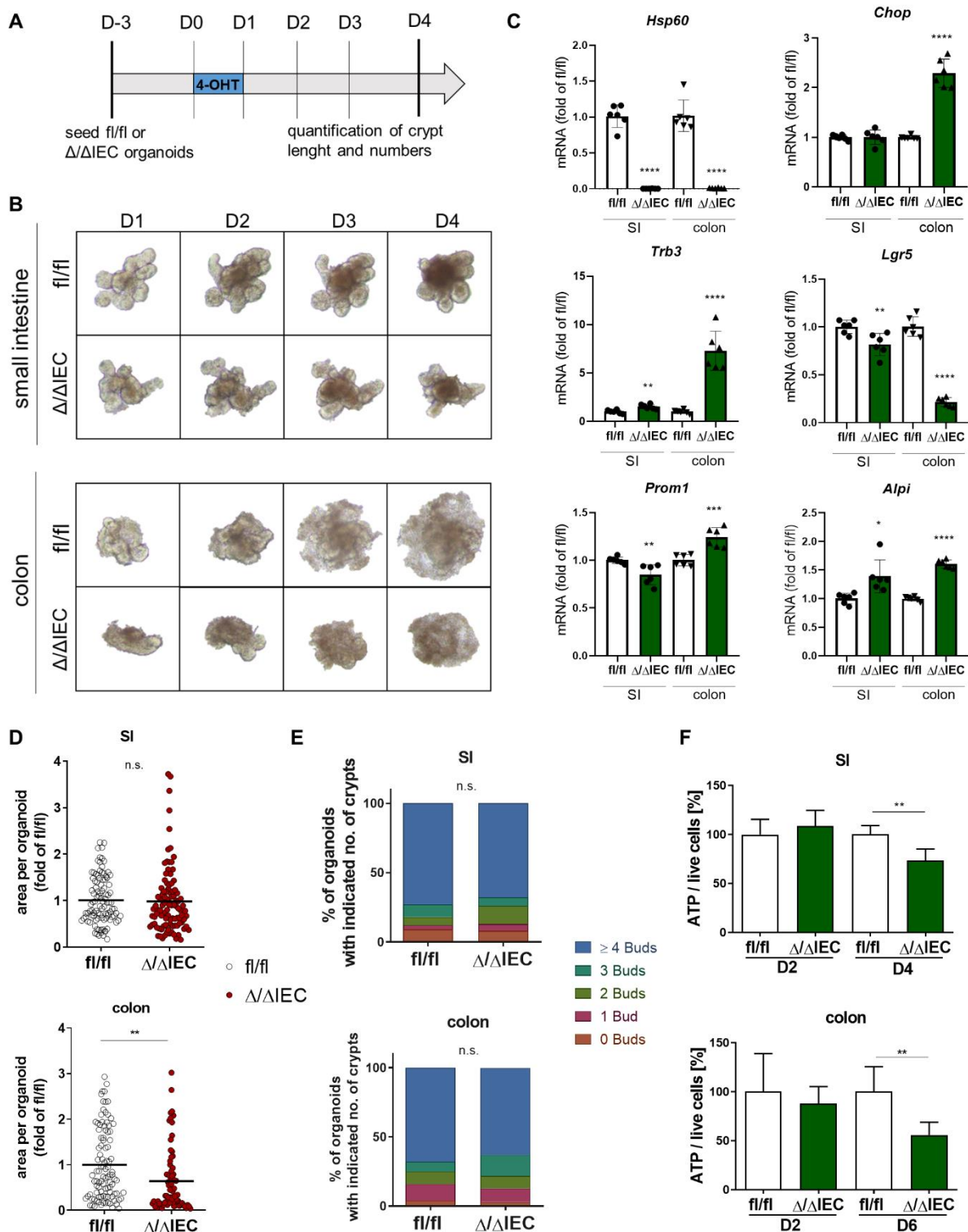
Figure 10: MT-UPR signaling is induced *in vitro* in intestinal organoids.

(A) Experimental setup. Hsp60 deletion is induced *ex vivo* in small intestinal (SI) and colonic organoids from Hsp60^Δ/ΔIEC mice (Ctrl: Hsp60^fl/fl mice) by adding tamoxifen (500nM) for 24h to the culture media. Organoids are then monitored for up to 6 days. **(B)** Representative pictures of respective organoids. **(C)** mRNA expression levels of organoids for *Hsp60*, MT-UPR relevant genes (*Chop, Trb3*) and epithelial subpopulations (*Lgr5, Prom1, Alpi*). **(D)** Quantification of the organoid area and **(E)** *de novo* crypt formation (budding) in both genotypes of small intestinal and colonic organoids at day (D) 4. **(F)** Measurement of ATP levels per live cells in both genotypes of small intestinal and colonic organoids and day (D) 2 and 4. Statistics: (C,F) ANOVA followed by pairwise comparison testing (Tukey). (D) t-test. (E) Mann-Whitney test. Mean ± SD, n=6. Asterisks indicate significant differences *P<0.05, **P<0.01, ***P<0.001; ****P<0.0001.

4.3. Mitochondrial dysfunction causes metabolic injury in IECs

After analyzing the MT-UPR signaling induced upon Hsp60 loss, the impact was characterized on tissue level. Previous studies showed that loss of stemness and regenerative crypt architecture in the small intestine of Hsp60$^{\Delta/\Delta IEC}$ mice induced the paracrine release of Wnt-related signals from injured tissue regions, leading to compensatory proliferation of residual stem cells that escaped *Hsp60* deletion [77].

Histological analysis in all intestinal tissue segments revealed that Hsp60 deficiency, and subsequent mitochondrial impairment, induced an aberrant tissue architecture characterized by the resorption of damaged crypts and compensatory hyperproliferation of cells that regained Hsp60. This injury phenotype is followed by healing responses leading to tissue reconstitution and regain of homeostasis (Figure 11A-C; Supplementary figure 2). The score for tissue aberration was developed together with Dr. Katja Steiger (TUM; Institute for Pathology) and ranges from 0 (no aberration), 1 (crypt hyperplasia), 2 (crypt hyperplasia with branched crypts, focal atypia), 3 (augmented atypia) to 4 (atypia in > 50% of epithelium). The score for wounded crypts was generated similarly and entailed the amount of damaged/apoptotic crypts ranging from 0 (no epithelial damage), 1 (mild epithelial damage), 2 (moderate epithelial damage), to 3 (strong epithelial damage). Interestingly, the colonic tissue depicted slightly delayed alterations in the crypt structure compared to the proximal part of the intestine. While tissue reconstitution was completed in the small intestine by day 8 (Figure 12A,B), the colonic phenotype started on day 4 after Hsp60 loss, presenting the most pronounced tissue architectural changes on day 8, with healing being completed 3 weeks after tamoxifen-induced *Hsp60* deletion. In this context, the terminology 'metabolic injury' as a self-autonomous mechanism of tissue wounding in response to mitochondrial perturbation is introduced. Highly proliferative tissue regions are characterized by strong expression of Hsp60, originating from stem cells that escaped Hsp60 deletion (Figure 11D-F) and vice versa, Hsp60 deficiency abrogates Ki67 expression indicative of reduced proliferation in the crypt (Figure 11G,H).

To sum up, these results indicate that loss of Hsp60 induces metabolic injury in IECs. Moreover, it can be hypothesized that a disturbed cell metabolism is a susceptibility condition that might foster (recurrent) inflammation in the gastrointestinal tract.
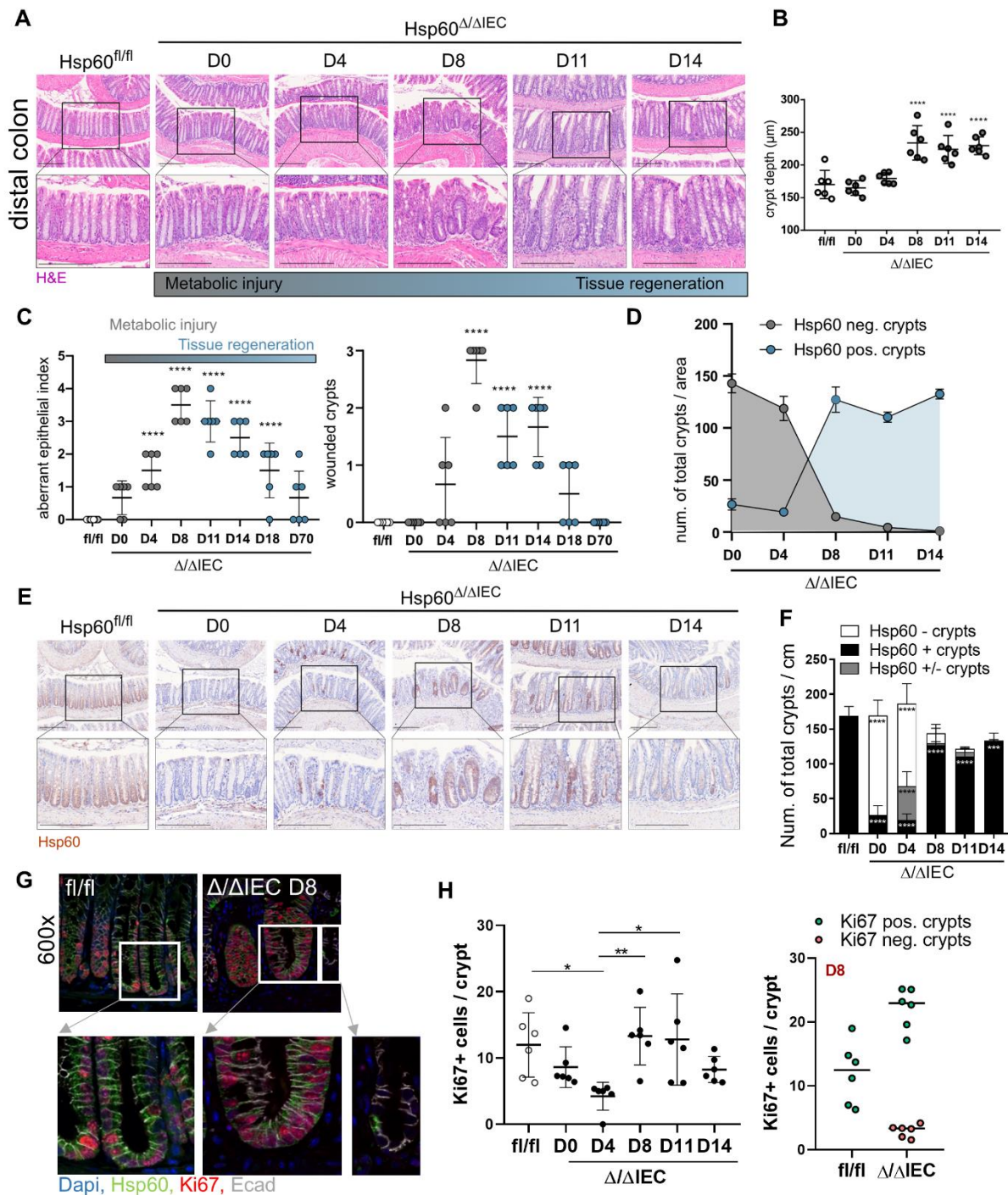
Figure 11: Hsp60 deletion induces metabolic injury in colonocytes.
(A) Representative H&E stained sections of colonic swiss roles and corresponding higher magnifications for Hsp60$^{\Delta/\Delta IEC}$ mice on days (D) 0, 4, 8, 11, and 14 (scale bars = 200µM). **(B)** Quantification of crypt depth over all time points. **(C)** Colonic tissue was scored histologically for an aberrant epithelial architecture and wounded crypts. **(D)** Quantification of Hsp60 positive and negative crypts in Hsp60$^{\Delta/\Delta IEC}$ mice over time. **(E)** Representative immunohistochemically stained colonic swiss rolls for Hsp60 in Hsp60$^{\Delta/\Delta IEC}$ mice on days (D) 0, 4, 8, 11 and 14 (scale bars = 200µM). **(F)** Quantification of Hsp60 positive and negative crypts in Hsp60$^{\Delta/\Delta IEC}$ compared to Hsp60$^{fl/fl}$ mice. **(G)** Representative immunofluorescence co-staining of Hsp60 (green), Ki67 (red), and E-cadherin (grey) in Hsp60$^{\Delta/\Delta IEC}$ and Hsp60$^{fl/fl}$ mice at day (D) 8 (600x). Lower panel: higher magnification (2400x) of the indicated sections. Dapi = blue. **(H)** Quantification of Ki67 positive and negative crypts at day (D) 8 and Ki67 positive cells per crypt over all time points. Statistics: (B,C,H) ANOVA followed by pairwise comparison testing (Tukey). (F) Two-way ANOVA followed by multiple comparisons (Tukey). Mean ± SD, n=6. Asterisks indicate significant differences *P<0.05, **P<0.01, ***P<0.001; ****P<0.0001.
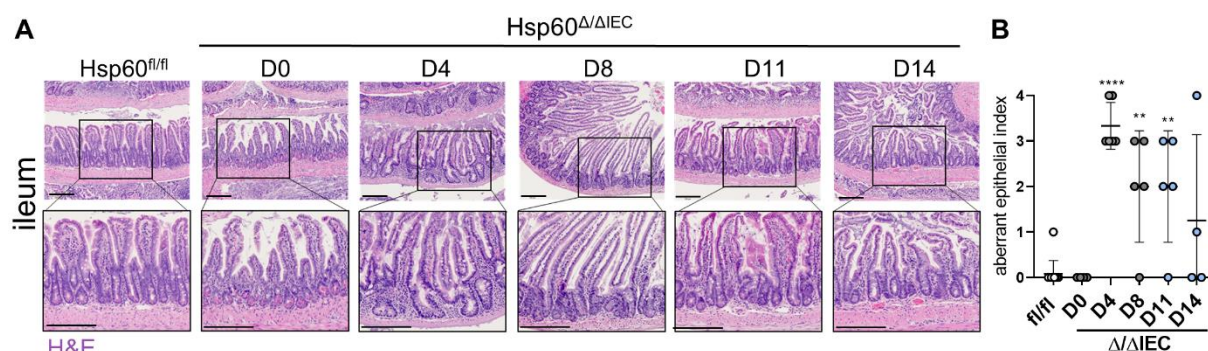
Figure 12: The kinetic of metabolic injury and regeneration is faster in the ileum.
(A) Representative H&E stained sections of ileal swiss roles and corresponding higher magnifications for Hsp60$^{\Delta/\Delta IEC}$ mice on days (D) 0, 4, 8, 11, and 14 (scale bars = 200µM). **(B)** Ileal tissue was scored histologically for an aberrant epithelial architecture. Statistics: (B) ANOVA followed by pairwise comparison testing (Tukey). Mean ± SD, n=6. Asterisks indicate significant differences *P<0.05, **P<0.01, ***P<0.001; ****P<0.0001.

4.4. IP-MS/MS of Hsp60 shows involvement of binding partners mainly in cellular and metabolic processes

Hsp60 functions as a chaperone in the mitochondrial matrix and thus folds and interacts with a diverse range of proteins. To gain insight into Hsp60-associated proteins, co-immunoprecipitation, and subsequent MS/MS analysis was performed in the small intestinal cell line ModeK and the colonic cell line PTK6.

MS/MS raw data was used to generate protein intensities (iBAQ), filtered (LFQs: 3-5), and normalized. The high abundance of Hsp60 in both vulcano plots confirmed a successful pulldown of Hsp60 (Supplementary figure 3A). After applying a cutoff (FDR < 0.05), 71 proteins were significantly enriched and hence associated with Hsp60 in ModeK cells and 80 proteins in PTK6 cells (Supplementary figure 3B). A comparison between both cell lines revealed 18 overlapping proteins, of which 4 were localized to mitochondria (Dars, Etfa, Hsd17b10, Tufm) (Supplementary figure 3C). PANTHER GO term analysis of these 18 proteins demonstrated an involvement in six biological processes (level 1), including response to stimulus, signaling, cellular process, metabolic process, biological regulation, and localization (Supplementary figure 3D). Cellular process (41.7%) and metabolic process (36.1%) represented the two major biological processes, suggesting a crucial role of Hsp60 and its binding partners in regulating cellular and metabolic processes. This aligns with the *in vivo* data, where a deletion of Hsp60 and hence potential dysregulation of its binding partners induced metabolic alteration in IECs. In addition, a PANTHER overrepresentation test (FISHER) identified 8 significantly enriched biological processes comprising amide and peptide metabolic/biosynthetic processes as well as translation (Supplementary figure 3E).

Since these processes are often altered in cancer, the 18 overlapping genes were analyzed using the TCGA data set (PanCancer Atlas; large-scale genomics data set from colorectal adenocarcinoma). Overall, queried genes were altered in 308 (59%) of queried patients/samples (total N=526). Interestingly, the disease-free survival was significantly reduced in the altered compared to the non-altered group (Supplementary figure 3F), demonstrating an essential role of Hsp60-associated proteins in maintaining cellular health.

In summary, numerous Hsp60 binding partners were identified in intestinal cell lines. GO-term analysis highlighted the essential role of these Hsp60 associated proteins in regulating cellular and metabolic processes. Moreover, clinical data provided critical insights into the involvement of these proteins in cancer development.

4.5. Mitochondrial stress impairs cellular metabolism

Based on previous studies, a microarray analysis of colonocytes at day 2 revealed changes in IEC metabolism upon Hsp60 loss, including reduced respiration, increased glycolysis, and changes in amino acid and lipid metabolism.

A NanoString analysis of a metabolic panel of ~ 800 genes was performed to further investigate the metabolic changes in Hsp60$^{\Delta/\Delta IEC}$ mice on three different time points (D0, D8, D14) in colonic tissue from Hsp60$^{\Delta/\Delta IEC}$ mice. In total, 45 genes showed a fold change greater than 2 at day 0, including 31 up- and 14 downregulated genes (Figure 13A). Of these 45 genes, 10 were mitochondria localized, including *Shmt2, Pck2, Pycr1, Hk2, Cps1, Pdk3, Hadh, Otc, Scdp2,* and *Pdk4*. Effects were attenuated at day 8 with 35 altered genes (15 up-, 20 downregulated) and on day 14 with 38 altered genes (13 up-, 25 downregulated) (Figure 13B). Interestingly, 5 genes overlapped over all three time points, namely *Apoa1, Cps1, H2-Q10, Ido1,* and *Otc*. KEGG pathway analysis of the 45 regulated genes at day 0 highlighted the enrichment of glycine, serine and threonine metabolism, biosynthesis of amino acids and carbon metabolism, arginine biosynthesis, and tryptophan metabolism (Figure 13C). The genes altered in the latter pathway include *Ido1, Tph1, Aoc1, Kyat3,* and *Hadh*, which overlap with genes found in the microarray analysis. In addition to altered fold changes, genes were tested for differential expression in response to covariates. Volcano plots of differentially expressed genes (DEGs) showed 51 significantly altered genes at day 0 (29 up-, 22 downregulated), 44 genes at day 8 (28 up-, 15 downregulated), and 52 genes at day 14 (41 up-, 11 downregulated) (Figure 13D). The results of differential expression testing were summarized at the gene set level using a global significance score of Hsp60$^{\Delta/\Delta IEC}$ compared to Hsp60$^{fl/fl}$ mice. Most prominent changes were observed at day 0 with upregulated glutamine

metabolism, amino acid synthesis and amino acid transporters, and downregulated DNA damage repair, endocytosis, tryptophan/kynurenine metabolism, IDH12 activity, fatty acid synthesis and fatty acid oxidation. Importantly, the energy metabolism of the epithelium shifted from mitochondrial OXPHOS to glycolysis (Figure 13E). In addition, gene expression levels of the mitochondria-localized glycolysis gene hexokinase 2 (*Hk2*), the mitochondria localized regulator of glucose metabolism pyruvate dehydrogenase kinase 4 (*Pdk4*), the cytosolic glucose transporter *Slc37a2*, as well as cyclooxygenase-I (*Cox-I*), a part of the mitochondrial respiratory chain, were validated (Figure 13F). The expression levels confirm increased glycolysis and decreased respiration, corroborating the microarray and NanoString analysis results.

Concluding, it could be demonstrated that colonocytes are metabolically impaired after Hsp60 loss, indicating a tremendous cellular metabolic vulnerability upon activated MT-UPR signaling.

Figure 13: Hsp60 deletion induces changes in cellular metabolism.

(A) Heatmap of a NanoString analysis of a metabolic panel of 800 genes in colonic tissue at day 0. Depicted are genes with a fold-change greater than ± 2. (green): mitochondria localized genes. (red): Tryptophan metabolism-associated genes. **(B)** Venn-diagram illustration of the number of genes with a fold-change greater than ± 2 at day (D) 0, 8, and 14 in Hsp60$^{\Delta/\Delta IEC}$ compared to Hsp60$^{fl/fl}$ mice. **(C)** KEGG pathway analysis of the 45 altered genes at day 0. **(D)** Vulcano plots of differentially regulated genes (DEGs) (FDR < 0.05) at day (D) 0, 8, and 14 in Hsp60$^{\Delta/\Delta IEC}$ compared to Hsp60$^{fl/fl}$ mice. **(E)** Summary of DEGs at gene set level to create a global significance score for different metabolic pathways. **(F)** mRNA expression levels of colonic tissue for metabolic genes (*Hk2, Pdk4, Slc37a2, Cox-I*). Statistics: ANOVA followed by pairwise comparison testing (Tukey). Mean ± SD, n=6. Asterisks indicate significant differences *P<0.05, **P<0.01, ***P<0.001; ****P<0.0001.
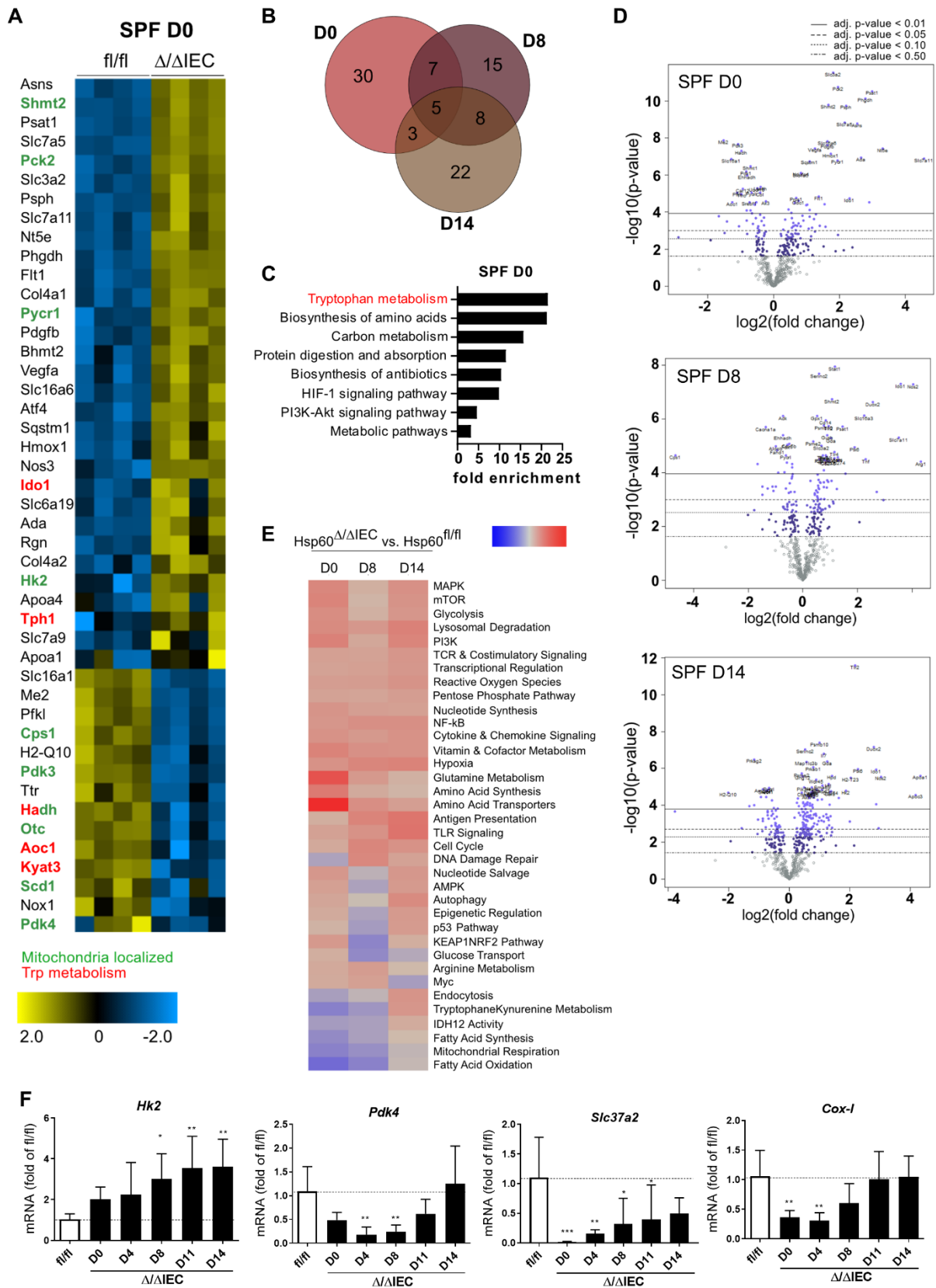
Figure 13: Hsp60 deletion induces changes in cellular metabolism.
(Figure legend previous page)

4.6. Metabolic injury alters arginine and tryptophan metabolism

Changes in arginine and tryptophan metabolism were demonstrated in both the microarray and NanoString datasets. To further investigate these metabolic alterations, qRT-PCR analysis of the tryptophan-degrading enzyme indolamine-2,3-dioxygenase (*Ido1*) as well as the arginine degrading enzymes arginase-1/2 (*Arg1/2*) and inducible nitric oxide synthase 2 (*Nos2*) was performed in colonic tissue from Hsp60$^{\Delta/\Delta IEC}$ mice. An induction of *Ido1, Nos2,* and *Arg1* was observed from day 4, indicating enhanced tryptophan and L-arginine metabolism during metabolic injury. *Arg2,* on the other hand, was reduced during metabolic injury and increased from day 11 on, suggesting its involvement in tissue regeneration (Figure 14A).

In addition, Ido1 immunofluorescence staining of colonic tissue sections revealed no signal at day 0 and day 4 in IECs or underlying lamina propria. Interestingly, on day 8, Ido1 was expressed in IECs in both wounded crypts and the crypt base of hyperproliferative crypts (Figure 14B). Immunofluorescence co-staining of Ido1 revealed that Ido1-positive cells were Hsp60 and Ki67 negative. Moreover, they were positive for the secretory markers mucin 2 (Muc2) and matrix metalloproteinase 7 (Mmp7) (Figure 14C), suggesting the epithelial release of secretory metabolites by wounded enterocytes (Hsp60 negative, Ki67 negative) to support healing processes of the stem cell compartment. At day 11 and day 14, IECs were again Ido1 negative, however, a strong Ido1 expression was present in the lamina propria, indicating a switch of Ido1 expression from IECs to immune cells and fibroblasts.

Concluding, these data reveal changes in arginine and tryptophan metabolism of colonocytes and immune cells during metabolic injury and subsequent regeneration.
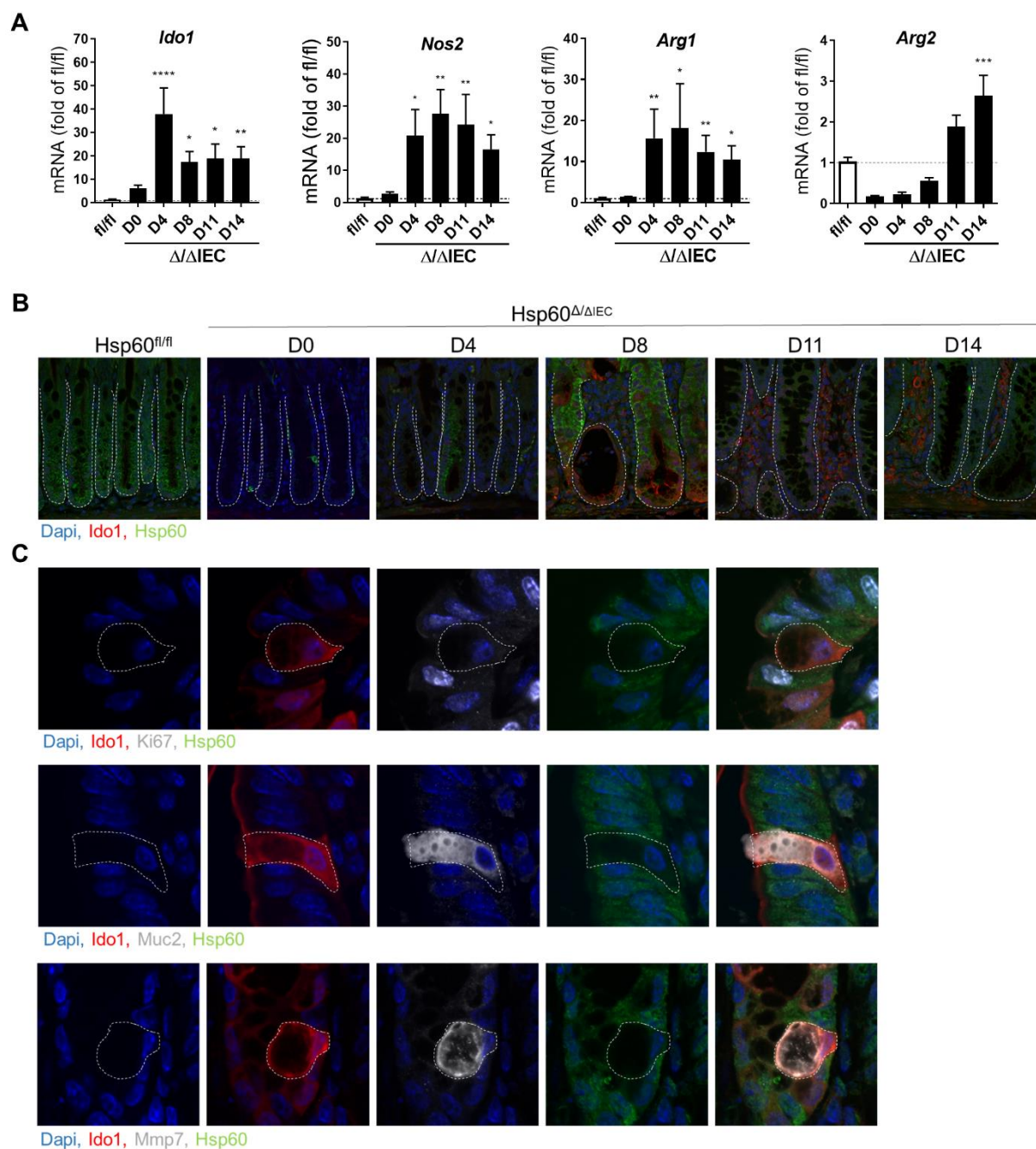
Figure 14: Arginine and tryptophan metabolism are altered during injury and repair.
(A) mRNA expression levels of colonic tissue for arginine and tryptophan-related genes (*Ido1, Nos2, Arg1,* and *Arg2*) in Hsp60$^{\Delta/\Delta IEC}$ compared to Hsp60$^{fl/fl}$ mice. **(B)** Representative immunofluorescence co-staining of Hsp60 (green) and Ido1 (red) in Hsp60$^{\Delta/\Delta IEC}$ and Hsp60$^{fl/fl}$ mice from day (D) 0 to 14 (600x). Dapi = blue. **(C)** Representative immunofluorescence co-staining of Hsp60 (green) and Ido1 (red) with Ki67 (grey; upper panel), Muc2 (grey; middle panel), or Mmp7 (grey; lower panel). Statistics: (A) ANOVA followed by pairwise comparison testing (Tukey). Mean ± SD, n=6. Asterisks indicate significant differences *P<0.05, **P<0.01, ***P<0.001; ****P<0.0001.

4.7. Tryptophan metabolites amplify MT-UPR signaling in organoids

Since changes in tryptophan metabolism were observed during metabolic injury, the contribution of tryptophan metabolites to mitochondrial stress was subsequently examined *in vitro*. It was hypothesized that the microbiota induces metabolic injury via tryptophan depletion and indole synthesis. This could lead in parallel to an increased kynurenine pathway (increased Ido1) as a rescue mechanism for the host. The kynurenine metabolites could salvage but potentially harm the host in high doses.

Intestinal organoids were generated from Hsp60$^{fl/fl}$ mice, and Hsp60 deletion was induced *in vitro* via tamoxifen (Hsp60$^{\Delta/\Delta IEC}$). On day 4, organoids were treated for 48h with host-derived kynurenine metabolites (1-L-methyltryptophan (1-D-MT), 3-hydroxy anthranilic acid (3HAA)) as well as bacterial-derived indoles (IAA, IPA, IS) (Figure 15A,B).

While the Ido1 antagonist 1-D-MT did not impact MT-UPR signaling (*Chop, Trb3*) and stemness (*Lgr5*), the Ido1 downstream kynurenine metabolite 3HAA enormously amplified MT-UPR signaling (*Chop, Trb3*) and reduced stemness (*Lgr5*) (Figure 15C). Interestingly, growth was increased with 3HAA treatment independent of the genotype, indicating that 3HAA might induce a proliferative response (Figure 15D). In comparison, the indole IPA but not IAA and IS elevated MT-UPR signaling (*Chop, Trb3*) while stemness (*Lgr5*) stayed unchanged (Figure 15F). The profound impact of these indoles is reflected by organoid growth patterns, comprising increased growth with IAA and IPA treatment in Wt organoids in parallel to unchanged *de novo* crypt formation (budding). While Hsp60 organoids seemed insensitive to IAA, IPA and IS slightly increased growth and budding (Figure 15E).

Together, these data implicate an impact of 3HAA and IPA on MT-UPR signaling, suggesting a role of these metabolites in aggravating mitochondrial dysfunction and hence metabolic injury. Counterintuitively, these changes are accompanied by increased growth and differentiation. Thus, bacterial-derived IPA and host-produced 3HAA might amplify mitochondrial dysfunction, which briefly pushes the proliferation and differentiation of stem cells, depleting the stem cell pool to counteract the metabolic changes.
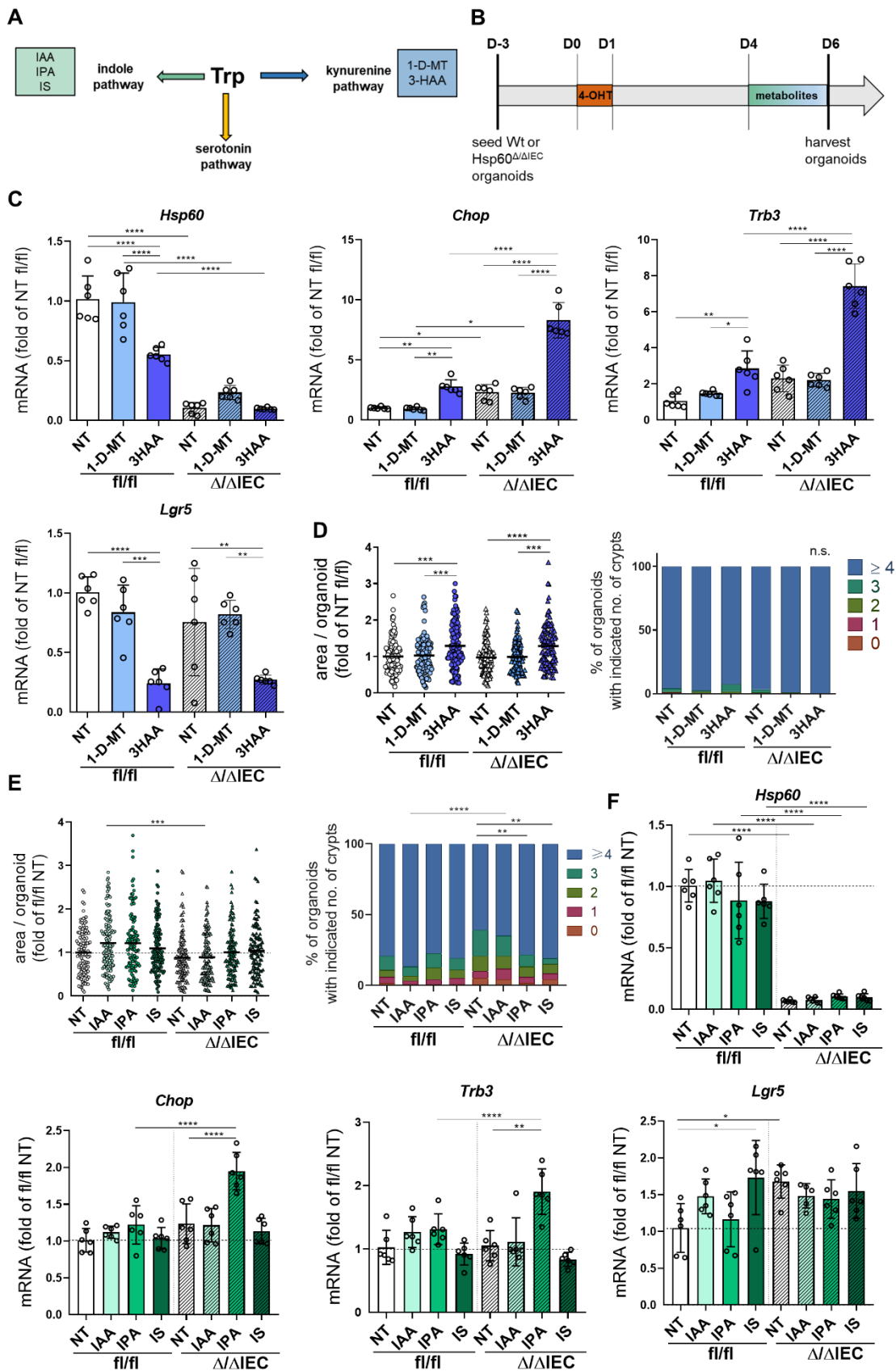
Figure 15. Tryptophan-derived metabolites amplify MT-UPR signaling *in vitro*.
(A) Schematic illustration of the three different pathways metabolizing tryptophan and some downstream metabolites. **(B)** Experimental setup. Hsp60 deletion is induced *ex vivo* in small intestinal organoids from Hsp60$^{\Delta/\Delta IEC}$ mice (Ctrl: Hsp60$^{fl/fl}$ mice) by adding tamoxifen (500nM) for 24h to the culture media. Following Hsp60

loss, organoids are treated with IAA (200µM), IPA (100µM), IS (200µM), 1-D-MT (1mM), or 3HAA (200µM) for 2 days. mRNA expression levels of *Hsp60, Trb3, Chop* and *Lgr5* of organoids treated with **(C)** 1-D-MT/3HAA or **(F)** IAA/IPA/IS. **(D,E)** Quantification of organoid area and *de novo* crypt formation (budding) at day (D) 6 for the respective organoids and treatments. Statistics: (C-F) ANOVA followed by pairwise comparison testing (Tukey). (D,E) Mann-Whitney test. Mean ± SD, n=6. Asterisks indicate significant differences *P<0.05, **P<0.01, ***P<0.001; ****P<0.0001. IAA: indole-acetic-acid; IPA: indole-propionic-acid; IS: indoxyl-sulfate; 1-D-MT: 1-L-methyltryptophan; 3HAA: 3-hydroxyanthranilic acid.

4.8. Mild mitochondrial impairment does not induce metabolic injury

A second novel mouse model for mitochondrial impairment was generated to further explore the link between mitochondrial dysfunction and tissue homeostasis. Similar to the Hsp60$^{\Delta/\Delta IEC}$ model, Cre-mediated recombination is required to induce conditional deletion of the mitochondrial chaperone ClpP specifically in IECs after feeding tamoxifen-containing diet for one week (ClpP$^{\Delta/\Delta IEC}$ mice).

To reveal the impact of a ClpP deficiency on colonic IECs, ClpP$^{\Delta/\Delta IEC}$ mice were analyzed at five different time points (D0, D4, D8, D11, D14) after the end of tamoxifen treatment and complete ClpP deletion (Figure 16A). DNA isolated from mouse tail or colonic tissue was used to detect the presence or absence of *Villin*CreER^{T2} and the Hsp60 flox or KO allele (Figure 16B). In contrast to the Hsp60$^{\Delta/\Delta IEC}$ model, weight development was similar in ClpP$^{\Delta/\Delta IEC}$ and control ClpP$^{fl/fl}$ mice (Figure 16C). To confirm the deletion of *ClpP*, colonic tissue was processed for qRT-PCR (Figure 16D). The length of all intestinal segments (duodenum, jejunum, ileum, colon), as well as the weight of all organs (cecum, stomach, pancreas, spleen, thymus, liver, kidney, muscle), including MLNs, did not differ (Figure 16E, Supplementary figure 4). Complete *ClpP* deletion at day 0 was associated with transiently activated MT-UPR signaling. While the MT-UPR transcription factor *Chop* was not altered, the downstream MT-UPR target genes *Trb3* and *Chac1* showed a significant increase at day 0. However, *Atf4* and *Atf5* were unchanged at the analyzed time points (Figure 16F). Histological analysis of colonic tissue revealed a slight increase in crypt length from day 8 to 14 (Figure 16G,H). Nevertheless, the score for aberrant epithelial architecture was 0 in all mice over all time points. In Hsp60$^{\Delta/\Delta IEC}$ mice, the regenerative response towards metabolic injury was associated with an activated immune system. Contrary to this, ClpP$^{\Delta/\Delta IEC}$ mice demonstrated no strong induction of inflammatory markers (*Saa3, Tnf*) (Figure 16I). In line, *Ido1, Arg1,* and *Nos2* were unchanged, indicating no metabolic alterations (Figure 16J).

From these data, it can be concluded that, in contrast to the Hsp60$^{\Delta/\Delta IEC}$ model, the ClpP$^{\Delta/\Delta IEC}$ model results in milder signs of mitochondrial impairment and develops no spontaneous tissue alteration, allowing us to study different susceptibility thresholds of MT-UPR in the intestinal epithelium.
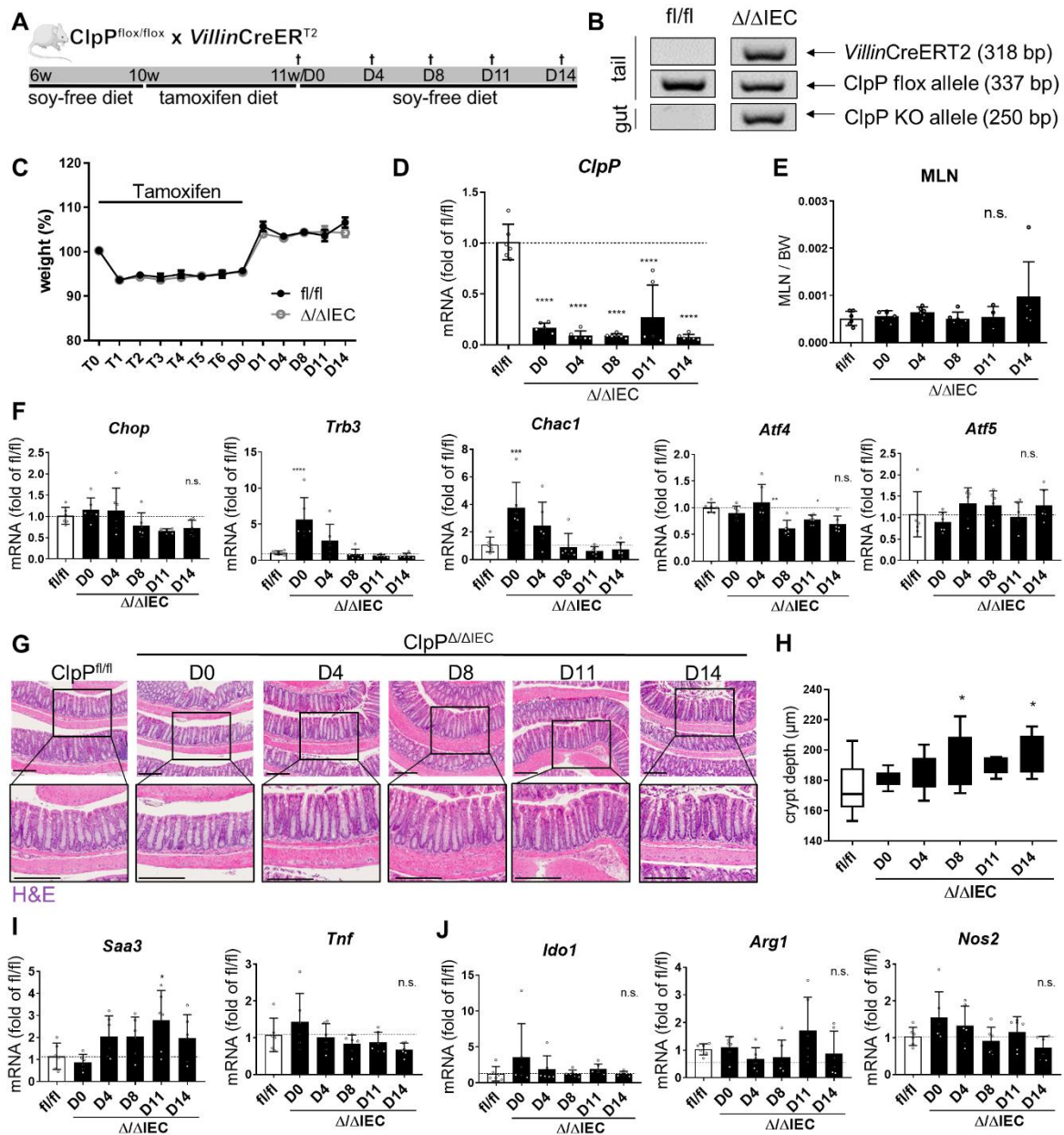
Figure 16: Loss of ClpP induces mild mitochondrial impairment without tissue aberration.
(A) Experimental setup illustrating the IEC-specific deletion of ClpP in mice (ClpP$^{\Delta/\Delta IEC}$ mice, Ctrl: ClpP$^{fl/fl}$) by oral feeding with tamoxifen supplemented food. Mice were sacrificed at day (D) 0, 4, 8, 11, 14 after end of tamoxifen treatment and full ClpP deletion. **(C)** Weight curves of ClpP$^{\Delta/\Delta IEC}$ and ClpP$^{fl/fl}$ mice from the start of tamoxifen feeding until D14. **(D)** mRNA levels of colonic tissue for *ClpP* expression. **(E)** MLN weight relative to body weight in ClpP$^{\Delta/\Delta IEC}$ mice from day (D) 0 to 14 and ClpP$^{fl/fl}$ mice. **(F)** mRNA expression levels of colonic tissue for MT-UPR relevant genes *Chop, Trb3, Chac1, Atf4,* and *Atf5*. **(G)** Representative H&E stained sections of colonic swiss roles and corresponding higher magnifications for ClpP$^{\Delta/\Delta IEC}$ mice on day (D) 0, 4, 8, 11 and 14 (scale bars = 200µM). **(H)** Quantification of crypt depth over all time points. **(I)** mRNA expression levels of colonic tissue for the cytokine *Tnf* and the systemic inflammation marker *Saa3*. **(J)** mRNA expression levels of colonic tissue for arginine and tryptophan relates genes (*Ido1, Nos2, Arg1*). Statistics: ANOVA followed by pairwise comparison testing (Tukey). Mean ± SD, n=6. Asterisks indicate significant differences *P<0.05, **P<0.01, ***P<0.001; ****P<0.0001.

4.9. Hyperproliferation does not induce tumorigenesis after metabolic injury

The transiently increased proliferative capacity in Hsp60$^{\Delta/\Delta IEC}$ mice could be a susceptibility factor for colonic cancer development. It was thus investigated if a pro-cancerous milieu could render hyperproliferative crypts susceptible to tumor development. In doing so, Hsp60$^{\Delta/\Delta IEC}$ mice were injected with the colon carcinogen azoxymethane (AOM) at days 4 and 11 after tamoxifen treatment and sampled at day 18 (initial) and D70 (long term) (Figure 17A). AOM increases colonic tumor susceptibility by intercalating into DNA and inducing double-strand breaks.

No differences in weight development were observed between Hsp60$^{\Delta/\Delta IEC}$ mice injected with AOM or PBS (Figure 17B). In line, all organs and intestinal segments did not differ, except for an increase in colon length in Hsp60$^{\Delta/\Delta IEC}$ mice injected with AOM compared to PBS controls and Hsp60$^{fl/fl}$ mice injected with AOM (Figure 17C; Supplementary figure 5). Gene expression analysis of colonic tissue showed no MT-UPR signaling (*Chop, Trb3*) at these late time points, indicating that AOM does not prolong MT-UPR signaling (Figure 17D).

On tissue level, H&E staining and respective quantification showed an increased crypt depth and tissue aberration score at day 18 in Hsp60$^{\Delta/\Delta IEC}$ mice. However, these effects did not differ between AOM or PBS treatment and vanished at day 70 (Figure 17E-G). In line, Hsp60 expression was almost fully recovered at day 18 and was unaffected by AOM (Figure 17H,I).

These results indicate that compensatory hyperproliferation following metabolic injury does not lead to a loss of proliferative control upon adding a chemical substance inducing colonic tumors.

Figure 17: Hyperproliferation does not induce loss of proliferative control.
(A) Experimental setup illustrating the IEC-specific deletion of Hsp60 in mice (Hsp60$^{\Delta/\Delta IEC}$ mice, Ctrl: Hsp60$^{fl/fl}$) by oral feeding with tamoxifen supplemented food. Mice were i.p. injected with AOM (Ctrl: PBS) at days (D) 4 and 11 and sacrificed at day (D) 18 or 70 after end of tamoxifen treatment and full Hsp60 deletion. **(B)** Weight curves of Hsp60$^{\Delta/\Delta IEC}$ and Hsp60$^{fl/fl}$ mice with AOM/PBS from tamoxifen feeding until D70. **(C)** Colon length (cm) and MLN weight relative to body weight in the respective mice at day (D) 18 and 70. **(D)** mRNA expression levels of colonic tissue for MT-UPR relevant *genes (Chop, Trb3)*. **(E)** Representative H&E stained sections of colonic swiss roles and corresponding higher magnifications for Hsp60$^{\Delta/\Delta IEC}$ mice with AOM/PBS on day (D) 18 and 70 (scale bars = 200µM). **(F)** Quantification of crypt depth in all respective groups. **(G)** Colonic tissue was scored histologically for an aberrant epithelial architecture. **(H)** Quantification of Hsp60 positive and negative crypts in Hsp60$^{\Delta/\Delta IEC}$ compared to Hsp60$^{fl/fl}$ mice. **(I)** Representative immunohistochemically stained colonic swiss rolls for Hsp60 for Hsp60$^{\Delta/\Delta IEC}$ mice with AOM/PBS on day (D) 18 and 7 (scale bars = 200µM). Statistics: (C,D,F,G) ANOVA followed by pairwise comparison testing (Tukey). (H) Two-way ANOVA followed by multiple comparisons (Tukey). Mean ± SD, n=6. Asterisks indicate significant differences *P<0.05, **P<0.01, ***P<0.001; ****P<0.0001.
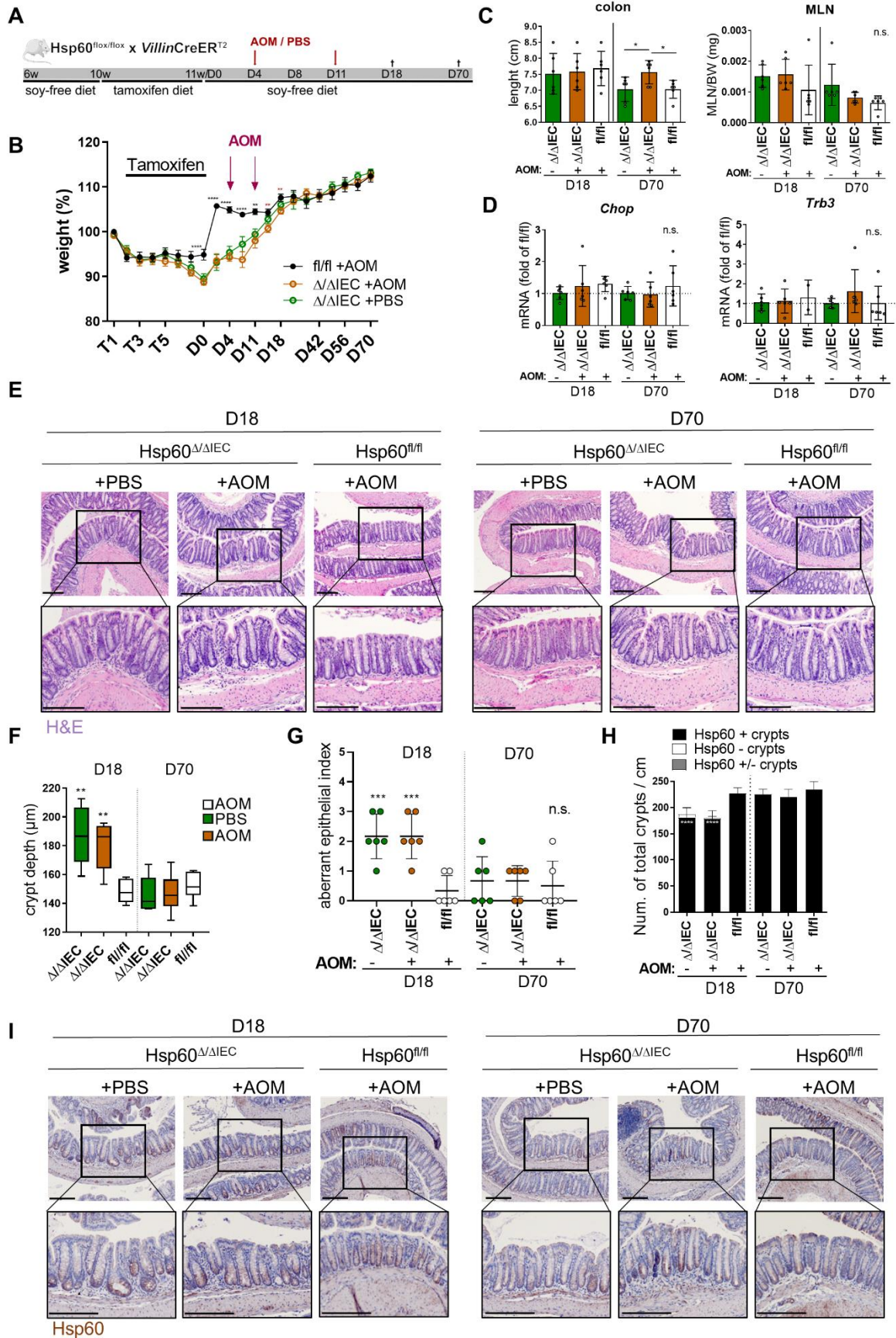
Figure 17: Hyperproliferation does not induce loss of proliferative control.
(Figure legend previous page)

4.10. Co-culture of organoids with mesenchymal cells induces Wnt signaling and organoid growth

The intestinal microenvironment contains distinct cell populations interacting with IECs and influencing their proliferative rate. For instance, intestinal mesenchymal cells, including fibroblasts and myofibroblasts, are located in the intestinal lamina propria and are essential regulators of IEC homeostasis by producing a wide range of Wnt factors.

To characterize the epithelial-mesenchymal cross-talk and the impact of mesenchymal cells on IEC proliferation, a co-culture system of Hsp60$^{\Delta/\Delta IEC}$ organoids and intestinal mesenchymal cells was established (Figure 18A). Organoids were seeded into a transwell, and *Hsp60* knockout was induced via tamoxifen addition to the media. After tamoxifen was removed, mesenchymal cells were seeded into the bottom of the well, and the co-culture was analyzed 4 days later (Figure 18B).

qRT-PCR revealed a complete *Hsp60* deletion and activation of MT-UPR signaling (*Trb3*) independent of mesenchymal cells (Figure 18C). Interestingly, mesenchymal cells strongly increased organoid area in both control and Hsp60 deficient organoids while *de novo* crypt formation remained unchanged (Figure 18D-F), indicating that mesenchymal cells secrete growth-promoting signals. These signals did not lead to a further drop in stemness (*Lgr5*) in Hsp60$^{\Delta/\Delta IEC}$ organoids but increased the transit-amplifying compartment (*Prom1*) (Figure 18G). At the same time, mesenchymal cells showed a tendency towards an increase in *Ido1* that was more pronounced in Hsp60$^{\Delta/\Delta IEC}$ compared to control organoids. *Nos2* was increased similarly in control organoids in co-culture with mesenchymal cells. Still, the latter significantly decreased expression levels in Hsp60$^{\Delta/\Delta IEC}$ organoids (Figure 18H), revealing an impact of mesenchymal cells on IEC metabolism. In addition, expression of the Wnt factor *Wnt9a* was induced in organoids co-cultured with IECs independent of the genotype (Figure 18I). This is in line with the observed increase in area, indicating that mesenchymal cells produce Wnt factors by themselves and stimulate IECs to produce them.

Concluding, mesenchymal cells strongly impact the proliferative capacity of IECs, highlighting the cross-talk between the microenvironment and IECs during metabolic injury.
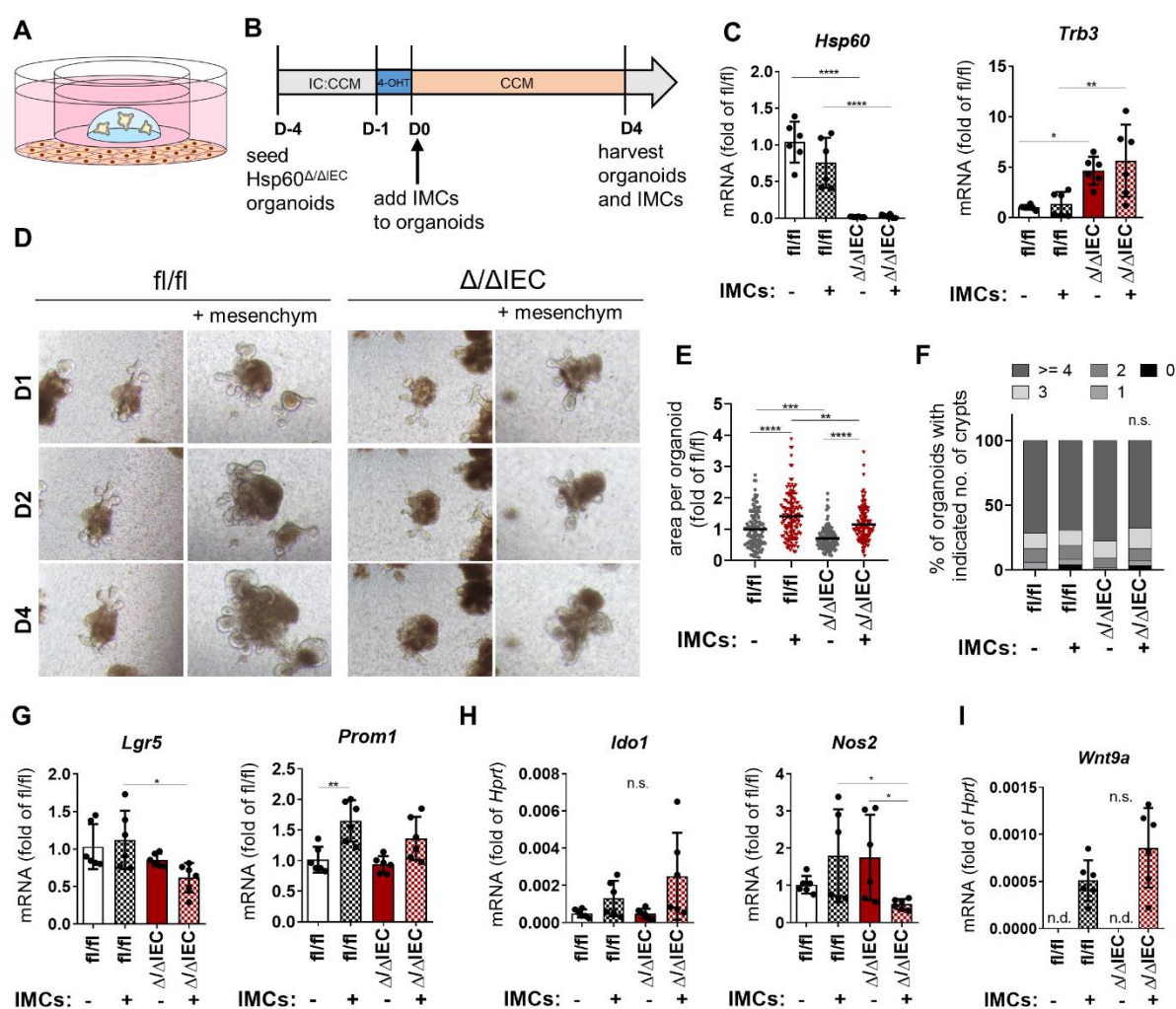
Figure 18: Co-culture of organoids with mesenchymal cells impacts IEC proliferation and metabolism.
(A,B) Experimental setup. Hsp60 deletion is induced *ex vivo* in small intestinal (organoids from Hsp60$^{\Delta/\Delta IEC}$ mice (Ctrl: Hsp60$^{fl/fl}$ mice) by adding tamoxifen (500nM) for 24h to the culture media. After the removal of tamoxifen, intestinal mesenchymal cells are seeded into the transwell to generate a co-culture system, and organoids are then monitored up to 4 days. **(C)** mRNA expression levels of organoids for *Hsp60* and the MT-UPR relevant gene *Trb3*. **(D)** Representative pictures of respective organoids. **(E)** Quantification of organoid area and **(F)** *de novo* crypt formation (budding) at day (D) 4. mRNA expression levels of organoids for **(G)** epithelial subpopulation markers (*Lgr5, Prom1*), **(H)** for arginine and tryptophan relates genes (*Ido1, Nos2*) and **(I)** the Wnt factor *Wnt9a*. Statistics: (C,E,G-I) ANOVA followed by pairwise comparison testing (Tukey). (F) Mann-Whitney test. Mean ± SD, n=6. Asterisks indicate significant differences *P<0.05, **P<0.01, ***P<0.001; ****P<0.0001. IMCs: intestinal mesenchymal cells.

Previous studies showed that Hsp60-deficient IECs secrete Wnt10a. This and potentially other epithelial cell-derived Wnt factors comprise paracrine feedback loops contributing to tissue healing. To analyze Wnt production by IECs, Hsp60$^{\Delta/\Delta IEC}$ organoids were kept on BCM media for 4 days to induce maximal differentiation (Figure 19A). Gene expression analysis confirmed *Hsp60* deletion and MT-UPR induction (*Trb3*) (Figure 19B). As observed in previous experiments, *Hsp60* deletion affected organoid morphology (Figure 19C). Interestingly, Hsp60

deficient organoids upregulated their production of the Wnt factors *Wnt3*, *Wnt4,* and *Wnt9b* (Figure 19E).

To further reveal the impact of metabolically injured IECs and their increase in Wnt production, the media from Hsp60$^{\Delta/\Delta IEC}$ organoids was harvested and used to stimulate intestinal mesenchymal cells (Figure 19A). After 3 days, mesenchymal cells stimulated with control media showed average growth and elongated filaments, indicative of quiescent fibroblasts. Intestinal mesenchymal cells cultured with Hsp60$^{\Delta/\Delta IEC}$ media, however, revealed an increase in mesenchymal cell numbers and a phenotype characterized by cytoplasmic actin-containing stress fibers (Figure 19D), suggesting conversion of quiescent fibroblasts into differentiated myofibroblasts. On gene expression level, their synthesis of the growth factors epiregulin (*Ereg*) and R-spondin 1 (*RSpo1*) was downregulated, while the prostaglandin-endoperoxide synthase 2 (*Ptgs2*) stayed unchanged (Figure 19F).

These results indicate that metabolically injured crypts secrete distinct signals, including Wnt factors, that impact intestinal mesenchymal cell morphology and function in the lamina propria surrounding the stem cell niche.
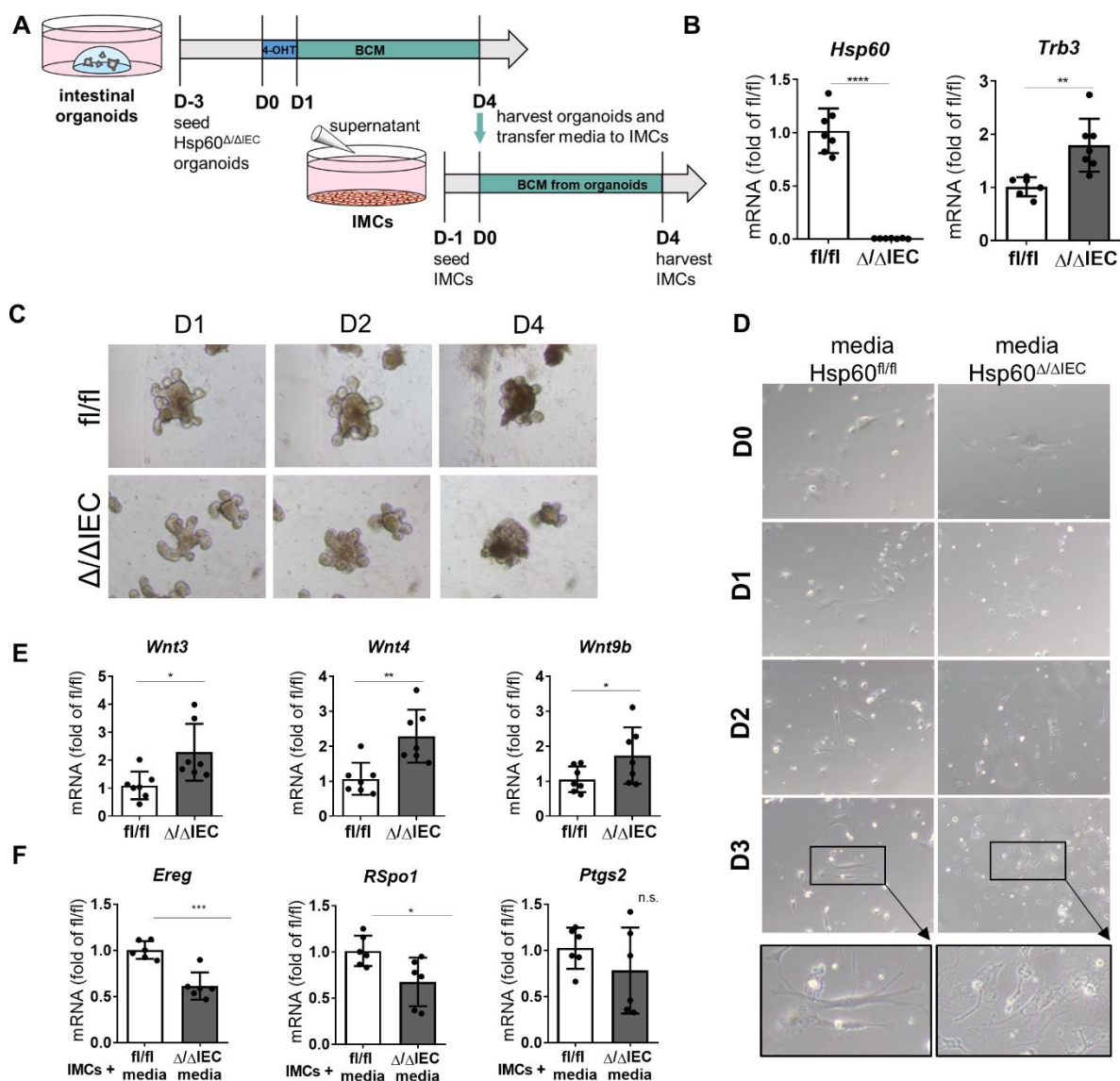
Figure 19: Metabolically injured IECs secrete Wnt factors and impact intestinal mesenchymal cells.
(A) Experimental setup. Hsp60 deletion is induced *ex vivo* in small intestinal organoids from Hsp60$^{\Delta/\Delta IEC}$ mice (Ctrl: Hsp60$^{fl/fl}$ mice) by adding tamoxifen (500nM) for 24h to the culture media. Organoids are cultured for 3 days in BCM, which is subsequently transferred to intestinal mesenchymal cells (IMCs). These are then monitored for 4 days. **(B)** mRNA expression levels of organoids for *Hsp60* and the MT-UPR relevant gene *Trb3*. **(C)** Representative pictures of respective organoids. **(D)** Representative pictures of respective IMCs. mRNA expression levels of IMCs for **(E)** several Wnt factors (*Wnt3, Wnt4, Wnt9b*) and **(F)** growth factors (*Ereg, RSpo1, Ptgs2*). Statistics: (B,E,F) Unpaired t-test assuming Gaussian distribution. Mean ± SD, n=6. Asterisks indicate significant differences *P<0.05, **P<0.01, ***P<0.001; ****P<0.0001. IMCs: intestinal mesenchymal cells.

4.11. Co-culture of Wt with Hsp60-deficient organoids increases crypt length and *de novo* crypt formation

To further prove that paracrine feedback loops exist in metabolically injured IECs, a co-culture system of wild-type (Wt) and Hsp60$^{\Delta/\Delta IEC}$ organoids was established. Wt or Hsp60$^{\Delta/\Delta IEC}$

organoids were seeded and treated with tamoxifen to induce *Hsp60* deletion. After 4 days of complete *Hsp60* deletion, Wt organoids were seeded into the same well (Figure 20A). Co-culture of Wt and Hsp60$^{\Delta/\Delta IEC}$ organoids enhanced crypt length and *de novo* crypt formation of Wt organoids (Figure 20B-D), demonstrating the applicability of this experimental setup. At the expense of proliferation, gene expression analysis revealed a reduction of stemness (*Lgr5*), transit-amplifying compartment (*Prom1*), as well as differentiated IECs (*Alpi*) Figure 20E. These results suggest that paracrine signals from metabolically injured crypts enhance proliferation and tissue healing.
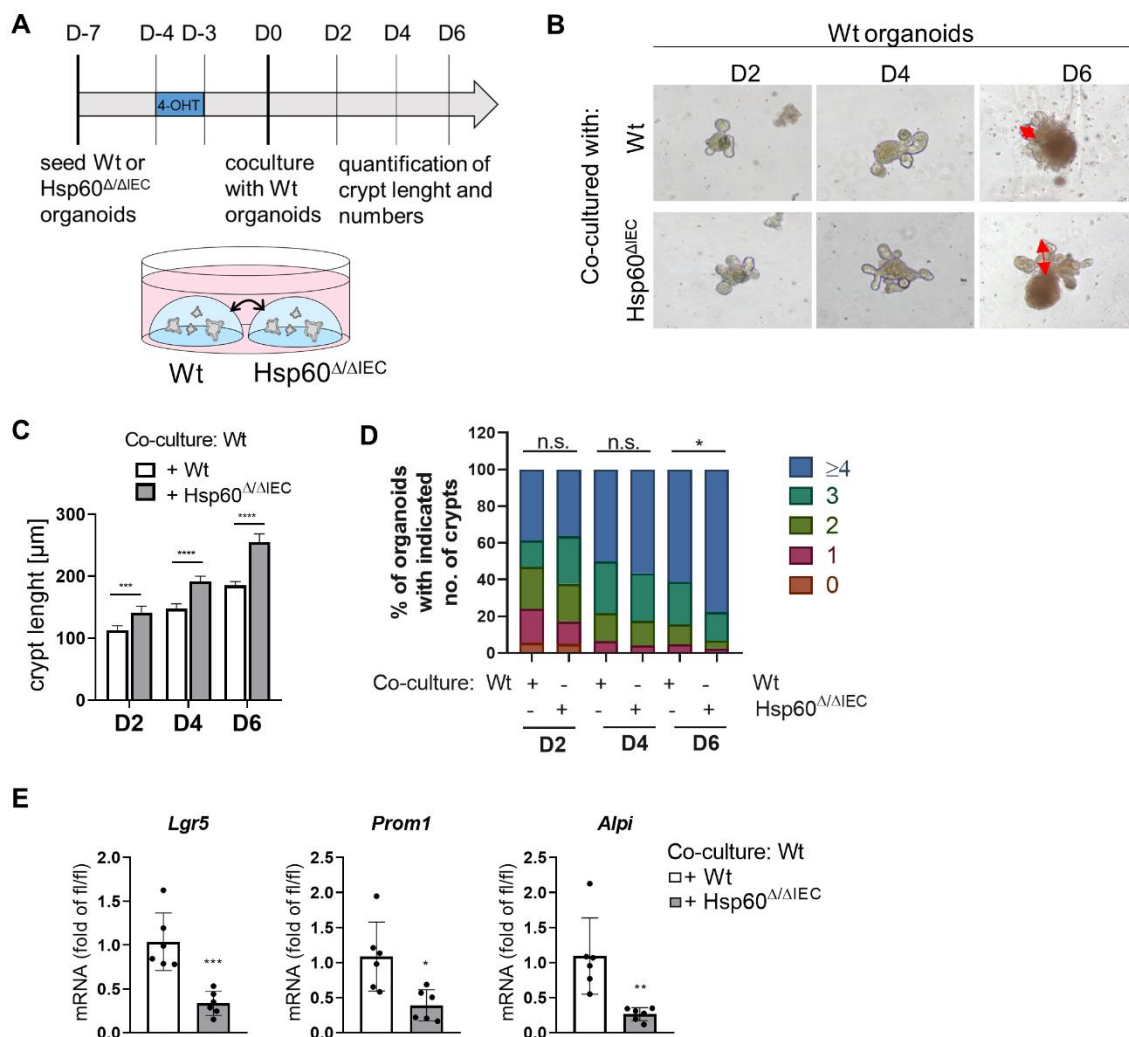
Figure 20: Metabolically injured IECs orchestrate proliferation via paracrine feedback loops.
(A) Experimental setup. Hsp60 deletion is induced *ex vivo* in small intestinal (SI) and colonic organoids from Hsp60$^{\Delta/\Delta IEC}$ mice (Ctrl: Hsp60$^{fl/fl}$ mice) by adding tamoxifen (500nM) for 24h to the culture media. Organoids are then grown for 4 days, and wild-type (Wt) organoids are seeded into the same well to generate a direct co-culture system. **(B)** Representative pictures of respective organoids. **(C)** Quantification of crypt length and **(D)** *de novo* crypt formation (budding) at day (D) 6 under all respective conditions. **(E)** mRNA expression levels of organoids for epithelial subpopulation markers (*Lgr5, Prom1, Alpi*). Statistics: (C) ANOVA followed by pairwise comparison testing (Tukey). (D) Mann-Whitney test. (E) Unpaired t-test assuming Gaussian distribution. Mean ± SD, n=6. Asterisks indicate significant differences *P<0.05, **P<0.01, ***P<0.001; ****P<0.0001.

4.12. Immune cell recruitment during tissue injury and healing

It is common knowledge that tissue injury and healing are associated with activating the immune system. Since an increase in MLN weight was observed during metabolic injury (Figure 21A), inflammatory changes in the colon of Hsp60$^{\Delta/\Delta IEC}$ mice were further characterized. Consistent with the expectations, immune cell aggregation increased during the regenerative response in colonic tissue (Figure 21B). Moreover, crypt abscesses in metabolically injured crypts (Figure 21C) accompanied this phenotype. Changes in colitogenic severity were measured using a tissue pathology index, which includes infiltration of immune cells into the mucosa, submucosa, and muscularis, as well as epithelial damage and atypia/dysplasia. Inflammation was elevated in the proximal colon from day 4, and the distal colon from day 8 and day 14 already displayed a reduction in all colonic segments, indicating transient immune cell recruitment during healing responses (Figure 21D). This aligns with data from a previous Chipcytometry analysis (performed by S. Khaloian; unpublished data) showing increased Ly6G+ cells and CD8+ T-cells in the lamina propria during metabolic injury. Additionally, qRT-PCR analysis of colonic tissue revealed a gradual induction of the inflammatory marker serum amyloid A-3 (*Saa3*), as well as a coordinated expression of pro- (*Tnf*) and anti-inflammatory (*Il10*) cytokines. Interestingly, IL-22 was transiently induced during metabolic injury (Figure 21E). Since IL-22 triggers Stat3 activation, immunohistochemistry of pStat3 was performed. While pStat3 was absent on days 0 and 4, it was intensely but patchy expressed on day 8, mildly expressed on day 11, and absent again on day 14 (Figure 21F), corroborating putative direct signal transduction of IL-22 in the formation of regenerative crypts.

Concluding, these data demonstrate that a homeostatic response towards mitochondrial perturbation of the epithelium involves activation of the immune system and induction of a specific cytokine response.
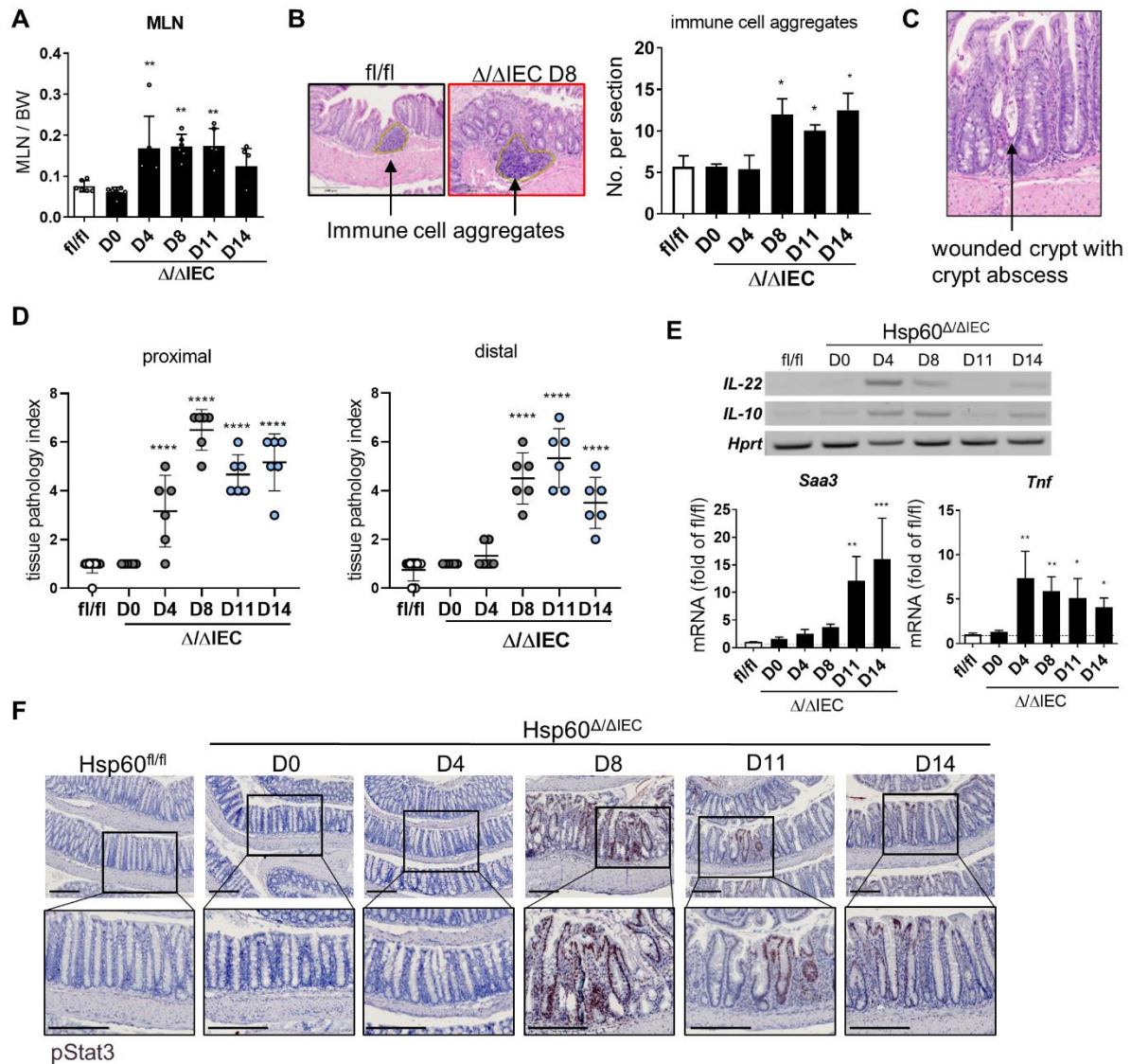
Figure 21: Metabolic injury triggers inflammation in the colon.
(A) MLN weight relative to body weight in Hsp60$^{\Delta/\Delta IEC}$ mice from day (D) 0 to 14 and Hsp60$^{fl/fl}$ mice. **(B)** Representative H&E stained sections of colonic swiss roles depicting immune cell aggregates at D0. Quantification of the number of immune cell aggregates per swiss role over all time points. **(C)** Representative H&E stained section highlighting a wounded crypt with a crypt abscess in Hsp60$^{\Delta/\Delta IEC}$ mice. **(D)** Colonic swiss roles were histologically scored for inflammation in the proximal and distal colon over all time points (range of score 0 (not inflamed) – 12 (highly inflamed). **(E)** mRNA expression levels and respective agarose gels of PCR products of colonic tissue for the cytokines *Il22, Il10, Tnf,* and the systemic inflammation marker *Saa3*. **(F)** Representative immunohistochemically stained colonic swiss rolls for pStat3 in Hsp60$^{\Delta/\Delta IEC}$ mice on day (D) 0, 4, 8, 11 and 14 (scale bars = 200μM). Statistics: ANOVA followed by pairwise comparison testing (Tukey). Mean ± SD, n=6. Asterisks indicate significant differences *P<0.05, **P<0.01, ***P<0.001; ****P<0.0001.

4.13. Co-culture of organoids with macrophages attenuates metabolic injury

The microenvironment underlying the stem cell niche contains a heterogeneous immune cell population that is described to secrete IL-10. One crucial cell type in the first line of defense playing a pivotal role in tissue homeostasis are macrophages. To obtain these immune cells, hematopoietic stem cells were isolated from the bone marrow and differentiated into macrophages using M-CSF. Staining of the macrophage marker Cd11b and subsequent FACS analysis confirmed the presence of differentiated macrophages (data not shown).

To further characterize the epithelial-macrophage cross-talk and the impact of macrophages on IECs, a co-culture system of Hsp60$^{\Delta/\Delta IEC}$ organoids and macrophages was established (Figure 22A). Organoids were seeded into a transwell and *Hsp60* knockout was induced via tamoxifen addition to the media. After tamoxifen was removed, macrophages were seeded into the bottom of the well and the co-culture was analyzed 4 days later (Figure 22B).

Transcriptional profiling revealed a complete *Hsp60* deletion and activation of MT-UPR signaling (*Trb3*) that was significantly dampened in the presence of macrophages (Figure 22C), suggesting that macrophages produce specific factors/cytokines that improve IEC function. In line, macrophages increased the area of Hsp60$^{\Delta/\Delta IEC}$ organoids back to control levels, while the area of control organoids stayed unchanged (Figure 22D,E). This indicates a potential rescue of the loss of proliferative capacity in IECs lacking *Hsp60*. However, macrophages did not alter stemness (*Lgr5*) or IEC differentiation (*Prom1, Alpi*) (data not shown).

Interestingly, the increase of *Ido1* induced by the loss of *Hsp60* was attenuated in the presence of macrophages. The levels of *Nos2*, on the contrary, were not affected. In addition, macrophages restored reduced *Hk2* levels but did not impact the reduction in *Pdk4* and *Cox-I*, suggesting a distinct impact of macrophages on epithelial metabolism (Figure 22F,G).

Taken together, these results add additional evidence that macrophages and their secreted cytokines regulate IEC metabolism and facilitate proliferation and healing.
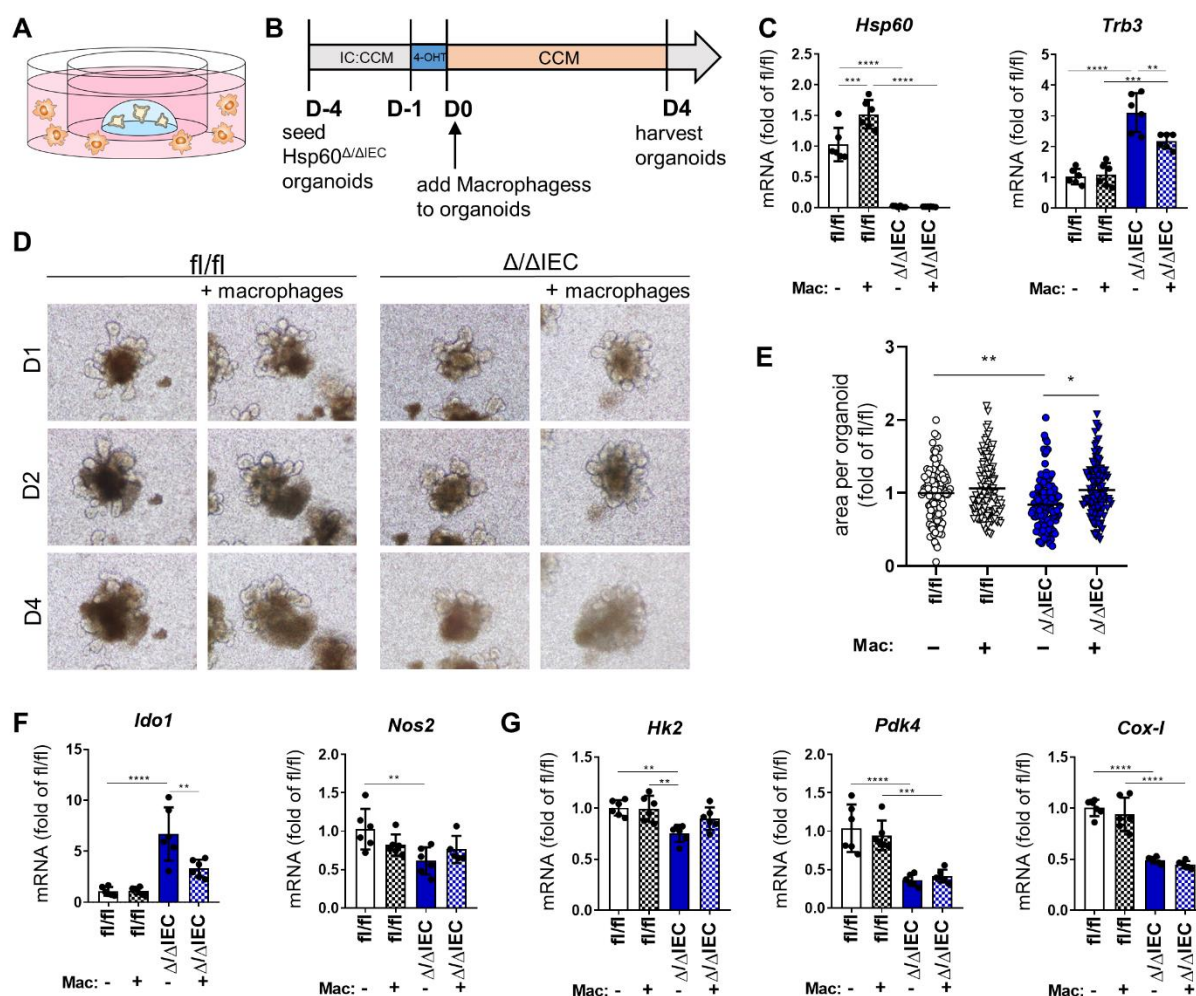
Figure 22: Co-culture of organoids with macrophages attenuates metabolic injury.
(A,B) Experimental setup. Hsp60 deletion is induced *ex vivo* in small intestinal (organoids from Hsp60$^{\Delta/\Delta IEC}$ mice (Ctrl: Hsp60$^{fl/fl}$ mice) by adding tamoxifen (500nM) for 24h to the culture media. After removal of tamoxifen, macrophages are seeded into the transwell to generate a co-culture system, and organoids are then monitored up to 4 days. **(C)** mRNA expression levels of organoids for *Hsp60* and the MT-UPR relevant gene *Trb3*. **(D)** Representative pictures of respective organoids. **(E)** Quantification of organoid area. mRNA expression levels of organoids for **(F)** arginine and tryptophan relates genes (*Ido1, Nos2*) and **(G)** metabolic genes (*Hk2, Pdk4, Cox-I*). Statistics: (C,E,F,G) ANOVA followed by pairwise comparison testing (Tukey). Mean ± SD, n=6. Asterisks indicate significant differences *P<0.05, **P<0.01, ***P<0.001; ****P<0.0001.

Immune cells do not only impact IECs, but vice versa, IECs send signals to immune cells. To reveal the impact of metabolically injured IECs on macrophages, media from Hsp60$^{\Delta/\Delta IEC}$ organoids was harvested (control: Hsp60$^{fl/fl}$) and used to stimulate differentiated macrophages (Figure 23A).

Macrophages did not alter their proliferative capacity but depicted changes in their morphology after 4 days. Macrophages before and after stimulation with control media showed an elongated cell body and few cytoplasmic extensions. On the contrary, macrophages stimulated with media from Hsp60 deficient organoids revealed an enlarged amoeboid cell shape with

rounder cell bodies (Figure 23B). Gene expression analysis revealed a reduction in the anti-inflammatory cytokine *Il10* and the pro-inflammatory cytokine *Il1ß*, while *Tnf* remained unchanged (Figure 23C).

These data indicate distinct polarization of macrophages induced by signals from metabolically injured IECs. More detailed analysis is, however, required to elucidate the type of activated macrophages.
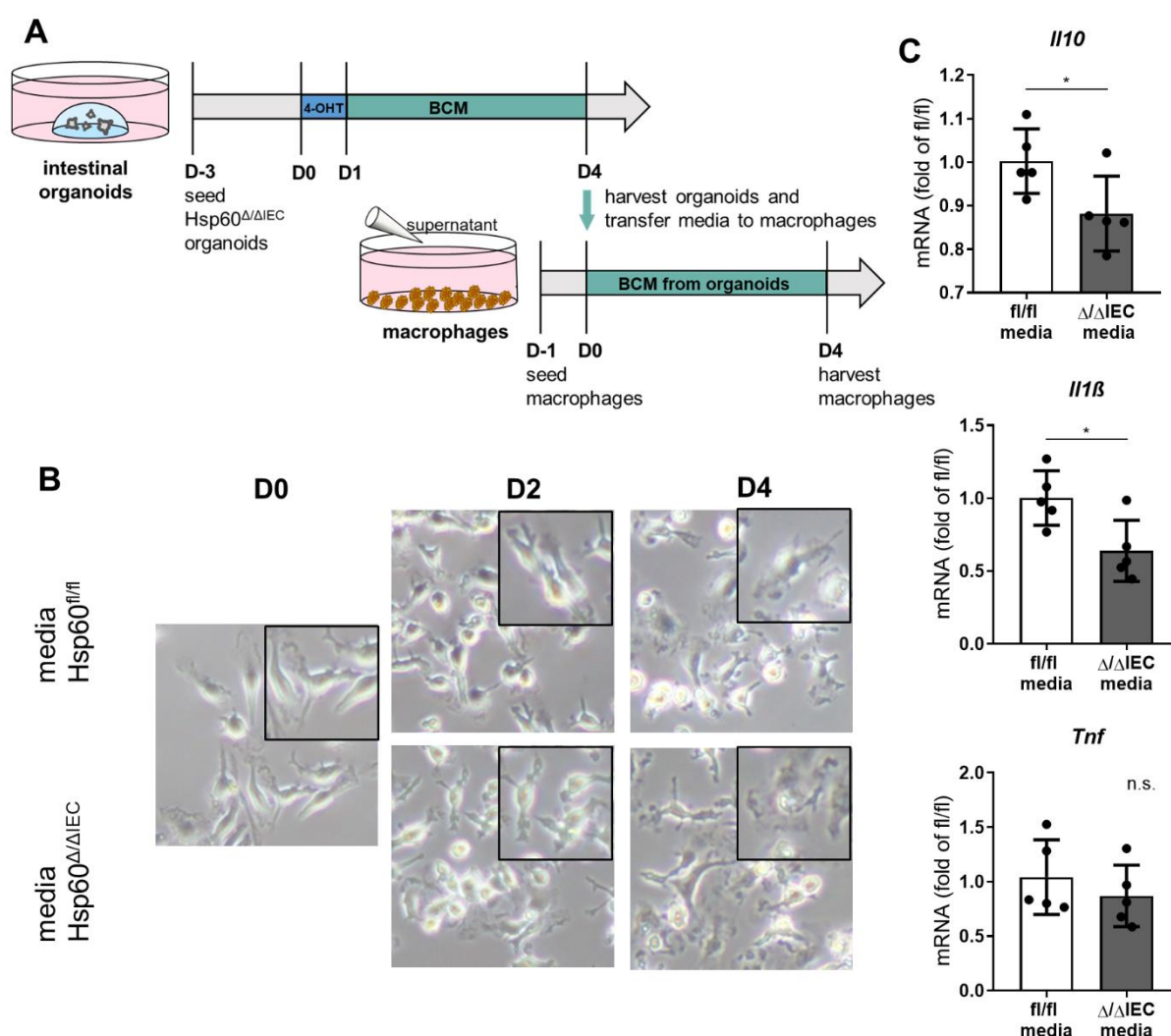

Figure 23: Metabolically injured IECs impact macrophage morphology and secretion profile.
(A) Experimental setup. Hsp60 deletion is induced *ex vivo* in small intestinal organoids from Hsp60$^{\Delta/\Delta IEC}$ mice (Ctrl: Hsp60$^{fl/fl}$ mice) by adding tamoxifen (500nM) for 24h to the culture media. Organoids are cultured 3 days in BCM, which is subsequently transferred to macrophages. These are then monitored for 4 days. **(B)** Representative pictures of respective macrophages. **(C)** mRNA expression levels of macrophages for the cytokines *Il10, Il1ß,* and *Tnf.* Statistics: Unpaired t-test assuming Gaussian distribution. Mean ± SD, n=6. Asterisks indicate significant differences *P<0.05, **P<0.01, ***P<0.001; ****P<0.0001.

4.14. Metabolic injury aggravates susceptibility to chronic inflammation

Previous work showed that MT-UPR signaling is linked to IBD-related inflammation in experimental models and patients [73]. To address the role of the pro-inflammatory cytokine IL-10 in affecting mitochondrial function, metabolic injury and regenerative responses, a new mouse model with an inducible IEC-specific knockout of Hsp60 and a whole-body knockout of IL-10 was generated (Hsp60$^{\Delta/\Delta IEC}$;*Il10*$^{-/-}$ mice). Hsp60$^{\Delta/\Delta IEC}$;*Il10*$^{-/-}$ mice were analyzed at three different time points (D4, D8, D14) after end of tamoxifen treatment and complete Hsp60 deletion (Figure 24A). They showed persistent weight loss (Figure 24B) and reduced overall survival (Figure 24C).

On tissue level, H&E staining and subsequent quantification revealed elongated crypts in Hsp60$^{\Delta/\Delta IEC}$;*Il10*$^{-/-}$ mice at day 4 before developing severe tissue aberration. At day 8, the time point with the most pronounced phenotype, hyperproliferative and wounded crypts were present with and without IL-10 in Hsp60 deficient mice, however, crypts were more elongated in double knockout mice. Most striking, at day 14, the time point where Hsp60$^{\Delta/\Delta IEC}$ mice were almost recovered, 2 out of 6 Hsp60$^{\Delta/\Delta IEC}$;*Il10*$^{-/-}$ mice displayed an accelerated inflammatory phenotype, suggesting a disrupted regenerative response to metabolic injury in the absence of IL-10 (Figure 24D,E). The aberrant epithelial architecture was transiently elevated in Hsp60 deficient mice with and without IL-10 in the proximal segment of the colon. However, tissue aberration did not significantly increase in the distal colon at day 14 in Hsp60$^{\Delta/\Delta IEC}$;*Il10*$^{-/-}$ mice (Figure 24F). In line, the tissue pathology index revealed a persistent increased inflammation in the distal colon, while the elevation was transient in the proximal part (Figure 24G). These results may implicate that the IEC microenvironment contributes to regeneration after metabolic injury, while the intestinal crypt architecture per se is not drastically altered without IL-10. In comparison, the ileum displayed no acceleration of injury (Figure 25A,B), indicating that one/several cell populations play a distinct role during the regenerative process in the colon but not in the small intestine.

Figure 24: The absence of IL-10 disrupts the regenerative response to metabolic injury.

(A) Experimental setup illustrating the IEC-specific deletion of Hsp60 in IL-10 knockout mice (Hsp60$^{\Delta/\Delta IEC}$;*Il10*$^{-/-}$ mice, Ctrl: Hsp60$^{\Delta/\Delta IEC}$;*Il10*$^{+/+}$ and Hsp60$^{fl/fl}$;*Il10*$^{-/-}$) by oral feeding with tamoxifen supplemented food. Mice were sacrificed at day (D) 4, 8, and 14 after end of tamoxifen treatment and full Hsp60 deletion. **(B)** Weight curves of the respective mice from tamoxifen feeding until D14. **(C)** Kaplan-Meier curve for survival (percent) of mice from all three genotypes until day (D) 14. **(D)** Representative H&E stained sections of colonic swiss roles and corresponding higher magnifications for Hsp60$^{\Delta/\Delta IEC}$;*Il10*$^{-/-}$ mice and respective controls on day (D) 4, 8 and 14 (scale bars = 200µM). **(E)** Quantification of crypt depth in all three genotypes over all time points. **(F)** Colonic tissue was scored histologically for an aberrant epithelial architecture. **(G)** Colonic swiss roles were histologically scored for inflammation in the proximal and distal colon over all time points (range of score 0 (not inflamed) – 12 (highly inflamed). Statistics: (C) Multiple t-test using the Two-stage linear step-up procedure of Benjamini, Krieger and Yekutieli. (E,F,G) ANOVA followed by pairwise comparison testing (Tukey). Mean ± SD, n=6. Asterisks indicate significant differences *P<0.05, **P<0.01, ***P<0.001; ****P<0.0001.
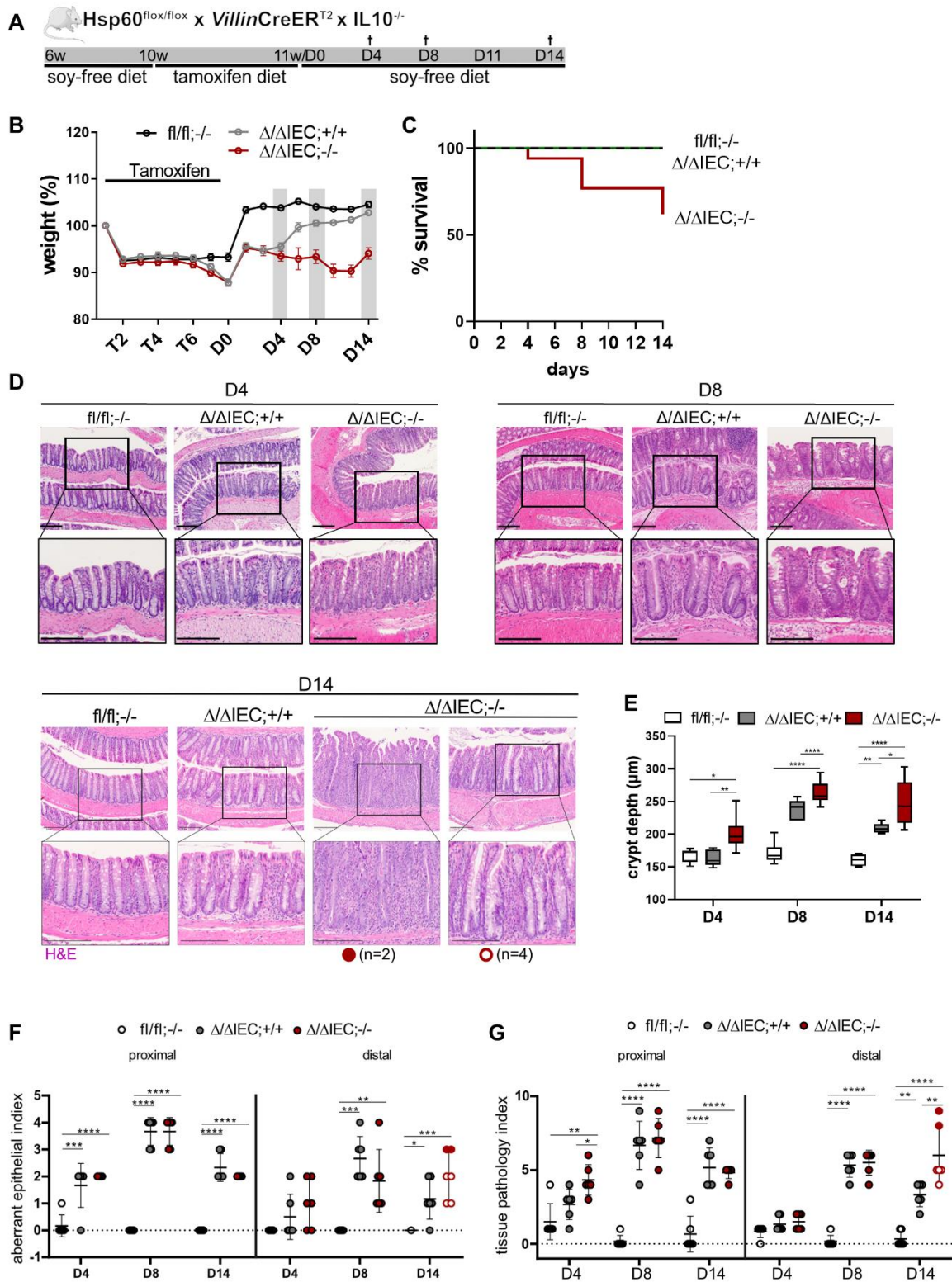
Figure 24: The absence of IL-10 disrupts the regenerative response to metabolic injury.
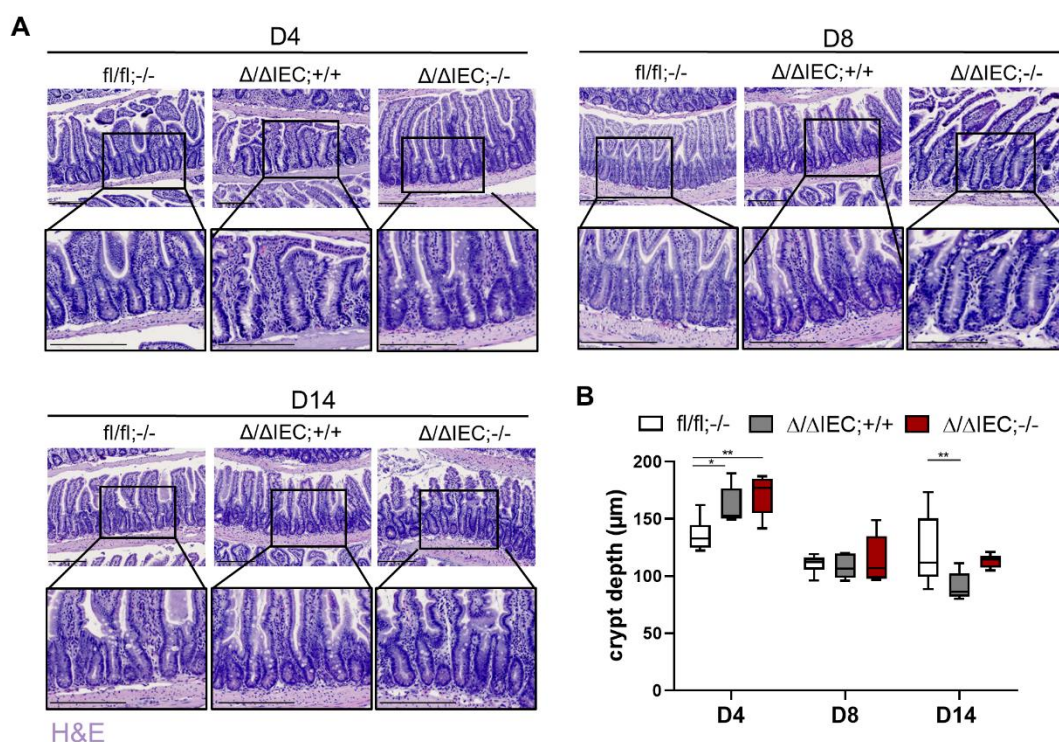(Figure legend previous page)

Figure 25: Metabolic injury does not accelerate in the ileum without IL-10.
(A) Representative H&E stained sections of ileal tissue and corresponding higher magnifications for Hsp60$^{\Delta/\Delta IEC}$;*Il10*$^{-/-}$ and control (Hsp60$^{fl/fl}$;*Il10*$^{-/-}$ and Hsp60$^{\Delta/\Delta IEC}$;*Il10*$^{+/+}$) mice from day (D) 4 to 14. **(B)** Quantification of crypt depth for all genotypes and time points. Statistics: ANOVA followed by pairwise comparison testing (Tukey). Mean ± SD, n=6. Asterisks indicate significant differences *P<0.05, **P<0.01, ***P<0.001; ****P<0.0001.

Furthermore, transcriptional profiling of colonic tissue confirmed a loss of *Hsp60* and *Il10* as well as a transient induction of MT-UPR signaling (*Chop*, *Trb3*) that did not differ between Hsp60$^{\Delta/\Delta IEC}$;*Il10*$^{+/+}$ and Hsp60$^{\Delta/\Delta IEC}$;*Il10*$^{-/-}$ mice. (Figure 26A,B). In addition, stem cells (*Lgr5*), transit-amplifying cells (*Prom1*), and enterocytes (*Alpi*) were downregulated at days. However, there was no significant difference in the altitude between Hsp60$^{\Delta/\Delta IEC}$ and Hsp60$^{\Delta/\Delta IEC}$;*Il10*$^{-/-}$ mice (Figure 26C), suggesting that the absence of IL-10 does not impact the initial MT-UPR signaling and differentiation of IECs.
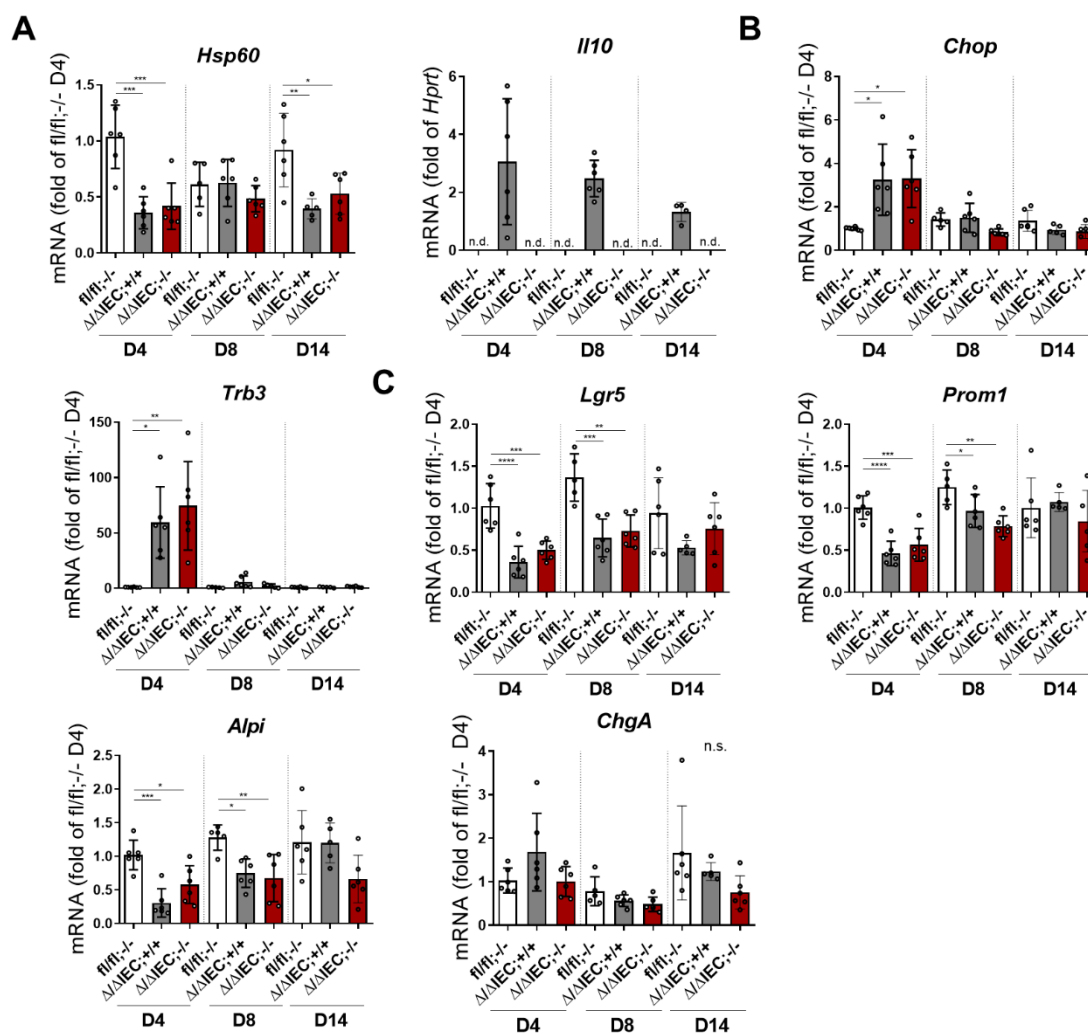
Figure 26: The absence of IL-10 does not impact MT-UPR signaling and colonocyte subpopulations.
(A) mRNA expression levels of colonic tissue for *Hsp60* and *Il10* to validate the knockouts in Hsp60$^{\Delta/\Delta IEC}$;*Il10*$^{-/-}$, Hsp60$^{\Delta/\Delta IEC}$;*Il10*$^{+/+}$ and Hsp60$^{fl/fl}$;*Il10*$^{-/-}$ mice over all time points (day (D) 4, 8, 14) after full Hsp60 deletion. **(B)** mRNA expression levels of colonic tissue for MT-UPR relevant *genes* (*Chop, Trb3*) and **(C)** epithelial subpopulations (*Lgr5, Prom1, Alpi*). Statistics: ANOVA followed by pairwise comparison testing (Tukey). Mean ± SD, n=6. Asterisks indicate significant differences *P<0.05, **P<0.01, ***P<0.001; ****P<0.0001.

IHC staining of Hsp60 showed that protein levels recovered starting from day 4 in both genotypes and were strongly present in hyperproliferative crypts at day 8 as well as elongated crypts in inflamed mice at day 14 (Figure 27A,B; Supplementary figure 6). In parallel, Ki67 expression was dramatically elevated at day 8 in Hsp60$^{\Delta/\Delta IEC}$;*Il10*$^{+/+}$ and Hsp60$^{\Delta/\Delta IEC}$;*Il10*$^{-/-}$ mice. However, the increase persisted in the double knockout mice at day 14, indicating sustained augmented proliferation of the intestinal epithelium as an indicator for disrupted regeneration (Figure 27C,D; Supplementary figure 6).

All these data suggest that mitochondrial perturbation of the epithelium dramatically accelerates the inflammatory phenotype in *Il10*$^{-/-}$ mice, supporting the hypothesis that metabolic injury plays a vital role in disease acceleration and recurrence of IBD.
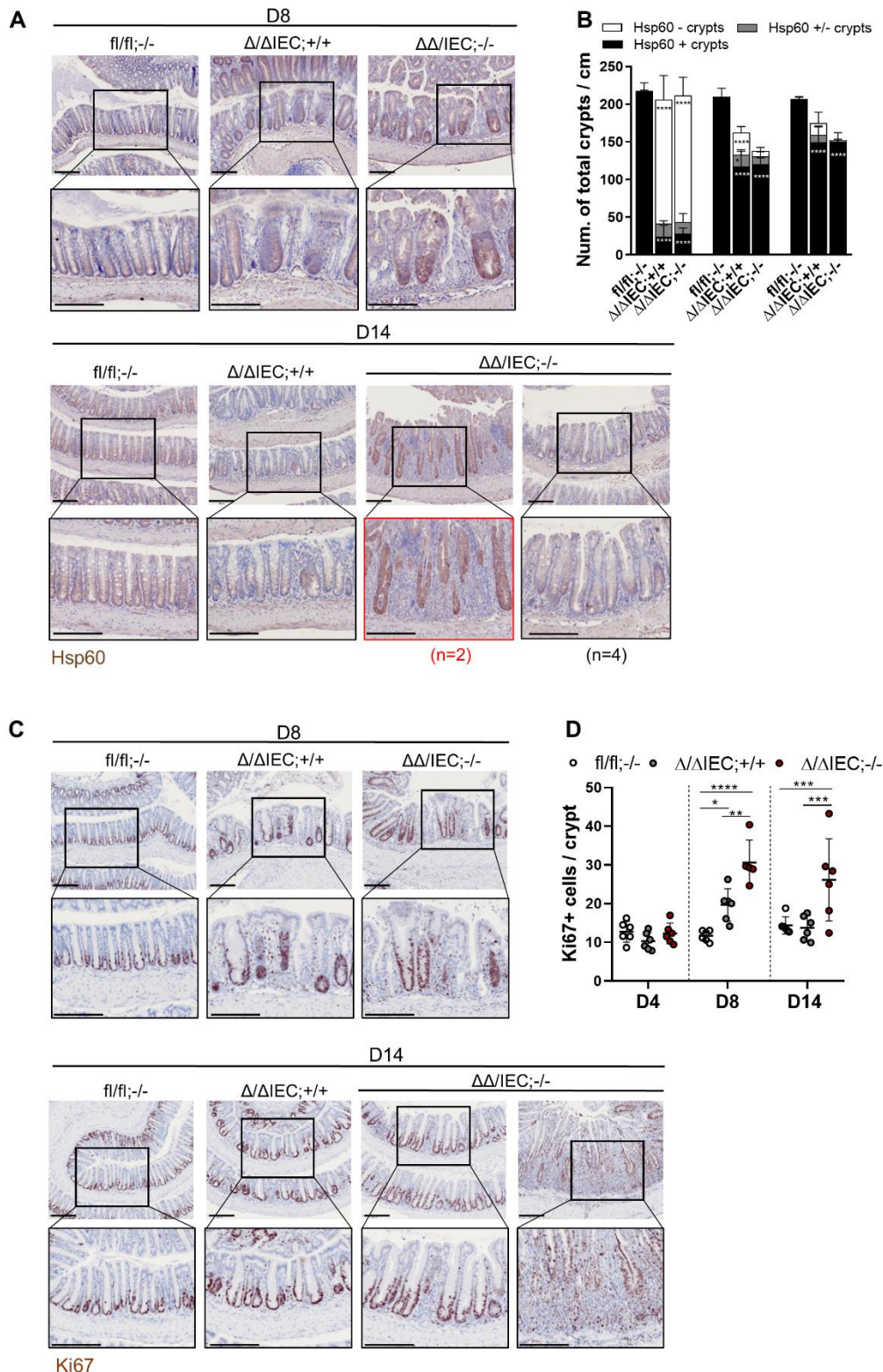
Figure 27: The absence of IL-10 augments the proliferative response to metabolic injury.
(A) Representative immunohistochemically stained colonic swiss rolls and corresponding higher magnifications for Hsp60 in Hsp60$^{\Delta/\Delta IEC}$;*Il10*$^{-/-}$ and respective control mice on day (D) 8 and 14 (scale bars = 200µM). **(B)** Quantification of Hsp60 positive and negative crypts in all three genotypes. **(C)** Representative immunohistochemically stained colonic swiss rolls and corresponding higher magnifications for Ki67 in Hsp60$^{\Delta/\Delta IEC}$;*Il10*$^{-/-}$ and respective control mice on day (D) 8 and 14 (scale bars = 200µM). **(D)** Quantification of Ki67 positive cells per crypts at day (D) 4, 8, and 14 in all respective genotypes. Statistics: (B,D) ANOVA followed by pairwise comparison testing (Tukey). Mean ± SD, n=6. Asterisks indicate significant differences *P<0.05, **P<0.01, ***P<0.001; ****P<0.0001.

68

A closer look at the organ weights revealed a significant increase in MLN and spleen weight in Hsp60$^{\Delta/\Delta IEC}$;*Il10*$^{-/-}$ mice compared to controls (Figure 28A). The length of duodenum, jejunum, and ileum was increased, while the colon length stayed unchanged. Moreover, stomach weight was increased, and cecum weight decreased (Supplementary figure 7).

Transcriptional profiling of colonic tissue demonstrated a prolonged induction of *Saa3* and *Tnf* in Hsp60$^{\Delta/\Delta IEC}$;*Il10*$^{-/-}$ mice compared to controls (Figure 28B). ELISA of Saa3 in plasma samples from day 14 confirmed these findings, providing convincing evidence of an accelerated inflammatory response to metabolic injury without IL-10 (Figure 28C). In line, pStat3 expression was present in the whole colonic tissue at day 8 in Hsp60$^{\Delta/\Delta IEC}$;*Il10*$^{-/-}$ mice in comparison to a patchy expression in Hsp60$^{\Delta/\Delta IEC}$;*Il10*$^{+/+}$ mice. While it was almost absent at day 14 in the latter, its expression persisted in Hsp60$^{\Delta/\Delta IEC}$;*Il10*$^{-/-}$ mice (Figure 28D).

To sum up, these results yield additional evidence that immune cells regulate IEC metabolism to orchestrate IEC proliferation and thus healing. It can be hypothesized that IL-10 balances the scale and enables regeneration after metabolic injury.

Figure 28: Chronic inflammation accelerates in response to metabolic injury.
(A) MLN and spleen weight relative to body weight in Hsp60$^{\Delta/\Delta IEC}$;*Il10*$^{-/-}$ and control mice at day (D) 4, 8, and 14 after full Hsp60 deletion. **(B)** mRNA expression levels of colonic tissue for the cytokine *Tnf* and the systemic inflammation marker *Saa3*. **(C)** ELISA of Saa3 in plasma samples from all three genotypes at sampling time point day (D) 14. **(D)** Representative immunohistochemically stained colonic swiss rolls for pStat3 in all three genotypes on day (D) 8 and 14 (scale bars = 200µM). Statistics: ANOVA followed by pairwise comparison testing (Tukey). Mean ± SD, n=6. Asterisks indicate significant differences *P<0.05, **P<0.01, ***P<0.001; ****P<0.0001.
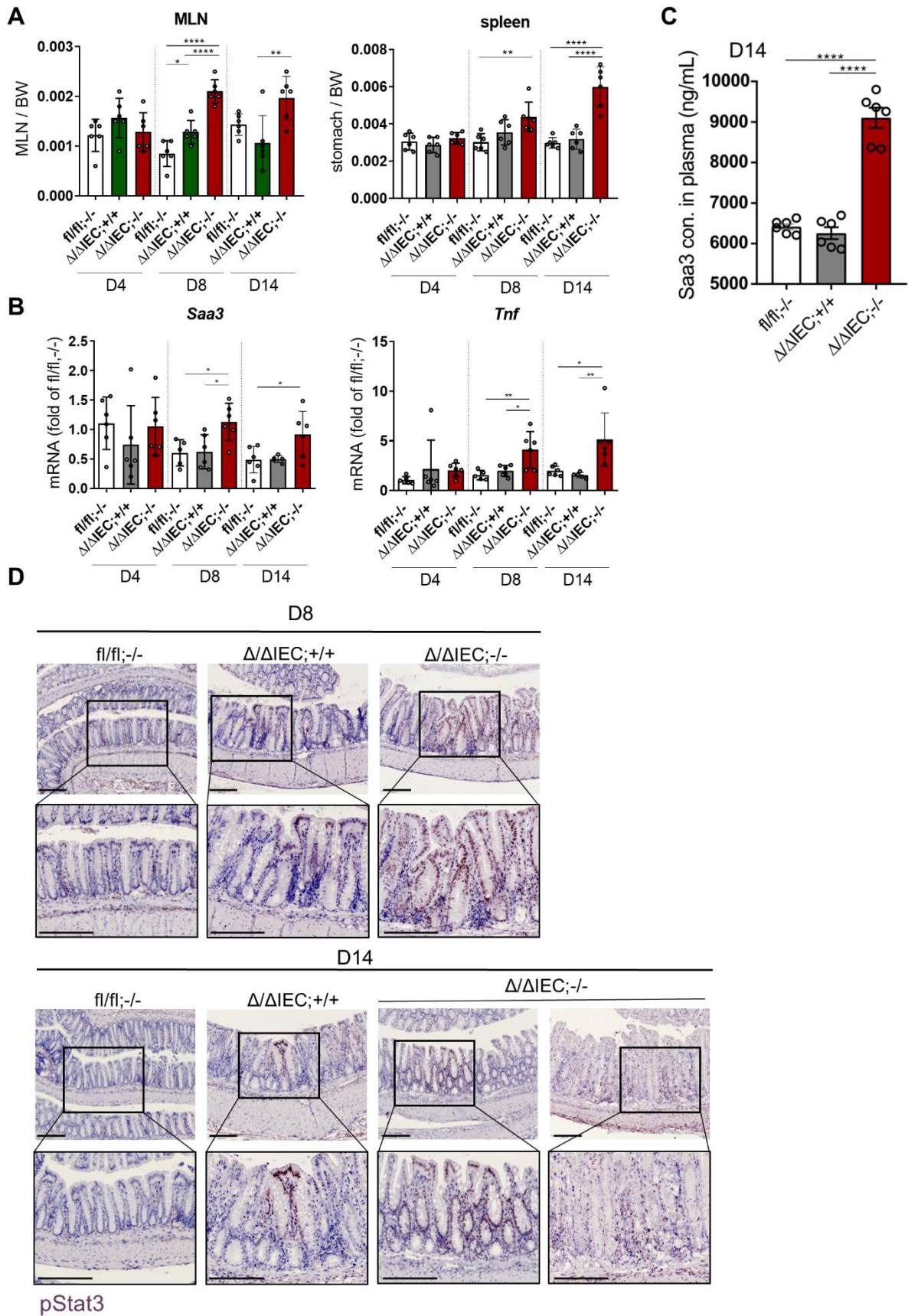
Figure 28: Chronic inflammation accelerates in response to metabolic injury.
(Figure legend previous page)

4.15. Lack of epithelial IL-10 augments MT-UPR signaling in organoids

Thus far, Hsp60$^{\Delta/\Delta IEC}$ organoids and their cross-talk with the microenvironment was analyzed *in vitro*. The data provide preliminary evidence that a cross-talk between the microenvironment and IECs and between IECs exists during metabolic injury. Next, it was addressed how IECs with mitochondrial impairment respond without epithelial IL-10. To answer this question, intestinal organoid cultures of Hsp60$^{\Delta/\Delta IEC}$;*Il10*$^{-/-}$ mice were generated. Since large intestinal organoids with a deletion of IL-10 were not viable in culture, the focus was on small intestinal organoids.

As described before, the loss of Hsp60 resulted in reduced growth and diminished *de novo* crypt formation (budding) at day 6. Loss of IL-10 alone showed an even more pronounced growth reduction and a decrease in *de novo* crypt formation compared to an Hsp60 deletion. While the area in organoids with a loss of both Hsp60 and IL-10 did not decrease further, their budding was significantly diminished (Figure 29A-C). Moreover, MT-UPR signaling (*Chop, Trb3, Atf5*) was dramatically increased in double knockout organoids, paralleled with a rapid decrease in the expression of the stem cell marker *Lgr5* (Figure 29D). While the glycolysis gene *Hk2* was unchanged, the glucose regulator *Pdk4* depicted a substantial reduction in the absence of IL-10, which was an even further reduction in the absence of both IL-10 and Hsp60. In addition to these alterations, reduced *Cox-I* levels in the double knockout organoids indicated a decrease in respiration (Figure 29E), which is consistent with previous findings. Interestingly, the expression level of *Il10* was reduced in Hsp60 knockout organoids, suggesting that metabolically injured IECs produce less paracrine IL-10 (Figure 29F).

In summary, these results suggest that the loss of epithelial IL-10 augments MT-UPR signaling *in vitro,* induces more substantial metabolic changes, and generates lower growth and *de novo* crypt formation rates.
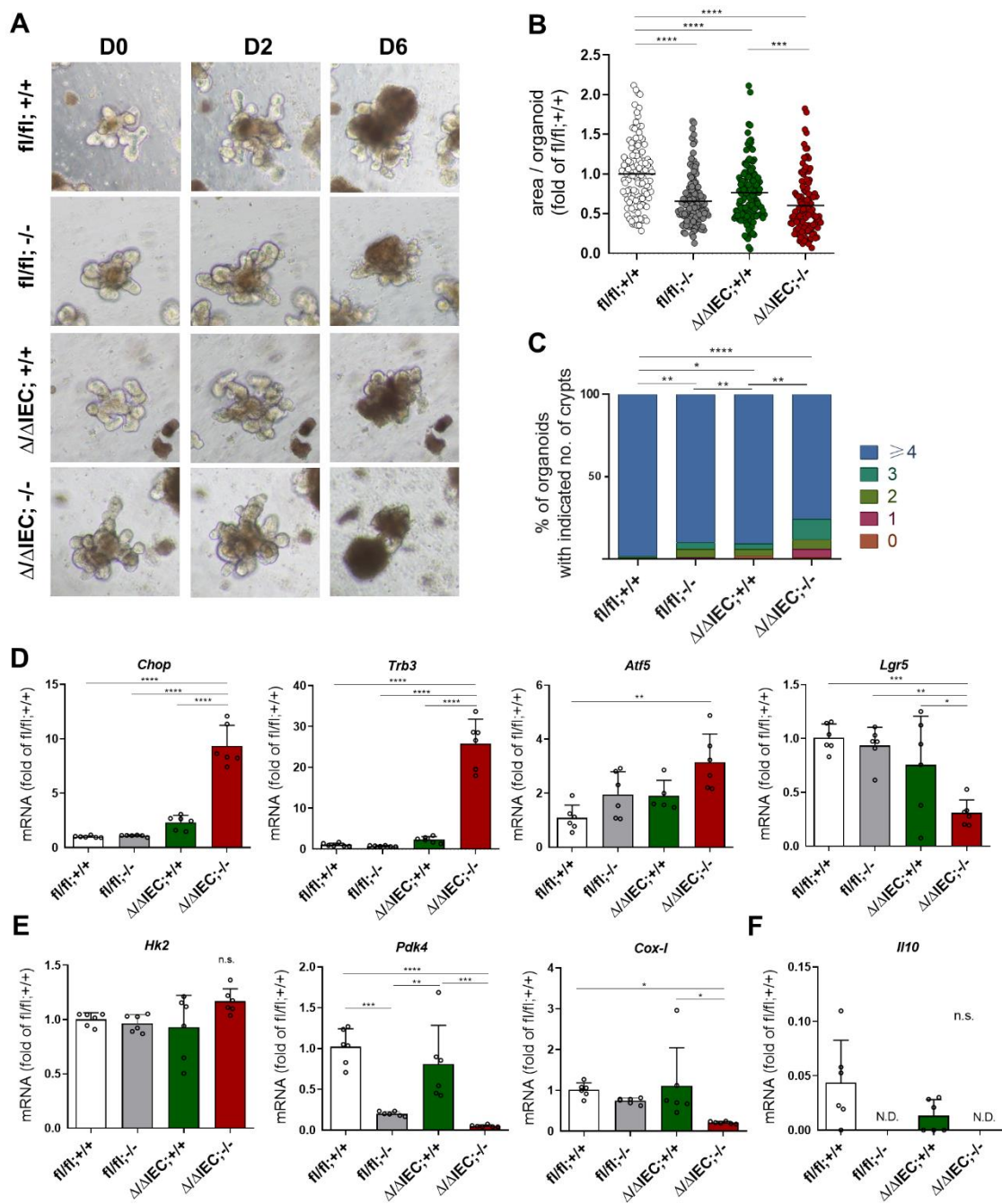
Figure 29: Epithelial IL-10 augments phenotypic changes, MT-UPR signaling and metabolic alterations *in vitro.*

(A) Representative pictures of organoids. Hsp60 deletion is induced *ex vivo* in small intestinal organoids from Hsp60$^{\Delta/\Delta IEC}$;*Il10*$^{-/-}$ mice (Ctrl: Hsp60$^{\Delta/\Delta IEC}$;*Il10*$^{+/+}$, Hsp60$^{fl/fl}$;*Il10*$^{-/-}$ and Hsp60$^{fl/fl}$;*Il10*$^{+/+}$) by adding tamoxifen (500nM) for 24h to the culture media. Organoids are then monitored up to 6 days. **(B)** Quantification of organoid area and **(C)** *de novo* crypt formation (budding) in all genotypes at day (D) 6. mRNA expression levels of organoids for **(D)** MT-UPR relevant *genes* (*Chop, Trb3, Atf5*), stemness (*Lgr5*)*,* **(E)** metabolic genes (*Hk2, Pdk4, Cox-I*) and **(F)** the cytokine *Il10*. Statistics: (B,D,E,F) ANOVA followed by pairwise comparison testing (Tukey). (C) Mann-Whitney test. Mean ± SD, n=6. Asterisks indicate significant differences *P<0.05, **P<0.01, ***P<0.001; ****P<0.0001.

4.16. IL-10 impacts IEC metabolism and proliferation *in vitro*

The cytokine IL-10 was identified as essential during metabolic injury i*n vivo* and *in vitro*. Hence, its effect on IECs was analyzed using organoid cultures. Hsp60$^{\Delta/\Delta IEC}$ (control: Hsp60$^{fl/fl}$) organoids were seeded, treated with tamoxifen to induce Hsp60 deletion, and stimulated with IL-10 in the media for 4 days (Figure 30A). The cytokine increased area, crypt length and *de novo* crypt formation in control organoids. Hsp60$^{\Delta/\Delta IEC}$ organoids, however, stayed unchanged (Figure 30B-E), suggesting a loss of IL-10 sensitivity upon Hsp60 deletion.

Gene expression analysis demonstrated a complete Hsp60 deletion and activation of MT-UPR signaling (*Trb3*) that was significantly dampened in the presence of IL-10 (Figure 30F). Interestingly, IL-10 did not show any effect on stemness (*Lgr5*) and IEC differentiation (*Alpi*) (Figure 30G). Moreover, while *Nos2* levels stayed unaltered, *Arg1* was increased upon Hsp60 deletion and further elevated in the presence of IL-10 (Figure 30H).

These results confirm the impact of IL-10 on IEC morphology and mitochondrial signaling. IL-10 does not affect the proliferative capacity of Hsp60$^{\Delta/\Delta IEC}$ organoids but rather dampens MT-UPR signaling and thus enhances regeneration. This aligns with the *in vivo* data showing that the lack of IL-10 disturbs regenerative processes after metabolic injury, increasing susceptibility to inflammation.
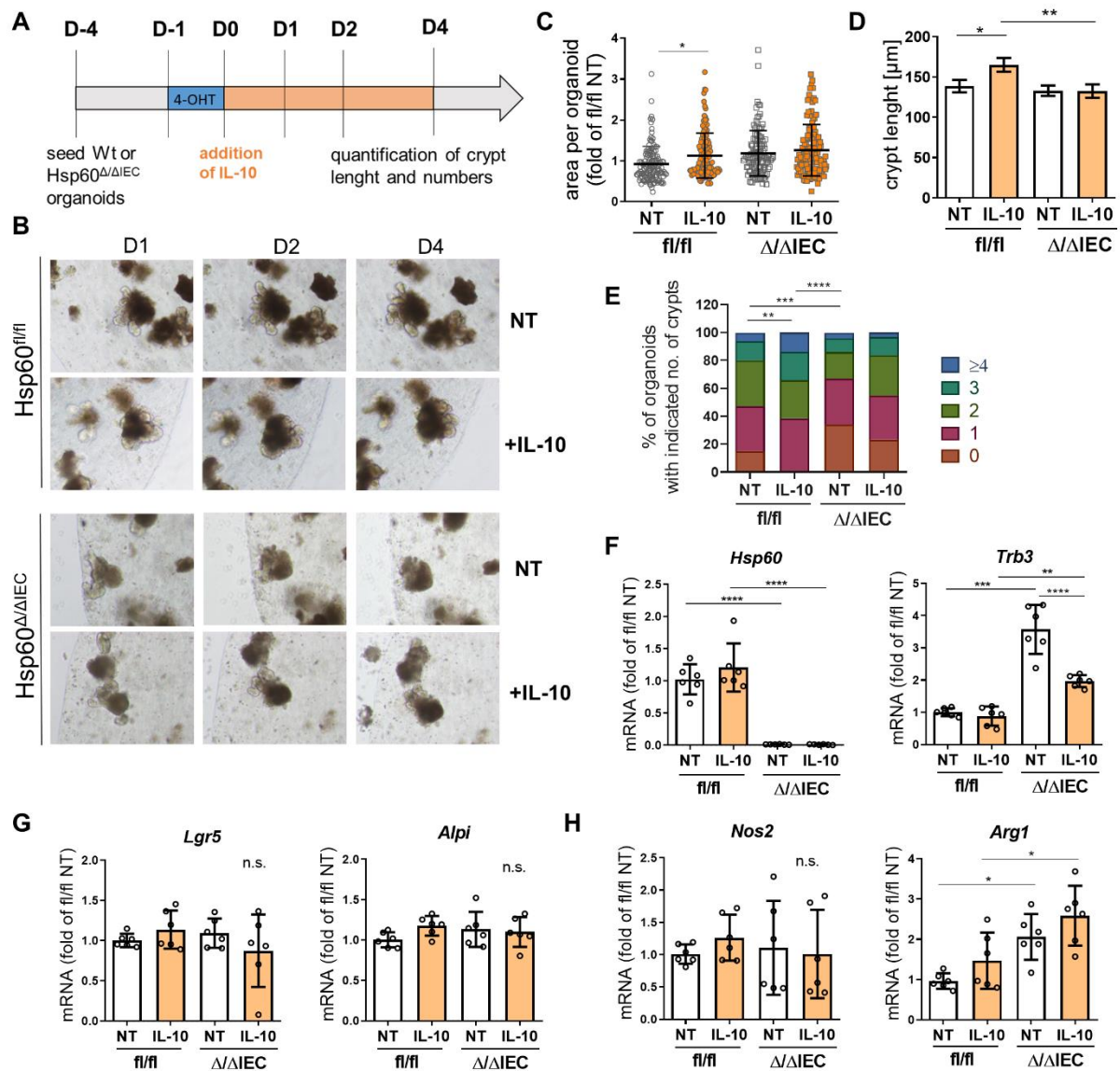
Figure 30: IL-10 impacts organoid morphology and cellular signaling.

(A) Experimental setup. Hsp60 deletion is induced *ex vivo* in small intestinal organoids from Hsp60$^{\Delta/\Delta IEC}$ mice (Ctrl: Hsp60$^{fl/fl}$ mice) by adding tamoxifen (500nM) for 24h to the culture media. Following Hsp60 loss, organoids are treated with IL-10 (50ng/ml) for 4 days. **(B)** Representative pictures of respective organoids. Quantification of **(C)** organoid area, **(D)** crypt length, and **(E)** *de novo* crypt formation (budding) at day 4. mRNA expression levels of organoids for **(F)** *Hsp60*, MT-UPR relevant gene (*Trb3*), **(G)** epithelial subpopulations (*Lgr5, Alpi*), and **(H)** arginine and tryptophan relates genes (*Nos2, Arg1*). Statistics: (C,D,F-H) ANOVA followed by pairwise comparison testing (Tukey). (E) Mann-Whitney test. Mean ± SD, n=6. Asterisks indicate significant differences *P<0.05, **P<0.01, ***P<0.001; ****P<0.0001.

4.17. Altered tryptophan and arginine metabolism persists in Hsp60$^{\Delta/\Delta IEC}$;*Il10$^{-/-}$* mice

Tryptophan and arginine metabolism were two major pathways transiently altered during metabolic injury and tissue regeneration. To evaluate these pathways in Hsp60$^{\Delta/\Delta IEC}$;*Il10$^{-/-}$*

mice, qRT-PCR analysis of the tryptophan degrading enzyme *Ido1* as well as *Arg1* and *Nos2* was performed in colonic tissue. Compared to Hsp60$^{\Delta/\Delta IEC}$ mice that showed a transient induction of *Ido1, Arg1,* and *Nos2,* their expression levels were persistently high over all time points in double knockout mice (Figure 31A). As mentioned, Ido1 IF staining of colonic tissue sections revealed a transient expression of Ido1 in the crypt base in response to metabolic injury at day 8 in Hsp60$^{\Delta/\Delta IEC}$ mice. In comparison, in Hsp60$^{\Delta/\Delta IEC}$;*Il10*$^{-/-}$ mice, the complete crypt, not only the crypt base, was Ido1 positive during the injury phase (day 8). At day 14, the signal was restricted to the crypt base in non-responder mice and patchy present along the whole crypt axis in both inflamed and non-inflamed areas of responder mice (Figure 31B). These data indicate that in the absence of IL-10, an altered tryptophan metabolism persists, potentially contributing to the acceleration of inflammation.
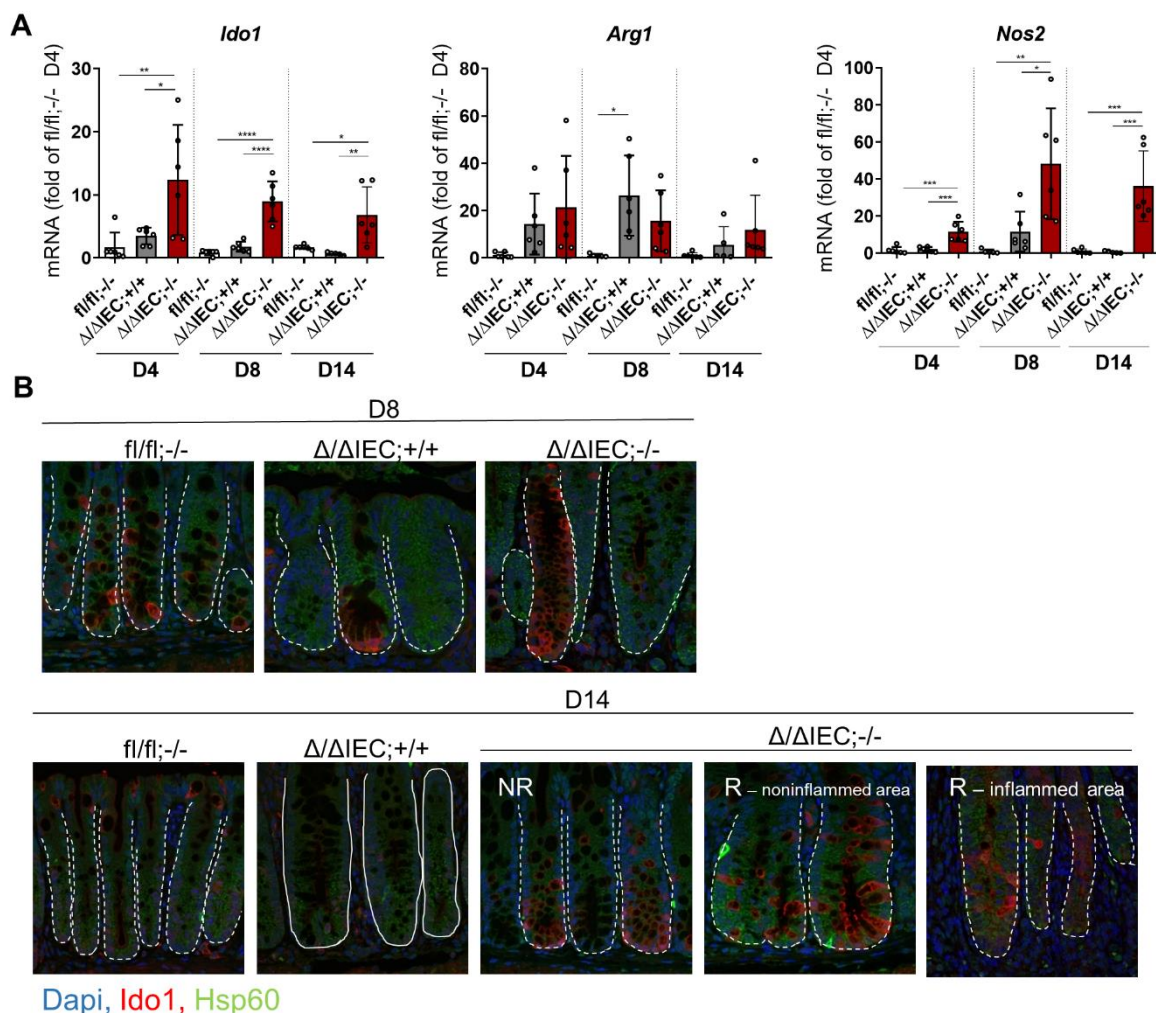

Figure 31: Altered tryptophan and arginine metabolism persist during inflammation.
(A) mRNA expression levels of colonic tissue for arginine and tryptophan relates genes (*Ido1, Nos2, Arg1*) in Hsp60$^{\Delta/\Delta IEC}$;*Il10*$^{-/-}$ and control mice at day (D) 4, 8 and 14 after full Hsp60 deletion. **(B)** Representative immunofluorescence co-staining of Hsp60 (green) and Ido1 (red) in Hsp60$^{\Delta/\Delta IEC}$;*Il10*$^{-/-}$ and control mice at day (D) 8 and 14 (600x). Dapi = blue. Statistics: (A) ANOVA followed by pairwise comparison testing (Tukey). Mean ± SD, n=6. Asterisks indicate significant differences *P<0.05, **P<0.01, ***P<0.001; ****P<0.0001.

4.18. ClpP deficiency triggers low-grade inflammation

Data mentioned above showed that metabolic injury in Hsp60$^{\Delta/\Delta IEC}$ mice dramatically accelerated the inflammatory phenotype in IL-10 knockout mice. To analyze if ClpP$^{\Delta/\Delta IEC}$ mice and thus mild mitochondrial impairment similarly induce susceptibility to IBD, a new mouse model with an inducible IEC-specific knockout of ClpP in combination with a whole body knockout of *Il10* (ClpP$^{\Delta/\Delta IEC}$;*Il10*$^{-/-}$ mice) was generated. ClpP$^{\Delta/\Delta IEC}$;*Il10*$^{-/-}$ mice were characterized on day 8 (the time point with the strongest phenotype) after the end of tamoxifen treatment and complete ClpP deletion (Figure 32A).

Mice showed no significant changes in weight development between ClpP$^{\Delta/\Delta IEC}$;*Il10*$^{-/-}$ and control ClpP$^{\Delta/\Delta IEC}$;*Il10*$^{+/+}$ mice, but significantly higher weight compared to ClpP$^{fl/fl}$;*Il10*$^{-/-}$ mice (Figure 32B). In line, no changes were observed on tissue level in the distal colon (Figure 32C). However, 3 out of 6 mice demonstrated a patchy accelerated inflammatory phenotype in the proximal colon, which was corroborated in the tissue pathology index (Figure 32D,E), suggesting a disrupted regenerative response to mild mitochondrial impairment in the absence of IL-10. Strikingly, in contrast to Hsp60$^{\Delta/\Delta IEC}$;*Il10*$^{-/-}$ mice, where the inflammation was present throughout the distal colon, it was localized in a patchy manner to the proximal colon in ClpP$^{\Delta/\Delta IEC}$;*Il10*$^{-/-}$ mice. These findings are confirmed by elongated crypts and a mildly increased aberrant epithelial architecture score in the proximal compared to the distal colon in ClpP$^{\Delta/\Delta IEC}$;*Il10*$^{-/-}$ mice (Figure 32F,G). Like the proximal colon, the ileum showed a mildly elevated aberrant epithelium and inflammation (Supplementary figure 8B,C), corroborating the findings that mild mitochondrial impairment impacts tissue inflammation in a spatial-driven way.

Transcriptional profiling of colonic tissue confirmed a loss of *ClpP* and *Il10* (Figure 33A). MT-UPR signaling (*Chop*, *Trb3*) was not elevated at day 8 (Figure 33B). However, this aligns with data from the ClpP$^{\Delta/\Delta IEC}$ mice showing activated MT-UPR signaling only from day 0 to 4. In addition, stemness was not reduced (Figure 33C), as well as the pro-inflammatory cytokine *Tnf*. Surprisingly, *Saa3* was significantly increased in ClpP$^{\Delta/\Delta IEC}$;*Il10*$^{-/-}$ mice, indicating elevated systemic inflammation (Figure 33D). In addition, MLN weights demonstrated a significant increase in ClpP$^{\Delta/\Delta IEC}$;*Il10*$^{-/-}$ mice, while all other organ weights and intestinal segment lengths were unchanged (Figure 33E; Supplementary figure 8A).

Together, these results show that mitochondrial impairment without metabolic injury induces a less pronounced inflammatory phenotype. This might suggest that MT-UPR signaling alone is not a major susceptibility factor, but combined with a disturbed cellular metabolism, it can skew the balance toward pathogenesis.
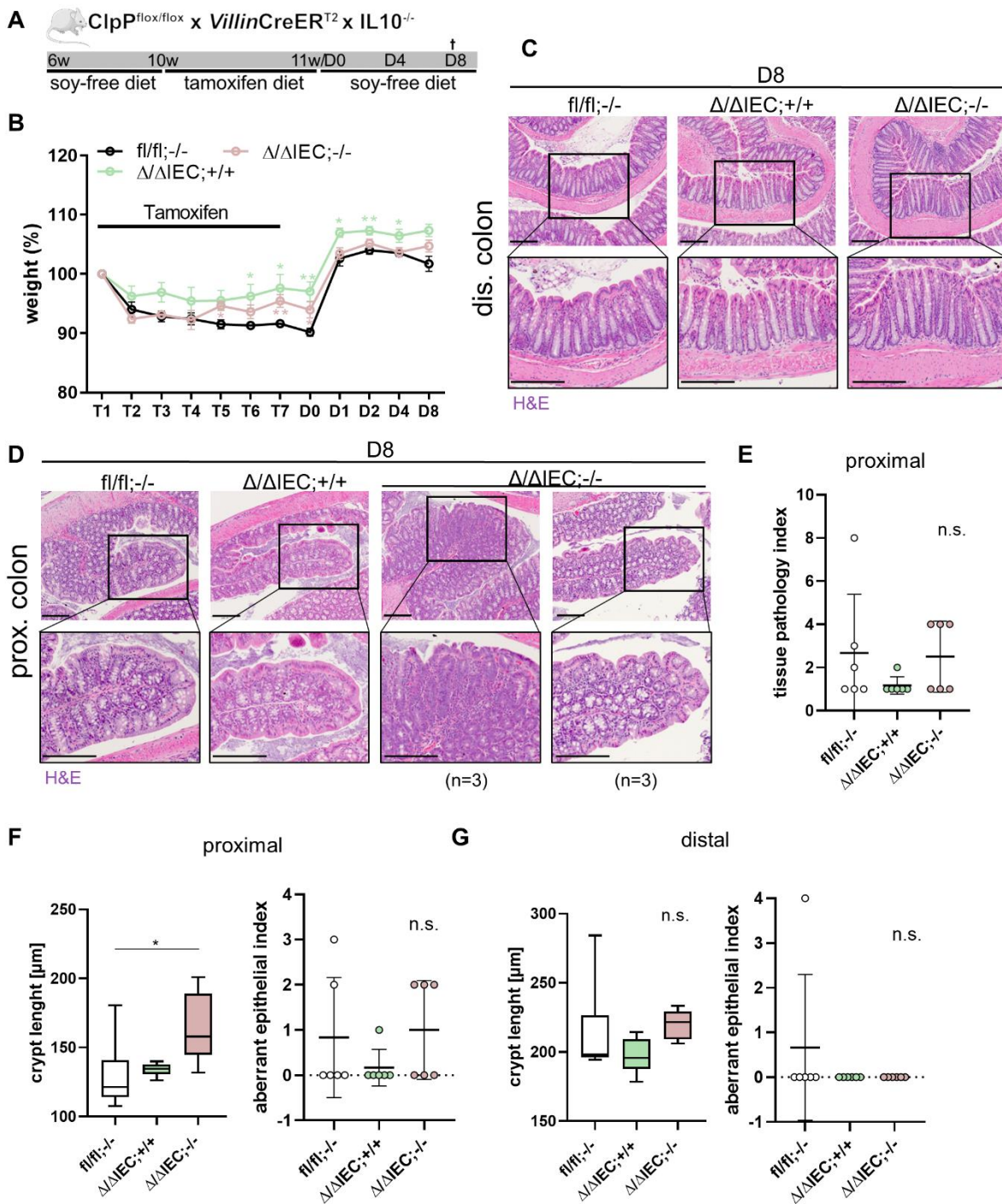
Figure 32: Mild mitochondrial impairment induces mild inflammation in the proximal colon.
(A) Experimental setup illustrating the IEC-specific deletion of ClpP in IL-10 knockout mice (ClpP$^{\Delta/\Delta IEC}$;*Il10*$^{-/-}$ mice, Ctrl: ClpP$^{\Delta/\Delta IEC}$;*Il10*$^{+/+}$ and ClpP$^{fl/fl}$;*Il10*$^{-/-}$) by oral feeding with tamoxifen supplemented food. Mice were sacrificed at day (D) 8, after end of tamoxifen treatment and full ClpP deletion. **(B)** Weight curves of the respective mice from tamoxifen feeding until day (D) 8. Representative H&E stained sections of swiss roles from the distal **(C)** and proximal **(D)** colon and corresponding higher magnifications for ClpP$^{\Delta/\Delta IEC}$;*Il10*$^{-/-}$ and respective control mice on day (D) 8 (scale bars = 200μM). **(E)** Colonic swiss roles were histologically scored for inflammation in the proximal colon at day (D) 8 (range of score 0 (not inflamed) – 12 (highly inflamed)). Quantification of crypt depth and histological score for aberrant epithelium in the **(F)** proximal and **(G)** distal colon of all three genotypes at day (D) 8. Statistics: (B) Multiple t-test using the Two-stage linear step-up procedure of Benjamini, Krieger and Yekutieli. (E-G) ANOVA followed by pairwise comparison testing (Tukey). Mean ± SD, n=6. Asterisks indicate significant differences *P<0.05, **P<0.01, ***P<0.001; ****P<0.0001.
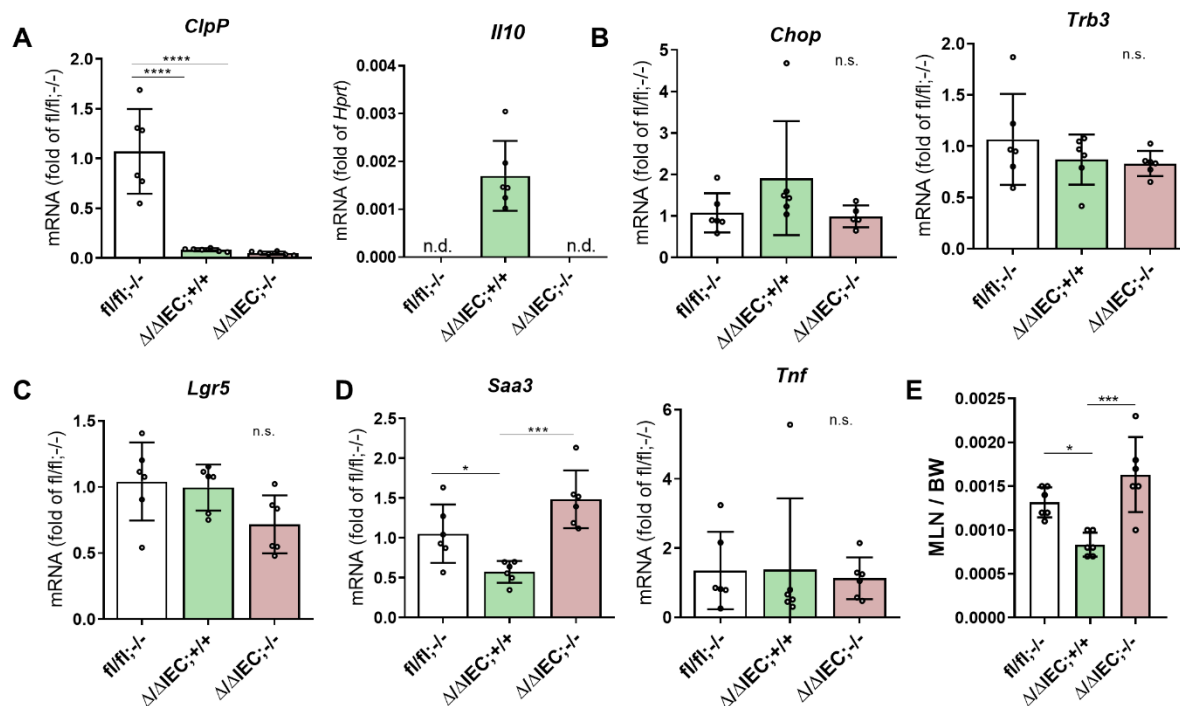
Figure 33: Mild mitochondrial impairment induces a mild systemic inflammatory response.
(A) mRNA expression levels of colonic tissue for *ClpP* and *Il10* to validate the knockouts in ClpP$^{\Delta/\Delta IEC}$;*Il10*$^{-/-}$, ClpP$^{\Delta/\Delta IEC}$;*Il10*$^{+/+}$ and ClpP$^{fl/fl}$;*Il10*$^{-/-}$ mice at day (D) 8 after full ClpP deletion. **(B)** mRNA expression levels of colonic tissue for MT-UPR relevant *genes* (*Chop,Trb3*) and **(C)** the stemness marker *Lgr5*. **(D)** mRNA expression levels of colonic tissue for the cytokine *Tnf* and the systemic inflammation marker *Saa3*. **(E)** MLN weight relative to body weight in all three genotypes at day (D) 8. Statistics: (A-E) ANOVA followed by pairwise comparison testing (Tukey). Mean ± SD, n=6. Asterisks indicate significant differences *P<0.05, **P<0.01, ***P<0.001; ****P<0.0001.

In comparison to Hsp60$^{\Delta/\Delta IEC}$;*Il10*$^{-/-}$ organoids, ClpP$^{\Delta/\Delta IEC}$;*Il10*$^{-/-}$ organoids did not reveal any changes in morphology, MT-UPR signaling and IEC metabolism (Supplementary figure 9), indicating that mild mitochondrial impairment alone does not impact IEC function and metabolism in the absence of IL-10. This aligns with the *in vivo* data, suggesting that while mitochondrial dysfunction causes increased susceptibility to IBD, mitochondrial stress alone cannot predispose the host.

4.19. Metabolic injury drives dysbiotic changes in the intestinal microbiota

IECs are not only in cross-talk with the host microenvironment but also with luminal bacteria. Previous data show that mitochondrial impairment leads to a disrupted Paneth cell phenotype [68]. Since Paneth cells are absent in the colon, mucus-filled goblet cells (GCs) constitute a vital cell type essential for microbiome-host cross-talk. This secretory cell type produces mucus to maintain a barrier between bacteria and host and is susceptible to altered cellular metabolism. To characterize the adaptive response of GCs during metabolic injury, mucin was stained using alcian blue/periodicacid-Schiff (PAS-AB) in colonic tissue sections of Hsp60$^{\Delta/\Delta IEC}$ mice. A significant loss of mucus-filled GCs was observed from day 4 on, preceding the peak onset of tissue injury (Figure 34A,B).

To further analyze the intestinal microbiome during metabolic injury, 16S rRNA amplicon sequencing of the colonic content was performed. Metabolic injury in Hsp60$^{\Delta/\Delta IEC}$ mice was associated with rapid changes in the bacterial profile, including a drop in species richness (α-diversity) (Figure 34C) and changes in the community profile (β-diversity) (Figure 34D). Both α-and β diversity showed a transient change from day 4 to 11, with day 14 nearly recovered to control levels. A Kruskal-Wallis test of the relative abundance of all genera over all time points revealed 6 significantly altered genera, including *Bacteroides, Parabacteroides, Parasutterella, Alistipes, Barnesiella*, and *Clostridium IV* spp. (Figure 34E). Interestingly, *Bacteroides* spp. showed the highest overall abundance and were transiently increased in response to mitochondrial perturbation. *In silico* analysis of the respective zOTUs of all *Bacteroides* spp. identified *B. acidifaciens, B. caecimuris, B. stercorirosoris,* and *P. vulgatus* (Figure 34F). To identify bacteria on species level, shallow shotgun metagenomics of colonic content was performed at days 0 and 8 in Hsp60$^{\Delta/\Delta IEC}$ mice. In total, 31 species were detected, including *B. caecimuris, B. uniformis,* and *P. vulgatus* (Table 15). These three strains depicted an increase in abundance, corroborating the findings from 16S amplicon sequencing. In parallel, *P. distasonis* and *P. goldsteinii,* as well as *Lachnospiraceae bacterium 28 4, E. coli, and Turicimonas muris,* were elevated. Contrary, *Enterorhabdus caecimuris, Muribaculaceae bacterium DSM 103720, Muribaculum intestinale, Prevotella sp MGM2,* and *Faecalibaculum rodentium* demonstrated reduced species level abundance. These data reveal that in parallel to tissue aberration in response to mitochondrial dysfunction, the additional groundbreaking feature of metabolic injury is an adaptive response of the bacterial community in the colon. The microbiome-host cross-talk during metabolic injury is shaped by signals from the injured host to the microbiota, and vice versa, signals from the microbiota to the host.

It is important to mention that during mild mitochondrial impairment, 16S rRNA analysis of colonic content revealed no changes in α- and β-diversity (Supplementary figure 10), indicating that mild mitochondrial impairment without metabolic alterations does not impact microbial community profiles.
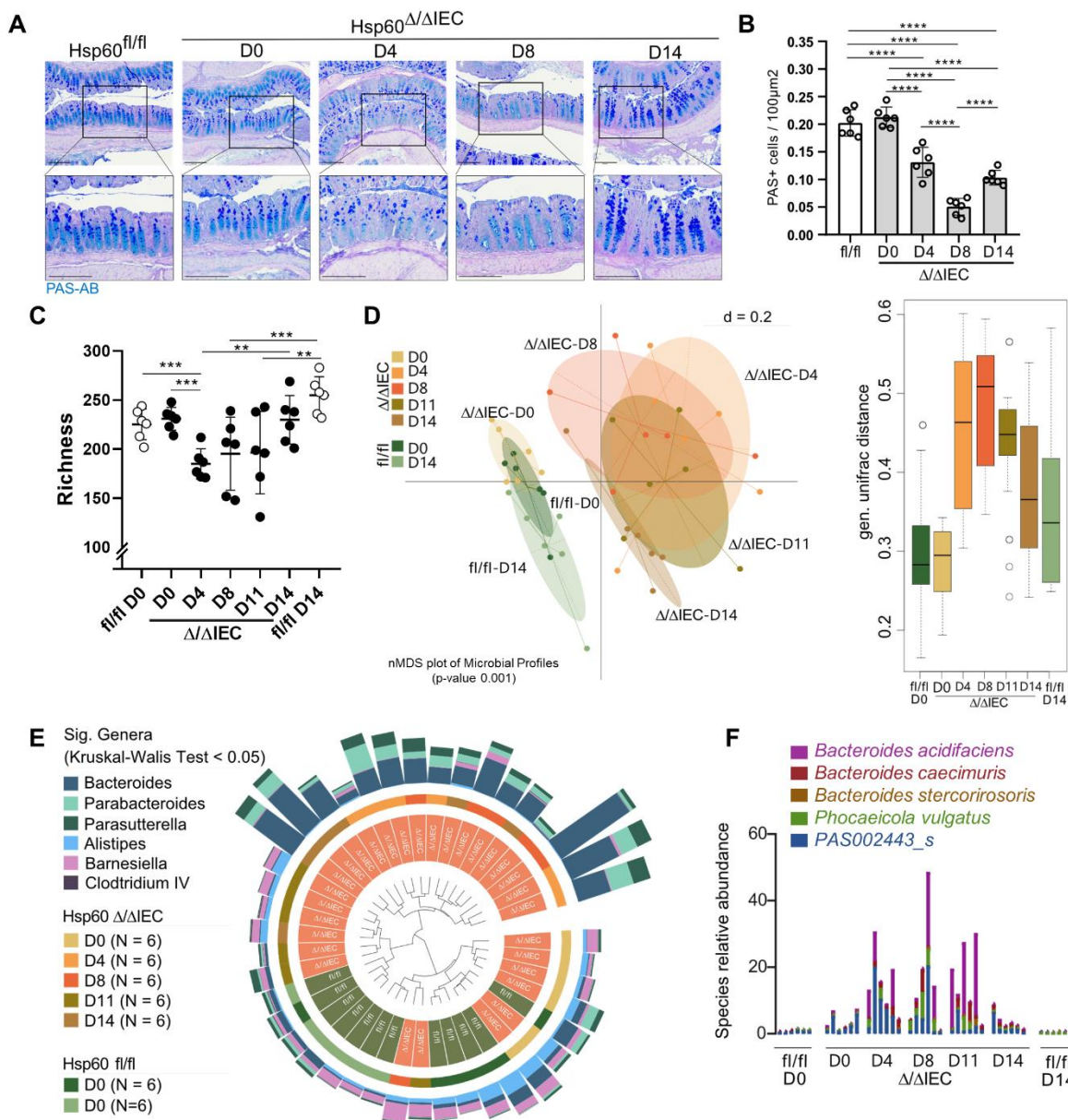

Figure 34: The intestinal microbiota is affected by metabolic injury.
(A) Representative PAS-AB stainings for mucus-filled goblet cells (GCs) of colonic swiss roles and corresponding higher magnifications for Hsp60$^{\Delta/\Delta IEC}$ mice on day (D) 0, 4, 8, 11 and 14 (scale bars = 200μM). **(B)** Quantification of GCs per 100μm². **(C)** Alpha-diversity as represented by community richness from colonic content of Hsp60$^{\Delta/\Delta IEC}$ mice on day (D) 0, 4, 8, 11, and 14 based on 16S rRNA sequencing. **(D)** Beta-diversity depicted as an nMSD plot and generalized UniFrac distance of bacterial composition from colonic content of respective mice and time points. **(E)** Taxonomic tree with relative abundances of significant genera (Kruskal-Wallis Test < 0.05) from colonic content of respective mice and time points. **(F)** *In silico* analysis of the respective zOTUs of all *Bacteroides* spp. of respective mice and time points. Statistics: (B,C) ANOVA followed by pairwise comparison testing (Tukey). Mean ± SD, n=6. Asterisks indicate significant differences *P<0.05, **P<0.01, ***P<0.001; ****P<0.0001.

Table 15: Bacterial species identified using shallow shotgun sequencing.

p Actinomycetota	
Enterorhabdus caecimuris/Adlercreutzia caecimuris	**decreased D8**

p Bacteroidota	
Bacteroides caecimuris	**increased D8**
Bacteroides uniformis	**increased D0**
Bacteroides vulgatus/Phocaeicola vulgatus	**increased D8**
Muribaculaceae bacterium DSM 103720	**decreased D0, D8**
Muribaculum intestinale	**decreased D0, D8**
Prevotella sp MGM2	**decreased D8**
Parabacteroides distasonis	**increased D8**
Parabacteroides goldsteinii	**increased D8**
Mucispirillum schaedleri	**-**

p Bacillota	
Staphylococcus xylosus	**-**
Enterococcus faecalis	**-**
Lactobacillus intestinalis	**-**
Lactobacillus johnsonii	**-**
Lactobacillus murinus	**-**
Lactobacillus reuteri	**-**
Lactobacillus taiwanensis	**-**
Acetatifactor muris	**-**
Dorea sp 5 2	**-**
Lachnospiraceae bacterium 10 1	**-**
Lachnospiraceae bacterium 28 4	**increased D8**
Lachnospiraceae bacterium A2	**-**
Lachnospiraceae bacterium A4	**-**
Oscillibacter sp 1 3	**-**
Anaerotruncus sp G3 2012	**-**
Clostridium cocleatum	**-**
Faecalibaculum rodentium	**decreased D8**
Firmicutes bacterium ASF500	**-**

p Pseudomonadota	
Turicimonas muris	**increased D8**
Escherichia coli	**increased D8**
Klebsiella oxytoca	**-**

4.20. Microbial dysbiosis persists in Hsp60$^{\Delta/\Delta IEC}$;*Il10$^{-/-}$* mice

Since metabolic injury transiently induced dysbiotic changes of the intestinal microbiota in Hsp60$^{\Delta/\Delta IEC}$ mice, the intestinal microbiota was investigated during a disrupted regenerative response in Hsp60$^{\Delta/\Delta IEC}$;*Il10$^{-/-}$* mice.

It has already been shown that PAS-AB staining of mucin produced by GCs revealed a transiently reduced loss of mucus-filled GCs at day 8 in Hsp60$^{\Delta/\Delta IEC}$ mice. This phenotype was more pronounced in Hsp60$^{\Delta/\Delta IEC}$;*Il10$^{-/-}$* mice and the reduction persisted in inflamed Hsp60$^{\Delta/\Delta IEC}$;*Il10$^{-/-}$* mice at day 14 (Figure 35A,B), indicating an association of a disrupted regenerative response and a disrupted mucus barrier. It is important to mention that the epithelial barrier is essential for IEC homeostasis, and barrier disruption can permit luminal antigens to translocate into subepithelial tissue, activating the immune system.
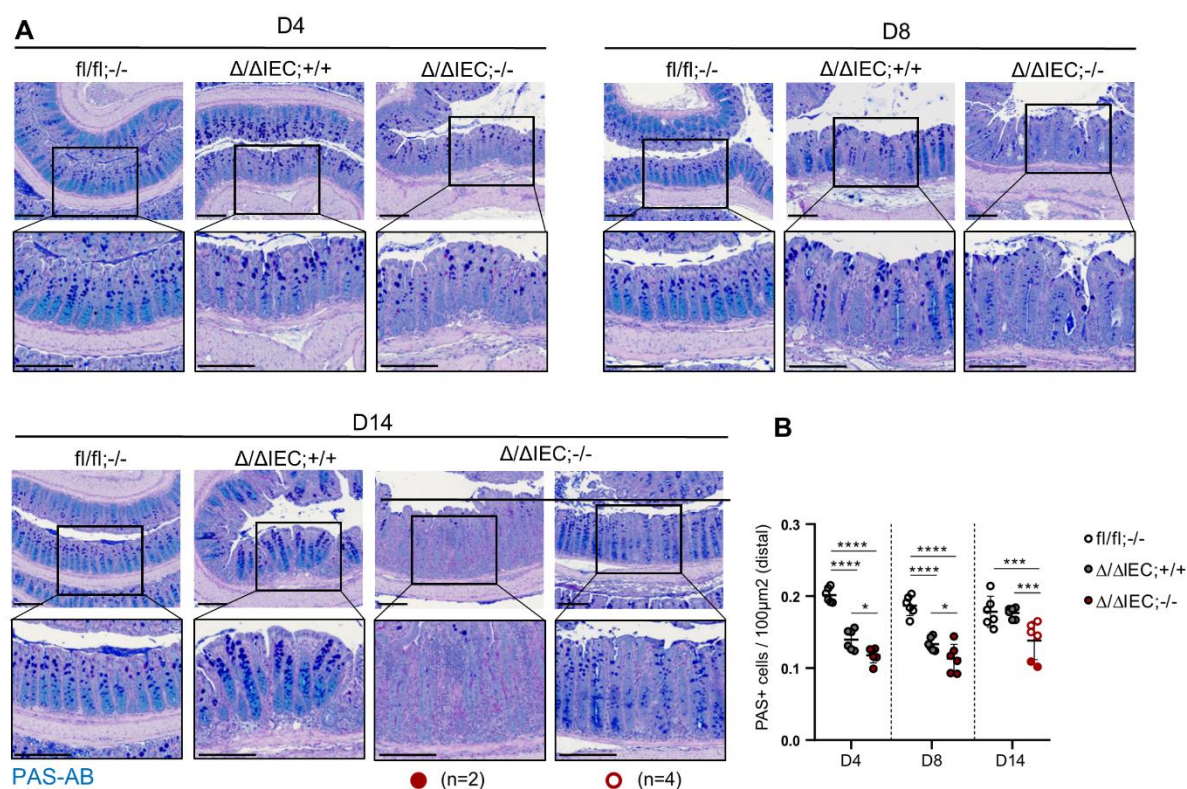
Figure 35: Mucus reduction persists in accelerated inflammation following disturbed regeneration after metabolic injury.
(A) Representative PAS-AB staining for mucus-filled goblet cells (GCs) of colonic swiss roles and corresponding higher magnifications for Hsp60$^{\Delta/\Delta IEC}$;*Il10$^{-/-}$* mice and respective controls on day (D) 4, 8 and 14 (scale bars = 200µM). **(B)** Quantification of GCs per 100µm^2. Statistics: (B) ANOVA followed by pairwise comparison testing (Tukey). Mean ± SD, n=6. Asterisks indicate significant differences *P<0.05, **P<0.01, ***P<0.001; ****P<0.0001.

To further examine intestinal microbiota composition, 16S amplicon sequencing of colonic content was performed in all three genotypes at days 8 and 14. A drop in species richness (α-diversity) and changes in the community profile (β-diversity) were observed at day 8 in both Hsp60$^{\Delta/\Delta IEC}$;*Il10*$^{+/+}$ and Hsp60$^{\Delta/\Delta IEC}$;*Il10*$^{-/-}$ mice, with an increased relative abundance of *Bacteroides* spp. (Figure 34A-C). While the change was transient in Hsp60$^{\Delta/\Delta IEC}$ mice, alterations in α-and β diversity were still present at day 14 in Hsp60$^{\Delta/\Delta IEC}$;*Il10*$^{-/-}$ mice (Figure 34D,E). Interestingly, the relative abundance (%) of *Bacteroides* spp. that increased in response to mitochondrial perturbation persisted in Hsp60$^{\Delta/\Delta IEC}$;*Il10*$^{-/-}$ mice (Figure 34F). These data illustrate that the microbiota is affected during a disturbed healing capacity, indicating the rapid adaptation of the intestinal microbiome to host physiology and disease susceptibility.

Notably, treatment with AOM (Supplementary figure 11) did not induce changes in mucus-filled GCs and the intestinal microbiota.
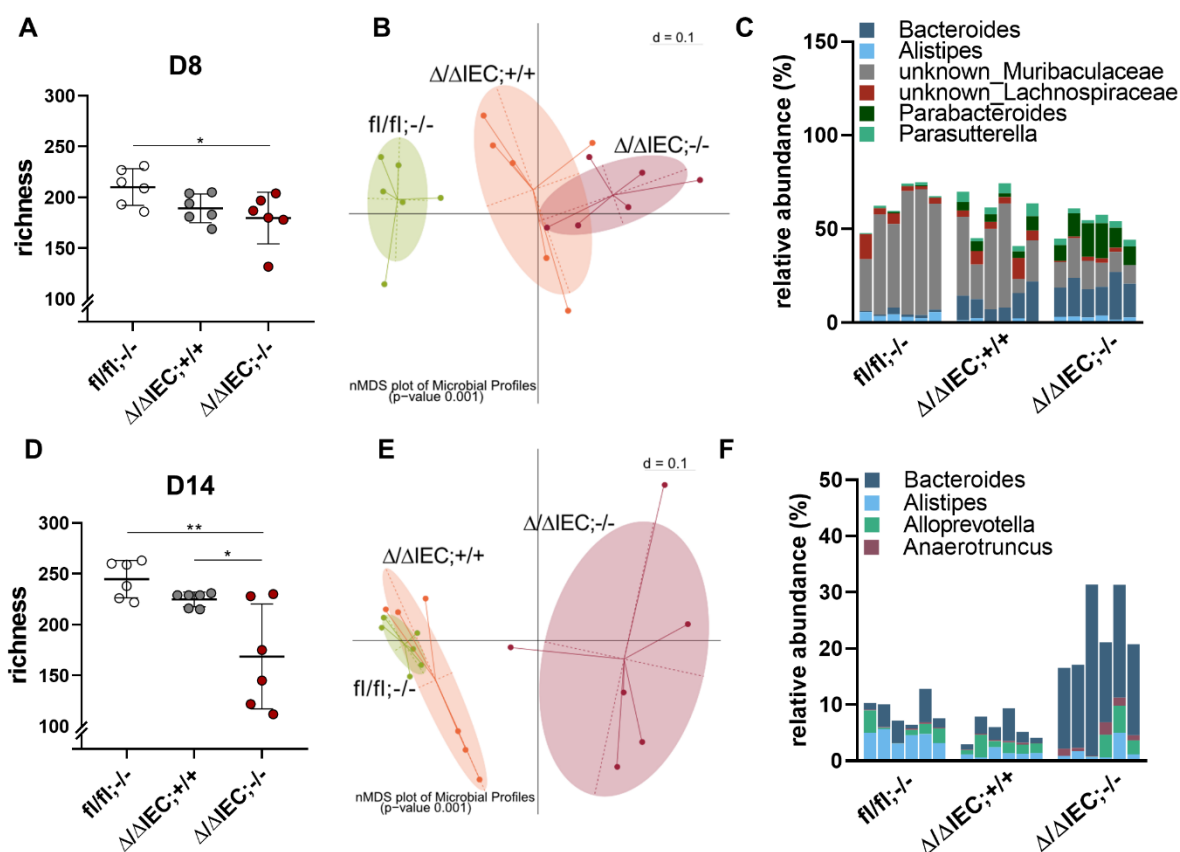
Figure 36: Persistent microbial dysbiosis and increased *Bacteroides* spp. are associated with accelerated inflammation following metabolic injury.
Alpha-diversity as represented by community richness from colonic content of Hsp60$^{\Delta/\Delta IEC}$;*Il10*$^{-/-}$ mice and respective controls based on 16S amplicon sequencing at **(A)** day (D) 8 and **(D)** D14. Beta-diversity depicted as nMSD plot of bacterial composition from colonic content of respective mice at **(B)** D8 and **(E)** D14. Relative abundance of significant genera (Kruskal-Wallis Test < 0.05) from colonic content of respective mice at **(C)** D8 and **(F)** D14. Statistics: (A,D) ANOVA followed by pairwise comparison testing (Tukey). Mean ± SD, n=6. Asterisks indicate significant differences *P<0.05, **P<0.01, ***P<0.001; ****P<0.0001.

4.21. Control of metabolic injury in the absence of bacteria

Mitochondrial impairment in Hsp60$^{\Delta/\Delta IEC}$ mice caused self-limiting injury in the colonic epithelium and was disrupted in the absence of IL-10 (Hsp60$^{\Delta/\Delta IEC}$;$Il10^{-/-}$ mice). During this process, an association between *Bacteroides* spp. and metabolic injury was observed, leading to the question of whether bacterial changes are the cause or consequence of metabolic injury and disease development. To address this question, germfree (GF) Hsp60$^{\Delta/\Delta IEC}$ mice were generated, and the same experimental setup as under SPF conditions was used (Figure 37A). Weight development was significantly reduced from day 0 to 4 compared to tamoxifen-exposed Hsp60$^{fl/fl}$ control mice and regenerated from D6 (Figure 37B). In contrast to SPF conditions, however, the weight reduction was significantly attenuated. DNA isolated from mouse tail or colonic tissue was also used to detect the presence or absence of *Villin*CreER^{T2} and the Hsp60 flox or KO allele (Figure 37C). To confirm the deletion of *Hsp60*, colonic tissue was processed for downstream RNA isolation and qRT-PCR analysis (Figure 37D). Next to a complete *Hsp60* deletion at day 0, a transiently activated MT-UPR signaling (*Chop, Trb3*) was detected (Figure 37E), indicating the model's functionality under germfree conditions similar to SPF housing.
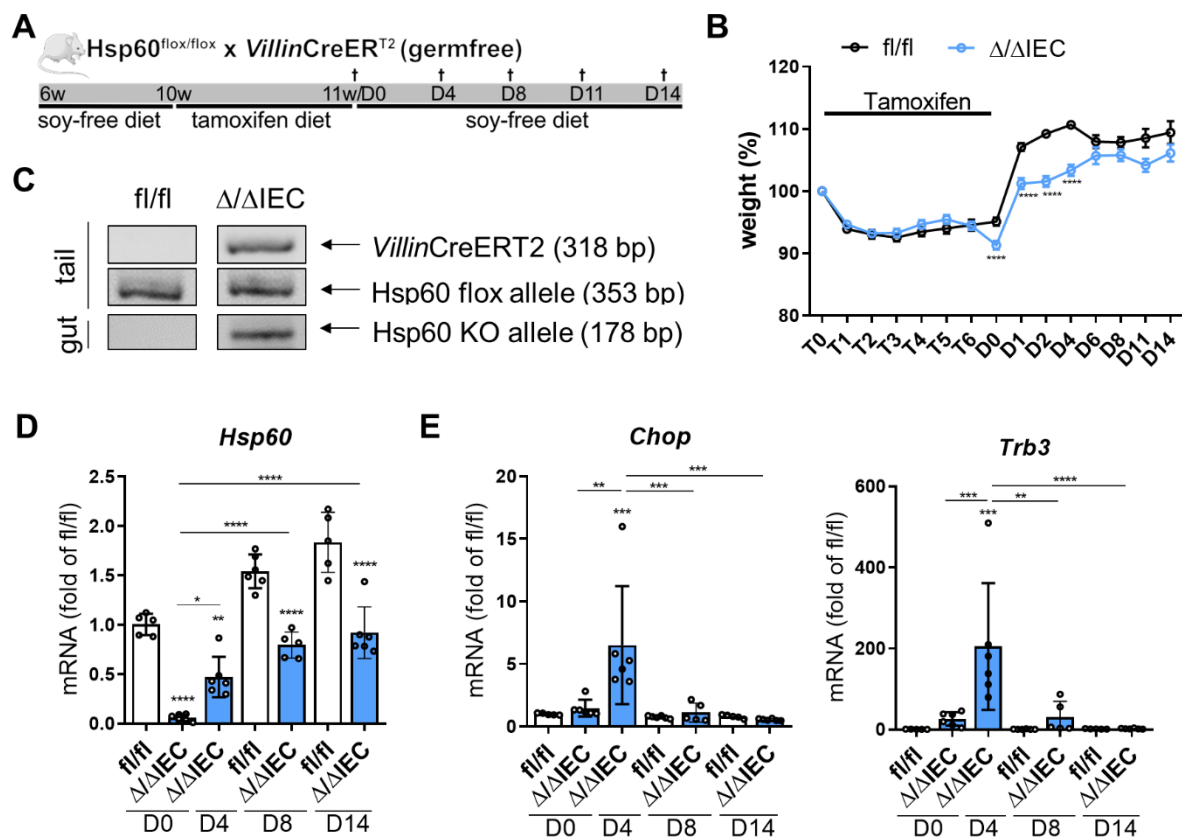

Figure 37: MT-UPR signaling is induced under germfree conditions similar to SPF housing.
(A) Experimental setup illustrating the IEC-specific deletion of Hsp60 in germfree (GF) mice (Hsp60$^{\Delta/\Delta IEC}$ mice, Ctrl: Hsp60$^{fl/fl}$) by oral feeding with tamoxifen supplemented food. Mice were sacrificed at day (D) 0, 4, 8, 14 after end of tamoxifen treatment and full Hsp60 deletion. **(B)** Weight curves of GF Hsp60$^{\Delta/\Delta IEC}$ and Hsp60$^{fl/fl}$ mice from the start

of tamoxifen feeding until D14. **(C)** Agarose gels depicting genotyping results for the CreERT2 transgene and Hsp60 flox allele in tails and Hsp60 KO specifically in the gut. mRNA expression levels of colonic tissue for **(D)** *Hsp60* and **(E)** MT-UPR relevant *genes* (*Chop,Trb3*). Statistics: (B) Multiple t-test using the Two-stage linear step-up procedure of Benjamini, Krieger and Yekutieli. (D,E) ANOVA followed by pairwise comparison testing (Tukey). Mean ± SD, n=6. Asterisks indicate significant differences *P<0.05, **P<0.01, ***P<0.001; ****P<0.0001.

Next, the impact of mitochondrial stress signaling was characterized on tissue level without bacteria. Histological analysis of colonic tissue revealed a complete absence of tissue injury in the distal colon with no changes in crypt depth (Figure 38A,B,E). In the proximal colon, however, tissue aberration was mildly present on days 8 and 14 and was accompanied by slightly elongated crypts (Figure 38C-E). Similarly, the ileum showed an aberrant epithelial architecture at days 0 and 4, which was lower than SPF conditions (Figure 39A,B). A comparison of the score for aberrant epithelial architecture over all four time points (D0, D4, D8, D14) and colonic segments (proximal, middle, distal) revealed a clear distinction between GF and SPF conditions. While tissue aberration was absent under all conditions at day 0, it was only present at day 4 in the proximal part of SPF mice. At day 8, the phenotype was strongest in all three colonic segments under SPF housing and significantly reduced in germfree mice's proximal part while absent in the mid and distal part (Figure 38F). Day 14 showed an overall reduction under all conditions in all segments, highlighting the self-limiting phenotype of metabolic injury. In summary, it can be concluded that bacterial signals are directly involved in regulating metabolic perturbations and the level of epithelial injury in the distal colon. In contrast, the phenotype in the proximal colon is cell autonomous.
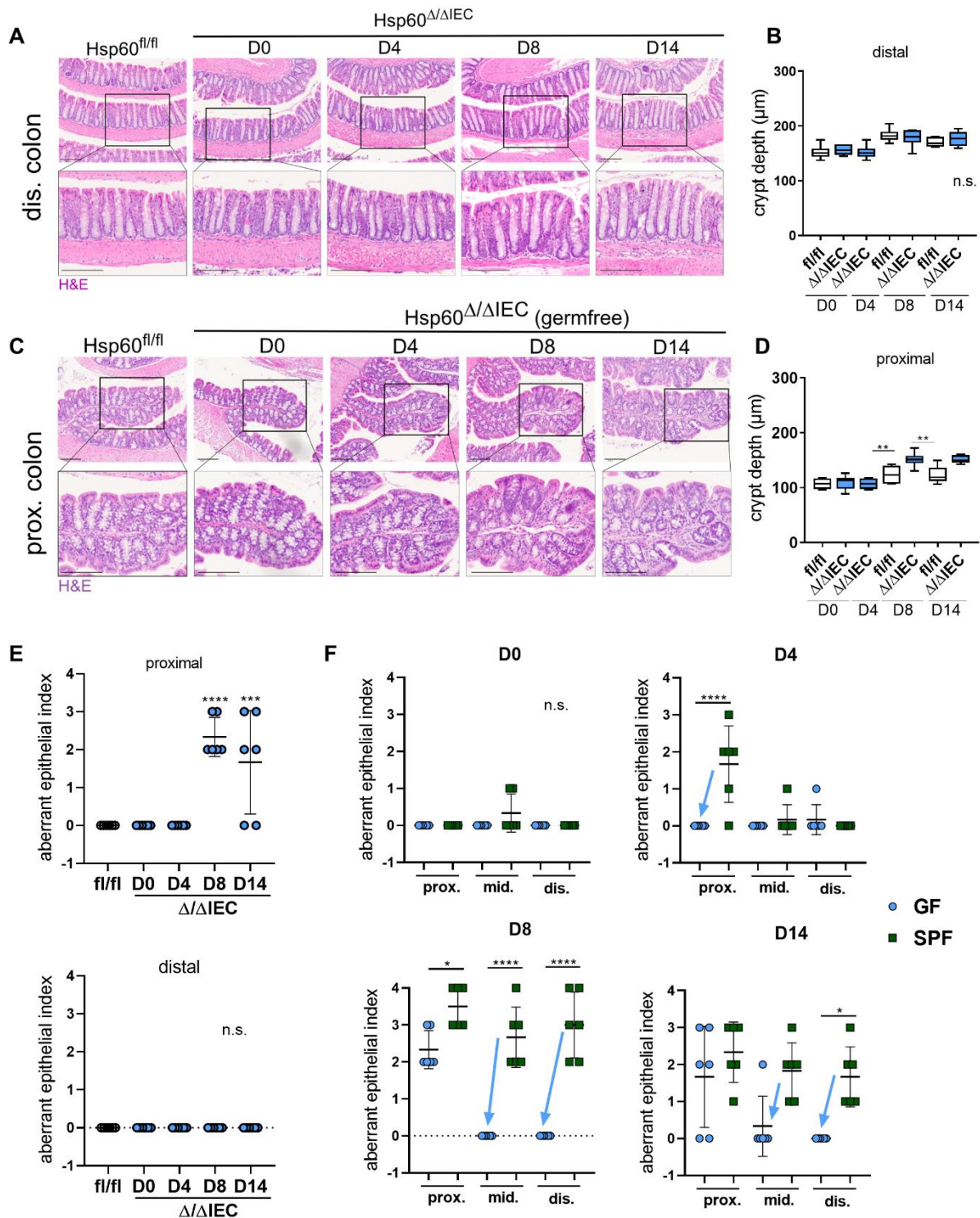
Figure 38: Bacterial signals spatially contribute to metabolic injury.
Representative H&E stained sections of **(A)** distal and **(C)** proximal colonic tissue and corresponding higher magnifications for germfree (GF) Hsp60$^{\Delta/\Delta IEC}$ mice on day (D) 0, 4, 8 and 14 (scale bars = 200µM). Quantification of crypt depth over all time points in the **(B)** distal and **(D)** proximal colonic segments. **(E)** Colonic tissue was scored histologically for an aberrant crypt architecture. **(F)** Comparison of the aberrant epithelial architecture score between GF and SPF housing in the proximal, middle, and distal colon on days (D) 0, 4, 8 and 14. Statistics: (B,D,E,F) ANOVA followed by pairwise comparison testing (Tukey). Mean ± SD, n=6. Asterisks indicate significant differences *P<0.05, **P<0.01, ***P<0.001; ****P<0.0001.
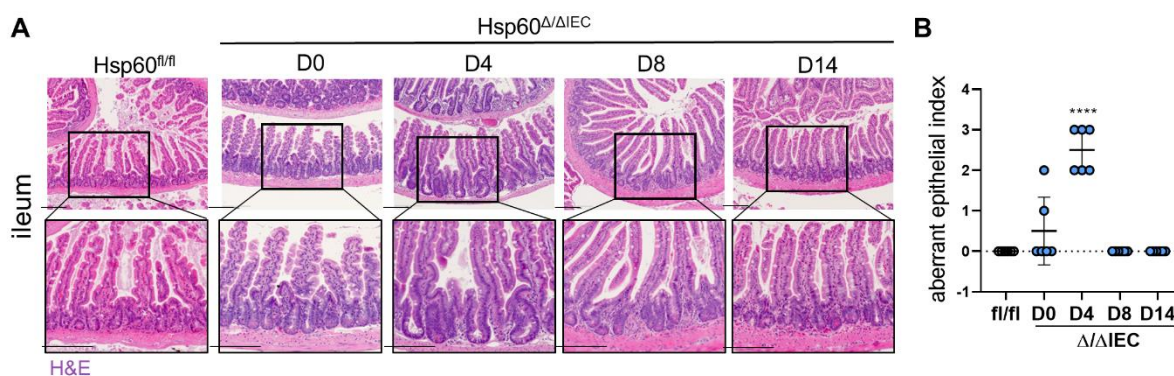
Figure 39: The ileum of germfree Hsp60$^{\Delta/\Delta IEC}$ mice shows mild metabolic injury.
(A) Representative H&E stained sections of ileal tissue and corresponding higher magnifications (scale bars = 200µM). **(B)** Tissue was scored histologically for an aberrant epithelial architecture. Statistics: ANOVA followed by pairwise comparison testing (Tukey). Mean ± SD, n=6. Asterisks indicate significant differences *P<0.05, **P<0.01, ***P<0.001; ****P<0.0001.

Hsp60 IHC staining and the respective quantification revealed a loss of Hsp60 (D0, D4) followed by a regain of Hsp60 expression from day 8 to 14 in the distal (Figure 40A-C) and proximal colon (Supplementary figure 12A) similar to SPF conditions. While Hsp60 deficiency abrogated Ki67 expression under SPF conditions, no such effect was observed in germfree Hsp60$^{\Delta/\Delta IEC}$ mice. In the distal colon, hyperproliferative crypts were absent, and quantification revealed only a slight increase in proliferation (Figure 40D,E). Contrary, the proximal colon showed hyperproliferative regions, which were inferior to SPF conditions (Supplementary figure 12B). In line, *in situ* hybridization of *Lgr5* showed a low number of *Lgr5* negative compared to *Lgr5* positive crypts at day 0 in the distal colon (Figure 40F,G). By contrast, Hsp60 deficiency under SPF housing is associated with a loss of stemness and proliferation [77], indicating that the intestinal microbiota affects the level of stemness and proliferation and thus tissue injury in a spatially driven way.
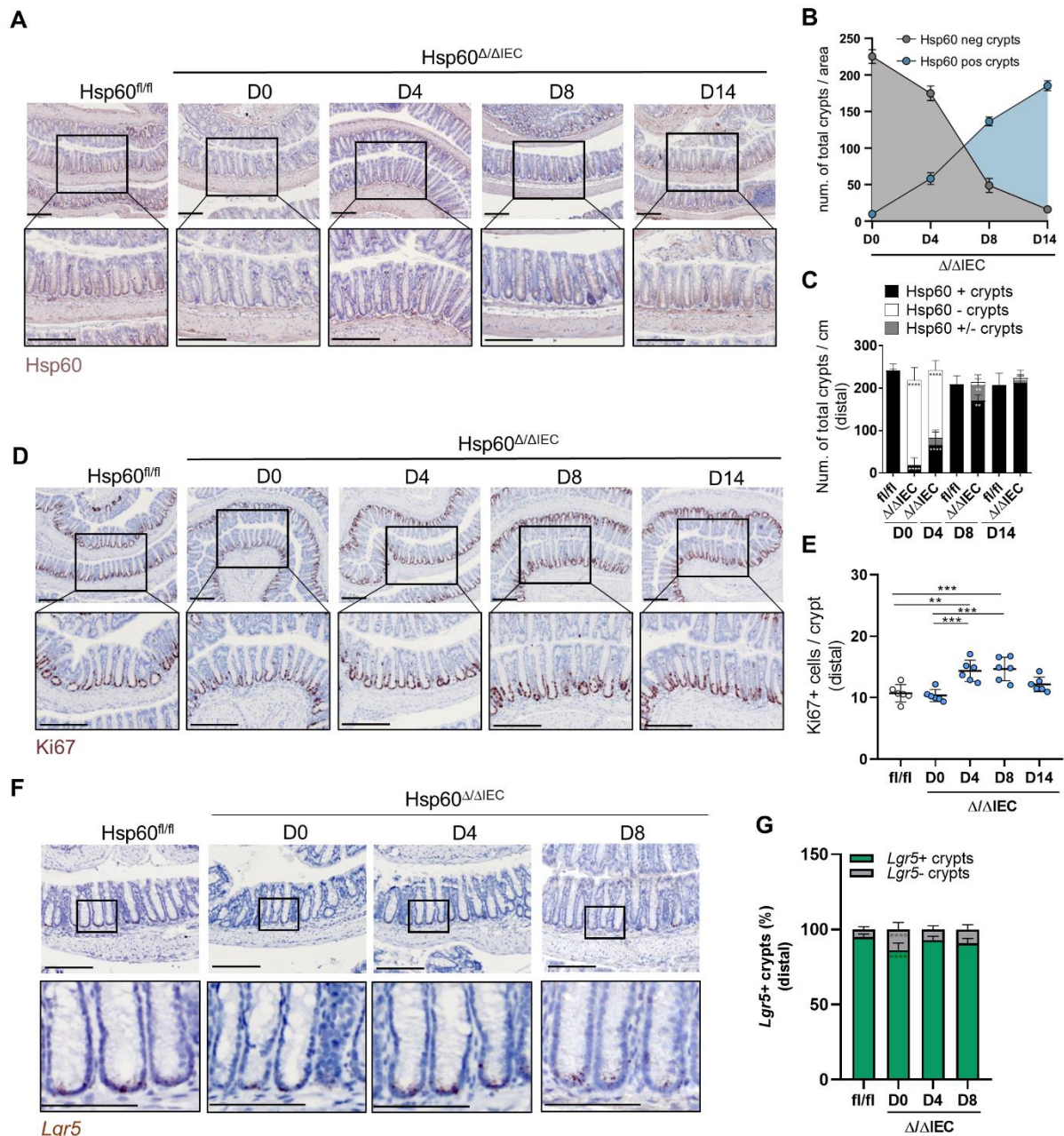
Figure 40: IEC proliferation and stemness are impacted by microbial signals under germfree housing.
(A) Representative immunohistochemically stained colonic swiss rolls for Hsp60 in germfree (GF) Hsp60$^{\Delta/\Delta IEC}$ mice on day (D) 0, 4, 8 and 14 (scale bars = 200µM). **(B)** Quantification of Hsp60 positive and negative crypts in GF Hsp60$^{\Delta/\Delta IEC}$ mice over time. **(C)** Quantification of Hsp60 positive and negative crypts in Hsp60$^{\Delta/\Delta IEC}$ compared to Hsp60$^{fl/fl}$ mice. **(D)** Representative immunohistochemically stained colonic swiss rolls for Ki67 in GF Hsp60$^{\Delta/\Delta IEC}$ mice on days (D) 0, 4, 8, and 14 (scale bars = 200µM). **(E)** Quantification of Ki67 positive cells per crypt over all time points. **(F)** Representative pictures of *Lgr5 in-situ* analysis from colonic swiss rolls in GF Hsp60$^{\Delta/\Delta IEC}$ mice on days (D) 0, 4, and 8(scale bars = 200µM). **(G)** Quantification of *Lgr5* positive and negative crypts. Statistics: (E) One-way and (C,G) two-way ANOVA followed by pairwise comparison testing (Tukey). Mean ± SD, n=6. Asterisks indicate significant differences *P<0.05, **P<0.01, ***P<0.001; ****P<0.0001.

4.22. Attenuated metabolic alterations in the absence of bacteria

To investigate metabolic alterations in germfree Hsp60$^{\Delta/\Delta IEC}$ mice at day 0 (the time point with the most pronounced metabolic changes under SPF conditions), a NanoString analysis of a metabolic panel of ~ 800 genes was performed. Only 10 genes showed a fold change greater than 2, including 8 upregulated and 2 downregulated genes (Figure 41A). In comparison, there were 45 altered genes under SPF conditions, overlapping all 8 upregulated genes (Figure 41B). Only 1 out of the 10 genes was mitochondria localized, namely *Hk2*. The volcano plot of DEGs showed 9 significant genes at day 0 (8 up-, 1 downregulated) (Figure 41C), which was much lower than 51 DEGs under SPF conditions.

The glycolysis marker *Hk2* showed a significant increase, which was milder than SPF conditions. Interestingly, the glucose metabolism regulator *Pdk4* was elevated, while it was decreased under SPF housing. In addition, the OXPHOS component *Cox-I* was reduced, similar to SPF housing (Figure 41D). These expression levels of metabolic genes suggest that metabolic alterations are also present under germfree conditions, however, they are milder or differently regulated.

KEGG pathway analysis of the 10 regulated genes on day 0 highlights the enrichment of glycine, serine and threonine metabolism, biosynthesis of amino acids, and carbon metabolism (Figure 41E), which overlap with the pathways under SPF conditions. However, protein digestion and absorption, HIF-1 signaling pathway, PI3K-Akt signaling pathway, and notably tryptophan metabolism were significantly enriched with bacteria but absent under germfree conditions. In addition, genes were tested for differential expression in response to covariates. While the metabolic enzymes *Ido1* and *Nos2* were significantly increased at day 4 on qPCR level, *Arg1* was not altered (Figure 41F). However, their expression levels were lower compared to SPF conditions. In line, no Ido1+ signal was detected at any time point in immunofluorescence staining in the distal colon (Figure 41G).

These data suggest that metabolic alterations in response to MT-UPR signaling in IECs are attenuated without bacteria, validating the impact of microbiome-cross-talk and microbial signals on IEC metabolism.
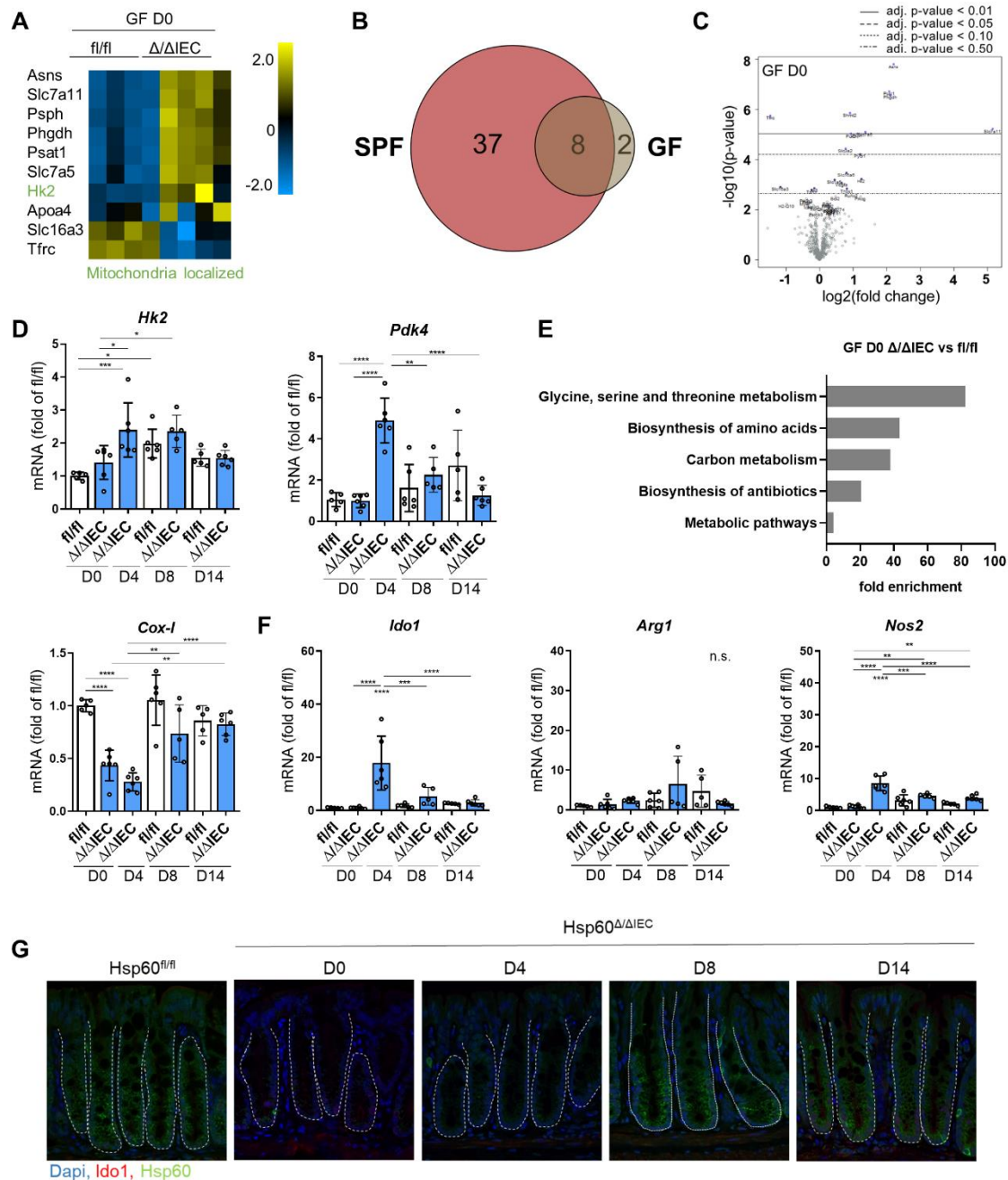
Figure 41: Metabolic alterations of IECs are diminished without bacteria.

(A) Heatmap of a NanoString analysis of a metabolic panel of 800 genes in colonic tissue of germfree (GF) Hsp60$^{\Delta/\Delta IEC}$ compared to Hsp60$^{fl/fl}$ mice at day 0. Depicted are genes with a fold-change greater than ± 2. (green): mitochondria localized genes. **(B)** Venn-diagram illustration of the number of genes with a fold-change greater than ± 2 at day (D) 0 comparing Hsp60$^{\Delta/\Delta IEC}$ mice under SPF and GF housing. **(C)** Vulcano plots of differentially regulated genes (DEGs) (FDR < 0.05) at day (D) 0 in GF Hsp60$^{\Delta/\Delta IEC}$ compared to Hsp60$^{fl/fl}$ mice. **(D)** mRNA expression levels of colonic tissue for metabolic genes (*Hk2, Pdk4, Slc37a2, Cox-I*). **(E)** KEGG pathway analysis of the 10 altered genes at day 0. **(F)** mRNA expression levels of colonic tissue for arginine and tryptophan relates genes (*Ido1, Nos2, Arg1*) in the respective mice. **(G)** Representative immunofluorescence co-staining of Hsp60 (green) and Ido1 (red) in GF Hsp60$^{\Delta/\Delta IEC}$ and Hsp60$^{fl/fl}$ mice over all time points (600x). Dapi = blue. Statistics: (D,F) ANOVA followed by pairwise comparison testing (Tukey). Mean ± SD, n=6. Asterisks indicate significant differences *P<0.05, **P<0.01, ***P<0.001; ****P<0.0001.

4.23. Inflammation is diminished in the absence of bacteria

Since metabolic injury led to the recruitment of immune cells under SPF conditions, this aspect was analyzed in the absence of bacteria. The weight of MLNs was significantly increased during metabolic injury in the absence of bacteria, however, this increase was 2-fold higher under SPF conditions (Figure 42A). The length of all intestinal segments (duodenum, jejunum, ileum, colon), as well as the weight of all organs (cecum, stomach, pancreas, spleen, thymus, liver, kidney, muscle), did not differ (Supplementary figure 13).

In parallel to absent tissue injury in the distal colon of GF Hsp60$^{\Delta/\Delta IEC}$ mice, inflammation was absent in the mid and distal colon over all time points. The proximal colon showed an increase on days 8 and 14, however, this was attenuated compared to SPF conditions (Figure 42B). A comparison of the tissue pathology index over all four time points and intestinal segments demonstrated that inflammation was present on day 4 under SPF but not GF conditions. On days 8 and 14, the inflammation gradually decreased from the proximal to the distal colon and was much more pronounced under SPF than GF conditions (Figure 42C).

Additionally, qRT-PCR analysis of colonic tissue revealed no induction of the inflammatory marker *Saa3* and the pro-inflammatory cytokine *Tnf* (Figure 42D). In line, IHC staining of pStat3 did not show any nuclear expression (Figure 42E), indicating no direct signal transduction of IL-22, as observed under SPF conditions.

Together these data demonstrate that in the absence of bacteria and hence lower levels of metabolic injury, the recruitment of immune cells is diminished.

Figure 42: Immune cell recruitment is diminished in the absence of bacteria.
(A) MLN weight relative to body weight in germfree (GF) Hsp60$^{\Delta/\Delta IEC}$ mice from days (D) 0 to 14. **(B)** Colonic tissue was scored histologically for inflammation in the proximal and distal colon over all time points (range of score 0 (not inflamed) – 12 (highly inflamed)). **(C)** Comparison of the tissue pathology index between GF and SPF housing in the proximal, middle and distal colon on day (D) 0, 4, 8 and 14. **(D)** mRNA expression levels of colonic tissue for the cytokine *Tnf* and the systemic inflammation marker *Saa3*. Statistics: (A-D) ANOVA followed by pairwise comparison testing (Tukey). Mean ± SD, n=6. Asterisks indicate significant differences *P<0.05, **P<0.01, ***P<0.001; ****P<0.0001.
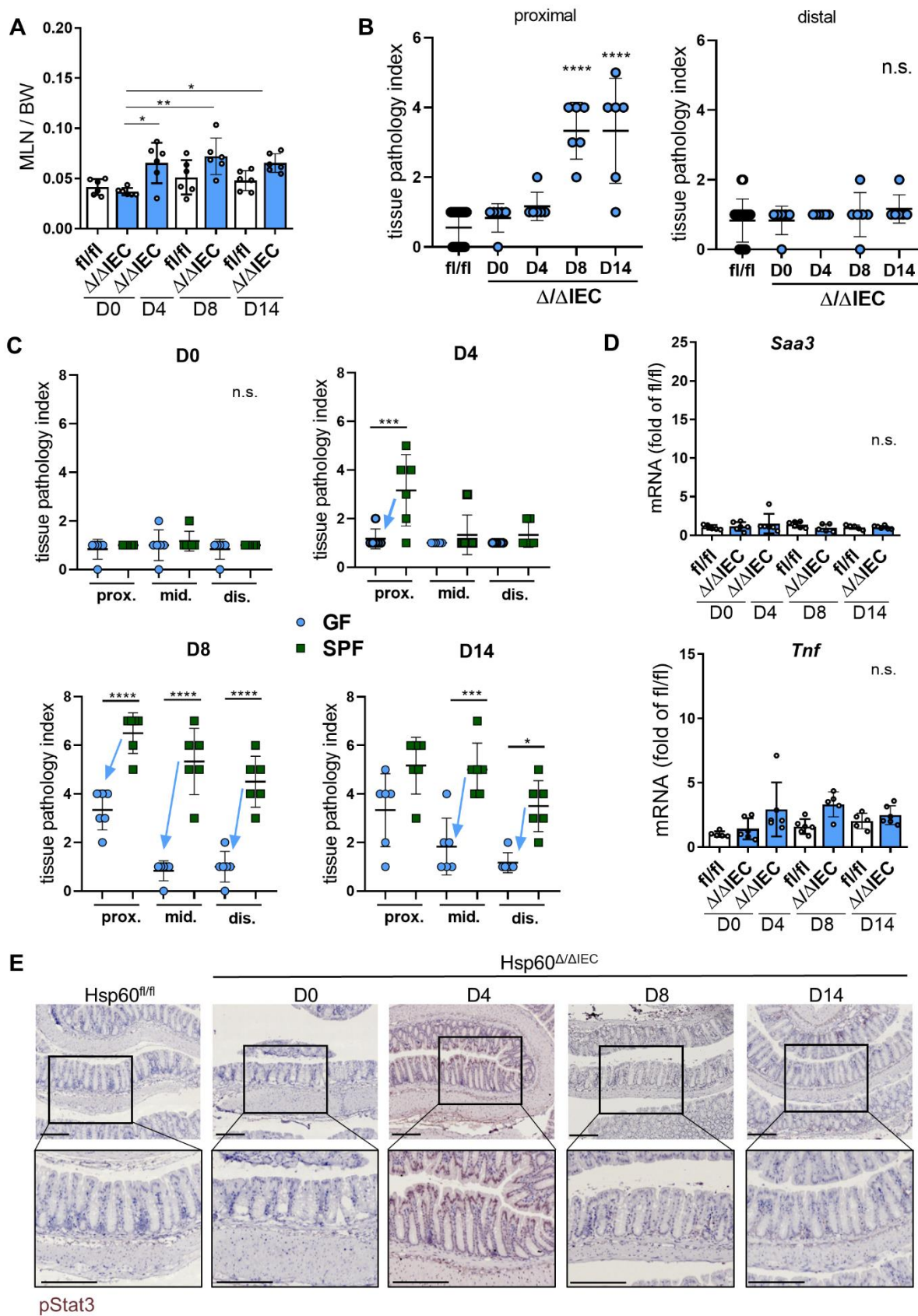
Figure 42: Immune cell recruitment is diminished in the absence of bacteria.

(Figure legend previous page)

Moreover, mucus production by GCs was analyzed in the epithelium of GF Hsp60$^{\Delta/\Delta IEC}$ mice. Mucus-filled GCs remained unchanged at all time points except for a slight reduction on day 8 in the distal (Figure 43A,B) and days 8 and 14 in the proximal colon (Supplementary figure 12C). However, the loss was minor (from 0.15 to 0.12 GCs / 100µm^2) in contrast to SPF housing (from 0.20 to 0.11 GCs / 100µm^2) and shorter (D8 GF vs. D4 – D8 SPF).

Concluding, these data support the hypothesis that bacterial signals are directly involved in regulating the severity of tissue injury in response to mitochondrial perturbation of the intestinal epithelium. However, it is important to highlight that the contribution of bacteria to metabolic injury is spatial. In the small intestine and proximal colon, metabolic injury is partly genetically driven, whereas in the distal colon, it is entirely bacterial driven.
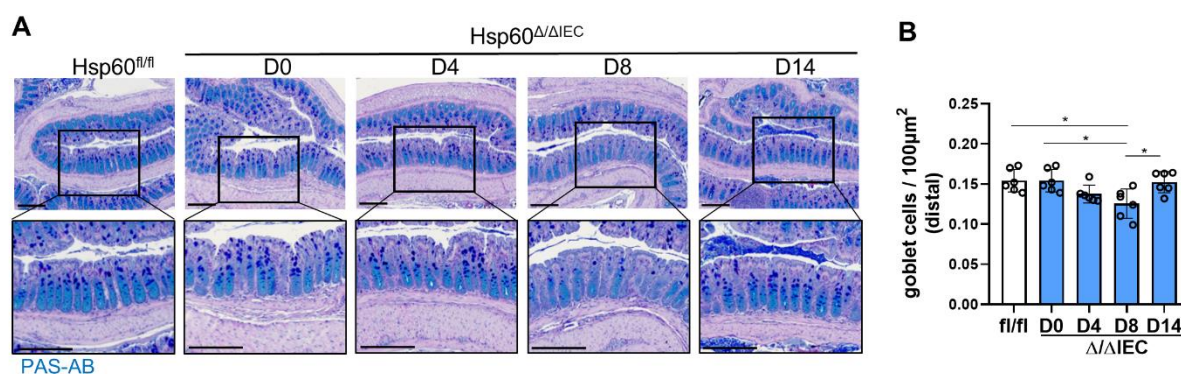
Figure 43: Mucus production is only mildly diminished without bacteria.
(A) Representative PAS-AB staining for mucus-filled goblet cells (GCs) of colonic swiss roles and corresponding higher magnifications for germfree (GF) Hsp60$^{\Delta/\Delta IEC}$ mice on day (D) 0, 4, 8 and 14 (scale bars = 200µM). **(B)** Quantification of GCs per 100µm^2. Statistics: (B) ANOVA followed by pairwise comparison testing (Tukey). Mean ± SD, n=6. Asterisks indicate significant differences *P<0.05, **P<0.01, ***P<0.001; ****P<0.0001.

4.24. Colonization with OMM^{12} triggers metabolic injury

Since bacteria control metabolic injury in the distal colon, it was next addressed whether a defined minimal consortium would be sufficient to trigger metabolic injury. Therefore, GF Hsp60$^{\Delta/\Delta IEC}$ mice were colonized with the Oligo-Mouse-Microbiota (OMM^{12}) synthetic bacterial community [166] and the same experimental setup as under GF and SPF conditions (Figure 44A) was used.

Weight development was significantly reduced from day 1 to 4 compared to tamoxifen exposed Hsp60$^{fl/fl}$ control mice and regenerated from day 8 (Figure 44B). In contrast to GF and SPF conditions, weight reduction reached an intermediate level between these two housing conditions. To confirm the deletion of *Hsp60*, transcriptional profiling of colonic tissue was performed. Next to a complete *Hsp60* deletion at day 0, a transiently activated MT-UPR signaling (*Chop, Trb3*) was detected (Figure 44C), indicating the model's functionality with selective colonization similar to SPF and GF housing. *Chop* and *Trb3* gradually declined in expression levels over time, which aligns with observed effects under SPF and GF housing.

Histological analysis of colonic tissue revealed increased crypt depth and aberrant epithelial architecture from day 4 on, indicating that OMM^{12} can sufficiently trigger metabolic injury in the distal colon (Figure 44D-F). The level of metabolic injury was intermediate between SPF and GF housing, suggesting that the injury's severity depends on the microbiota's complexity. In line with the injury kinetic, a regain of Hsp60 was observed from day 4, with 100% Hsp60 positive crypts at day 14 (Figure 44G), comparable to the regain of Hsp60 under SPF housing.
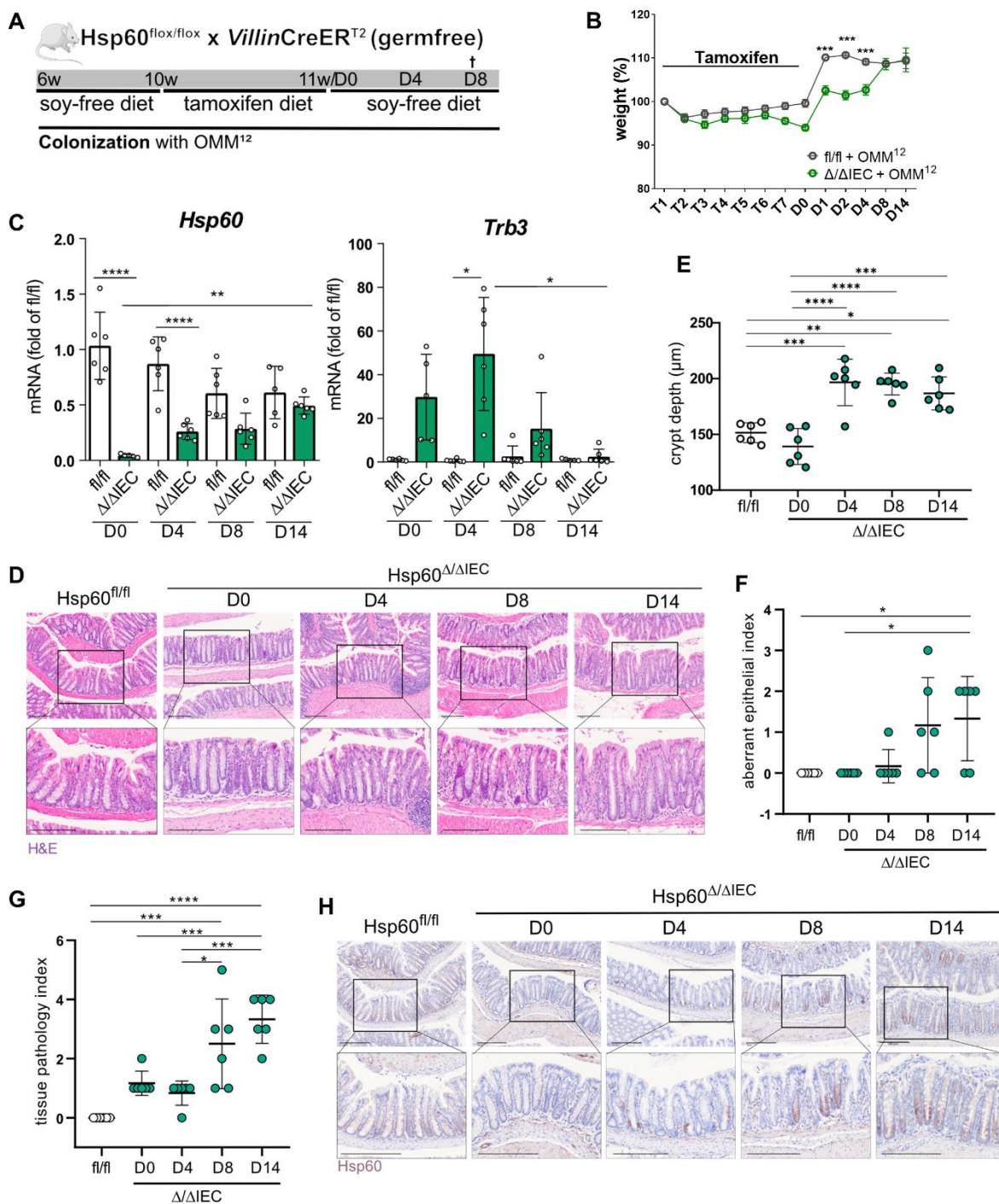
Figure 44: Colonization with OMM[12] triggers metabolic injury.
(A) Experimental setup. Mice were colonized with the minimal mouse consortium OMM[12] at the age of 6 weeks. This was followed by an IEC-specific deletion of Hsp60 (Hsp60[Δ/ΔIEC] mice, Ctrl: Hsp60^{fl/fl}) by oral feeding with tamoxifen supplemented food. Mice were sacrificed at days (D) 0, 4, 8, 14 after end of tamoxifen treatment and full Hsp60 deletion. **(B)** Weight curves of colonized Hsp60[Δ/ΔIEC] and Hsp60^{fl/fl} mice from the start of tamoxifen feeding until D14. **(C)** mRNA expression levels of colonic tissue for *Hsp60* and MT-UPR relevant *genes* (*Chop, Trb3*). **(D)** Representative H&E stained sections of colonic swiss roles and corresponding higher magnifications (scale bars = 200μM). **(E)** Quantification of crypt depth. **(F)** Distal colonic tissue was scored histologically for an aberrant epithelial architecture. **(G)** Distal colonic tissue was scored histologically for inflammation. **(H)** Representative immunohistochemically stained colonic swiss rolls for Hsp60 and corresponding higher magnifications for colonized Hsp60[Δ/ΔIEC] mice on day (scale bars = 200μM). Statistics: (C,E,F) ANOVA followed by pairwise comparison testing (Tukey). Mean ± SD, n=6. Asterisks indicate significant differences *P<0.05, **P<0.01, ***P<0.001; ****P<0.0001. Dr. D. Aguanno performed the experiment and data analysis.

Next, the abundance of all twelve bacterial species was analyzed using 16S targeted qPCR. *Bacteroides caecimuris* was elevated from day 4 on (Figure 45), supporting previous data showing an increase of *Bacteroides* spp. preceding metabolic injury. In addition, *Akkermansia muciniphila* and *Turicimonas muris* increased starting from day 4. All other bacterial species (*Clostridium innocuum, Muribaculum intestinale, Enterococcus faecalis, Flavonifractor plautii, Bifidobacterium animalis, Limosilactobacillus reuteri, Enterocloster clostridioformis,* and *Blautia coccoides*) did not reveal any changes in relative abundance. Unfortunately, *Actualibacter muris* was not detectable at qPCR level.
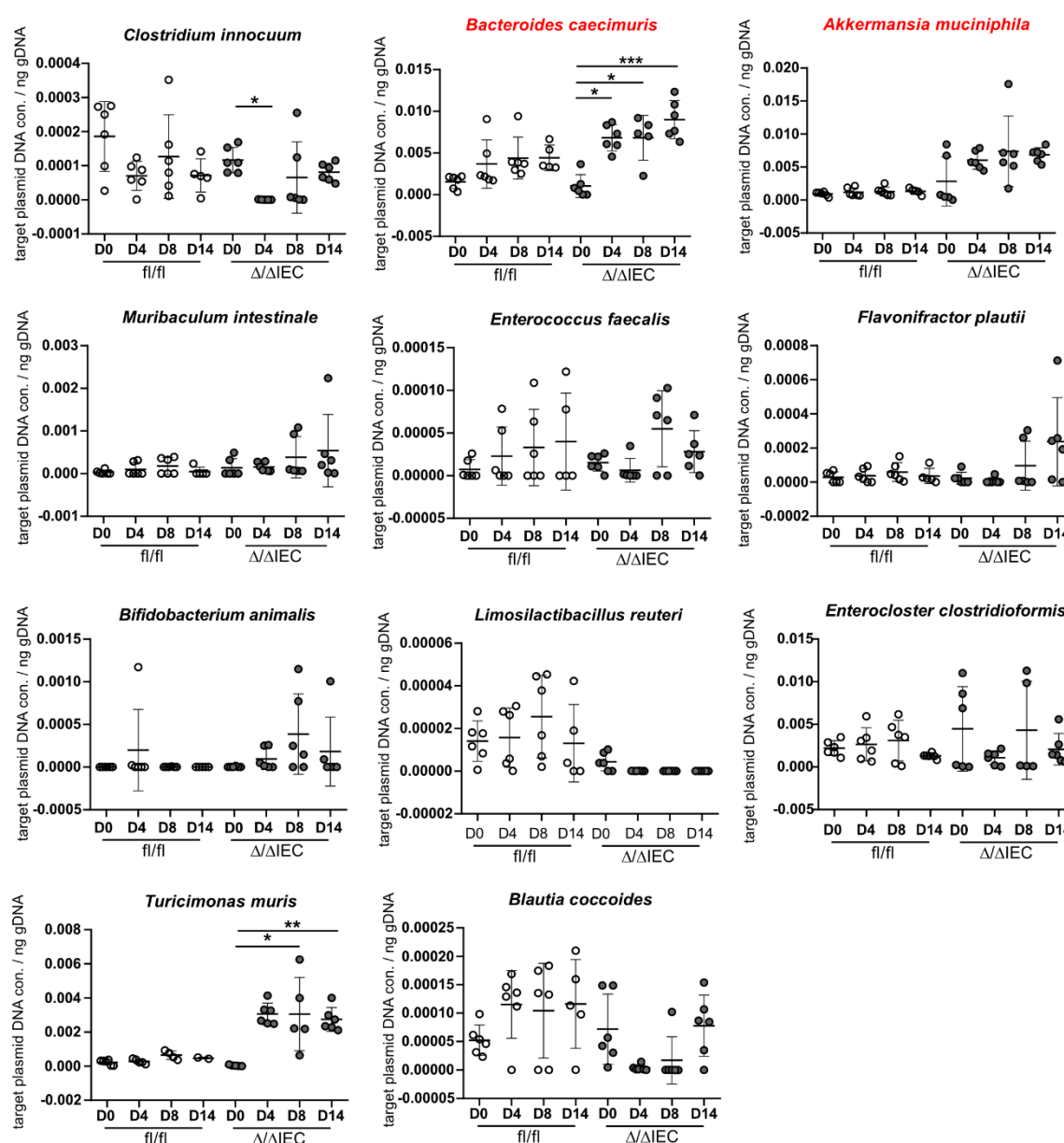
Figure 45: *Bacteroides caecimuris* is increased during metabolic injury.
Relative abundance of the twelve different bacterial species of the OMM[12] consortium in colonized Hsp60[Δ/ΔIEC] mice (Ctrl: Hsp60^{fl/fl}) measured in feces detected by 16S targeted qPCR at days (D) 0, 4, 8, and 14. Statistics: ANOVA followed by pairwise comparison testing (Tukey). Mean ± SD, n=6. Asterisks indicate significant differences *P<0.05, **P<0.01, ***P<0.001; ****P<0.0001. Dr. D. Aguanno performed the experiment and data analysis.

4.25. *Bacteroides caecimuris* induces metabolic injury

The next experiment aimed to dissect the role of specific bacteria and their metabolites in regulating metabolic injury. Hence, a mono-colonization with *B. caecimuris* (I48) was performed to examine if this single species can generate metabolic injury. In addition, a dual-colonization of *B. caecimuris* (I48) and *Akkermansia muciniphila* (YL44) was performed. Third, a mono-colonization with *L. reuteri* (I49) as a control was conducted. Mice were rectally gavaged twice at the age of 6 weeks, the same experimental setup as under SPF and GF conditions was used following colonization, and mice were sampled on day 8 (Figure 46A). Weight development of colonized Hsp60$^{\Delta/\Delta IEC}$ mice was significantly reduced from day 0 to 4 compared to tamoxifen exposed colonized Hsp60$^{fl/fl}$ control mice (Figure 46B). However, there was no significant difference in weight under GF conditions. Interestingly, the absolute body weight was significantly reduced in Hsp60$^{\Delta/\Delta IEC}$ mice colonized with *B. caecimuris* but not in the other two selective colonizations (Figure 46C).

Quantification of bacterial concentration as detected by I48, I49, and YL44 target plasmid DNA per gram feces confirmed successful colonization, with bacterial abundances unchanged between both genotypes in all three colonizations (Figure 46D-F). It is interesting to note that the presence of *A. muciniphila* reduced the bacterial abundance of *B. caecimuris* by half.

Additionally, gene expression analysis of colonic tissue showed that *Hsp60* levels were almost recovered at day 8, similar to other housing conditions. Moreover, MT-UPR signaling (*Trb3* but not *Chop*) was still increased, and *Lgr5* decreased, indicating reduced stemness following mitochondrial dysfunction (Figure 46G). Interestingly, *Lgr5* levels depicted a slight but insignificant increase in the dual-colonization in Hsp60 deficient mice, suggesting that adding *A. muciniphila* supports stemness (Figure 46H).

Interestingly, the metabolic genes *Hk2, Pdk4,* and *Cox-I* were unchanged in Hsp60$^{\Delta/\Delta IEC}$ mice colonized with *B. caecimuris*. While *Cox-I* stayed unaltered in the dual-colonization, *Pdk4* and *Hk2* gene expression levels were significantly elevated in the presence of *B. caecimuris* and *A. muciniphila* (Figure 46I). These data indicate that one or two bacterial species are enough to alter specific aspects of IEC metabolism.
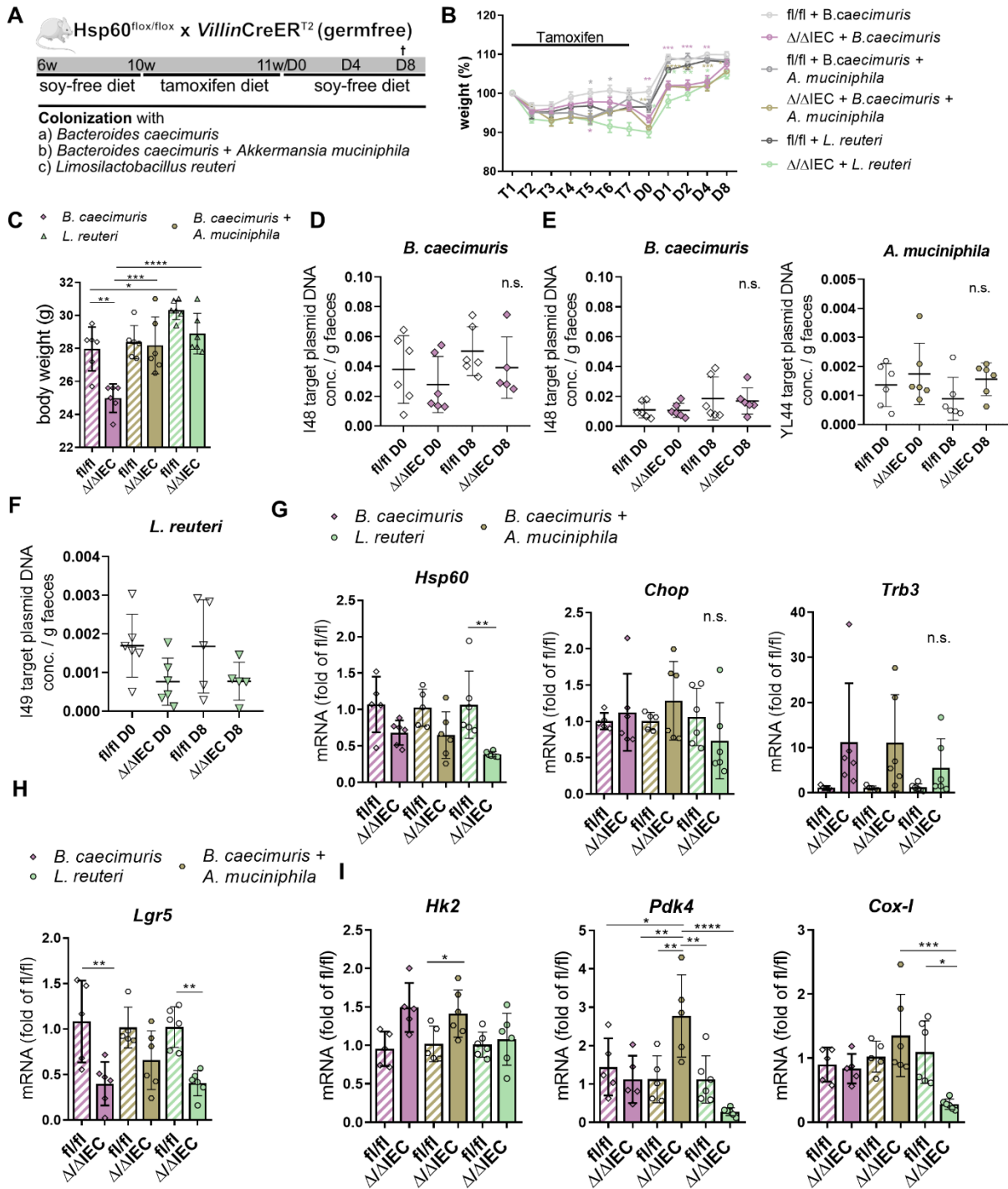
Figure 46: Selective colonization with _B. caecimuris_ does not alter MT-UPR signaling and stemness.

(A) Experimental setup. Mice were colonized with a) _Bacteroides caecimuris_, b) _Bacteroides caecimuris and Akkermansia muciniphila,_ or c) _L. reuteri_ at the age of 6 weeks. This was followed by an IEC-specific deletion of Hsp60 (Hsp60^Δ/ΔIEC mice, Ctrl: Hsp60^fl/fl) by oral feeding with tamoxifen supplemented food. Mice were sacrificed at day (D) 8 after end of tamoxifen treatment and full Hsp60 deletion. **(B)** Weight curves of colonized Hsp60^Δ/ΔIEC and Hsp60^fl/fl mice from the start of tamoxifen feeding until D8. **(C)** Absolute body weight of mice with different colonizations at the sampling time point day (D) 8. **(D,E)** Relative abundance of bacterial species in feces detected by 16S targeted qPCR at day (D) 0 and 8. mRNA expression levels of colonic tissue for **(F)** _Hsp60_, MT-UPR relevant genes (_Chop,Trb3_), stemness (_Lgr5_) and **(G)** metabolic genes (_Hk2, Pdk4, Slc37a2, Cox-I_). Statistics: (B) Multiple t-test using the Two-stage linear step-up procedure of Benjamini, Krieger and Yekutieli. (C-G) ANOVA followed by pairwise comparison testing (Tukey). Mean ± SD, n=6. Asterisks indicate significant differences *P<0.05, **P<0.01, ***P<0.001; ****P<0.0001.

Most importantly, histological analysis of colonic tissue revealed that colonization with *B. caecimuris* induced metabolic injury in the distal colon of Hsp60$^{\Delta/\Delta IEC}$ mice (Figure 47A,D), indicating that one specific bacterial species is sufficient to generate a pathological phenotype. Interestingly, adding *A. muciniphila* prevented the induction of metabolic injury, making this bacterial species and its metabolites an essential target in treating intestinal pathologies (Figure 47B). In line, *L. reuteri* did not induce metabolic injury, proving that the general presence of bacteria is insufficient to trigger metabolic injury. It is essential to mention that metabolic injury was induced in the presence of *B. caecimuris* in the proximal colon and ileum in a similar manner than under germfree conditions (Figure 47B,C,E,F), indicating that metabolic injury in these segments is genetically driven and not dependent on bacterial signals. However, adding *A. muciniphila* diminished the level of aberrant epithelial architecture in the proximal colon to levels lower than under germfree conditions (Figure 47D), again highlighting the beneficial potential of this bacterial species.

Concluding, these data demonstrate a link between a single bacterial species and the generation of an aggressive environment. They provide convincing evidence that *B. caecimuris* is directly involved in regulating the level of epithelial injury in the distal colon, which can be reversed by adding *A. muciniphila,* making it a potentially beneficial bacteria that might be used to treat patients.

Figure 47: *B. caecimuris* induces metabolic injury.

Representative H&E stained sections of **(A)** distal colonic swiss roles, **(C)** proximal colonic swiss roles, and **(E)** ileal swiss roles and corresponding higher magnifications for colonized (*B. caecimuris*, *B. caecimuris + A. muciniphila* or *L. reuteri*) Hsp60$^{\Delta/\Delta IEC}$ mice on day (D) 8 (scale bars = 200µM). Tissue from **(B)** distal colon, **(D)** proximal colon, and **(F)** ileum were scored histologically for an aberrant epithelial architecture. Statistics: One-way ANOVA followed by pairwise comparison testing (Tukey). Mean ± SD, n=6. Asterisks indicate significant differences *P<0.05, **P<0.01, ***P<0.001; ****P<0.0001.
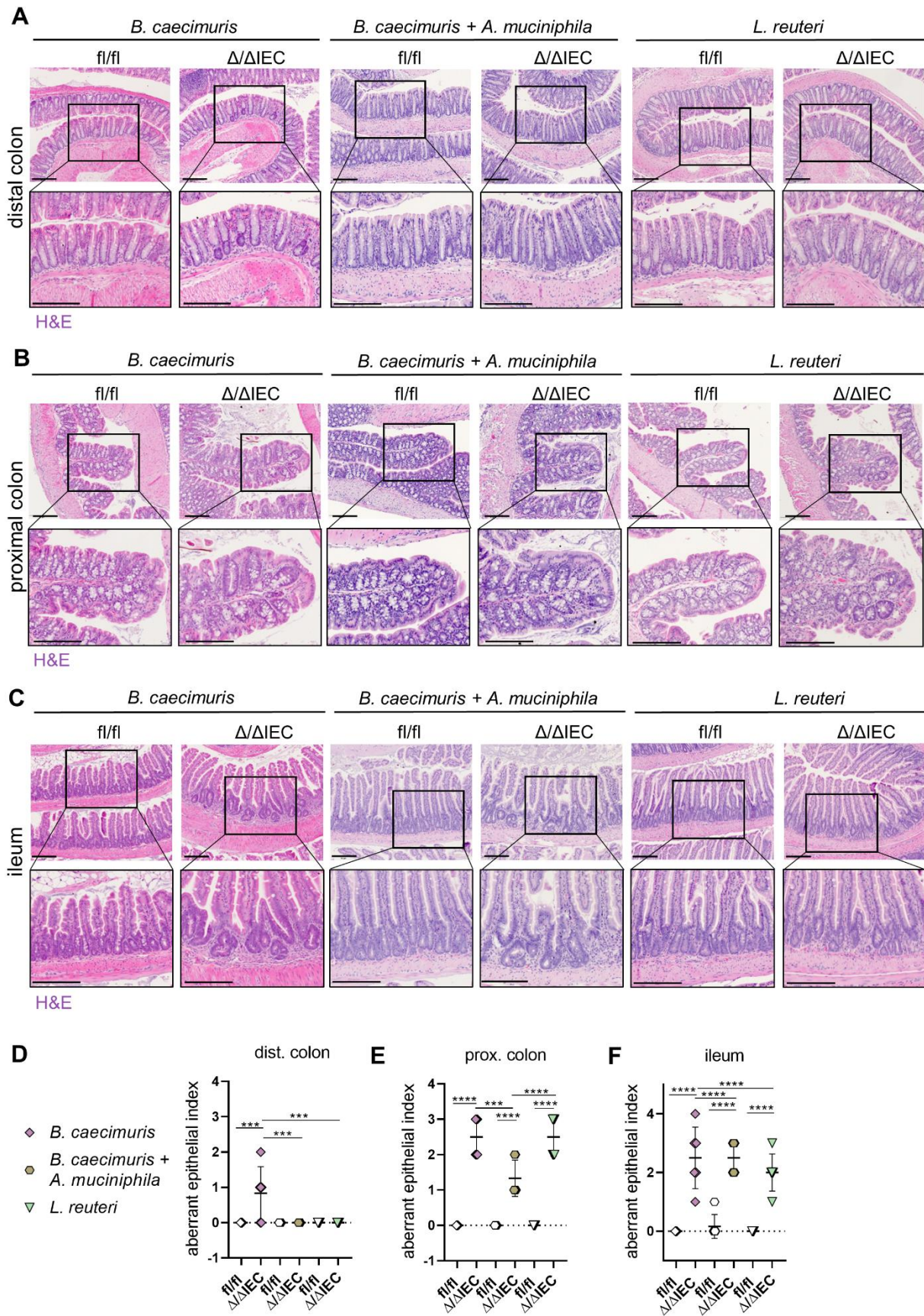
Figure 47: *B. caecimuris* induces metabolic injury.
(Figure legend previous page)

Furthermore, Hsp60 IHC staining revealed a partial regain of Hsp60 at day 8 in the distal colon in all three colonizations (Figure 48A,B), similar to germfree and SPF conditions. Of note, Hsp60 expression recovered slower in the proximal compared to the distal colon (Supplementary figure 15A,B).
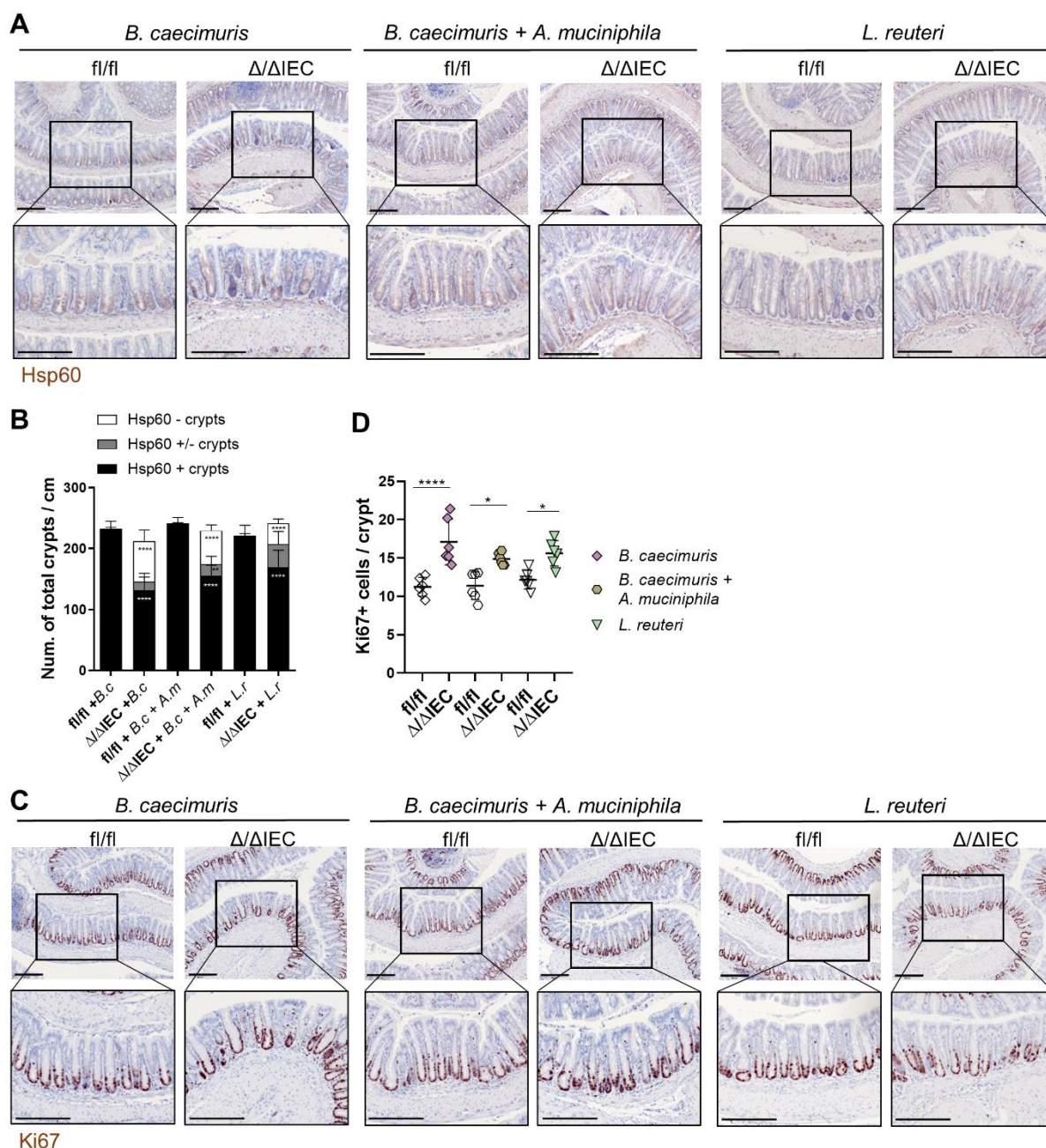

Figure 48: *B. caecimuris* includes a mild increase in proliferation.
(A) Representative immunohistochemically stained colonic swiss rolls for Hsp60 and corresponding higher magnifications for selective colonized Hsp60$^{\Delta/\Delta IEC}$ mice on day (D) 8 (scale bars = 200µM). **(B)** Quantification of Hsp60 positive and negative crypts. **(C)** Representative immunohistochemically stained colonic swiss rolls for Ki67 and corresponding higher magnifications for colonized Hsp60$^{\Delta/\Delta IEC}$ mice on day (D) 8 (scale bars = 200µM). **(D)** Quantification of Ki67 positive cells per crypt. Statistics: (D) One-way or (B) two-way ANOVA followed by pairwise comparison testing (Tukey). Mean ± SD, n=6. Asterisks indicate significant differences *P<0.05, **P<0.01, ***P<0.001; ****P<0.0001.

In parallel to a regain of Hsp60, increased proliferation in the distal colon was observed in all three colonizations, which did not significantly differ from germfree conditions. Still, a tendency towards an increase with *B. caecimuris* was shown (Figure 48C,D). The proximal colon revealed a similar picture, however, the dual-colonization significantly reduced proliferation compared to germfree conditions and *B. caecimuris* colonization (Supplementary figure 15C,D), supporting again the protective effect of this bacterial species.

Since the immune cell recruitment observed under SPF conditions was diminished under germfree housing, this aspect was further investigated in the colonization experiments. In line with the induction of metabolic injury via *B. caecimuris*, an increase in MLN weight was observed, which was milder in the other two colonizations (Figure 49A). Except for a slight decrease in cecum weight and an increase in pancreas weight with *B. caecimuris,* no other organs depict a difference (Supplementary figure 16).

Gene expression analysis of the inflammatory marker *Tnf* and *Saa3*, which were strongly induced under SPF conditions, showed no significant differences between genotypes and germfree housing (Figure 49B). Of note, *L. reuteri* reduced *Tnf* and *Saa3* without Hsp60. On the other hand, the tissue pathology index in the distal colon revealed an increased inflammation in the *B. caecimuris* colonization compared to germfree conditions, which was reversed upon colonization with both *B. caecimuris* and *A. muciniphila* (Figure 49C). The specificity of *B. caecimuris* as an inducer of a low-grade inflammation was also shown in the absence of inflammation in the *L. reuteri* colonization. Inflammation in the proximal colon, however, was increased similarly than under germfree conditions. (Figure 49C). In comparison to germfree, OMM[12], and SPF conditions, *B. caecimuris*-induced inflammation in the distal colon can be placed on an intermediate level between germfree and OMM[12], indicating that similar to the aberrant epithelial architecture, the complexity of the microbiota determines the injury intensity. In line, adding *A. muciniphila* reverses not only metabolic injury but also immune cell recruitment in the distal colon.

Furthermore, gene expression levels of the metabolic genes elevated during tissue injury under SPF housing were analyzed. *Ido1*, *Arg1,* and *Nos2* were elevated in the presence of *B. caecimuris* but not in the dual-colonization and *L. reuteri* colonization (Figure 49D). This indicates that *B. caecimuris* can induce the generation of kynurenines and nitric oxide, which can be inhibited in the presence of *A. muciniphila.*

These data corroborate previous findings and highlight the IEC-immune cell cross-talk in the lamina propria. An open question is whether the sustained overrepresentation of *Bacteroides* spp. in the dysbiotic bacterial community of Hsp60$^{\Delta/\Delta IEC}$;*Il10*$^{-/-}$ mice is functionally involved in

the loss of homeostatic tissue regeneration after metabolic wounding. Specific colonizations of germfree Hsp60IEC;Il10-/- mice are necessary to tackle this aspect.
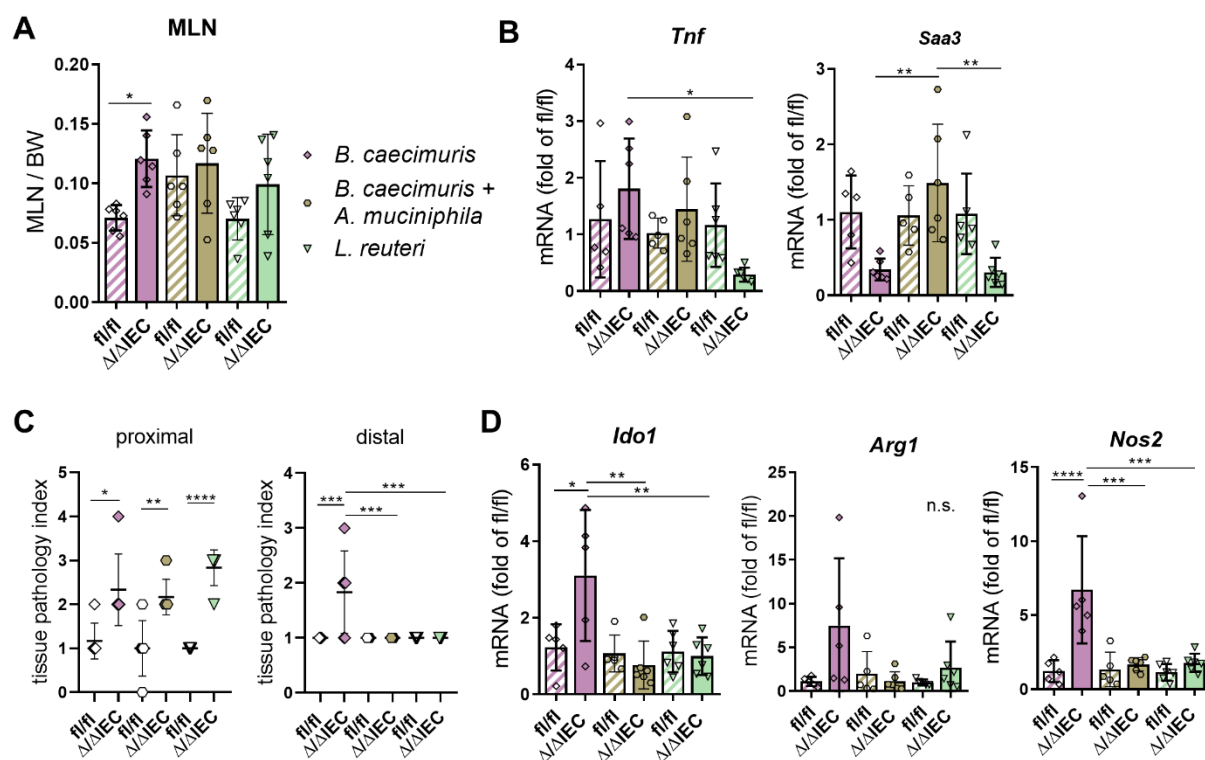

Figure 49: _B. caecimuris_ induces mild immune cell recruitment.
(A) MLN weight relative to body weight in colonized (_B. caecimuris_, _B. caecimuris_ + _A. muciniphila_ or _L. reuteri_) compared to GF Hsp60$^{\Delta/\Delta IEC}$ mice at day (D) 8. **(B)** mRNA expression levels of colonic tissue for the cytokine _Tnf_ and the systemic inflammation marker _Saa3_. **(C)** Colonic swiss roles were histologically scored for inflammation in the proximal and distal colon (range of score 0 (not inflamed) – 12 (highly inflamed. **(D)** mRNA expression levels of colonic tissue for arginine and tryptophan relates genes (_Ido1, Nos2, Arg1_). Statistics: (A-E) ANOVA followed by pairwise comparison testing (Tukey). Mean ± SD, n=6. Asterisks indicate significant differences *P<0.05, **P<0.01, ***P<0.001; ****P<0.0001.

Next to the IEC-immune system cross-talk, the microbial-host cross-talk was further investigated by staining and quantifying mucus-filled GCs. Mucus production was significantly reduced in the proximal but not distal colon of Hsp60$^{\Delta/\Delta IEC}$ mice colonized with _B. caecimuris_ or _B. caecimuris_ and _A. muciniphila_ (Figure 50A-D). However, in comparison to GF conditions, no differences were observed, suggesting that these specific bacteria do not further reduce mucus production during metabolic injury as observed under SPF housing. Notably, _L. reuteri_ led to an overall increase in mucus production in the distal but not proximal colon.
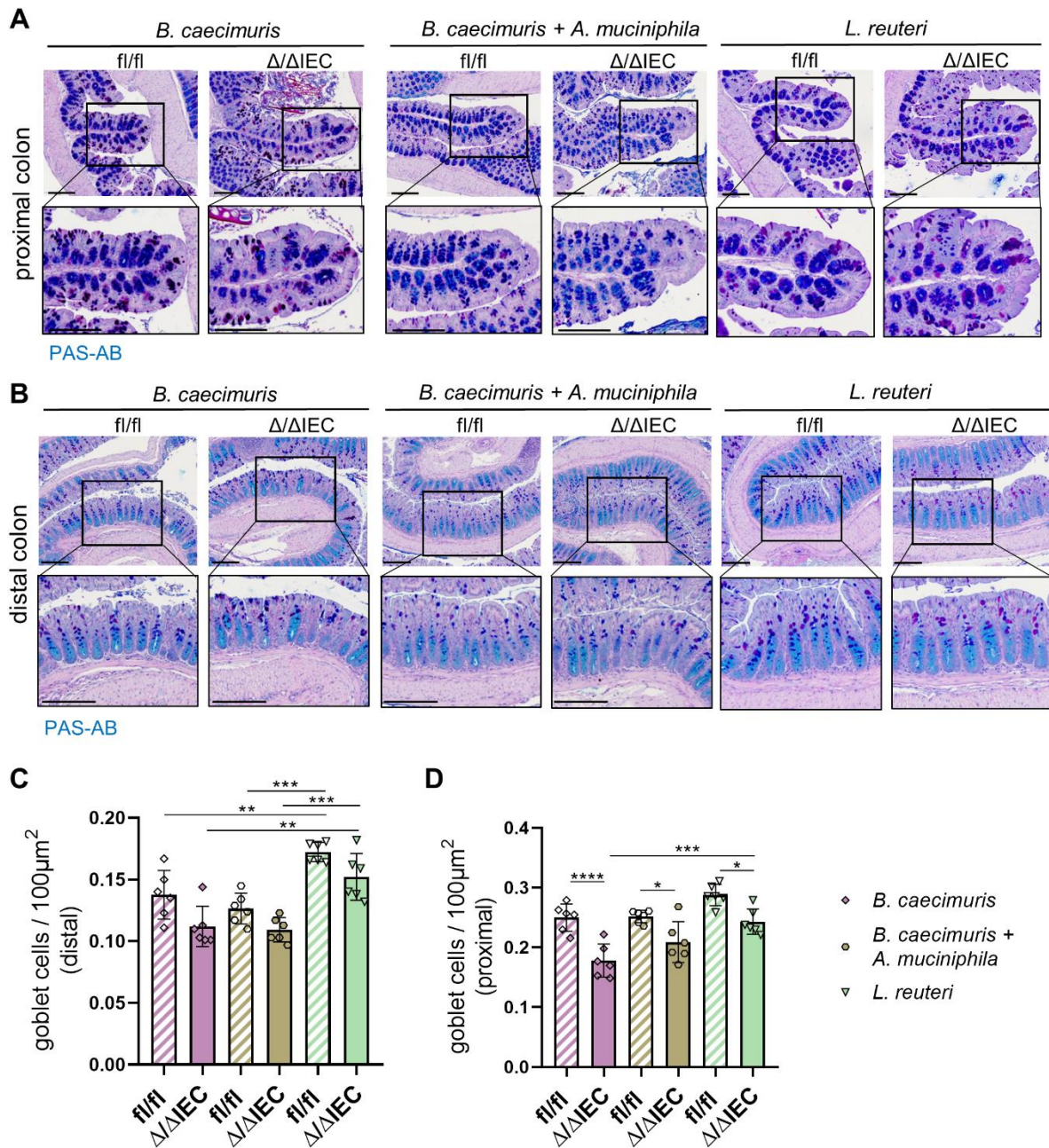
Figure 50: Bacterial colonization does not impact the number of mucus-producing goblet cells.

Representative PAS-AB stainings for mucus-filled goblet cells (GCs) of the **(A)** proximal and **(C)** distal region of colonic swiss roles and corresponding higher magnifications for colonized (*B. caecimuris*, *B. caecimuris + A. muciniphila* or *L. reuteri*) Hsp60$^{\Delta/\Delta IEC}$ mice on day (D) 8 (scale bars = 200µM). Quantification of GCs per 100µm^2 in the proximal **(B)** and **(D)** distal colon. Statistics: ANOVA followed by pairwise comparison testing (Tukey). Mean ± SD, n=6. Asterisks indicate significant differences *P<0.05, **P<0.01, ***P<0.001; ****P<0.0001.

5. Discussion

The present work aimed to understand the impact of epithelial cell metabolism on intestinal tissue homeostasis. The intestinal epithelium is an essential interface between the microbial ecosystem and the underlying mucosa, orchestrating immune-mediated and metabolic functions. Mitochondrial signaling and metabolism control the phenotype and function of IECs, and mitochondrial perturbation is associated with chronic inflammation [21]. In particular, Hsp60 deletion in murine IECs (Hsp60$^{\Delta/\Delta IEC}$) induces metabolic injury, defined as a disrupted mitochondrial metabolism accompanied by an irregular crypt architecture. While metabolic disruption causes self-resolving injury, it accelerates chronic inflammation in a susceptible host. In addition, metabolic injury initiates dysbiotic changes in the microbiota, predominantly a transient expansion of *Bacteroides* spp., which persists during inflammation. Interestingly, tissue injury is absent without bacteria, and colonization with the synthetic minimal mouse consortium OMM^{12} triggers metabolic injury and expands *Bacteroides caecimuris*. Moreover, selective mono-colonization with *Bacteroides caecimuris* causes metabolic injury, identifying this bacterial species as a critical player regulating mitochondrial metabolism and tissue homeostasis.

5.1. Mitochondrial dysfunction causes metabolic injury in the colon

Epithelial-specific Hsp60 deficiency induced MT-UPR signaling in colonocytes similar to small intestinal epithelial cells. *Chop* and its target gene *Trb3* were highly expressed at day 0 and reduced to control levels at day 8, indicating a transiently activated MT-UPR signaling pathway. These findings corroborate the model's functionality in colonocytes, similar to previously published data in small intestinal epithelial cells [77]. Interestingly, the NanoString analysis demonstrated that MT-UPR signaling induced changes in IEC metabolism, particularly amino acid synthesis, tryptophan/kynurenine metabolism, glutamine metabolism, and respiration. This aligns with previous data (generated by Dr. Emanuel Berger) showing metabolic processes to be the most regulated GO-term in a microarray analysis of colonocyte mRNA at day 2. The NanoString metabolic panel analysis is an essential extension of the microarray data, providing a higher resolution of metabolic alterations. For instance, KEGG pathway analysis at day 0 highlighted tryptophan metabolism as a significantly regulated pathway, including the significantly altered genes *Tph1, Aoc1, Kyat3, Hadh,* and *Ido1*. Tryptophan metabolism is strongly influenced by gut microbiota and diet and will thus be discussed later in detail. Another important attenuated pathway after Hsp60 deletion is respiration. Impaired OXPHOS is the underlying cause of a wide range of diseases caused by genetic alterations of

nuclear or mtDNA, increasing mitochondrial dysfunction as a recognized hallmark of distinct disorders often associated with metabolic abnormalities. For example, mitochondrial complex I deficiency is the most frequently observed enzyme defect in mitochondrial disorders [186], characterized by hampered NADH. Zielinski et al. [187] predict the metabolic flexibility of different mitochondrial respiratory chain deficiencies and identify several pathways that compensate for decreased mitochondrial NADH oxidation, including the glycerol phosphate shuttle and proline hydrogenase. In line, metabolic profiling of Leigh syndrome patients (French Canadian variant; mitochondrial respiratory chain disease due to loss-of-function mutations in *LRPPRC*) identifies a distinct metabolic signature with disturbances in lactate/pyruvate and acylcarnitine levels as well as amino acid metabolic pathways [188]. Several other studies report the role of oxidative stress and mitochondrial dysfunction in the pathogenesis of rare, inborn errors of metabolism and age-associated diseases [189-191]. This highlights that mitochondrial diseases are often associated with major critical respiration perturbations, causing energy production compensation through alternative metabolic pathways. Therefore, the mouse model is valuable for studying mitochondrial dysfunction and its impact on cellular metabolism and tissue homeostasis.

Conditional Hsp60 deletion in murine IECs revealed that impaired mitochondrial function initiated stem cell loss, followed by the subsequent appearance of a regenerative crypt architecture characteristic for intestinal injury responses [77]. While these results were obtained in the small intestine, Hsp60 deficiency was characterized in the colon. Histological evaluation of colonic tissue sections recapitulated the aberrant tissue architecture (resorption of damaged crypts and compensatory hyperproliferation) observed in small intestinal segments with a slight delay. While tissue injury was most substantial on day 2 in the small intestine, it reached its most pronounced injury phenotype on day 8 in the colon. Notably, more extended observation periods demonstrated that injury was followed by tissue reconstitution and regain of homeostasis. For the observed architectural changes, the terminology 'metabolic injury' as a self-autonomous mechanism of tissue wounding in response to mitochondrial perturbation is introduced [192]. Similar to the small intestine [77], hyperproliferative crypts were characterized by a regain of Hsp60 and an accumulation of Ki67-positive cells. The origin of these crypt foci remains unclear, however, they potentially emerge from previously derived escaper cells of unknown origin [193]. This might indicate that Hsp60+ escaper cells in the stem cell niche are hyperproliferative in response to distinct mediators from the surrounding microenvironment and injured IECs. For example, Berger et al. show that Hsp60 deficiency in IECs induces the paracrine release of Wnt-related signals, such as Rspo1 [77]. The occurrence of stem cell proliferation and disturbed crypt homeostasis has been reported in the literature under different circumstances, for instance, colorectal carcinogenesis [194] or radiation-

induced injury [195]. In the latter, surviving crypt-based columnar stem cells form new crypts by proliferative expansion and subsequent differentiation. The deletion of Hsp60 represents a comparable condition, where escaper cells proliferate, and crypts with compromised cells are resorbed. It is reasonable to assume that the survival of individual crypt-based columnar stem cells depends on the state of their cell cycle. For instance, radiated jejunal crypts depict fluctuations in radio sensitivity with maximal damage induced during mitosis [196]. Interestingly, while Lgr5+ stem cells are indispensable during radiation-induced intestinal regeneration, they are not required for repair following wounding during intestinal inflammation [197]. Consistent, Wang et al. [18] identified a colitis-associated regenerative stem cell population marked by HopX expression, arising from hypertrophic crypts to facilitate regeneration and mucosal repair in mouse models of colitis. Next to a rapid proliferation rate, these HopX+ regenerative stem cells are further characterized by co-expression of fetal-like markers, also described following DSS-induced intestinal injury [198]. Since the hyperproliferative crypts observed in the Hsp60-deficient mouse model highly expressed HopX, it can be hypothesized that they represent a specific cell population contributing to mucosal repair following metabolic injury. Due to their quiescent state, +4 stem cells expressing the marker HopX could escape Cre-mediated recombination, thus retaining their Hsp60 expression and cellular homeostasis to reestablish intestinal architecture following metabolic injury. In addition, differentiated cells can transdifferentiate into other cell types to facilitate repair. For instance, villus injury triggers transit-amplifying cells to differentiate and express fetal-like markers to restore barrier integrity [199]. Upon radiation-induced injury or chemically induced inflammation, Paneth cells are described to de-differentiate to acquire stem-like properties, causing a switch to a proliferative phenotype to ensure regenerative processes [6, 81, 82]. In line, enteroendocrine cells [200], Atoh1+ progenitors [201], Alpi+ enterocyte precursors [202], and Dll1+ progenitors [203] are shown to possess the ability to de-differentiate [204, 205], demonstrating enormous cellular plasticity of distinct IEC subpopulations.

In addition to the mouse model for metabolic injury (Hsp60$^{\Delta/\Delta IEC}$), a mouse model for mitochondrial UPR activation (ClpP$^{\Delta/\Delta IEC}$) was generated. The data revealed that IEC-specific loss of ClpP induced a milder MT-UPR signaling than the loss of Hsp60. Consistent, no tissue injury was observed, suggesting either a compensatory mechanism for the lack of one mitochondrial protease or the possibility that mitochondrial stress signaling is less critical than mitochondrial dysfunction. Prior literature shows that ClpP deletion is beneficial against diet-induced obesity, insulin resistance [206], and neurodegeneration [207]. On the other hand, ClpP deficiency induces non-alcoholic steatohepatitis (NASH) in mice [208], and chemo-activation of ClpP suppresses pancreatic ductal adenocarcinoma [209]. At a cellular level,

downregulation of ClpP in muscle cells impairs differentiation and cell proliferation [210] and induces mtDNA instability and a steady-state activation of IFN-I signaling [211]. These data and the obtained results suggest a multifactorial model where mild mitochondrial stress alone might benefit due to constant cellular alertness. In contrast, an additional trigger to mild mitochondrial stress is necessary to cause mitochondrial dysfunction and deleterious effects on tissue architecture.

5.2. The epithelial microenvironment impacts IEC metabolism

Ex vivo intestinal organoid cultures from the respective mouse models were generated to decipher cellular and molecular mechanisms. In addition, co-culture systems with intestinal mesenchymal cells and macrophages were established to dissect paracrine signaling mechanisms and model cellular communication.

Co-culture of Wt and Hsp60$^{\Delta IEC}$ organoids enhanced the growth of Wt organoids, suggesting that paracrine signals derived from metabolically injured crypts enhance proliferation and subsequent tissue healing. Since Hsp60-deficient organoids produce Wnt10a, Wnt3, Wnt4, and Wnt9b, it can be hypothesized that specific Wnt factors are responsible for the elevated proliferation and regeneration. Previously published data focusing on the small intestine of Hsp60 deficient mice demonstrate a paracrine release of Wnt-related signals from metabolically injured IECs, causing hyperproliferation of escaper cells to repopulate the epithelium [77]. In line, deletion of the Wnt target gene *Cd44* specifically in IECs, fails to increase Wnt activity and delays regeneration in DSS-treated mice [212], indicating the importance of paracrine-released Wnt for epithelial healing processes following injury. Of note, liver-specific Hsp60 deficiency results in cholangiocellular tumor formation induced by paracrine release of inflammatory and proliferative mediators [78].

In addition to paracrine signaling, fibroblasts surrounding the crypt niche are major Wnt and R-Spondin producers. Treatment of intestinal mesenchymal cells with supernatant from Hsp60$^{\Delta/\Delta IEC}$ organoids demonstrated a morphological conversion of quiescent fibroblasts into differentiated myofibroblasts, characterized by a different expression profile of growth factors. A fibroblast-organoid co-culture system revealed that these reprogrammed fibroblasts affect IEC proliferation, highlighting the cross-talk between the microenvironment and IECs during metabolic injury. This aligns with previously published data demonstrating that fibroblasts expand and produce R-Spondin3 [213] and Wnt5a [214] to facilitate epithelial regeneration after injury.

Next to mesenchymal cells, innate immune cells, including macrophages, neutrophils, and dendritic cells, are essential regulators of intestinal homeostasis. Like fibroblast, treatment of macrophages with supernatant from Hsp60$^{\Delta/\Delta IEC}$ organoids caused changes in macrophage phenotype and cytokine expression profile. Since macrophage activation entails metabolic reprogramming [215] and phenotypical modifications [216], the data indicate that signals from metabolically injured IECs activate macrophages to induce immune responses. Macrophages are a source of cytokines, growth factors, extracellular matrix components, and specific mediators that depend on the macrophage activation phenotype [217], and the cross-talk with IECs shapes their fate and cytokine profile and, therefore, contributes to inflammatory responses. While M1 macrophages exacerbate tissue injury and impair healing, M2 macrophages drive regeneration [218]. In addition, a co-culture system of macrophages with Hsp60 deficient organoids demonstrated that activated macrophages reciprocally regulate IEC metabolism and function. They dampened MT-UPR signaling, increased proliferation, and restored imbalanced metabolic enzymes, suggesting that this type of macrophages impact mitochondria and regulate tissue healing. In line, several pro- and anti-inflammatory cytokines (Tnf, IL-6, IL-22, IL-10) are shown to regulate mitochondrial metabolism [98, 105, 219] as well as intestinal stem cell activation and proliferation [95, 96, 220], highlighting epithelial – immune cell metabolic circuits [79].

5.3. Chronic inflammation is accelerated in response to metabolic injury

Under conditions of chronic inflammation, MT-UPR signaling persists throughout the intestinal epithelium with sustained expression of Hsp60 in small intestinal and colonic epithelial cells [73]. Furthermore, IBD is characterized by recurrent cycles of tissue injury and incomplete healing of IECs, making the intestinal stem cell niche and its flexible adjustment of mitochondrial metabolism imperative for tissue regeneration [79]. The Hsp60 deficient mouse model is characterized by an immediate but transient cytokine response to metabolic injury and an absence of persistent tissue inflammation. Considering these data, the mouse model for metabolic injury was crossed with IL-10 knockout mice. These mice develop colitis due to the absence of regulatory T-cells, which makes the immune system less tolerable and, thus, a useful susceptibility host. By exposing a host with mitochondrial dysfunction to a susceptible microenvironment, the aim was to identify the contribution of metabolic injury to the onset of inflammation. The central hypothesis implied that mitochondrial perturbation is the underlying (or at least strongly contributing) mechanism in inflammation-associated tissue injury. While the loss of IL-10 did not influence the amplitude of MT-UPR signaling, mice did not recover from their initial weight loss and demonstrated reduced overall survival. Importantly, 2 out of 6 mice showed an accelerated inflammatory phenotype at day 14, indicating a disrupted

regenerative response in the absence of IL-10. Since IL-10 is predominantly produced by immune cells, it can be hypothesized that the tissue environment controls healing processes. Consistent with this notion, macrophages' lack of IL-10 secretion compromises the recovery of drug (indomethacin)-induced small intestinal injury [221]. IL-10 acts on IECs via CREB-induced ß-catenin signaling, promoting epithelial cell proliferation and wound closure [103]. A closer look at the tissue pathology index in the experiment revealed that IL-10 knockout mice showed no inflammation at this early time, suggesting that mitochondrial dysfunction accelerates the onset of colitis and induces a massively increased susceptibility to chronic inflammation. Therefore, disturbed respiration due to impaired mitochondria concurrent with an unbalanced immune system is sufficient to hinder the resolution of a disturbed immune response. This is corroborated by a recent study demonstrating that Card9 deletion, specifically in neutrophils, causes mitochondrial dysfunction, leading to premature death and increased susceptibility to intestinal inflammation [222]. Furthermore, recent genome-wide association studies have explored a link between distinct IBD-related risk loci and mitochondrial gene polymorphisms [33, 223, 224]. Among these are *PPIF* [42], *SLC22A5* [225], *ATG16L1* [226], and *LRRK2* [227], adding a new aspect to the energy deficiency hypothesis [5, 79]. Overall, the pathogenesis of inflammation is a multi-hit model, where gene-environment interactions and mitochondrial functionality play an essential role.

To analyze if mild mitochondrial stress without metabolic injury is sufficient to accelerate the onset of IBD, IL-10 knockout mice were crossed with inducible IEC-specific ClpP deficient mice. Consistent with previous findings, mitochondrial impairment induced elongated crypts and a mild inflammatory phenotype. This finding is congruent with an earlier study showing reduced ClpP expression and subsequent mitochondrial stress in diet-induced NASH [208]. Compared to the model for metabolic injury, the inflammatory phenotype is milder, indicating that the level of mitochondrial perturbation might determine the amplitude of inflammation. Notably, the loss of ClpP (and IL-10) induced inflammation in the proximal colon, while lacking Hsp60 (and IL-10) localized inflammation to the distal colon.

The general picture arising from all these findings is that mitochondrial dysfunction (but not mild mitochondrial stress) impairs IEC metabolism and the regenerative capacity of the epithelium, in turn rendering the intestinal mucosa susceptible to inflammatory triggers [6, 79]. It was demonstrated that IL-10 contributes to the resolution of metabolic injury in the intestine by adapting IEC metabolism to healing. Failure of this regulatory loop disrupts control mechanisms of epithelial renewal, proliferation, and differentiation, leading to increased disease susceptibility and accelerated progression of IBD-related pathologies. Therefore, it is essential to highlight that injury not only focuses on the epithelium but also requires a tissue context.

5.4. Metabolic injury drives microbial dysbiosis and accelerates IBD

Ample evidence exists suggesting that the microbiome is sensed at the mucosal interface and that the host responds to both pathogenic and, importantly, non-pathogenic bacteria [121, 130, 228]. This microbiome-host interaction is required for intestinal tissue homeostasis, and disruption contributes to the initiation and progression of diseases such as IBD [229], GvHD [123], and type 2 diabetes [124]. An essential aspect of these studies is that all pathologies are associated with intestinal dysbiosis. While the microbiome's involvement in IBD has been intensively studied, data on the link between metabolic reprogramming and microbial composition is lacking. The experiments demonstrated that metabolic injury reduces colonic mucus production and induces a transient change in the bacterial profile, including a drop in species richness and changes in the community profile. It has been reported that several host-relevant factors, including inflammatory status, metal availability, interbacterial community structure, and xenobiotics, shape the intestinal microbiome [230]. Interestingly, an intriguing new concept suggests that reprogramming of colonocyte metabolism contributes to the dysbiotic adaptation of microbial communities [50], corroborating the hypothesis that a bi-directional cross-talk of microbiome and host at the intestinal interface impacts the cellular metabolism of IECs.

To date, not much is known indicating that metabolic alterations precede the onset of IBD, solely that IBD is associated with microbial dysbiosis that can lead to metabolic dysfunction [231]. It is still unclear if dysbiosis is the driver or a consequence of inflammation, and microbial dysbiosis's functional specificity and causes are poorly understood. The data showed that metabolic injury-induced intestinal dysbiosis is present before the onset of IBD and persists during inflammation. A closer look at the relative abundance of bacterial species during metabolic injury revealed a transient increase in *Bacteroides* spp., including *B. caecimuris, B. uniformis,* and *Phocaeicola vulgatus*, which persisted in a susceptible host. In line, numerous studies report gram-negative anaerobes, including *Bacteroides* species, to be enriched in CD [232-234] and UC [63, 235]. These data indicate that metabolic injury of the intestinal epithelium triggers dysbiotic expansion of *Bacteroides* spp., which drives chronic inflammation. Moreover, a cross-sectional study using fecal microbiota reports that a high degree of dysbiosis remains in IBD patients in remission, supporting the notion that dysbiotic patterns drive chronicity in IBD [236]. An increased luminal oxygen concentration characterizes IBD patients. In this context, it remains unclear where the increased oxygen in the gut lumen, caused by a reduced oxygen consumption of the injured epithelium, ends up and how it impacts anaerobic bacteria. Interestingly, an intraluminal oxygen gradient induces a radial gradient of microbes, with oxygen-tolerant organisms close to the mucosa and non-tolerant bacteria residing in the

lumen [237, 238]. Therefore, it can be assumed that a small fraction of mucosal adherent bacteria compensate for alterations in host oxygenation. This provides an explanation for the enrichment of aerobic and facultative anaerobes (including *Pseudomonadota* and *Actinomycetota*) in the inflamed epithelium, while obligate anaerobes (including *Bacteroides* and *Clostridiales*) prevail in fecal samples [239]. In addition to the microbe's respiration, other mechanisms exist to reduce oxygen, such as the oxidation of lipids and other organic substrates [240] or differences in intestinal vascularization [241].

5.5. Spatial contribution of bacteria to metabolic injury

To clarify the role of the microbiome on metabolic injury in response to mitochondrial perturbation, germfree Hsp60$^{\Delta/\Delta IEC}$ mice were analyzed. They showed a similar amplitude in MT-UPR activation than under SPF conditions. Still, they were characterized by a less severe weight loss, no activation of the immune system, and milder metabolic reprogramming. These data indicate that while the initial mitochondrial stress signaling is independent of bacterial signals, the reaction of IECs and their environment is influenced by bacteria. In line, the most exciting finding was that tissue aberration was mildly present in the ileum and proximal colon but absent in the middle and distal colon, providing convincing evidence that in addition to a genetic contribution in the proximal intestine, a spatial contribution of bacterial signals to metabolic injury exists.

The important question arising from this study is how bacteria orchestrate metabolic injury and a subsequent predisposition to IBD pathogenesis in a susceptible host. It can be hypothesized that compositional changes in the microbiome are associated with functional differences, including changes in bacterial-derived metabolites, which are sensed by the host and impact intestinal epithelial homeostasis. Several studies report a loss of microbial-metabolic circuits in the pathogenesis of IBD, including butyrate [58], acylcarnitine [59], purine [242], and tryptophan metabolism [61]. In line, data from the NanoString and KEGG pathway analysis revealed changes in amino acid synthesis, tryptophan/kynurenine metabolism, glutamine metabolism, and respiration under SPF conditions. Without bacteria, these metabolic alterations were attenuated, indicating the presence of cross-talk between microbes and the host (Figure 51).
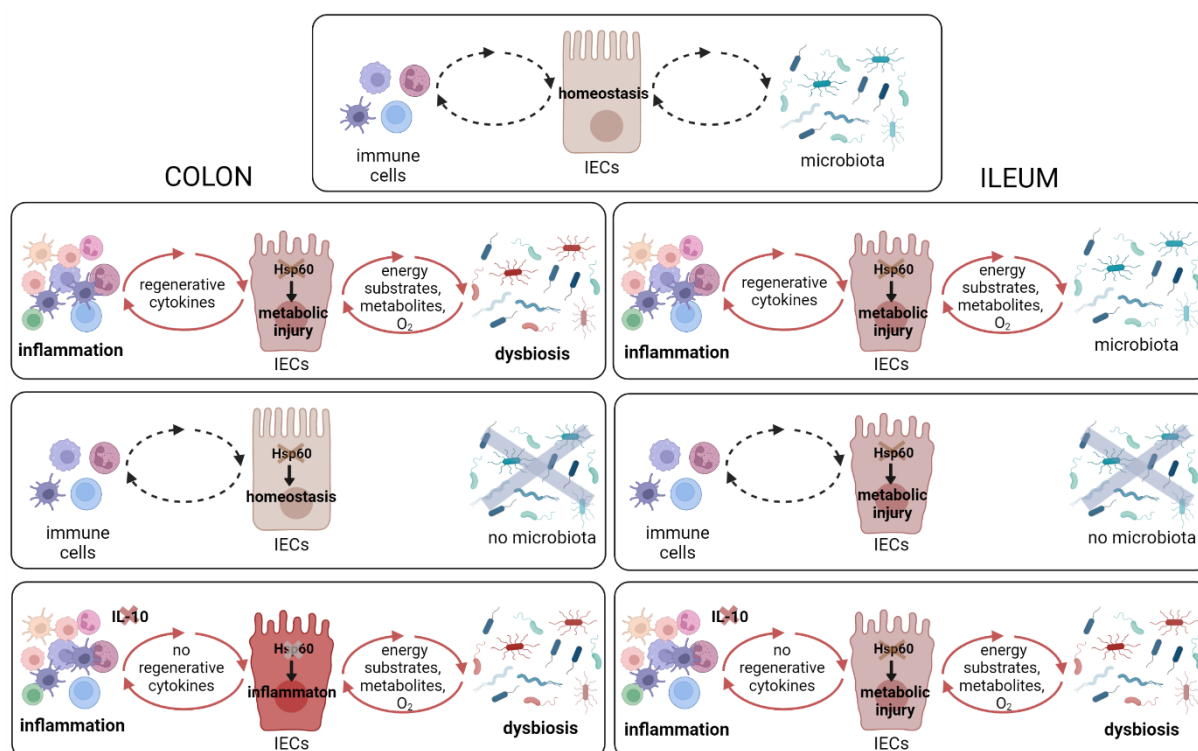
Figure 51: Overview of microbe-host cross-talks in the different mouse models.
Intestinal epithelial cells (IECs) communicate with immune cells and intestinal microbes to maintain homeostasis. Hsp60 deletion in IECs induces metabolic injury, which is associated with immune cell recruitment and altered microbial composition in the colon, leading to the production of regenerative cytokines and energy substrates/metabolites that induce healing processes. Without bacteria, Hsp60 deletion in IECs does not trigger metabolic injury in the colon, while a genetic contribution exists in the ileum. However, Hsp60-induced metabolic injury in a susceptible host accelerates chronic inflammation in the colon. Created with BioRender.com.

While small intestinal epithelial enterocytes consume predominantly glucose and glutamine for energy generation, the primary energy source of colonocytes are microbiota-derived short-chain fatty acids (SCFAs), including butyrate, acetate, and propionate [79]. Butyrate oxidation accounts for 70% of oxygen consumption to employ OXPHOS in differentiated colonocytes [243], which keeps the epithelium hypoxic and generates a metabolic barrier for proliferative progenitor/stem cells. A characteristic feature of metabolic injury in the mouse model is reduced respiration under SPF conditions, suggesting a shift from OXPHOS to glycolysis. In contrast to bacteria-exposed colonocytes, germfree colonocytes are in an energy-deprived state and rely on glycolysis for energy production [244], making them independent of fatty acid oxidation. Upon MT-UPR signaling, they do not need to switch their energy generation pathway, creating lower metabolic alterations and, thus, injury. The metabolic state and hence level of oxygen consumption of a cell before the induction of mitochondrial dysfunction may contribute to the absence of metabolic injury under germfree conditions in the distal colon.

Next to regulating genes involved in energy metabolism, butyrate further controls proliferation and differentiation, strengthens the intestinal barrier and possesses immunomodulatory functions [245]. Interestingly, germfree colonocytes demonstrate a reduced proliferative capacity, which can be reversed upon treatment with Gram-positive commensal bacteria or a mix of SCFA [246]. The absence of bacterial-derived SCFAs and thus reduced epithelial turnover in germfree colonocytes could explain the absence of metabolic injury in the distal colon of germfree Hsp60 deficient mice. Taken altogether, the mode of energy generation and rate of epithelial turnover is linked to the severity of metabolic injury (Figure 52). Small intestinal enterocytes show a rapid metabolic injury (day 2), in line with a high epithelial turnover and glutamine oxidation. Butyrate oxidizing colonocytes are characterized by an intermediate epithelial turnover rate and a delayed metabolic injury (day 8). In contrast, germfree colonocytes rely on glycolysis, possess a lower turnover rate, and show no metabolic injury.
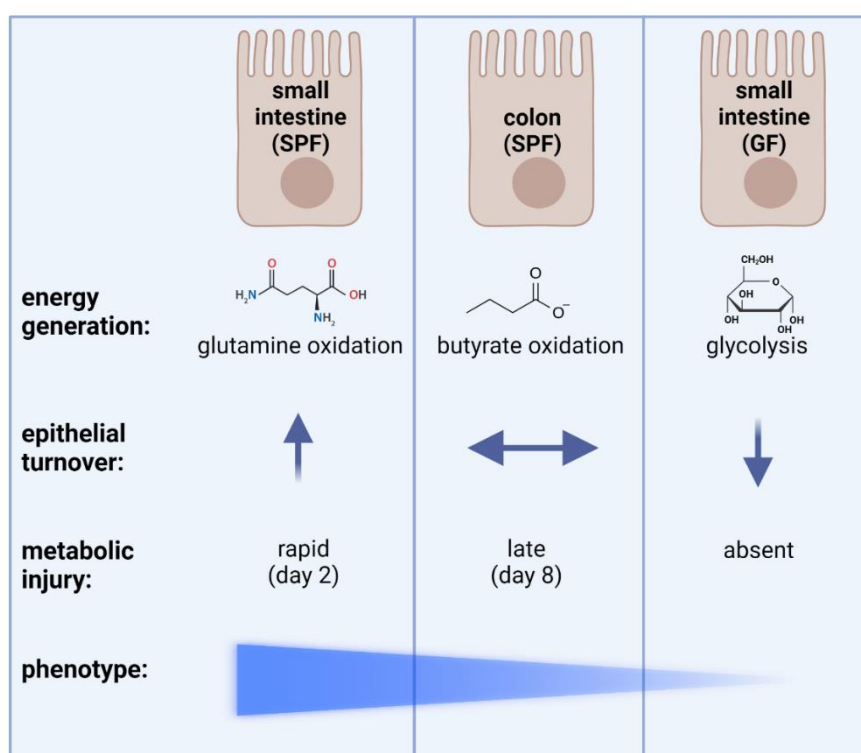
Figure 52: Energy generation and epithelial turnover impact the severity of metabolic injury in IECs.
Schematic overview of different modes of energy generation and epithelial turnover in small intestinal and colonic IECs under SPF conditions compared to colonocytes under germfree (GF) housing. Small intestinal enterocytes show a rapid metabolic injury (day (D) 2), a high epithelial turnover, and glutamine oxidation. Butyrate oxidizing colonocytes are characterized by an intermediate epithelial turnover rate and a delayed metabolic injury (day (D) 8). Germfree colonocytes rely on glycolysis, possess a lower turnover rate, and show no metabolic injury.

In addition to energy metabolism, tryptophan metabolism is essential in regulating metabolic injury. The essential amino acid tryptophan can be metabolized via three different pathways,

including the host's kynurenine and serotonin pathway and the indole pathway in bacteria. Approximately 95% of orally ingested tryptophan is catabolized through the kynurenine pathway by Ido1 in epithelial and immune cells, generating several active metabolites, including kynurenine, kynurenic acid, 3-hydroxyanthranilic acid (3HAA), and quinolinic acid [247]. As mentioned, the NanoString and subsequent KEGG pathway analysis highlighted tryptophan metabolism as a significantly regulated pathway during metabolic injury, including the significantly elevated genes *Tph1* and *Ido1*. In line, immunofluorescence staining of Ido1 revealed a transiently increased expression in the crypt base of metabolically injured (Hsp60 negative) colonocytes but not small intestinal enterocytes, indicating spatially contributing enzyme activities as a downstream mechanism of host mucosal responsiveness. It can be speculated that metabolically injured, secretory Ido1+ colonocytes set up an environment via paracrine mechanisms to support the hyperproliferation of escaper cells, similar to a small intestinal epithelial release of Wnt10a [77]. Additionally, tryptophan (4-6%) can be transformed by the gut microbiota through the indole pathway via tryptophanases [248] or tryptophan decarboxylases [249], producing indole and several indole-derived metabolites, including indole-acetaldehyde, indole-3-acetic acid (IAA) and indole-3-propionic acid (IPA). Many indole derivatives and kynurenines act as ligands for the aryl hydrocarbon receptor (Ahr) and have been shown to regulate barrier integrity [250] and immune cell homeostasis. For instance, tryptophan metabolites induce IL-22 signaling in IECs through Ahr [148], corroborating the findings showing increased IL-22 and pStat3 expression during metabolic injury. Moreover, administration of indole metabolites induces IL-10R1 on cultured intestinal epithelia through Ahr [251], and kynurenine-Ahr signaling accelerates IL-10-dependent wound closure *in vitro* [147]. This aligns with the results demonstrating that immune cells showed increased *Ido1* expression during epithelial regeneration after metabolic injury.

In parallel to decreased levels of tryptophan and its indole derivatives, fecal samples from IBD patients are characterized by increased levels of kynurenine. The authors hypothesize that kynurenine is produced by activated immune cells via Ido1, whereas indole transformation by the gut microbiota and subsequent Ahr signaling is impaired [61]. These findings agree with other studies that report a rewiring of tryptophan metabolism [252] and increased *IDO1* expression [156, 253] associated with disease activity in CD and UC patients. Moreover, a meta-analysis of transcriptome datasets from IBD patients revealed elevated kynurenine levels and downstream metabolites, including quinolinate, a substrate for NAD+ synthesis [254]. Another study shows a positive correlation between tryptophan catabolism and Graft-versus-host disease (GVHD)-associated inflammation [155]. This corroborates findings from the Hsp60;*Il10*$^{-/-}$ mice, which depicted a persistent Ido1 expression in colonocytes during inflammation. Conversely, increased tryptophan levels are the most differentiating feature in

newly diagnosed pediatric IBD patients [255]. An increased shuttle of tryptophan into the kynurenine pathway at the mucosal surface could be a way to refuel the energy deficiency in metabolically injured IECs. Moreover, this could diminish the generation of indole derivatives through the gut microbiota, impacting Ahr signaling and immune homeostasis, leading to increased intestinal permeability and bacterial translocation. Interestingly, *IDO1* expression is downregulated by butyrate in human IECs [256], indicating an influence of the microbiota on its expression levels. Consistently, germfree mice show a decrease in their kynurenine: tryptophan ratio, which is restored upon colonization [257]. This aligns with the findings that show low Ido1 levels in germfree mice during metabolic injury. Overall, these data support the concept that the microbiota provides energy substrates and signaling molecules, which affect host susceptibility to metabolic injury and healing processes, and vice versa, host responsiveness can induce adaptive changes in the microbiota.

5.6. *Bacteroides caecimuris* triggers metabolic injury

Germfree Hsp60-deficient mice were colonized with the minimal consortium OMM12 to tackle which bacteria control metabolic injury. Interestingly, tissue aberration was present in all three colonic segments, and severity levels were intermediate between GF and SPF conditions. This indicates that a defined bacterial consortium is sufficient to trigger metabolic injury. Changes in bacterial abundance highlighted an increase in *A. muciniphila* and, importantly, *B. caecimuris*, which aligns with the observed increase in *Bacteroides* spp. under SPF conditions. To elaborate on these findings, a mono-colonization of germfree Hsp60-deficient mice with *B. caecimuris* was performed. The results yielded the remarkable discovery that *B. caecimuris* induced metabolic injury in the distal colon similar to OMM^{12}, generating a link between an enriched bacteria and the generation of an aggressive environment. This provides strong evidence that a specific bacterium can manipulate colonocyte metabolism, thus affecting host susceptibility to metabolic injury and subsequent regeneration or acceleration. In line, the eradication of *Bacteroides* spp. using antibiotics has been described to be protective against colitis development in DSS-treated mice [258]. Consistently, mice with a high abundance of *Bacteroidaceae* are susceptible to DSS [259], and commensal Bacteroides induce colitis in susceptible mice [260], supporting a pathogenic role of *Bacteroides* spp. during intestinal pathogenesis.

The specific mechanism of how *B. caecimuris,* and very likely other *Bacteroides* species, induce metabolic injury remains to be elucidated. Emerging evidence suggests that gut microbes signal to the mitochondria of mucosal cells, including epithelial cells and immune cells [7], via bacterial-derived metabolites that impact mitochondrial metabolism and contribute

to tissue pathogenesis. For instance, *B. thetaiotaomicron* alters the metabolic landscape towards a gluconeogenic environment, mediating a pro-virulence effect of *C. rodentium* [261]. In line, enrichment of 12 *Bacteroides* species, including *B. caecimuris,* demonstrates a causal relationship with metabolic alterations in type-2 diabetes patients [262]. As discussed above, metabolic injury is associated with altered tryptophan metabolism in the host. In line, a tryptophan-deficient diet-induced elevated levels of systemic inflammation and microbial dysbiosis [159]. Since *B. caecimuris* is reported to produce the indole IAA *in vitro* [263], it can be hypothesized that metabolic injury is linked to alterations in tryptophan metabolism generated by microbe-host cross-talk. Interestingly, IPA but not IAA increased MT-UPR signaling in organoids similar to 3HAA, suggesting that both host-derived and bacterial-derived tryptophan metabolites can amplify mitochondrial stress signaling and might be able to aggravate metabolic injury. Contrary to this, IBD patients are characterized by reduced serum and fecal levels of several tryptophan derivatives, including IAA and IPA [61, 264]. An interesting study revealed that the microbiota from Card9 null mice, a colitis model, fails to metabolize tryptophan into AhR ligands, and inoculation with tryptophan metabolizing Lactobacillus species attenuates inflammation [61]. Moreover, 3-indol-carbinol weakens colitis through IL-22 induction, promoting butyrate-producing bacteria growth [265]. Similarly, *B. ovatus* produced IAA stimulates IL-22 secretion by immune cells, reducing chemically driven colonic inflammation in mice [266]. IAA reduces the levels of pro-inflammatory cytokines and increases the anti-inflammatory cytokine IL-10, alleviating ankylosing spondylitis, a systemic, chronic and inflammatory autoimmune disease [267]. Consistent with this notion, IPA alleviates oxidative damage accompanied by ER stress and mitochondrial dysfunction [268], reduces obesity-induced metabolic dysfunction [269], and is proposed as a potential compound for treating metabolic syndrome [270]. In contrast to this well-established protective role of indoles, a few studies report a disadvantageous role, corroborating the observed results. For instance, supraphysiological concentrations of IPA directly affect mitochondrial function in cardiomyocytes by reducing their maximal respiration and respiratory spare capacity, two indicators for mitochondrial dysfunction. Moreover, cells are less metabolically active, revealing lower proliferation rates. The authors hypothesize that IPA first increases mitochondrial capacity but eventually induces mitochondrial damage by higher, supraphysiological concentrations under cellular stress conditions [271]. In line, IPA exerts cytostatic effects by increasing oxidative/nitrosative stress via upregulation of iNos and enhancing mitochondrial ROS [272]. Indeed, gene expression levels of *iNos/Nos2* were elevated during metabolic injury under SPF conditions and *B. caecimuris* mono-colonization but not under germfree conditions. Aberrant NO signaling is a central feature of many diseases and is described to regulate oxygen consumption by affecting mitochondrial respiration [273]. Concluding, these data suggest that while physiological concentrations of indoles are

protective, higher concentrations might be able to amplify mitochondrial stress and thus have a pivotal role in impacting metabolic injury.

The link between increased bacterial-derived indole production and host Ido1 enzyme activity must still be fully elucidated. It can be assumed that the depletion of tryptophan by *B. caecimuris* increases Ido1 as a rescue mechanism for the host to diminish immune cell activation upon metabolic injury. Another possibility is that increased Ido1 might directly affect MT-UPR signaling, aiming to restore cellular homeostasis, which influences the intestinal microbiota's composition and metabolite production. This possibility is corroborated by a study showing an inverse correlation between Ido1 activity and IAA levels upon high-fat feeding in mice and a shift of tryptophan metabolism towards increased plasma kynurenine and reduced IAA levels in feces of obesity and type-2 diabetic patients [274].

Next to *B. caecimuris, A. muciniphila* was increased during metabolic injury in the OMM[12] colonization. While healthy controls are associated with beneficial unclassified *Akkermansia* spp. [236], *A. muciniphila* is reported to be reduced in IBD patients [275, 276] and can improve chemically-induced colitis in mice by exerting anti-inflammatory effects [277, 278]. Hence, it can be hypothesized that *A. muciniphila* might be increased during metabolic injury as a counter-regulatory mechanism. Indeed, Hsp60-deficient mice with a dual-colonization of *B. caecimuris* and *A. muciniphila* showed no metabolic injury in the distal colon. How *A. muciniphila* ablates the *B. caecimuris*-induced injury remains to be elucidated, however, a beneficial regulation of IEC metabolism can be assumed. For instance, *A. muciniphila* treatment increases aspartate levels in the gut, ameliorating oxidative stress-induced cell apoptosis [279]. In line, aspartate alleviates colonocyte damage by promoting ISC proliferation and differentiation via regulation of mitochondrial metabolism [280], indicating protective microbial-host cross-talk. Of note. *A. muciniphila* is tryptophanase positive, thus being able to generate indoles. This contradicts the hypothesis that indoles contribute to metabolic injury, making further research on the mechanism underlying the bacterial-driven induction of metabolic injury essential.

5.7. Conclusion and perspective

Intestinal epithelial cell metabolism emerged as a novel player in the pathogenesis of inflammation. However, the cross-talk between the intestinal microbiome and host in regulating mitochondrial function and metabolism remains elusive. Considering the metabolic requirements of the epithelial interface, it can be assumed that disruption of microbial-metabolic cross-talks and impaired metabolic flexibility of IECs contribute to the initiation and progression of tissue injury and chronic inflammation [79]. Hsp60 deletion in murine IECs induces metabolic injury, defined as a disrupted mitochondrial metabolism accompanied by an irregular crypt architecture. This injury phenotype is characterized by the loss of stemness, loss of goblet cells, as well as mucus production. While metabolic disruption causes self-resolving injury, it accelerates chronic inflammation in a susceptible host. In addition, metabolic injury initiates dysbiotic changes in the microbiota, predominantly a transient expansion of *Bacteroides* spp., which persists during inflammation. Interestingly, tissue injury is absent without bacteria, and colonization with the synthetic minimal mouse consortium OMM[12] triggers metabolic injury and expands *B. caecimuris*. Moreover, selective mono-colonization with *B. caecimuris* causes metabolic injury, identifying this bacterial species as a critical player regulating mitochondrial metabolism and tissue homeostasis.
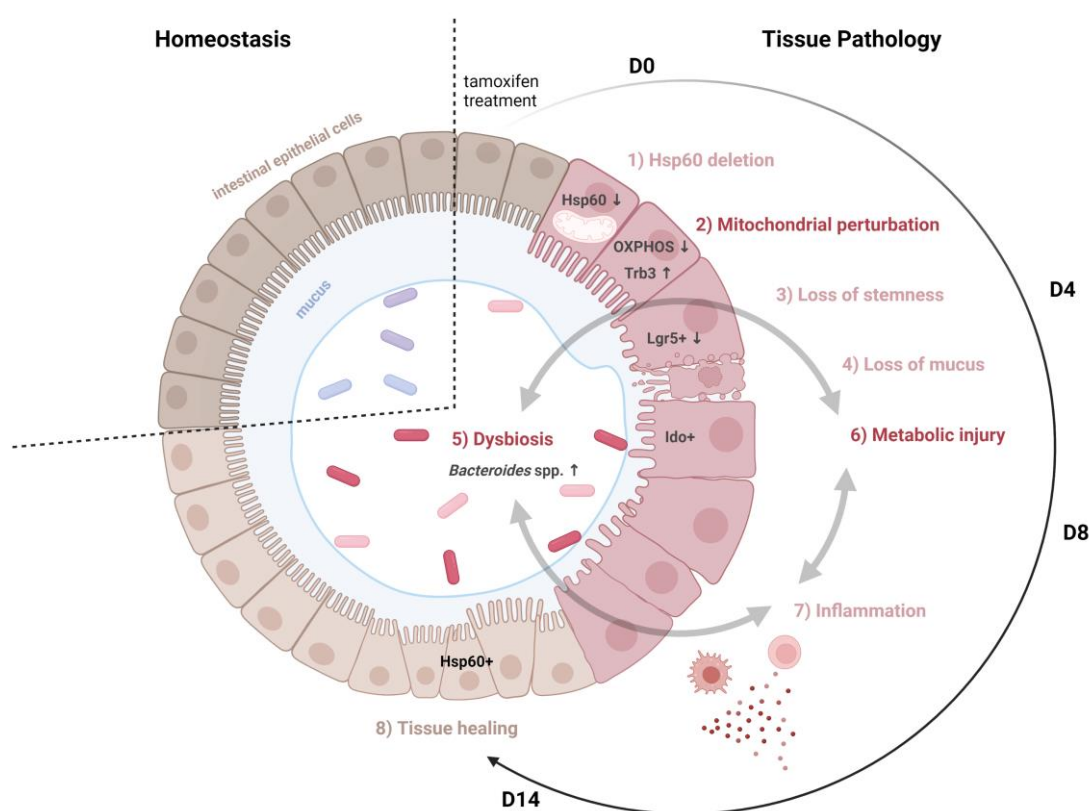
Figure 53: Graphical summary.
(Figure legend next page)

Hsp60 deletion is induced in intestinal epithelial cells by tamoxifen feeding and is complete at day 0, leading to mitochondrial perturbation in Hsp60-negative cells. Colonocyte metabolism shifts towards decreased OXPHOS and increased glycolysis, while MT-UPR is induced (marker: Trb3) as an early response to Hsp60 loss. Progressively at day 4, intestinal crypts display a loss of stemness due to the disappearance of Lgr5+ intestinal stem cells and a weakening of the mucus barrier. In parallel, dysbiotic changes occur in the intestinal lumen, notably the expansion of *Bacteroides* spp.. Indeed, all these changes lead to tissue injury at day 8 in the colon, characterized by hyperproliferative crypts and resorption of damaged crypts (referred to as metabolic injury) that are Ido1 positive. The injury phenotype is accompanied by immune cell recruitment and loss of inflammatory regulatory mechanisms in a colitis-susceptible model. Gain of Hsp60 through the repopulation of the epithelium by Hsp60-positive escaper cells progresses at day 14 before reaching a homeostatic state. Created with BioRender.com.

D: day; Hsp60+: heat shock protein 60-positive; Lgr5+: Leucine-rich repeat-containing G-protein coupled receptor 5-positive; AhR: aryl hydrocarbon receptor; OXPHOS: oxidative phosphorylation; MT-UPR: mitochondrial unfolded protein response; Trb3: Tribbles pseudokinase 3; Ido1: indoleamine 2, 3-dioxygenase 1.

Several future directions are promising to expand the understanding of the interactions between microbes and the host, particularly mitochondria, at mucosal surfaces and its impact on intestinal homeostasis and disease development. To identify the exact molecular mechanism underlying *B. caecimuris*-induced metabolic injury, identifying specific metabolites and *in vivo* induction of metabolic injury caused by a single metabolite or a combined cocktail could be an approach. In addition, it is essential to characterize Hsp60-deficiency in a pro-inflammatory environment under germfree conditions and analyze if *B. caecimuris* colonization alone can induce inflammation following metabolic injury. From a therapeutic perspective, different approaches modulating mitochondrial metabolism or tackling microbial composition and metabolic function might represent attractive strategies to improve metabolic injury during inflammation. For instance, focusing on bacterial-derived components targeting mitochondria or repurposing metabolic drugs to manipulate mitochondrial metabolism may be beneficial. Moreover, the delivery of recombinant enzymes manipulating specific metabolic pathways could represent an exciting approach. In addition, phage therapy or specific bacterial eradication therapies might offer a possible alternative to tackle microbial dysbiosis during chronic or recurrent inflammation. In summary, the present work identified a link between microbes and mitochondrial dysfunction as a susceptibility factor in the pathogenesis of IBD. Rewiring mitochondrial metabolism may pave the way for new therapeutic strategies in the pathogenesis of intestinal inflammation.
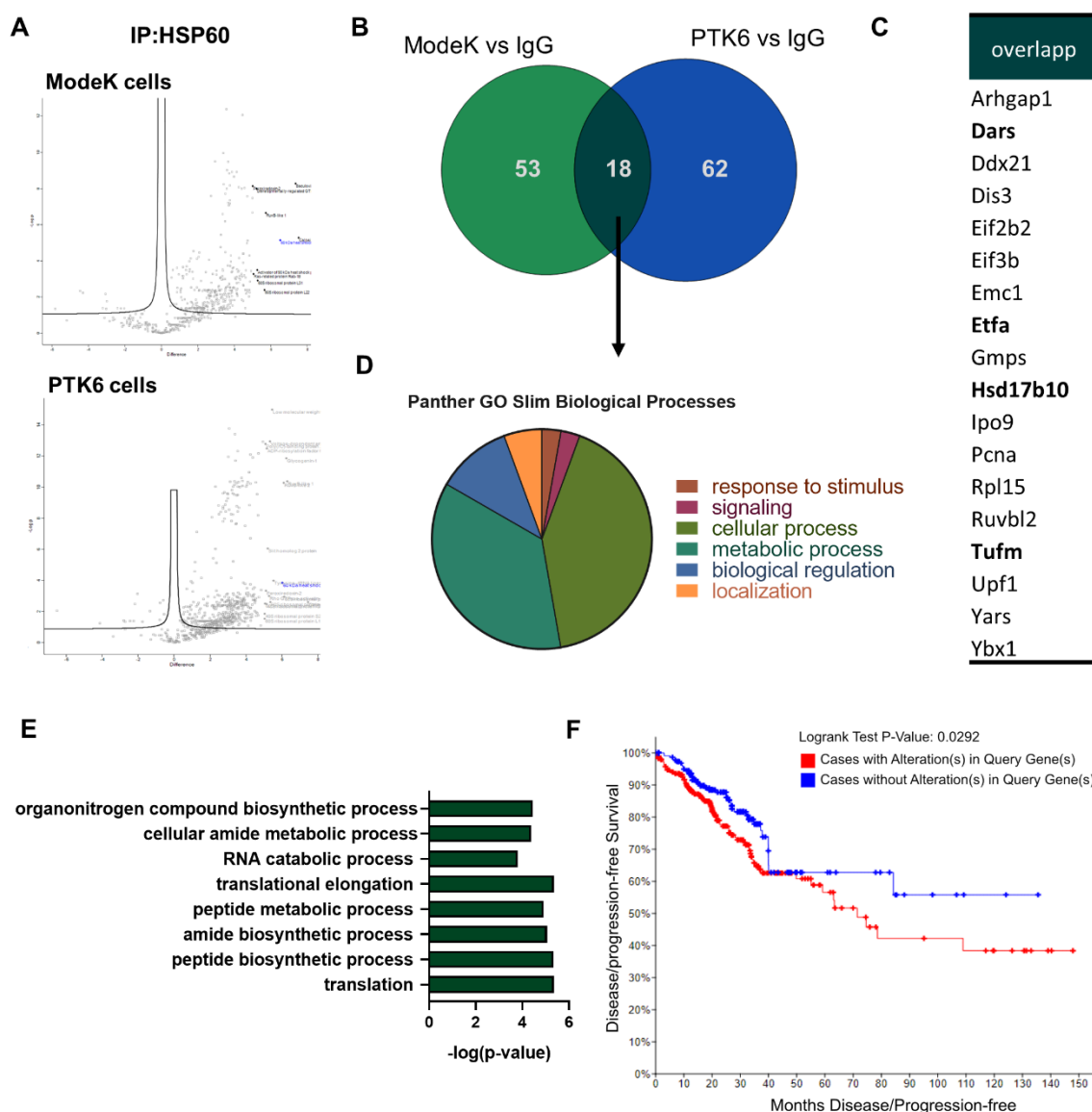
Supplement
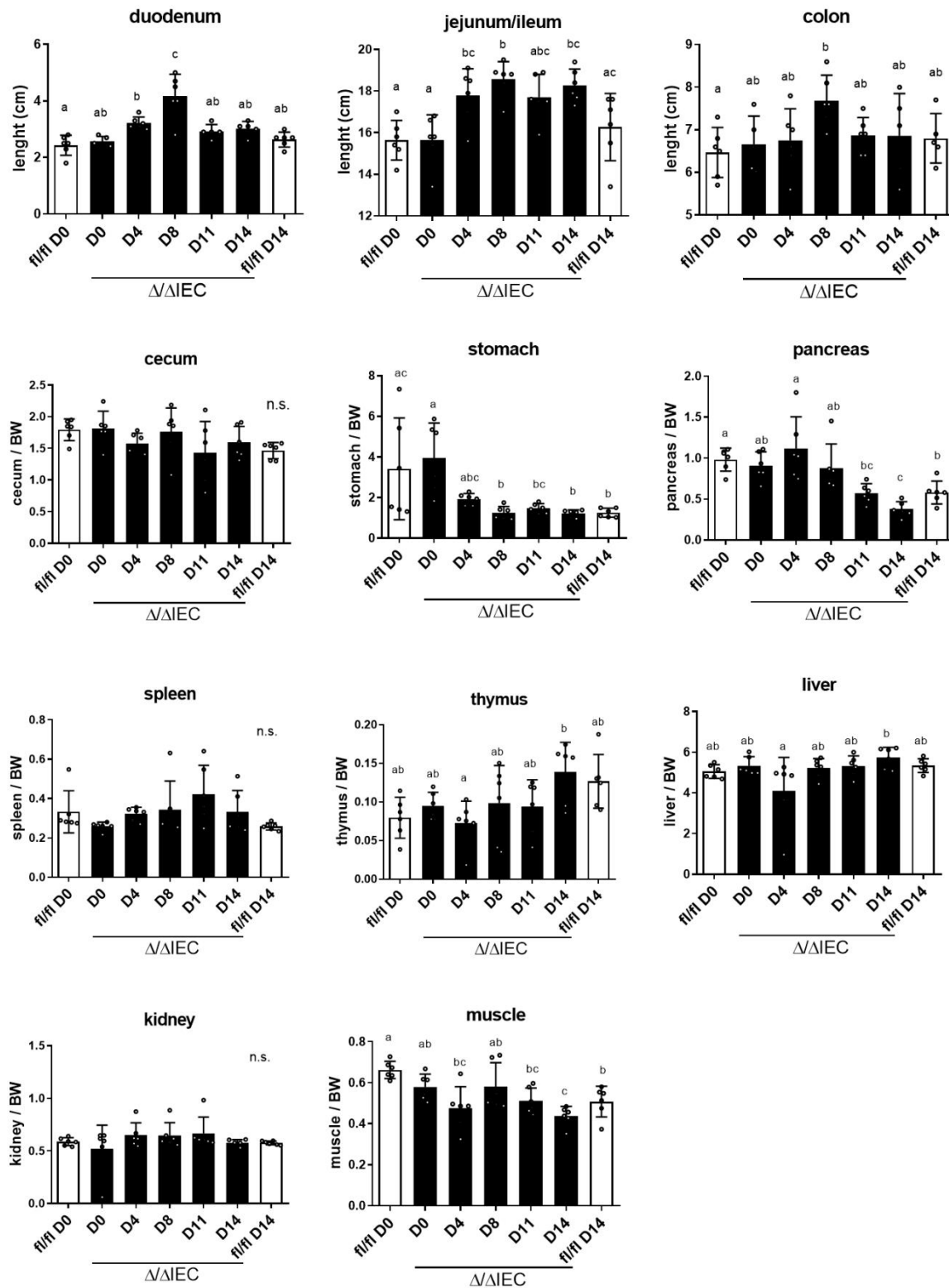
Supplementary figure 1: Organ weights from Hsp60$^{\Delta/\Delta IEC}$ mice over different time points.

Length of intestinal segments and organ weights from Hsp60$^{\Delta/\Delta IEC}$ and control (Hsp60$^{fl/fl}$) mice from day (D) 0 to 14. Statistics: ANOVA followed by pairwise comparison testing (Tukey). Mean ± SD, n=6.
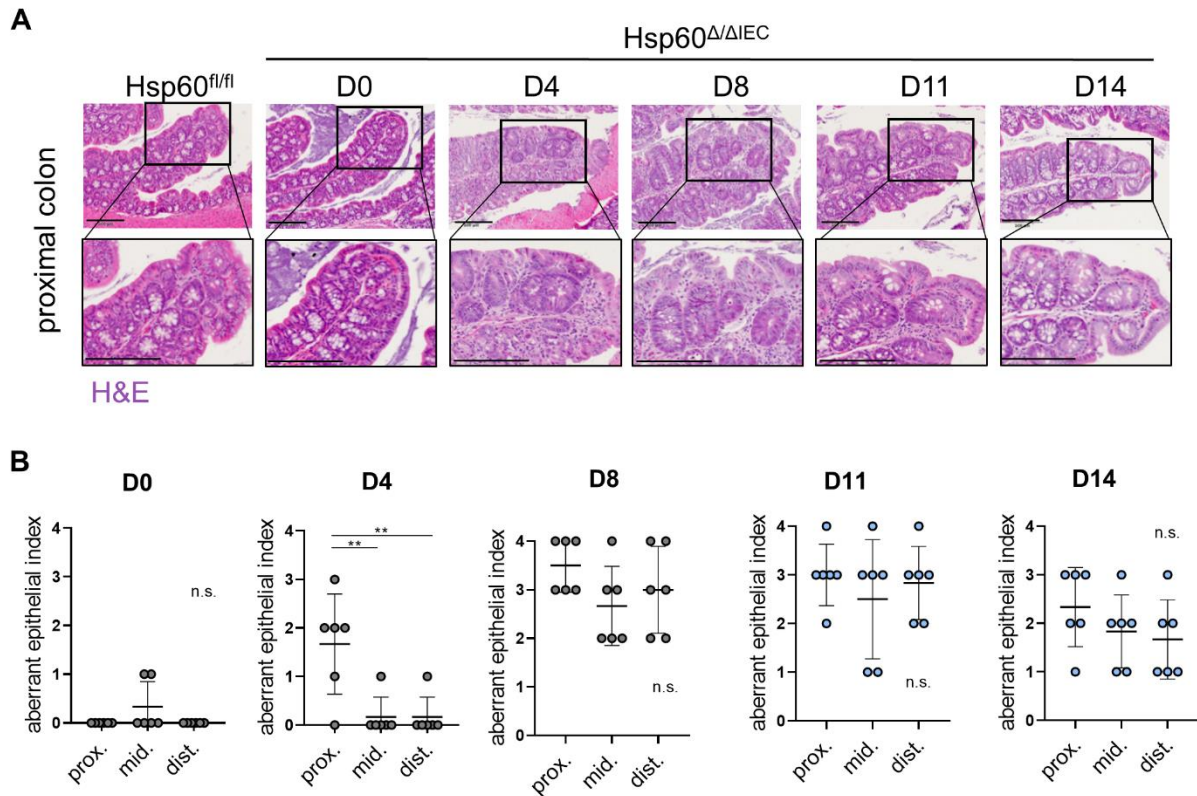
Supplementary figure 2: Histology and scores from proximal colon of Hsp60$^{\Delta/\Delta IEC}$ mice.

(A) Representative H&E stained sections of proximal colon and corresponding higher magnifications for Hsp60$^{\Delta/\Delta IEC}$ mice on day (D) 0, 4, 8 and 14 (scale bars = 200µM). **(B)** Tissue was scored histologically for an aberrant epithelial architecture in the different colonic segments (proximal, middle, and distal) over all time points. Statistics: ANOVA followed by pairwise comparison testing (Tukey). Mean ± SD, n=6. Asterisks indicate significant differences *P<0.05, **P<0.01, ***P<0.001; ****P<0.0001.

A IP:HSP60

ModeK cells

PTK6 cells

B

ModeK vs IgG   PTK6 vs IgG

53   18   62

C

overlapp
Arhgap1
Dars
Ddx21
Dis3
Eif2b2
Eif3b
Emc1
Etfa
Gmps
Hsd17b10
Ipo9
Pcna
Rpl15
Ruvbl2
Tufm
Upf1
Yars
Ybx1

D Panther GO Slim Biological Processes

- response to stimulus
- signaling
- cellular process
- metabolic process
- biological regulation
- localization

E

organonitrogen compound biosynthetic process
cellular amide metabolic process
RNA catabolic process
translational elongation
peptide metabolic process
amide biosynthetic process
peptide biosynthetic process
translation

-log(p-value)

F

Logrank Test P-Value: 0.0292
Cases with Alteration(s) in Query Gene(s)
Cases without Alteration(s) in Query Gene(s)

Disease/progression-free Survival

Months Disease/Progression-free

Supplementary figure 3: IP-MS/MS of Hsp60 binding partners reveals an involvement in cellular and metabolic processes.

(A) Vulcano plots of proteins identified by IP-MS/MS analysis of Hsp60 in the intestinal cell lines ModeK and PTK6. **(B)** Venn-diagram illustration of the number of proteins bound to Hsp60 in ModeK compared to PTK6 cells. **(C)** List of the 18 overlapping proteins between ModeK and PTK6 cells. Mitochondria-localized proteins are written in bold. **(D)** Panther GO Slim biological process analysis of the 18 overlapping proteins. **(E)** Significantly enriched biological processes identified via PANTHER overrepresentation test (FISHER). **(F)** Kaplan-Meier analysis of disease/progression-free survival of cancer patients with alterations in the 18 overlapping genes in the TCGA dataset (N=526).

123
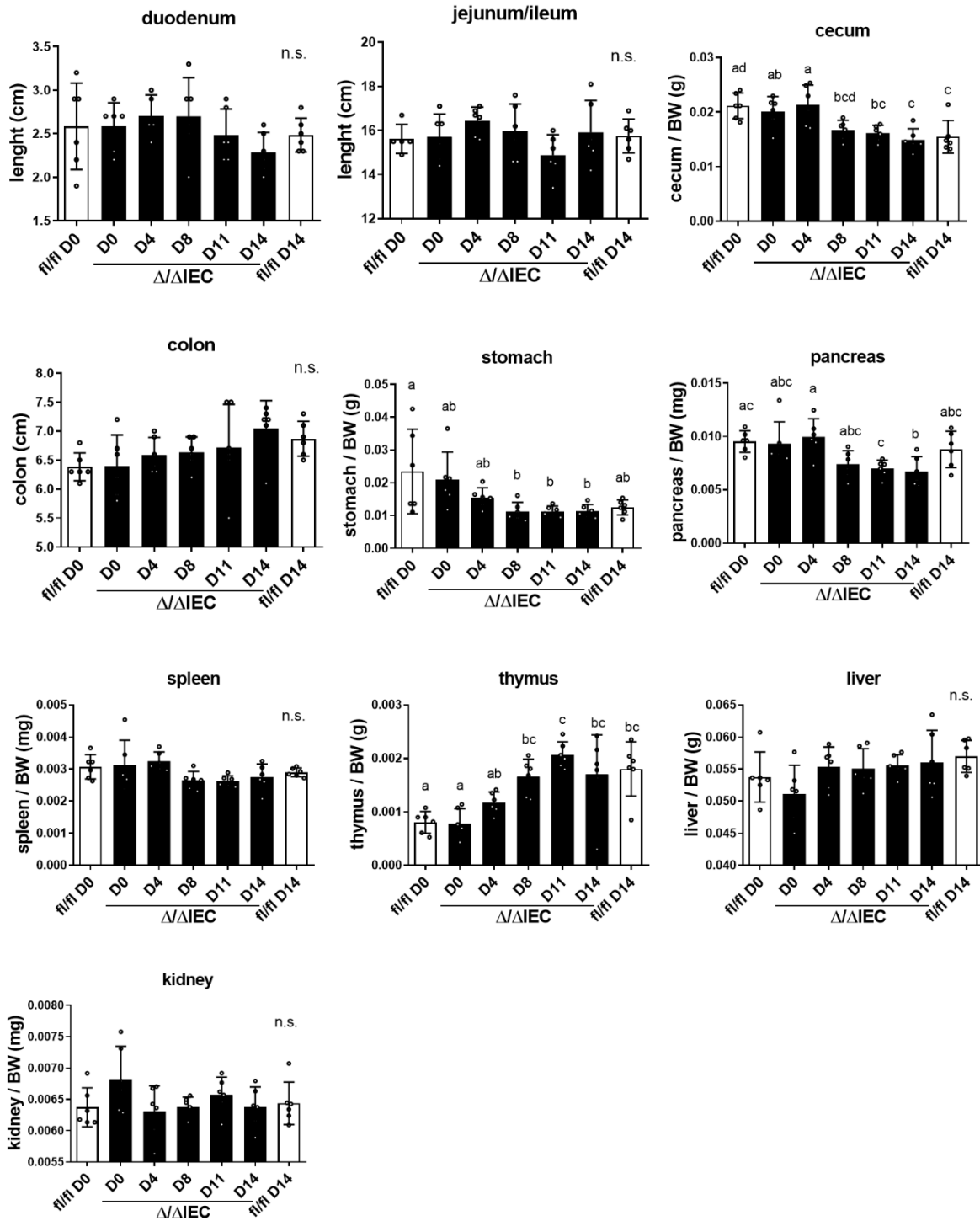
Supplementary figure 4: Organ weights from ClpP$^{\Delta/\Delta IEC}$ mice over different time points.

Length of intestinal segments and organ weights from ClpP$^{\Delta/\Delta IEC}$ and control (ClpP$^{fl/fl}$) mice from day (D) 0 to 14. Statistics: ANOVA followed by pairwise comparison testing (Tukey). Mean ± SD, n=6.
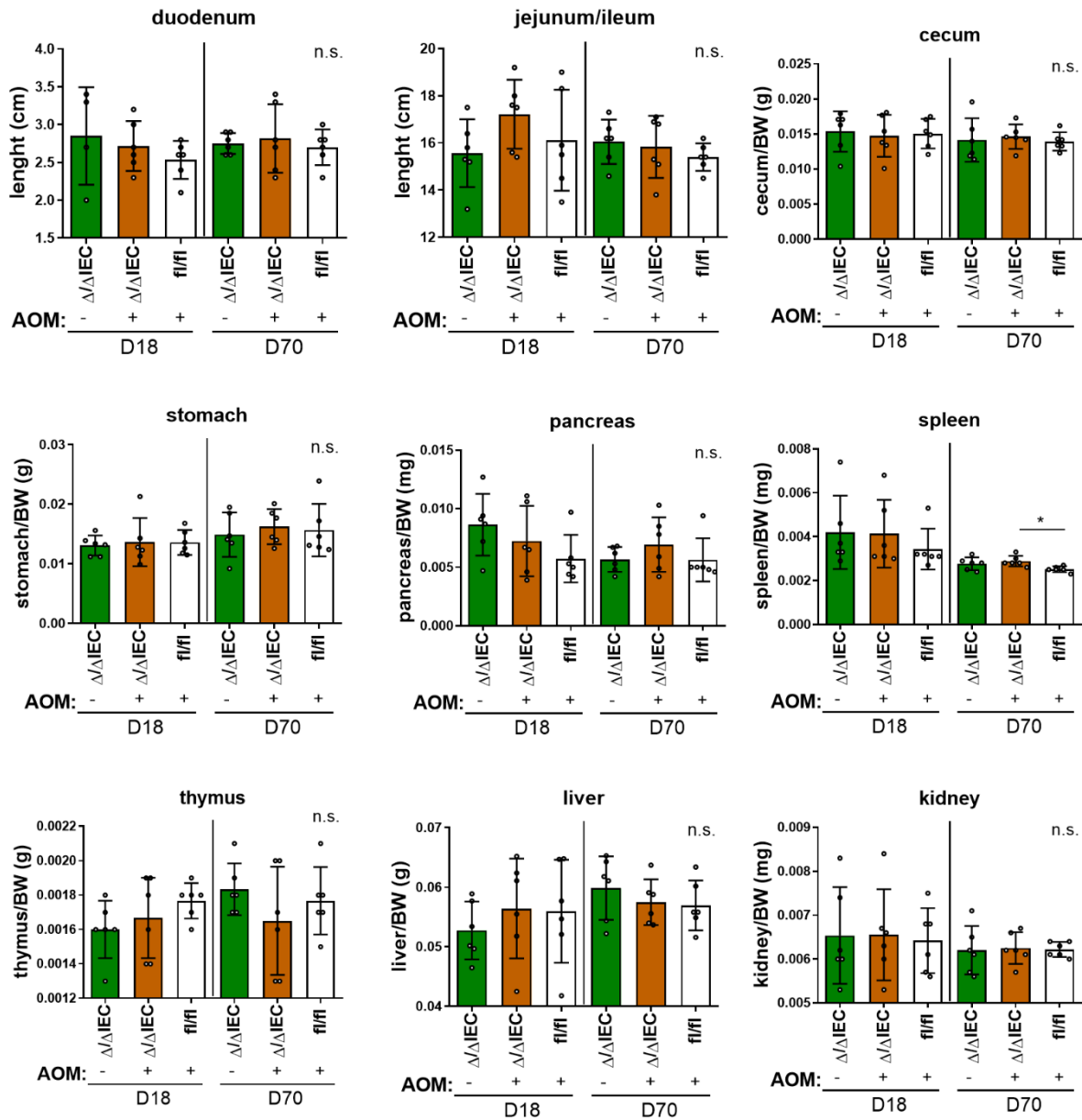
Supplementary figure 5: Organ weights from Hsp60$^{\Delta/\Delta IEC}$ mice with AOM over different time points.

Length of intestinal segments and organ weights from Hsp60$^{\Delta/\Delta IEC}$ and control (Hsp60$^{fl/fl}$) mice treated with AOM or PBS as a control from day (D) 18 and 70. Statistics: ANOVA followed by pairwise comparison testing (Tukey). Mean ± SD, n=6. Asterisks indicate significant differences *P<0.05, **P<0.01, ***P<0.001; ****P<0.0001.
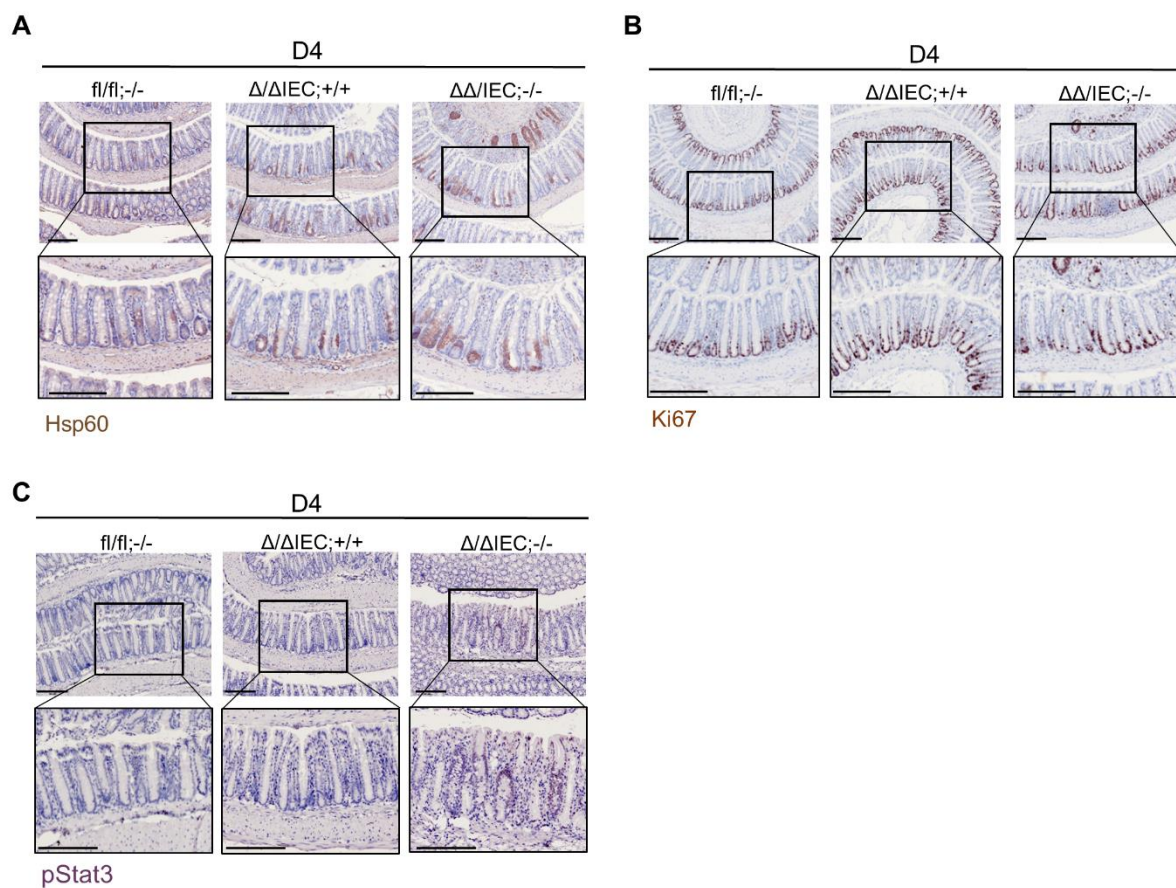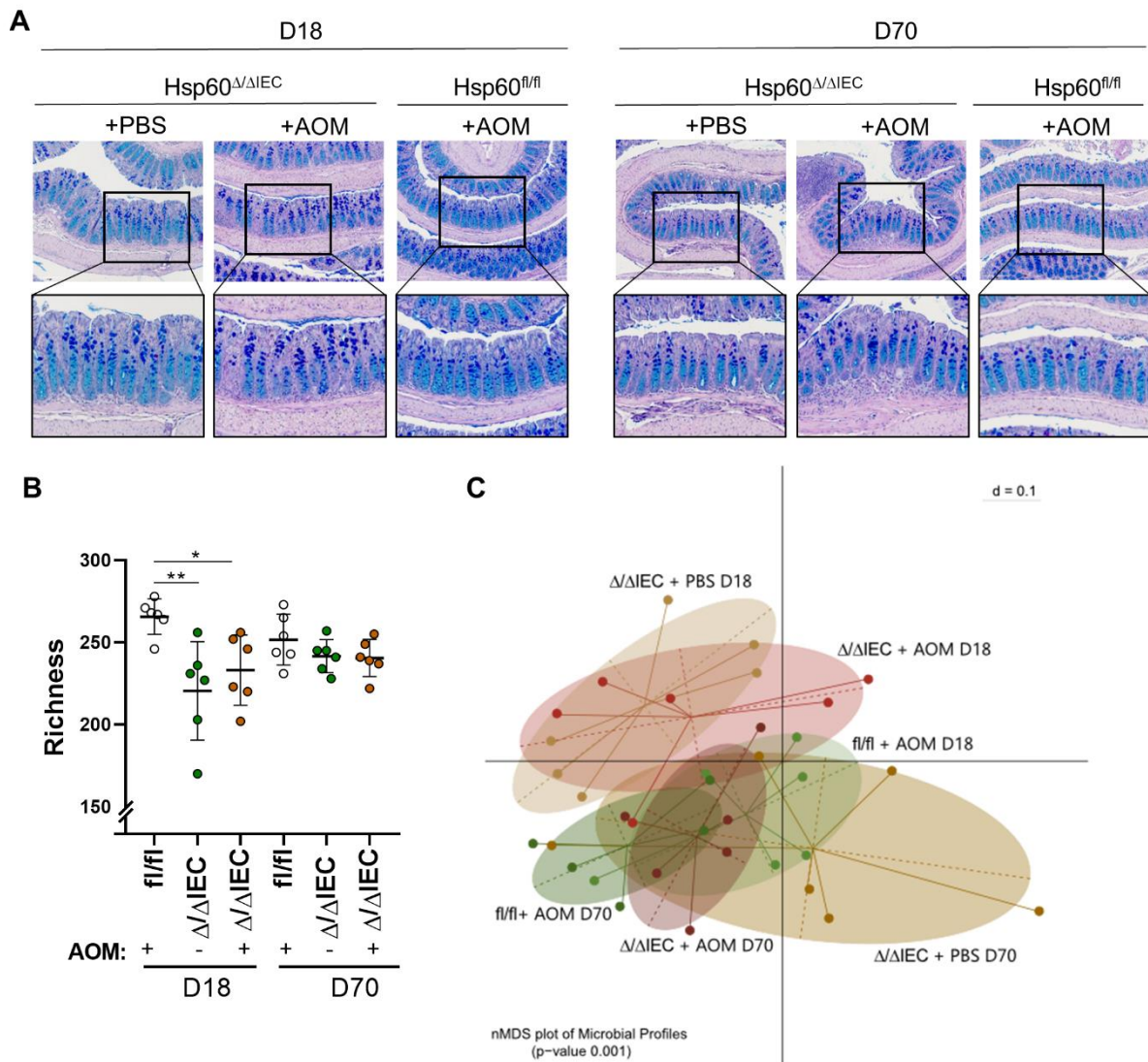
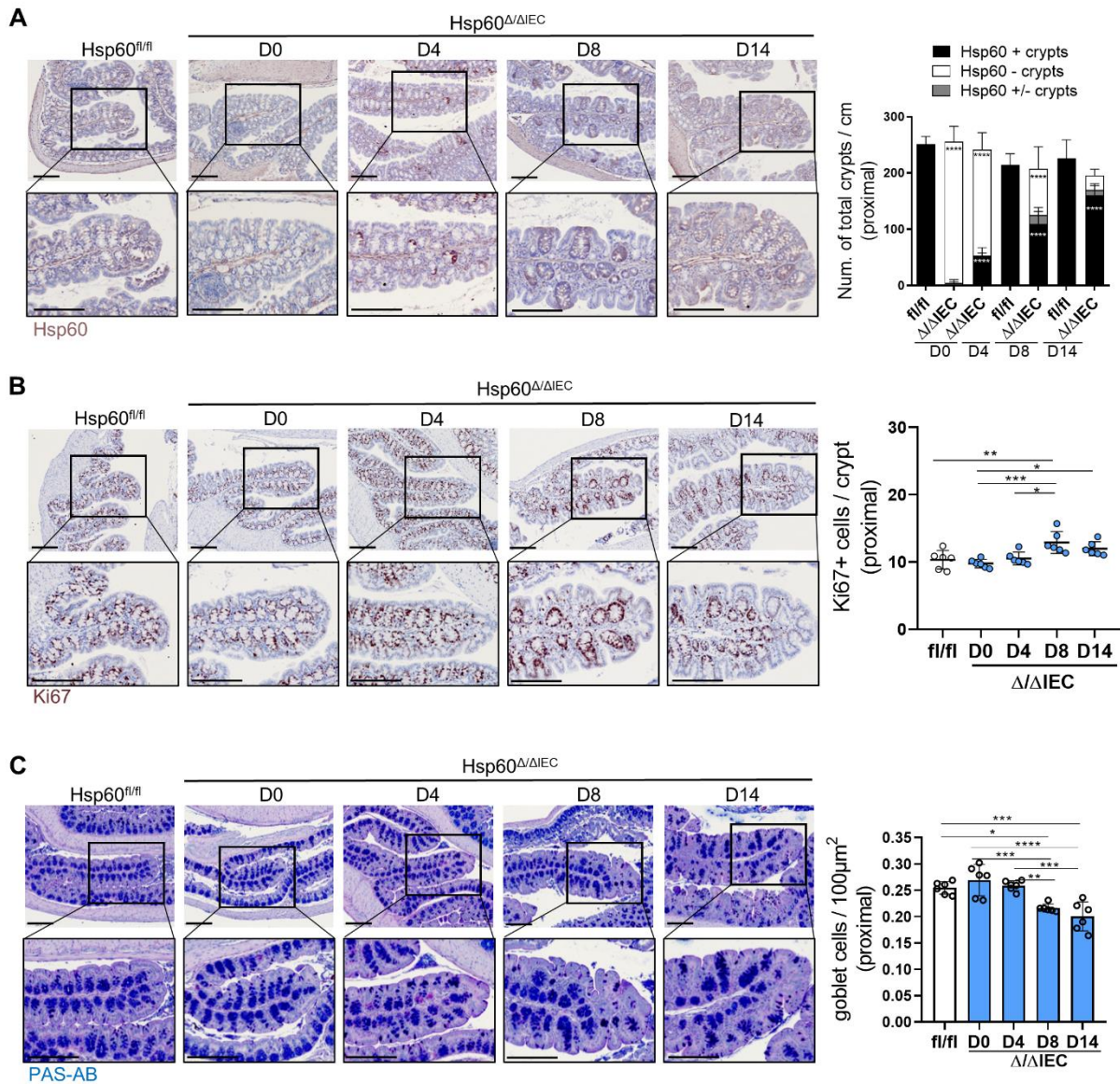**Supplementary figure 6: IHC staining from day 4 of Hsp60$^{\Delta/\Delta IEC}$;*Il10*$^{-/-}$ mice.**

Representative immunohistochemically stained colonic swiss rolls for **(A)** Hsp60, **(B)** Ki67 and **(C)** pStat3 and corresponding higher magnifications for Hsp60$^{\Delta/\Delta IEC}$;*Il10*$^{-/-}$ and control (Hsp60$^{fl/fl}$;*Il10*$^{-/-}$ and Hsp60$^{\Delta/\Delta IEC}$;*Il10*$^{+/+}$) mice at day (D) 4 (scale bars = 200µM).
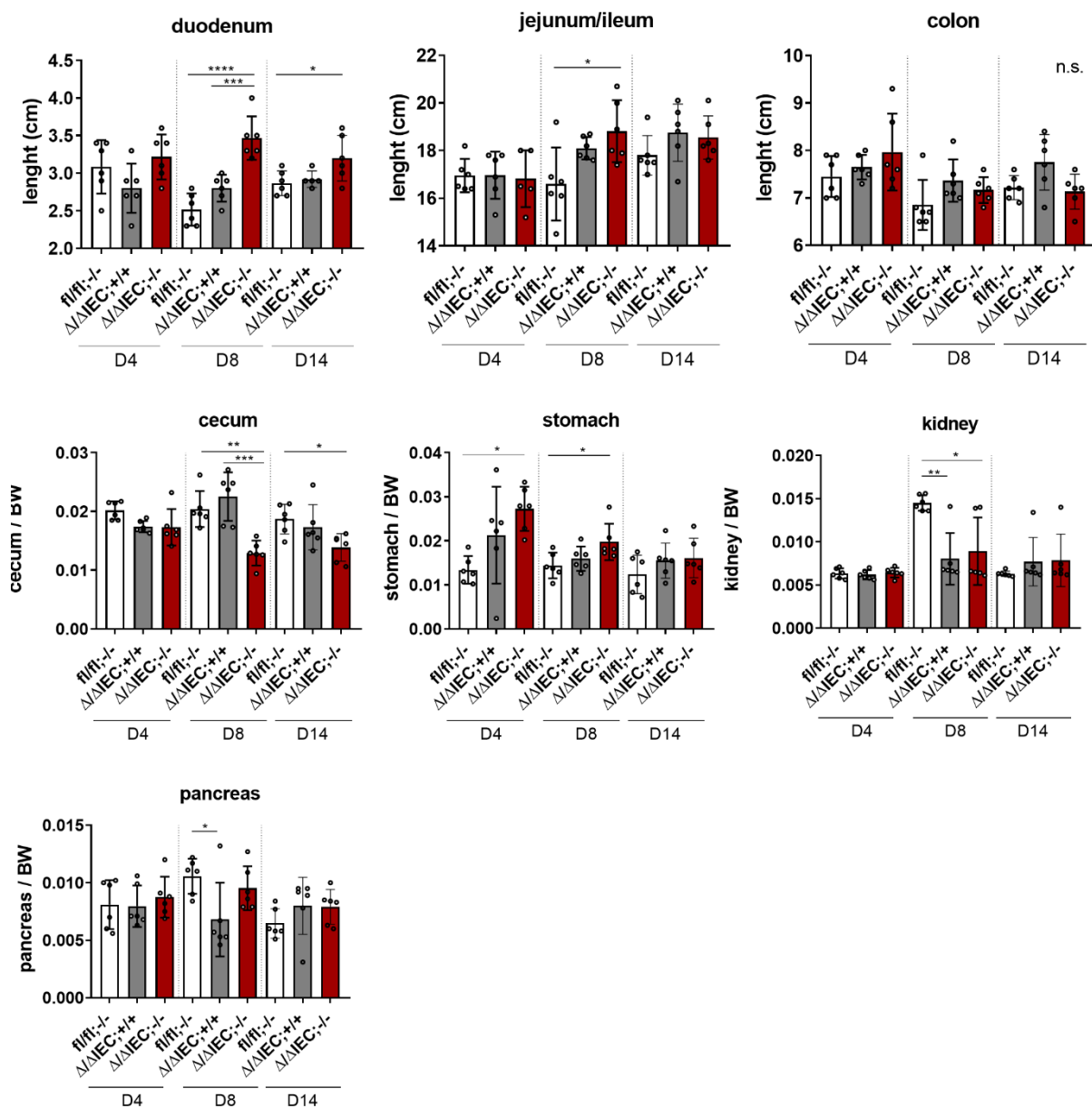
Supplementary figure 7: Organ weights from Hsp60$^{\Delta/\Delta IEC}$;$Il10^{-/-}$ mice over different time points.

Length of intestinal segments and organ weights from Hsp60$^{\Delta/\Delta IEC}$;$Il10^{-/-}$ and control (Hsp60$^{fl/fl}$;$Il10^{-/-}$ and Hsp60$^{\Delta/\Delta IEC}$;$Il10^{+/+}$) mice from day (D) 4 to 14. Statistics: ANOVA followed by pairwise comparison testing (Tukey). Mean ± SD, n=6. Asterisks indicate significant differences *P<0.05, **P<0.01, ***P<0.001; ****P<0.0001.
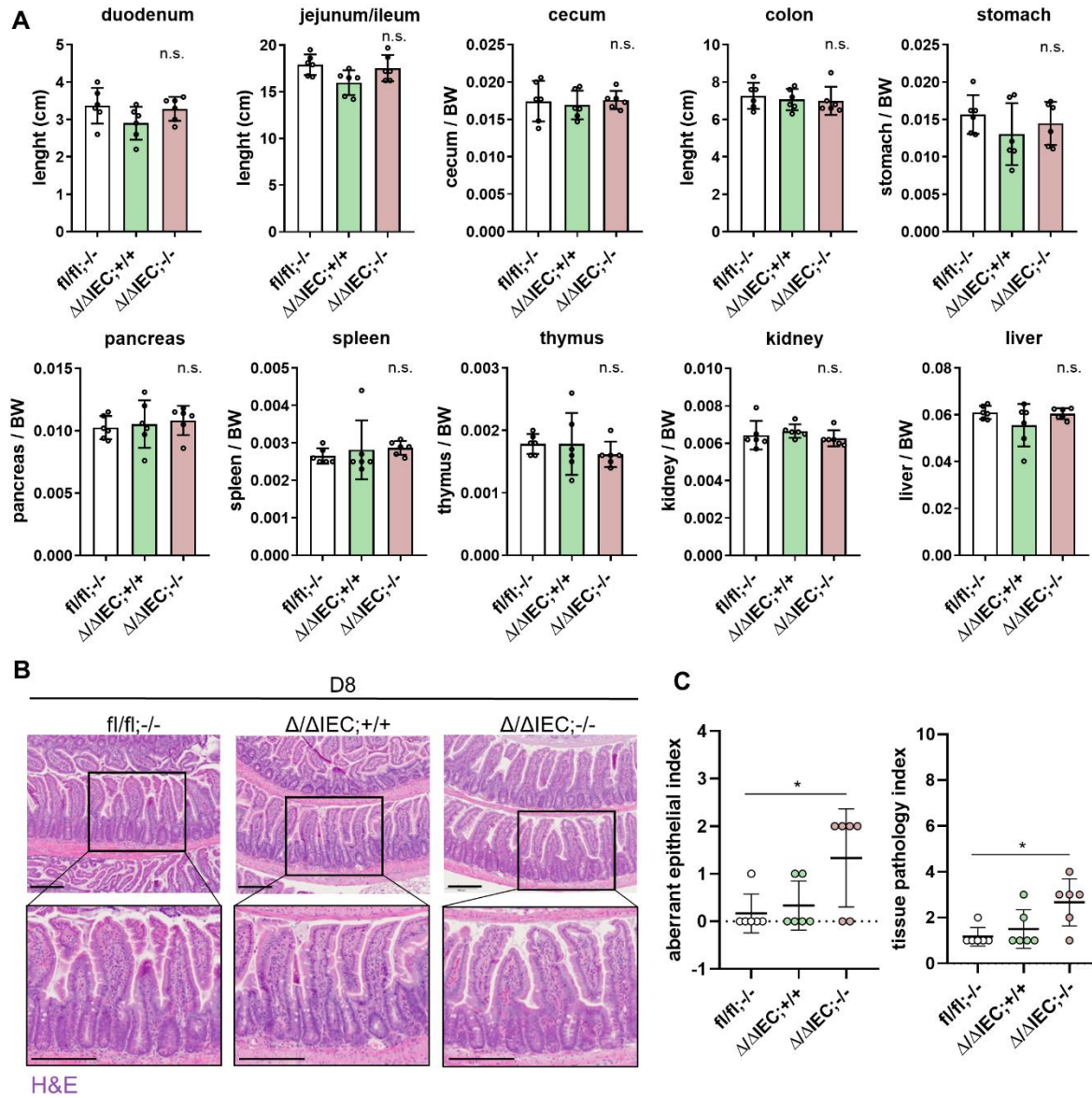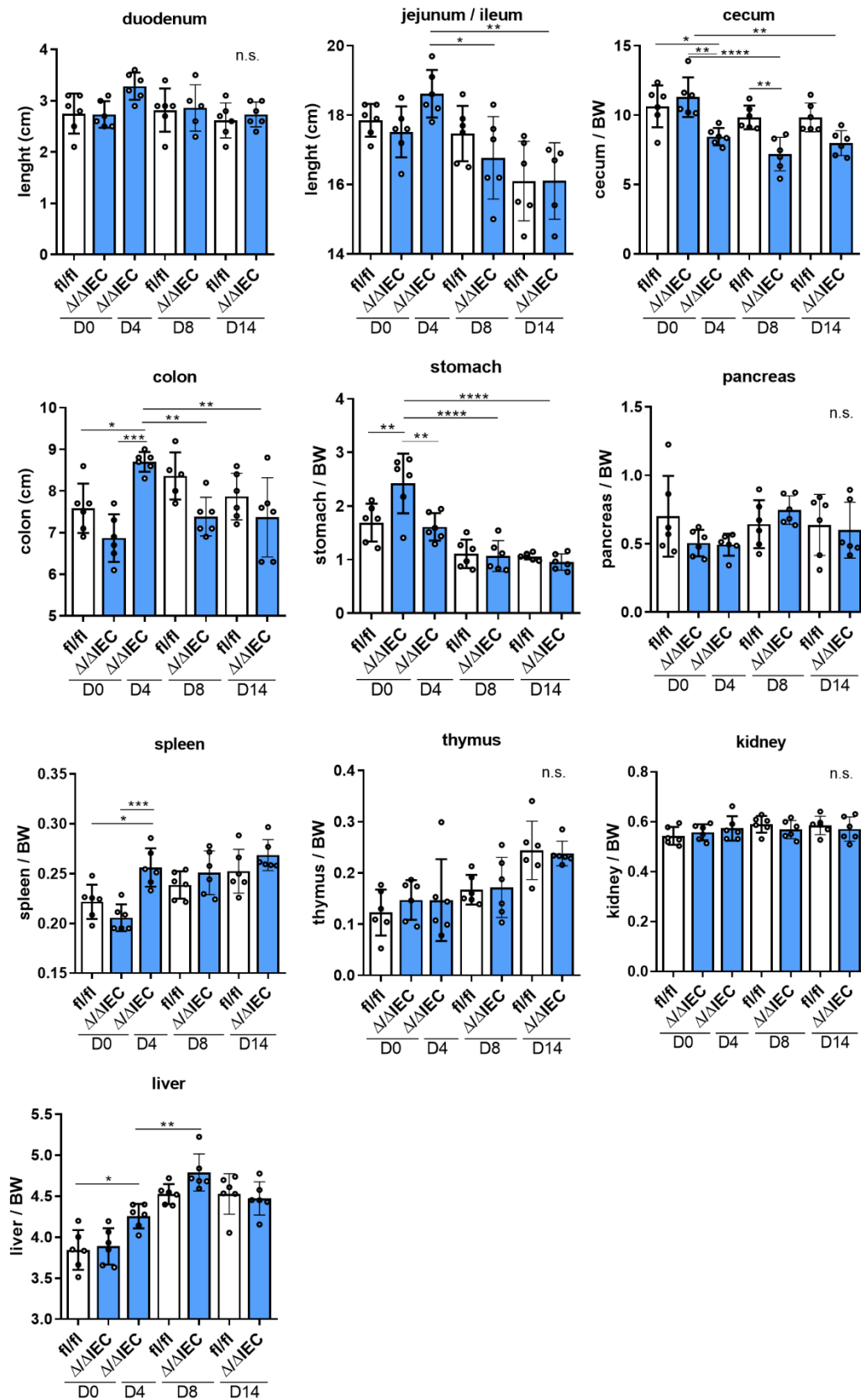
Supplementary figure 8: Organ weights and ileal histology from ClpP$^{Δ/ΔIEC}$;*Il10*$^{-/-}$ mice.
(A) Length of intestinal segments and organ weights from ClpP$^{Δ/ΔIEC}$;*Il10*$^{-/-}$ and control (ClpP$^{fl/fl}$;*Il10*$^{-/-}$ and ClpP$^{Δ/ΔIEC}$;*Il10*$^{+/+}$) mice at day (D) 8. **(B)** Representative H&E stained sections of ileal tissue and corresponding higher magnifications (scale bars = 200μM). **(C)** Tissue was scored histologically for an aberrant epithelial architecture and tissue pathology index. Statistics: ANOVA followed by pairwise comparison testing (Tukey). Mean ± SD, n=6. Asterisks indicate significant differences *P<0.05, **P<0.01, ***P<0.001; ****P<0.0001.
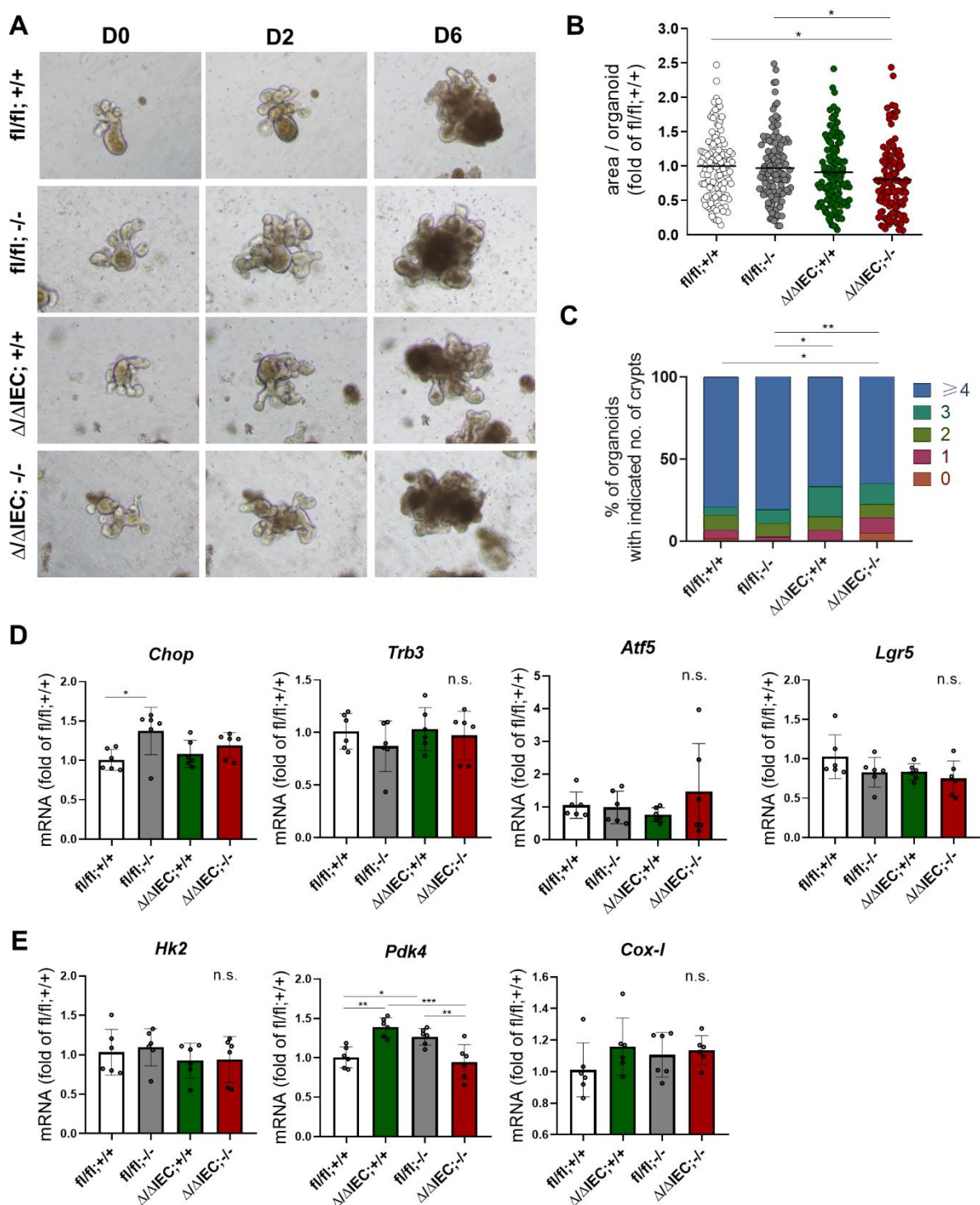
Supplementary figure 9: Morphology and gene expression of ClpP$^{\Delta/\Delta IEC}$;*Il10*$^{-/-}$ organoids.

(A) Representative pictures of organoids. ClpP deletion is induced *ex vivo* in small intestinal organoids from ClpP$^{\Delta/\Delta IEC}$;*Il10*$^{-/-}$ mice (Ctrl: ClpP$^{\Delta/\Delta IEC}$;*Il10*$^{+/+}$, ClpP$^{fl/fl}$;*Il10*$^{-/-}$ and ClpP$^{fl/fl}$;*Il10*$^{+/+}$) by adding tamoxifen (500nM) for 24h to the culture media. Organoids are then monitored up to 6 days. **(B)** Quantification of organoid area and **(C)** *de novo* crypt formation (budding) in all genotypes at day (D) 6. mRNA expression levels of organoids for **(D)** MT-UPR relevant *genes* (*Chop, Trb3, Atf5*), stemness (*Lgr5*) and **(E)** metabolic genes (*Hk2, Pdk4, Cox-I*). Statistics: (B,D,E) ANOVA followed by pairwise comparison testing (Tukey). (C) Mann-Whitney test. Mean ± SD, n=6. Asterisks indicate significant differences *P<0.05, **P<0.01, ***P<0.001; ****P<0.0001.
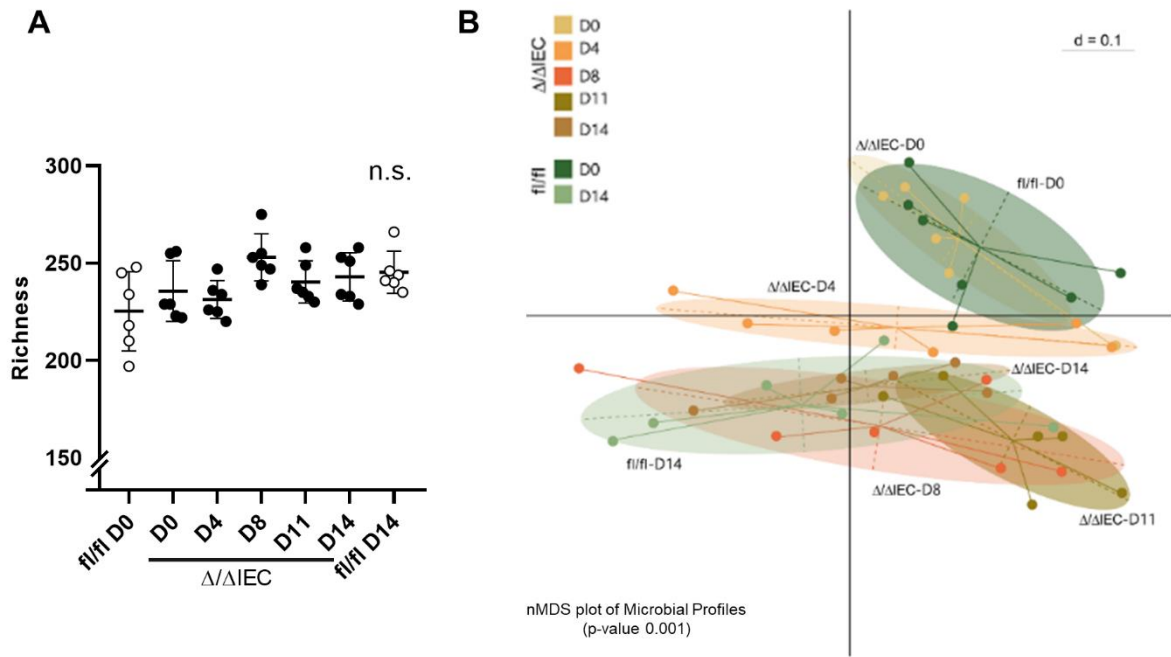
Supplementary figure 10: 16S rRNA profiling from ClpP$^{\Delta/\Delta IEC}$ mice over different time points.

(A) Alpha-diversity as represented by community richness from colonic content of ClpP$^{\Delta/\Delta IEC}$ mice and respective controls (ClpP$^{fl/fl}$) based on 16S rRNA sequencing from day (D) 0 to 14. **(B)** Beta-diversity depicted as nMSD plot of bacterial composition from colonic content of respective mice. Statistics: ANOVA followed by pairwise comparison testing (Tukey). Mean ± SD, n=6. Asterisks indicate significant differences *P<0.05, **P<0.01, ***P<0.001; ****P<0.0001.

Supplementary figure 11: PAS-AB staining and 16S rRNA profiling from Hsp60$^{\Delta/\Delta IEC}$ mice with AOM.

(A) Representative PAS-AB staining for mucus-filled goblet cells (GCs) of the distal region of colonic swiss roles and corresponding higher magnifications from Hsp60$^{\Delta/\Delta IEC}$ and control (Hsp60$^{fl/fl}$) mice treated with AOM or PBS as a control from day (D) 18 and 70. **(B)** Alpha-diversity as represented by community richness from colonic content of respective mice based on 16S rRNA sequencing. **(C)** Beta-diversity depicted as nMSD plot of bacterial composition from colonic content of respective mice. Statistics: ANOVA followed by pairwise comparison testing (Tukey). Mean ± SD, n=6. Asterisks indicate significant differences *P<0.05, **P<0.01, ***P<0.001; ****P<0.0001.

Supplementary figure 12: IHC staining from the proximal colon of germfree Hsp60$^{Δ/ΔIEC}$ mice.

(A) Representative immunohistochemically stained colonic swiss rolls and respective quantifications for **(A)** Hsp60, **(B)** Ki67, and **(C)** pStat3 and corresponding higher magnifications for the proximal colon of germfree Hsp60$^{Δ/ΔIEC}$ and control (Hsp60$^{fl/fl}$) mice from day (D) 0 to14 (scale bars = 200µM).

Supplementary figure 13: Organ weights from germfree Hsp60$^{\Delta/\Delta IEC}$ mice over different time points.

Length of intestinal segments and organ weights from germfree Hsp60$^{\Delta/\Delta IEC}$ and control (Hsp60$^{fl/fl}$) mice from day (D) 0 to 14. Statistics: ANOVA followed by pairwise comparison testing (Tukey). Mean ± SD, n=6. Asterisks indicate significant differences *P<0.05, **P<0.01, ***P<0.001; ****P<0.0001.
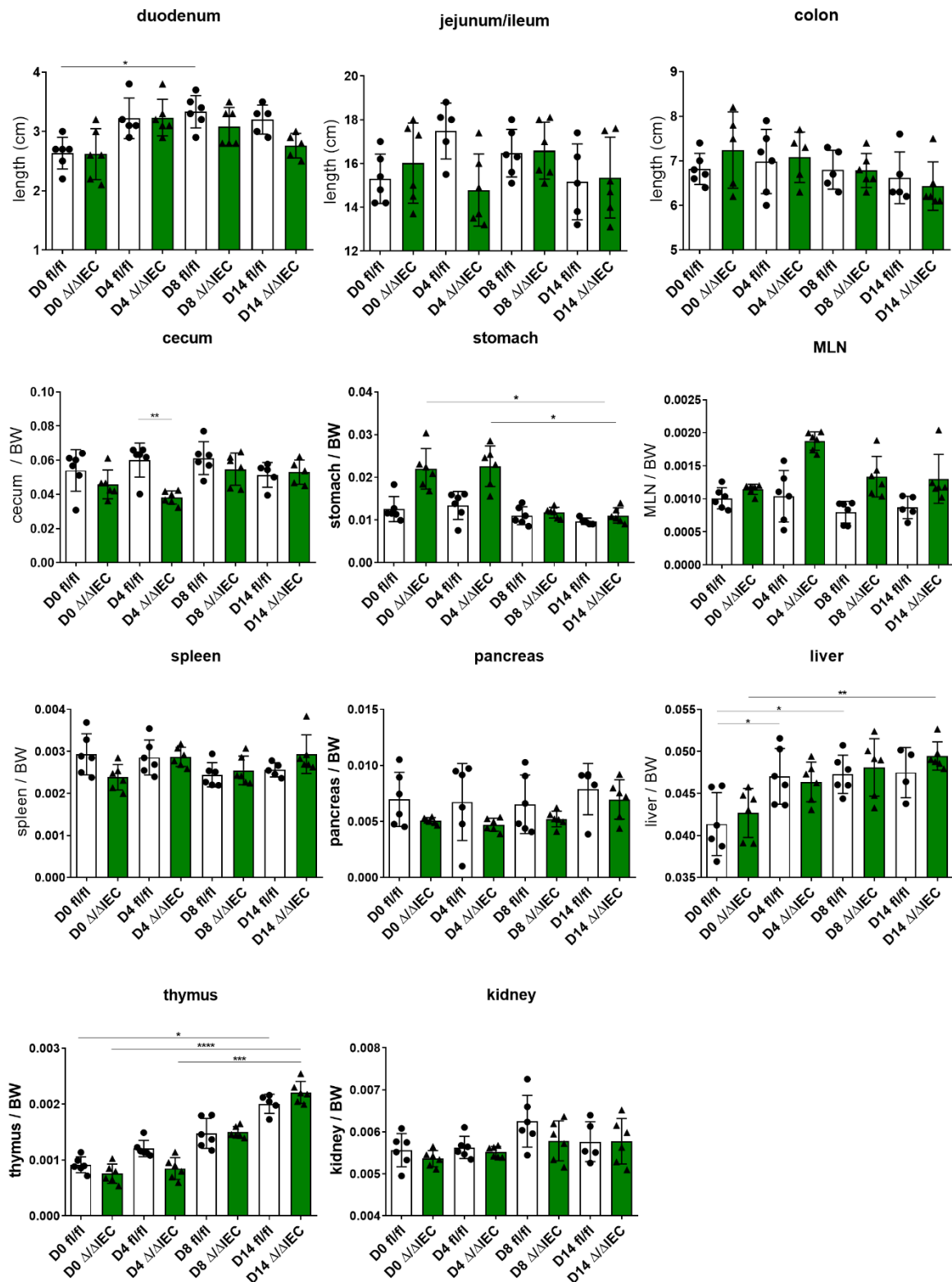
Supplementary figure 14: Organ weights from Hsp60$^{\Delta/\Delta IEC}$ mice colonized with OMM^{12}.

Length of intestinal segments and organ weights from Hsp60$^{\Delta/\Delta IEC}$ and control (Hsp60$^{fl/fl}$) mice colonized with OMM^{12} from day (D) 0 to 14. Statistics: ANOVA followed by pairwise comparison testing (Tukey). Mean ± SD, n=6. Asterisks indicate significant differences *P<0.05, **P<0.01, ***P<0.001; ****P<0.0001.
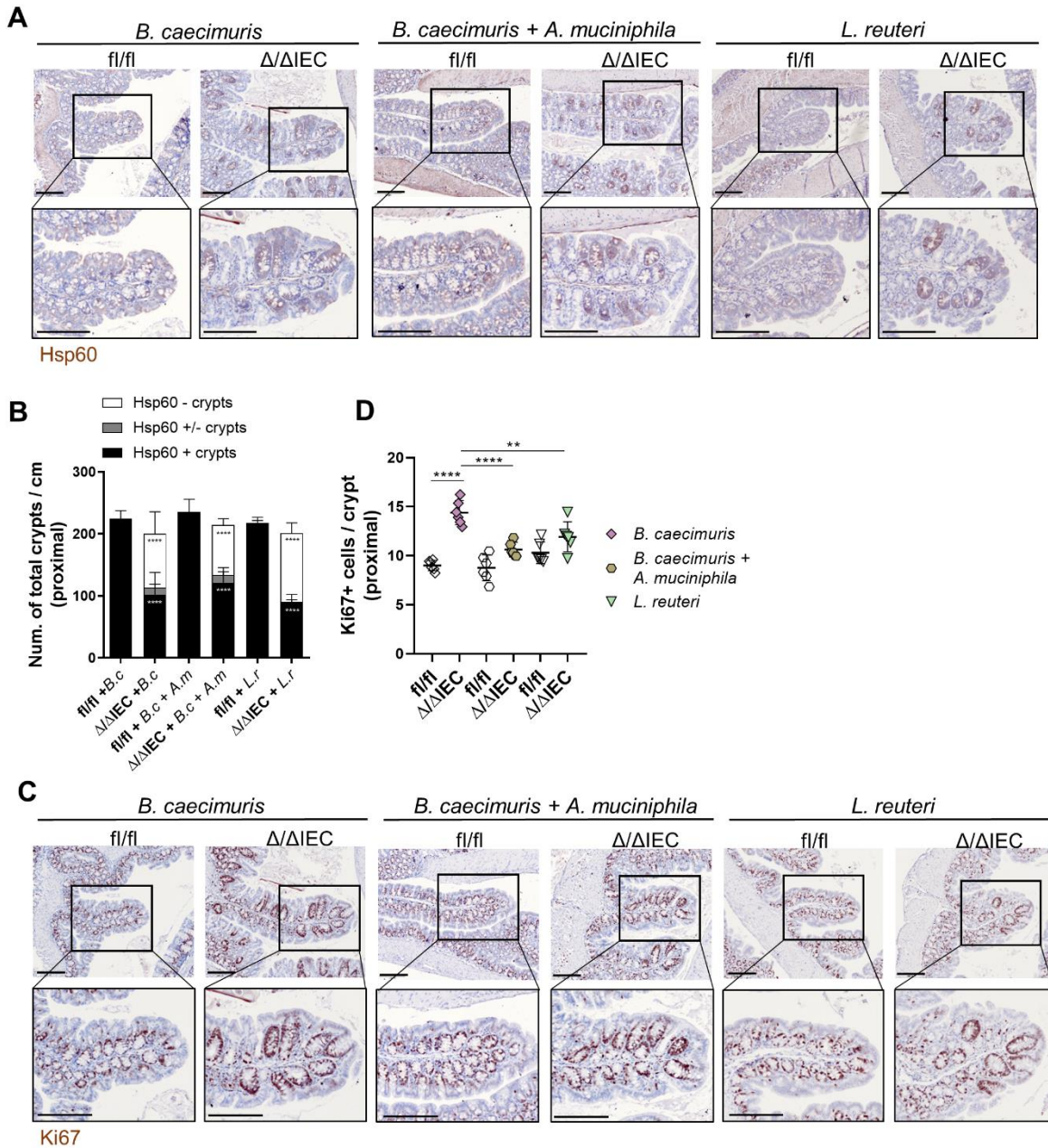
Supplementary figure 15: IHC staining from the proximal colon of selective colonized Hsp60$^{\Delta/\Delta IEC}$ mice.

Representative immunohistochemically stained colonic swiss rolls and respective quantifications for **(A)** Hsp60 and **(B)** Ki67 and corresponding higher magnifications for the proximal colon of selective colonized Hsp60$^{\Delta/\Delta IEC}$ and control (Hsp60$^{fl/fl}$) mice at day (D) 8 (scale bars = 200µM). Statistics: One or two-way ANOVA followed by pairwise comparison testing (Tukey). Mean ± SD, n=6. Asterisks indicate significant differences *P<0.05, **P<0.01, ***P<0.001; ****P<0.0001.
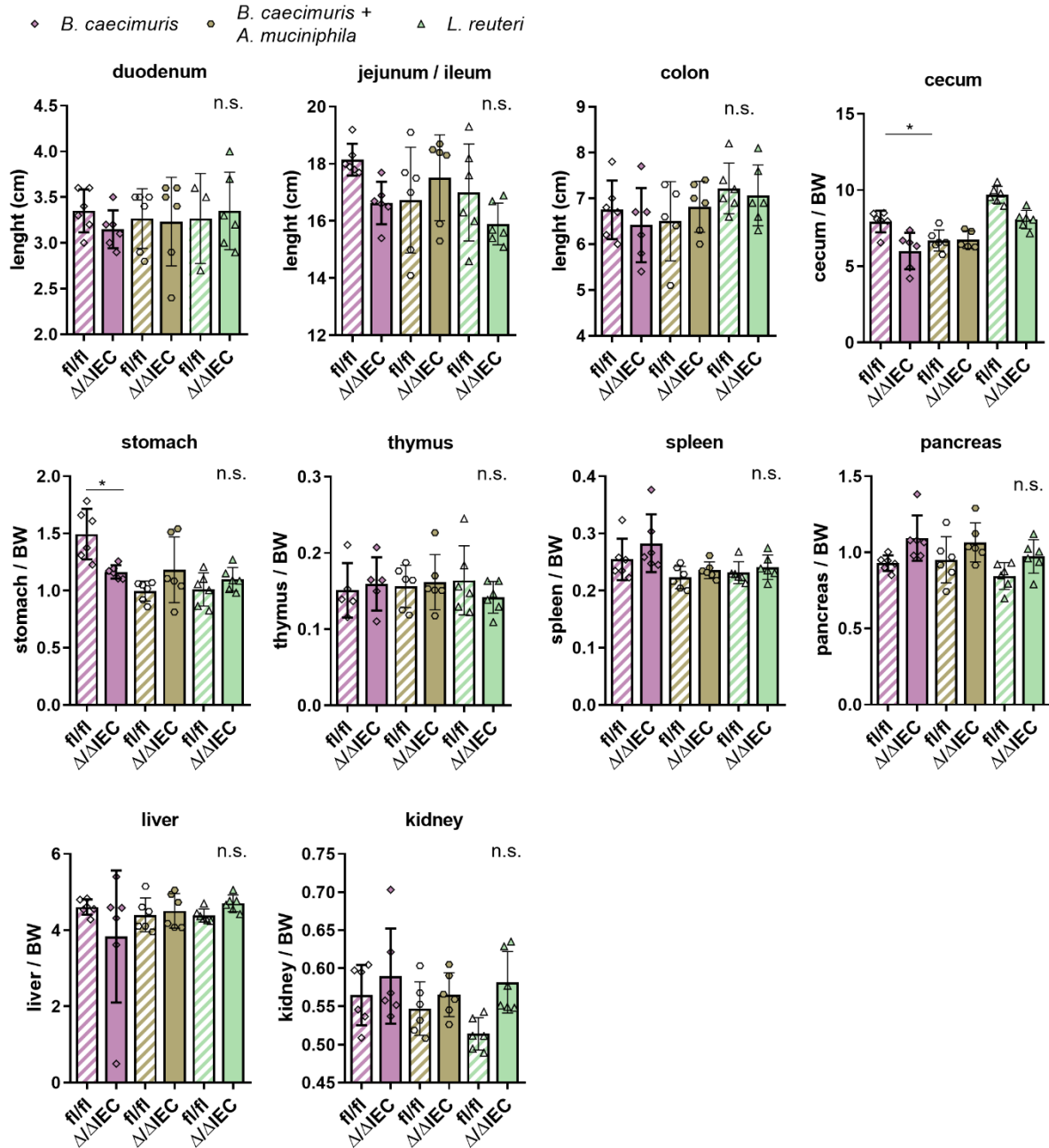
Supplementary figure 16: Organ weights from selective colonized Hsp60$^{\Delta/\Delta IEC}$ mice over different time points.

Length of intestinal segments and organ weights from selective colonized Hsp60$^{\Delta/\Delta IEC}$ and control (Hsp60$^{fl/fl}$) mice at day (D) 8. Mice were colonized with *B. caecimuris*, *B. caecimuris* and *A. muciniphila* or *L. reuteri*. Statistics: ANOVA followed by pairwise comparison testing (Tukey). Mean ± SD, n=6. Asterisks indicate significant differences *P<0.05, **P<0.01, ***P<0.001; ****P<0.0001.

List of Figures

List of Tables

List of Supplementary Figures

ABBREVIATIONS

Abbreviations

AA	Antibiotic Antimycotic
AhR	aryl hydrocarbon receptor
Alpi	intestinal alkaline phosphatase
ANOVA	analysis of variance
Aoc1	amine oxidase copper containing 1
AOM	azoxymethane
Apoa1	apolipoprotein A1
Arg1/2	arginase 1/2
Atf4/5/6	activating transcription factor 4/5/6
ATP	adenosine triphosphate
Bmi	polycomb complex protein
bp	base pair
BSA	bovine serum albumin
CAC	colitis-associated colon cancer
CCM	crypt culture media
CD	Crohn's disease
Chac1	cation transport regulator-like protein 1
ChgA	chromogranin A
Chop	C/EBP homologous protein
ClpP	caseinolytic mitochondrial matrix peptidase
Co-IP	co-immunoprecipitation
Cox-I	cyclooxygenase-1
CO_2	carbon dioxide
Cps1	carbamoyl-phosphate synthase 1
CRC	colorectal cancer
Ctrl	control
D	day
Dapi	4',6-Diamidino-2-phenylindol
Dars	aspartyl-tRNA synthetase
DEG	differentially expressed gene
DMEM	Dulbecco's Modified Eagle's Medium
dH_2O	distilled water
DNA	deoxyribonucleic acid
DSS	dextran sulfate sodium
DTT	dithiothreitol
EDTA	ethylenediaminetetraacetic acid
EGF	epidermal growth factor
ELISA	enzyme-linked immunosorbent assay
Ereg	epiregulin
Etfa	electron transfer flavoprotein subunit alpha
EtOH	ethanol
FCS	fetal calf serum
FFPE	formalin-fixed, paraffin-embedded
FDR	false discovery rate
fl/fl	flox/flox
g	gram
GC	goblet cell
gDNA	genomic DNA
GF	germfree
Gpr	G-protein coupled receptor
Grem1	gremlin 1
GvHD	graft-versus-host diseases
h	hour
Hadh	hydroxyacyl-CoA dehydrogenase
HCl	hydrogen chloride
Hk2	hexokinase 2

XI

Hprt	hypoxanthine-guanine phosphoribosyltransferase
Hsp60	heat shock protein 60
HopX	homeodomain-only protein
Hsd17b10	17beta-hydroxysteroid dehydrogenase type 10
H&E	hematoxylin and eosin
H_2O	water
H_2O_2	hydrogen peroxide
IAA	indole acetic acid
IBD	inflammatory bowel diseases
Ido1	indolamine 2,3-dioxygenase 1
IEC	intestinal epithelial cell
IF	immunofluorescence
IgG	immunoglobulin G
IHC	immunohistochemistry
IL	interleukin
ILC	innate lymphoid cell
IMC	intestinal mesenchymal cell
i.p.	intraperitoneal
IPA	indole propionic acid
ISC	intestinal stem cell
kg	kilogram
KCl	potassium chloride
Ki67	kiel 67
KO	knockout
Kyat3	kynurenine aminotransferase 3
L	liter
Lgr5	leucine-rich repeat-containing G protein-coupled receptor 5
Lrig1	leucine-rich repeats and immunoglobulin-like domains 1
m	meter
M	molar
M-CSF	macrophage colony-stimulating factor
mg	milligram
ml	milliliter
MLN	mesenteric lymph node
mM	millimolar
Mmp7	metalloproteinase 7
min	minutes
mod	modified
mRNA	messenger ribonucleic acid
MS/MS	tandem mass spectrometry
mTOR	mammalian target of rapamycin
MT-UPR	mitochondrial unfolded protein response
Muc2	mucin 2
ng	nomogram
NIR	Near-infrared
nM	nanomolar
N2	nitrogen
Nos2	nitric oxide synthase 2
Nrg1	neuregulin 1
n.s.	not significant
4-OHT	tamoxifen
Olfm4	olfactomedin 4
OMM12	Oligo-Mouse-Microbiota
O.N.	over night
Otc	ornithine transcarbamylase
OXPHOS	oxidative phosphorylation
PAS-AB	Periodicacid-Schiff/ alcian blue
PBS	Phosphate-buffered saline
Pck2	phosphoenolpyruvate carboxykinase 2
PCR	polymerase chain reaction

Pdk3/4	pyruvate dehydrogenase kinase 3/4
Pgc1a	peroxisome proliferator-activated receptor gamma coactivator 1 a
Ptgs2	prostaglandin-endoperoxide synthase 2
Prom1	prominin 1
Pycr1	pyrroline-5-carboxylate reductase 1
RNA	ribonucleic acid
qRT-PCR	quantitative real-time PCR
ROS	reactive oxygen species
rpm	rounds per minute
RPMI	Roswell Park Memorial Institute Medium
rRNA	ribosomal RNA
RSpo1	R-spondin 1
RT	room temperature
Saa3	serum amyloid A-3
SC	stem cell
SCFAs	short-chain fatty acids
SD	standard deviation
sec	seconds
Shmt2	serine hydroxymethyltransferase 2
SPF	specific pathogen-free
Stat3	signal transducer and activator of transcription 3
TBST	tris-buffered saline with tween20
TCA	tricarboxylic acid cycle
TCGA	The Cancer Genome Atlas
Tdo2	tryptophan-2,3-dioxygenase 2.
Tert	telomerase reverse transcriptase
Tg	transgenic
Tnf	tumor necrosis factor
Tph1	tryptophan hydroxylase 1
Trb3	tribbles homolog 3
Tufm	tu translation elongation factor, mitochondrial
UC	ulcerative colitis
Wnt	wingless
Wt	wild-type
w/v	weight per volume
zOTU	zero-radius operational taxonomic unit
µm	micrometer
µM	micromolar
µl	microliter
Δ/ΔIEC	homozygous knockout specifically in IECs
-/-	homozygous knockout
+/+	wild-type allele
°C	degree celsius
%	percent
1-D-MT	1-L-methyltryptophan
3HAA	3-hydroxyanthranilic acid

List of References

1. Gilbert, J.A., et al., *Current understanding of the human microbiome.* Nat Med, 2018. **24**(4): p. 392-400.
2. Caruso, R., B.C. Lo, and G. Nunez, *Host-microbiota interactions in inflammatory bowel disease.* Nat Rev Immunol, 2020. **20**(7): p. 411-426.
3. Gao, Z., et al., *Microbiota disbiosis is associated with colorectal cancer.* Front Microbiol, 2015. **6**: p. 20.
4. Jarmakiewicz-Czaja, S., et al., *Genetic and Epigenetic Etiology of Inflammatory Bowel Disease: An Update.* Genes (Basel), 2022. **13**(12).
5. Ho, G.T. and A.L. Theiss, *Mitochondria and Inflammatory Bowel Diseases: Toward a Stratified Therapeutic Intervention.* Annu Rev Physiol, 2022. **84**: p. 435-459.
6. Urbauer, E., E. Rath, and D. Haller, *Mitochondrial Metabolism in the Intestinal Stem Cell Niche-Sensing and Signaling in Health and Disease.* Front Cell Dev Biol, 2020. **8**: p. 602814.
7. Jackson, D.N. and A.L. Theiss, *Gut bacteria signaling to mitochondria in intestinal inflammation and cancer.* Gut Microbes, 2020. **11**(3): p. 285-304.
8. Falk, P.G., et al., *Creating and maintaining the gastrointestinal ecosystem: what we know and need to know from gnotobiology.* Microbiol Mol Biol Rev, 1998. **62**(4): p. 1157-70.
9. Peterson, L.W. and D. Artis, *Intestinal epithelial cells: regulators of barrier function and immune homeostasis.* Nat Rev Immunol, 2014. **14**(3): p. 141-53.
10. Helander, H.F. and L. Fandriks, *Surface area of the digestive tract - revisited.* Scand J Gastroenterol, 2014. **49**(6): p. 681-9.
11. Barker, N., *Adult intestinal stem cells: critical drivers of epithelial homeostasis and regeneration.* Nat Rev Mol Cell Biol, 2014. **15**(1): p. 19-33.
12. Barker, N. and H. Clevers, *Leucine-rich repeat-containing G-protein-coupled receptors as markers of adult stem cells.* Gastroenterology, 2010. **138**(5): p. 1681-96.
13. Kurashima, Y. and H. Kiyono, *Mucosal Ecological Network of Epithelium and Immune Cells for Gut Homeostasis and Tissue Healing.* Annu Rev Immunol, 2017. **35**: p. 119-147.
14. Sangiorgi, E. and M.R. Capecchi, *Bmi1 is expressed in vivo in intestinal stem cells.* Nat Genet, 2008. **40**(7): p. 915-20.
15. Montgomery, R.K., et al., *Mouse telomerase reverse transcriptase (mTert) expression marks slowly cycling intestinal stem cells.* Proc Natl Acad Sci U S A, 2011. **108**(1): p. 179-84.
16. Takeda, N., et al., *Interconversion between intestinal stem cell populations in distinct niches.* Science, 2011. **334**(6061): p. 1420-4.
17. Powell, A.E., et al., *The pan-ErbB negative regulator Lrig1 is an intestinal stem cell marker that functions as a tumor suppressor.* Cell, 2012. **149**(1): p. 146-58.
18. Wang, Y., et al., *Long-Term Culture Captures Injury-Repair Cycles of Colonic Stem Cells.* Cell, 2019. **179**(5): p. 1144-1159 e15.
19. Quiros, M. and A. Nusrat, *Contribution of Wound-Associated Cells and Mediators in Orchestrating Gastrointestinal Mucosal Wound Repair.* Annu Rev Physiol, 2019. **81**: p. 189-209.
20. Pastula, A. and J. Marcinkiewicz, *Cellular Interactions in the Intestinal Stem Cell Niche.* Arch Immunol Ther Exp (Warsz), 2019. **67**(1): p. 19-26.
21. Rath, E., A. Moschetta, and D. Haller, *Mitochondrial function - gatekeeper of intestinal epithelial cell homeostasis.* Nat Rev Gastroenterol Hepatol, 2018. **15**(8): p. 497-516.
22. Rath, E. and D. Haller, *Mitochondria at the interface between danger signaling and metabolism: role of unfolded protein responses in chronic inflammation.* Inflamm Bowel Dis, 2012. **18**(7): p. 1364-77.
23. Ni, H.M., J.A. Williams, and W.X. Ding, *Mitochondrial dynamics and mitochondrial quality control.* Redox Biol, 2015. **4**: p. 6-13.

24. Martinez-Reyes, I. and N.S. Chandel, *Mitochondrial TCA cycle metabolites control physiology and disease.* Nat Commun, 2020. **11**(1): p. 102.

25. Rodriguez-Colman, M.J., et al., *Interplay between metabolic identities in the intestinal crypt supports stem cell function.* Nature, 2017. **543**(7645): p. 424-427.

26. Ludikhuize, M.C., et al., *Mitochondria Define Intestinal Stem Cell Differentiation Downstream of a FOXO/Notch Axis.* Cell Metab, 2020. **32**(5): p. 889-900 e7.

27. Melber, A. and C.M. Haynes, *UPR(mt) regulation and output: a stress response mediated by mitochondrial-nuclear communication.* Cell Res, 2018. **28**(3): p. 281-295.

28. Horibe, T. and N.J. Hoogenraad, *The chop gene contains an element for the positive regulation of the mitochondrial unfolded protein response.* PLoS One, 2007. **2**(9): p. e835.

29. Zhao, Q., et al., *A mitochondrial specific stress response in mammalian cells.* EMBO J, 2002. **21**(17): p. 4411-9.

30. Fiorese, C.J., et al., *The Transcription Factor ATF5 Mediates a Mammalian Mitochondrial UPR.* Curr Biol, 2016. **26**(15): p. 2037-2043.

31. Shpilka, T. and C.M. Haynes, *The mitochondrial UPR: mechanisms, physiological functions and implications in ageing.* Nat Rev Mol Cell Biol, 2018. **19**(2): p. 109-120.

32. Zhang, W., et al., *Multi-omics analyses of human colorectal cancer revealed three mitochondrial genes potentially associated with poor outcomes of patients.* J Transl Med, 2021. **19**(1): p. 273.

33. Ho, G.T., et al., *MDR1 deficiency impairs mitochondrial homeostasis and promotes intestinal inflammation.* Mucosal Immunol, 2018. **11**(1): p. 120-130.

34. Ng, S.C., et al., *Worldwide incidence and prevalence of inflammatory bowel disease in the 21st century: a systematic review of population-based studies.* Lancet, 2017. **390**(10114): p. 2769-2778.

35. Bach, J.F., *The effect of infections on susceptibility to autoimmune and allergic diseases.* N Engl J Med, 2002. **347**(12): p. 911-20.

36. Piovani, D., et al., *Environmental Risk Factors for Inflammatory Bowel Diseases: An Umbrella Review of Meta-analyses.* Gastroenterology, 2019. **157**(3): p. 647-659 e4.

37. Kaser, A., S. Zeissig, and R.S. Blumberg, *Inflammatory bowel disease.* Annu Rev Immunol, 2010. **28**: p. 573-621.

38. Chang, J.T., *Pathophysiology of Inflammatory Bowel Diseases.* N Engl J Med, 2020. **383**(27): p. 2652-2664.

39. Sartor, R.B., *Mechanisms of disease: pathogenesis of Crohn's disease and ulcerative colitis.* Nat Clin Pract Gastroenterol Hepatol, 2006. **3**(7): p. 390-407.

40. Ellinghaus, D., et al., *Analysis of five chronic inflammatory diseases identifies 27 new associations and highlights disease-specific patterns at shared loci.* Nat Genet, 2016. **48**(5): p. 510-8.

41. Furey, T.S., P. Sethupathy, and S.Z. Sheikh, *Redefining the IBDs using genome-scale molecular phenotyping.* Nat Rev Gastroenterol Hepatol, 2019. **16**(5): p. 296-311.

42. Nasser, J., et al., *Genome-wide enhancer maps link risk variants to disease genes.* Nature, 2021. **593**(7858): p. 238-243.

43. Akdis, C.A., *Does the epithelial barrier hypothesis explain the increase in allergy, autoimmunity and other chronic conditions?* Nat Rev Immunol, 2021. **21**(11): p. 739-751.

44. Coleman, O.I. and D. Haller, *ER Stress and the UPR in Shaping Intestinal Tissue Homeostasis and Immunity.* Front Immunol, 2019. **10**: p. 2825.

45. Grootjans, J., et al., *The unfolded protein response in immunity and inflammation.* Nat Rev Immunol, 2016. **16**(8): p. 469-84.

46. Hugot, J.P., et al., *Association of NOD2 leucine-rich repeat variants with susceptibility to Crohn's disease.* Nature, 2001. **411**(6837): p. 599-603.

47. Ogura, Y., et al., *A frameshift mutation in NOD2 associated with susceptibility to Crohn's disease.* Nature, 2001. **411**(6837): p. 603-6.

48. Cadwell, K., et al., *A key role for autophagy and the autophagy gene Atg16l1 in mouse and human intestinal Paneth cells.* Nature, 2008. **456**(7219): p. 259-63.

49. Levine, B., N. Mizushima, and H.W. Virgin, *Autophagy in immunity and inflammation.* Nature, 2011. **469**(7330): p. 323-35.

50. Braunstein, J., et al., *T cells of the human intestinal lamina propria are high producers of interleukin-10.* Gut, 1997. **41**(2): p. 215-20.

51. Spencer, D.M., et al., *Distinct inflammatory mechanisms mediate early versus late colitis in mice.* Gastroenterology, 2002. **122**(1): p. 94-105.

52. Yadav, P., et al., *Genetic Factors Interact With Tobacco Smoke to Modify Risk for Inflammatory Bowel Disease in Humans and Mice.* Gastroenterology, 2017. **153**(2): p. 550-565.

53. Jostins, L., et al., *Host-microbe interactions have shaped the genetic architecture of inflammatory bowel disease.* Nature, 2012. **491**(7422): p. 119-24.

54. Duchmann, R., et al., *Tolerance exists towards resident intestinal flora but is broken in active inflammatory bowel disease (IBD).* Clin Exp Immunol, 1995. **102**(3): p. 448-55.

55. Darfeuille-Michaud, A., et al., *High prevalence of adherent-invasive Escherichia coli associated with ileal mucosa in Crohn's disease.* Gastroenterology, 2004. **127**(2): p. 412-21.

56. Vich Vila, A., et al., *Gut microbiota composition and functional changes in inflammatory bowel disease and irritable bowel syndrome.* Sci Transl Med, 2018. **10**(472).

57. Hall, A.B., et al., *A novel Ruminococcus gnavus clade enriched in inflammatory bowel disease patients.* Genome Med, 2017. **9**(1): p. 103.

58. Roediger, W.E., *The colonic epithelium in ulcerative colitis: an energy-deficiency disease?* Lancet, 1980. **2**(8197): p. 712-5.

59. Smith, S.A., et al., *Mitochondrial dysfunction in inflammatory bowel disease alters intestinal epithelial metabolism of hepatic acylcarnitines.* J Clin Invest, 2021. **131**(1).

60. Cader, M.Z., et al., *FAMIN Is a Multifunctional Purine Enzyme Enabling the Purine Nucleotide Cycle.* Cell, 2020. **180**(4): p. 815.

61. Lamas, B., et al., *CARD9 impacts colitis by altering gut microbiota metabolism of tryptophan into aryl hydrocarbon receptor ligands.* Nat Med, 2016. **22**(6): p. 598-605.

62. Metwaly, A., et al., *Integrated microbiota and metabolite profiles link Crohn's disease to sulfur metabolism.* Nat Commun, 2020. **11**(1): p. 4322.

63. Rath, H.C., et al., *Normal luminal bacteria, especially Bacteroides species, mediate chronic colitis, gastritis, and arthritis in HLA-B27/human beta2 microglobulin transgenic rats.* J Clin Invest, 1996. **98**(4): p. 945-53.

64. Choi, C.R., et al., *Clonal evolution of colorectal cancer in IBD.* Nat Rev Gastroenterol Hepatol, 2017. **14**(4): p. 218-229.

65. Soh, J.S., et al., *Immunoprofiling of Colitis-associated and Sporadic Colorectal Cancer and its Clinical Significance.* Sci Rep, 2019. **9**(1): p. 6833.

66. Ullman, T., et al., *Progression of flat low-grade dysplasia to advanced neoplasia in patients with ulcerative colitis.* Gastroenterology, 2003. **125**(5): p. 1311-9.

67. Watanabe, T., et al., *Ulcerative colitis-associated colorectal cancer shows a poorer survival than sporadic colorectal cancer: a nationwide Japanese study.* Inflamm Bowel Dis, 2011. **17**(3): p. 802-8.

68. Khaloian, S., et al., *Mitochondrial impairment drives intestinal stem cell transition into dysfunctional Paneth cells predicting Crohn's disease recurrence.* Gut, 2020. **69**(11): p. 1939-1951.

69. Schaubeck, M., et al., *Dysbiotic gut microbiota causes transmissible Crohn's disease-like ileitis independent of failure in antimicrobial defence.* Gut, 2016. **65**(2): p. 225-37.

70. van der Post, S., et al., *Structural weakening of the colonic mucus barrier is an early event in ulcerative colitis pathogenesis.* Gut, 2019. **68**(12): p. 2142-2151.

71. Johansson, M.E., et al., *Bacteria penetrate the normally impenetrable inner colon mucus layer in both murine colitis models and patients with ulcerative colitis.* Gut, 2014. **63**(2): p. 281-91.

72. Coleman, O.I., et al., *Activated ATF6 Induces Intestinal Dysbiosis and Innate Immune Response to Promote Colorectal Tumorigenesis.* Gastroenterology, 2018. **155**(5): p. 1539-1552 e12.

73. Rath, E., et al., *Induction of dsRNA-activated protein kinase links mitochondrial unfolded protein response to the pathogenesis of intestinal inflammation.* Gut, 2012. **61**(9): p. 1269-1278.

74. Theiss, A.L., et al., *Prohibitin is a novel regulator of antioxidant response that attenuates colonic inflammation in mice.* Gastroenterology, 2009. **137**(1): p. 199-208, 208.e1-6.

75. Theiss, A.L., et al., *Nanoparticle-based therapeutic delivery of prohibitin to the colonic epithelial cells ameliorates acute murine colitis.* Inflamm Bowel Dis, 2011. **17**(5): p. 1163-76.

76. Jackson, D.N., et al., *Mitochondrial dysfunction during loss of prohibitin 1 triggers Paneth cell defects and ileitis.* Gut, 2020. **69**(11): p. 1928-1938.

77. Berger, E., et al., *Mitochondrial function controls intestinal epithelial stemness and proliferation.* Nat Commun, 2016. **7**: p. 13171.

78. Yuan, D., et al., *Kupffer Cell-Derived Tnf Triggers Cholangiocellular Tumorigenesis through JNK due to Chronic Mitochondrial Dysfunction and ROS.* Cancer Cell, 2017. **31**(6): p. 771-789 e6.

79. Rath, E. and D. Haller, *Intestinal epithelial cell metabolism at the interface of microbial dysbiosis and tissue injury.* Mucosal Immunology, 2022. **15**(4): p. 595-604.

80. Venkateswaran, K., et al., *Mitigation of radiation-induced gastro-intestinal injury by the polyphenolic acetate 7, 8-diacetoxy-4-methylthiocoumarin in mice.* Sci Rep, 2019. **9**(1): p. 14134.

81. Schmitt, M., et al., *Paneth Cells Respond to Inflammation and Contribute to Tissue Regeneration by Acquiring Stem-like Features through SCF/c-Kit Signaling.* Cell Rep, 2018. **24**(9): p. 2312-2328 e7.

82. Yu, S., et al., *Paneth Cell Multipotency Induced by Notch Activation following Injury.* Cell Stem Cell, 2018. **23**(1): p. 46-59 e5.

83. Bayrer, J.R., et al., *LRH-1 mitigates intestinal inflammatory disease by maintaining epithelial homeostasis and cell survival.* Nat Commun, 2018. **9**(1): p. 4055.

84. Koren, E., et al., *ARTS mediates apoptosis and regeneration of the intestinal stem cell niche.* Nat Commun, 2018. **9**(1): p. 4582.

85. Rhodes, J.M. and B.J. Campbell, *Inflammation and colorectal cancer: IBD-associated and sporadic cancer compared.* Trends Mol Med, 2002. **8**(1): p. 10-6.

86. Xue, X. and D.M. Falcon, *The Role of Immune Cells and Cytokines in Intestinal Wound Healing.* Int J Mol Sci, 2019. **20**(23).

87. Mondanelli, G., et al., *Immunoregulatory Interplay Between Arginine and Tryptophan Metabolism in Health and Disease.* Front Immunol, 2019. **10**: p. 1565.

88. Munder, M., *Arginase: an emerging key player in the mammalian immune system.* Br J Pharmacol, 2009. **158**(3): p. 638-51.

89. Dowling, J.K., et al., *Mitochondrial arginase-2 is essential for IL-10 metabolic reprogramming of inflammatory macrophages.* Nat Commun, 2021. **12**(1): p. 1460.

90. Szondi, D.C., et al., *Arginase Signalling as a Key Player in Chronic Wound Pathophysiology and Healing.* Front Mol Biosci, 2021. **8**: p. 773866.

91. Somasundaram, V., et al., *Inducible nitric oxide synthase-derived extracellular nitric oxide flux regulates proinflammatory responses at the single cell level.* Redox Biol, 2020. **28**: p. 101354.

92. Andrews, C., M.H. McLean, and S.K. Durum, *Cytokine Tuning of Intestinal Epithelial Function.* Front Immunol, 2018. **9**: p. 1270.

93. Mahapatro, M., L. Erkert, and C. Becker, *Cytokine-Mediated Crosstalk between Immune Cells and Epithelial Cells in the Gut.* Cells, 2021. **10**(1).

94. Neurath, M.F., *Cytokines in inflammatory bowel disease.* Nat Rev Immunol, 2014. **14**(5): p. 329-42.

95. Jeffery, V., et al., *IL-6 Signaling Regulates Small Intestinal Crypt Homeostasis.* J Immunol, 2017. **199**(1): p. 304-311.

96. Bradford, E.M., et al., *Epithelial TNF Receptor Signaling Promotes Mucosal Repair in Inflammatory Bowel Disease.* J Immunol, 2017. **199**(5): p. 1886-1897.

97. Song, X., et al., *Growth Factor FGF2 Cooperates with Interleukin-17 to Repair Intestinal Epithelial Damage.* Immunity, 2015. **43**(3): p. 488-501.

98. Hahn, W.S., et al., *Proinflammatory cytokines differentially regulate adipocyte mitochondrial metabolism, oxidative stress, and dynamics.* Am J Physiol Endocrinol Metab, 2014. **306**(9): p. E1033-45.

99. Ouyang, W. and A. O'Garra, *IL-10 Family Cytokines IL-10 and IL-22: from Basic Science to Clinical Translation.* Immunity, 2019. **50**(4): p. 871-891.

100. Morhardt, T.L., et al., *IL-10 produced by macrophages regulates epithelial integrity in the small intestine.* Sci Rep, 2019. **9**(1): p. 1223.

101. Nguyen, H.D., H.M. Aljamaei, and A.W. Stadnyk, *The Production and Function of Endogenous Interleukin-10 in Intestinal Epithelial Cells and Gut Homeostasis.* Cell Mol Gastroenterol Hepatol, 2021. **12**(4): p. 1343-1352.

102. Kominsky, D.J., et al., *IFN-gamma-mediated induction of an apical IL-10 receptor on polarized intestinal epithelia.* J Immunol, 2014. **192**(3): p. 1267-76.

103. Quiros, M., et al., *Macrophage-derived IL-10 mediates mucosal repair by epithelial WISP-1 signaling.* J Clin Invest, 2017. **127**(9): p. 3510-3520.

104. Engelhardt, K.R. and B. Grimbacher, *IL-10 in humans: lessons from the gut, IL-10/IL-10 receptor deficiencies, and IL-10 polymorphisms.* Curr Top Microbiol Immunol, 2014. **380**: p. 1-18.

105. Ip, W.K.E., et al., *Anti-inflammatory effect of IL-10 mediated by metabolic reprogramming of macrophages.* Science, 2017. **356**(6337): p. 513-519.

106. Shkoda, A., et al., *Interleukin-10 blocked endoplasmic reticulum stress in intestinal epithelial cells: impact on chronic inflammation.* Gastroenterology, 2007. **132**(1): p. 190-207.

107. Spit, M., B.K. Koo, and M.M. Maurice, *Tales from the crypt: intestinal niche signals in tissue renewal, plasticity and cancer.* Open Biol, 2018. **8**(9).

108. Gregorieff, A., et al., *Expression pattern of Wnt signaling components in the adult intestine.* Gastroenterology, 2005. **129**(2): p. 626-38.

109. Sato, T., et al., *Paneth cells constitute the niche for Lgr5 stem cells in intestinal crypts.* Nature, 2011. **469**(7330): p. 415-8.

110. Kabiri, Z., et al., *Stroma provides an intestinal stem cell niche in the absence of epithelial Wnts.* Development, 2014. **141**(11): p. 2206-15.

111. Koch, S., et al., *The Wnt antagonist Dkk1 regulates intestinal epithelial homeostasis and wound repair.* Gastroenterology, 2011. **141**(1): p. 259-68, 268 e1-8.

112. Schatoff, E.M., B.I. Leach, and L.E. Dow, *Wnt Signaling and Colorectal Cancer.* Curr Colorectal Cancer Rep, 2017. **13**(2): p. 101-110.

113. Qi, Z., et al., *BMP restricts stemness of intestinal Lgr5(+) stem cells by directly suppressing their signature genes.* Nat Commun, 2017. **8**: p. 13824.

114. Stzepourginski, I., et al., *CD34+ mesenchymal cells are a major component of the intestinal stem cells niche at homeostasis and after injury.* Proc Natl Acad Sci U S A, 2017. **114**(4): p. E506-E513.

115. Jarde, T., et al., *Mesenchymal Niche-Derived Neuregulin-1 Drives Intestinal Stem Cell Proliferation and Regeneration of Damaged Epithelium.* Cell Stem Cell, 2020. **27**(4): p. 646-662 e7.

116. Bae, J.S., et al., *Depletion of MOB1A/B causes intestinal epithelial degeneration by suppressing Wnt activity and activating BMP/TGF-beta signaling.* Cell Death Dis, 2018. **9**(11): p. 1083.

117. Backhed, F., et al., *Host-bacterial mutualism in the human intestine.* Science, 2005. **307**(5717): p. 1915-20.

118. Segata, N., et al., *Composition of the adult digestive tract bacterial microbiome based on seven mouth surfaces, tonsils, throat and stool samples.* Genome Biol, 2012. **13**(6): p. R42.

119. Oren, A., et al., *Emendation of Rules 5b, 8, 15 and 22 of the International Code of Nomenclature of Prokaryotes to include the rank of phylum.* Int J Syst Evol Microbiol, 2021. **71**(6).

120. Donia, M.S. and M.A. Fischbach, *HUMAN MICROBIOTA. Small molecules from the human microbiota.* Science, 2015. **349**(6246): p. 1254766.

121. Hooper, L.V., et al., *Molecular analysis of commensal host-microbial relationships in the intestine.* Science, 2001. **291**(5505): p. 881-4.

122. Lloyd-Price, J., et al., *Multi-omics of the gut microbial ecosystem in inflammatory bowel diseases.* Nature, 2019. **569**(7758): p. 655-662.

123. Peled, J.U., et al., *Microbiota as Predictor of Mortality in Allogeneic Hematopoietic-Cell Transplantation.* N Engl J Med, 2020. **382**(9): p. 822-834.

124. Reitmeier, S., et al., *Arrhythmic Gut Microbiome Signatures Predict Risk of Type 2 Diabetes.* Cell Host Microbe, 2020. **28**(2): p. 258-272 e6.

125. Chamaillard, M. and K. Radulovic, *Defining dysbiosis threatens Koch's postulates and current dogma on the role of Paneth cells in Crohn's disease.* Gut, 2016. **65**(2): p. 190-1.

126. Jain, P., Z.Q. Luo, and S.R. Blanke, *Helicobacter pylori vacuolating cytotoxin A (VacA) engages the mitochondrial fission machinery to induce host cell death.* Proc Natl Acad Sci U S A, 2011. **108**(38): p. 16032-7.

127. Mannick, E.E., et al., *Gene expression in gastric biopsies from patients infected with Helicobacter pylori.* Scand J Gastroenterol, 2004. **39**(12): p. 1192-200.

128. Ornelas, A., et al., *Microbial Metabolite Regulation of Epithelial Cell-Cell Interactions and Barrier Function.* Cells, 2022. **11**(6): p. 944.

129. Everard, A., et al., *Intestinal epithelial MyD88 is a sensor switching host metabolism towards obesity according to nutritional status.* Nature Communications, 2014. **5**(1): p. 5648.

130. Haller, D., et al., *Non-pathogenic bacteria elicit a differential cytokine response by intestinal epithelial cell/leucocyte co-cultures.* Gut, 2000. **47**(1): p. 79-87.

131. Lukovac, S., et al., *Differential modulation by Akkermansia muciniphila and Faecalibacterium prausnitzii of host peripheral lipid metabolism and histone acetylation in mouse gut organoids.* mBio, 2014. **5**(4).

132. Tan, J., et al., *The role of short-chain fatty acids in health and disease.* Adv Immunol, 2014. **121**: p. 91-119.

133. Kaiko, G.E., et al., *The Colonic Crypt Protects Stem Cells from Microbiota-Derived Metabolites.* Cell, 2016. **167**(4): p. 1137.

134. Macpherson, A.J. and K.D. McCoy, *Standardised animal models of host microbial mutualism.* Mucosal Immunol, 2015. **8**(3): p. 476-86.

135. Johansson, M.E., et al., *Normalization of Host Intestinal Mucus Layers Requires Long-Term Microbial Colonization.* Cell Host Microbe, 2015. **18**(5): p. 582-92.

136. Zietek, T. and E. Rath, *Inflammation Meets Metabolic Disease: Gut Feeling Mediated by GLP-1.* Front Immunol, 2016. **7**: p. 154.

137. Inami, A., H. Kiyono, and Y. Kurashima, *ATP as a Pathophysiologic Mediator of Bacteria-Host Crosstalk in the Gastrointestinal Tract.* Int J Mol Sci, 2018. **19**(8).

138. Marinelli, L., et al., *Identification of the novel role of butyrate as AhR ligand in human intestinal epithelial cells.* Sci Rep, 2019. **9**(1): p. 643.

139. Kotlo, K., et al., *The olfactory G protein-coupled receptor (Olfr-78/OR51E2) modulates the intestinal response to colitis.* Am J Physiol Cell Physiol, 2020. **318**(3): p. C502-c513.

140. Kim, K.S., et al., *Activation of intestinal olfactory receptor stimulates glucagon-like peptide-1 secretion in enteroendocrine cells and attenuates hyperglycemia in type 2 diabetic mice.* Sci Rep, 2017. **7**(1): p. 13978.

141. Brinkmann, V., et al., *The Aryl Hydrocarbon Receptor (AhR) in the Aging Process: Another Puzzling Role for This Highly Conserved Transcription Factor.* Front Physiol, 2019. **10**: p. 1561.

142. Leoni, G., et al., *Wound repair: role of immune-epithelial interactions.* Mucosal Immunol, 2015. **8**(5): p. 959-68.

143. Hwang, H.J., et al., *Mitochondrial-targeted aryl hydrocarbon receptor and the impact of 2,3,7,8-tetrachlorodibenzo-p-dioxin on cellular respiration and the mitochondrial proteome.* Toxicol Appl Pharmacol, 2016. **304**: p. 121-32.

144. Liu, Z., et al., *Aryl hydrocarbon receptor activation maintained the intestinal epithelial barrier function through Notch1 dependent signaling pathway.* Int J Mol Med, 2018. **41**(3): p. 1560-1572.

145. Metidji, A., et al., *The Environmental Sensor AHR Protects from Inflammatory Damage by Maintaining Intestinal Stem Cell Homeostasis and Barrier Integrity.* Immunity, 2019. **50**(6): p. 1542.

146. Cervantes-Barragan, L., et al., *Lactobacillus reuteri induces gut intraepithelial CD4(+)CD8αα(+) T cells.* Science, 2017. **357**(6353): p. 806-810.

147. Lanis, J.M., et al., *Tryptophan metabolite activation of the aryl hydrocarbon receptor regulates IL-10 receptor expression on intestinal epithelia.* Mucosal Immunol, 2017. **10**(5): p. 1133-1144.

148. Zelante, T., et al., *Tryptophan catabolites from microbiota engage aryl hydrocarbon receptor and balance mucosal reactivity via interleukin-22.* Immunity, 2013. **39**(2): p. 372-85.

149. Li, S., J.W. Bostick, and L. Zhou, *Regulation of Innate Lymphoid Cells by Aryl Hydrocarbon Receptor.* Frontiers in Immunology, 2018. **8**.

150. Tan, J., et al., *How Changes in the Nutritional Landscape Shape Gut Immunometabolism.* Nutrients, 2021. **13**(3): p. 823.

151. Hwang, S.L., et al., *Indoleamine 2, 3-dioxygenase (IDO) is essential for dendritic cell activation and chemotactic responsiveness to chemokines.* Cell Res, 2005. **15**(3): p. 167-75.

152. Alvarado, D.M., et al., *Epithelial Indoleamine 2,3-Dioxygenase 1 Modulates Aryl Hydrocarbon Receptor and Notch Signaling to Increase Differentiation of Secretory Cells and Alter Mucus-Associated Microbiota.* Gastroenterology, 2019. **157**(4): p. 1093-1108 e11.

153. Meireson, A., M. Devos, and L. Brochez, *IDO Expression in Cancer: Different Compartment, Different Functionality?* Front Immunol, 2020. **11**: p. 531491.

154. Ciorba, M.A., *Indoleamine 2,3 dioxygenase in intestinal disease.* Curr Opin Gastroenterol, 2013. **29**(2): p. 146-52.

155. Landfried, K., et al., *Tryptophan catabolism is associated with acute GVHD after human allogeneic stem cell transplantation and indicates activation of indoleamine 2,3-dioxygenase.* Blood, 2011. **118**(26): p. 6971-4.

156. Nikolaus, S., et al., *Increased Tryptophan Metabolism Is Associated With Activity of Inflammatory Bowel Diseases.* Gastroenterology, 2017. **153**(6): p. 1504-1516.e2.

157. Gupta, N.K., et al., *Serum analysis of tryptophan catabolism pathway: correlation with Crohn's disease activity.* Inflamm Bowel Dis, 2012. **18**(7): p. 1214-20.

158. Roager, H.M. and T.R. Licht, *Microbial tryptophan catabolites in health and disease.* Nat Commun, 2018. **9**(1): p. 3294.

159. Yusufu, I., et al., *A Tryptophan-Deficient Diet Induces Gut Microbiota Dysbiosis and Increases Systemic Inflammation in Aged Mice.* Int J Mol Sci, 2021. **22**(9).

160. Islam, J., et al., *Dietary tryptophan alleviates dextran sodium sulfate-induced colitis through aryl hydrocarbon receptor in mice.* J Nutr Biochem, 2017. **42**: p. 43-50.

161. Scott, S.A., J. Fu, and P.V. Chang, *Microbial tryptophan metabolites regulate gut barrier function via the aryl hydrocarbon receptor.* Proc Natl Acad Sci U S A, 2020. **117**(32): p. 19376-19387.

162. Metwaly, A., S. Reitmeier, and D. Haller, *Microbiome risk profiles as biomarkers for inflammatory and metabolic disorders.* Nat Rev Gastroenterol Hepatol, 2022.

163. Kühn, R., et al., *Interleukin-10-deficient mice develop chronic enterocolitis.* Cell, 1993. **75**(2): p. 263-74.

164. Neufert, C., C. Becker, and M.F. Neurath, *An inducible mouse model of colon carcinogenesis for the analysis of sporadic and inflammation-driven tumor progression.* Nat Protoc, 2007. **2**(8): p. 1998-2004.

165. Eberl, C., et al., *Reproducible Colonization of Germ-Free Mice With the Oligo-Mouse-Microbiota in Different Animal Facilities.* Front Microbiol, 2019. **10**: p. 2999.

166. Brugiroux, S., et al., *Genome-guided design of a defined mouse microbiota that confers colonization resistance against Salmonella enterica serovar Typhimurium.* Nat Microbiol, 2016. **2**: p. 16215.

167. Erben, U., et al., *A guide to histomorphological evaluation of intestinal inflammation in mouse models.* Int J Clin Exp Pathol, 2014. **7**(8): p. 4557-76.

168. Livak, K.J. and T.D. Schmittgen, *Analysis of relative gene expression data using real-time quantitative PCR and the 2(-Delta Delta C(T)) Method.* Methods, 2001. **25**(4): p. 402-8.

169. Lagkouvardos, I., et al., *Gut metabolites and bacterial community networks during a pilot intervention study with flaxseeds in healthy adult men.* Mol Nutr Food Res, 2015. **59**(8): p. 1614-28.

170. Lagkouvardos, I., et al., *IMNGS: A comprehensive open resource of processed 16S rRNA microbial profiles for ecology and diversity studies.* Sci Rep, 2016. **6**: p. 33721.

171. Edgar, R.C., *UPARSE: highly accurate OTU sequences from microbial amplicon reads.* Nature Methods, 2013. **10**(10): p. 996-+.

172. Edgar, R.C., et al., *UCHIME improves sensitivity and speed of chimera detection.* Bioinformatics, 2011. **27**(16): p. 2194-2200.

173. Wang, Q., et al., *Naive Bayesian classifier for rapid assignment of rRNA sequences into the new bacterial taxonomy.* Applied and Environmental Microbiology, 2007. **73**(16): p. 5261-5267.

174. Quast, C., et al., *The SILVA ribosomal RNA gene database project: improved data processing and web-based tools.* Nucleic Acids Research, 2013. **41**(D1): p. D590-D596.

175. Lagkouvardos, I., et al., *Rhea: a transparent and modular R pipeline for microbial profiling based on 16S rRNA gene amplicons.* Peerj, 2017. **5**.

176. Subramanian, B., et al., *Evolview v3: a webserver for visualization, annotation, and management of phylogenetic trees.* Nucleic Acids Res, 2019. **47**(W1): p. W270-W275.

177. Hillmann, B., et al., *Evaluating the Information Content of Shallow Shotgun Metagenomics.* mSystems, 2018. **3**(6).

178. Segata, N., et al., *Metagenomic microbial community profiling using unique clade-specific marker genes.* Nat Methods, 2012. **9**(8): p. 811-4.

179. Huang da, W., B.T. Sherman, and R.A. Lempicki, *Bioinformatics enrichment tools: paths toward the comprehensive functional analysis of large gene lists.* Nucleic Acids Res, 2009. **37**(1): p. 1-13.

180. Huang, D.W., B.T. Sherman, and R.A. Lempicki, *Systematic and integrative analysis of large gene lists using DAVID bioinformatics resources.* Nature Protocols, 2009. **4**(1): p. 44-57.

181. Mi, H., et al., *PANTHER version 16: a revised family classification, tree-based classification tool, enhancer regions and extensive API.* Nucleic Acids Res, 2021. **49**(D1): p. D394-D403.

182. Vidal, K., et al., *Immortalization of mouse intestinal epithelial cells by the SV40-large T gene. Phenotypic and immune characterization of the MODE-K cell line.* J Immunol Methods, 1993. **166**(1): p. 63-73.

183. Whitehead, R.H., et al., *Conditionally immortalized colonic epithelial cell line from a Ptk6 null mouse that polarizes and differentiates in vitro.* J Gastroenterol Hepatol, 2008. **23**(7 Pt 1): p. 1119-24.

184. Mahe, M.M., et al., *Establishment of Gastrointestinal Epithelial Organoids.* Curr Protoc Mouse Biol, 2013. **3**(4): p. 217-40.

185. Sato, T. and H. Clevers, *Growing self-organizing mini-guts from a single intestinal stem cell: mechanism and applications.* Science, 2013. **340**(6137): p. 1190-4.

186. Swalwell, H., et al., *Respiratory chain complex I deficiency caused by mitochondrial DNA mutations.* European Journal of Human Genetics, 2011. **19**(7): p. 769-775.

187. Zielinski, L.P., et al., *Metabolic flexibility of mitochondrial respiratory chain disorders predicted by computer modelling.* Mitochondrion, 2016. **31**: p. 45-55.

188. Thompson Legault, J., et al., *A Metabolic Signature of Mitochondrial Dysfunction Revealed through a Monogenic Form of Leigh Syndrome.* Cell Rep, 2015. **13**(5): p. 981-9.

189. Nojiri, H., et al., *Oxidative stress causes heart failure with impaired mitochondrial respiration.* J Biol Chem, 2006. **281**(44): p. 33789-801.

190. Manczak, M., et al., *Mitochondria are a direct site of A beta accumulation in Alzheimer's disease neurons: implications for free radical generation and oxidative damage in disease progression.* Hum Mol Genet, 2006. **15**(9): p. 1437-49.

191. Wu, Y., M. Chen, and J. Jiang, *Mitochondrial dysfunction in neurodegenerative diseases and drug targets via apoptotic signaling.* Mitochondrion, 2019. **49**: p. 35-45.

192. Rath, E. and D. Haller, *Intestinal epithelial cell metabolism at the interface of microbial dysbiosis and tissue injury.* Mucosal Immunol, 2022. **15**(4): p. 595-604.

193. Madison, B.B., et al., *Cis elements of the villin gene control expression in restricted domains of the vertical (crypt) and horizontal (duodenum, cecum) axes of the intestine.* J Biol Chem, 2002. **277**(36): p. 33275-83.

194. Mills, S.J., et al., *Colonic crypt cell proliferation state assessed by whole crypt microdissection in sporadic neoplasia and familial adenomatous polyposis.* Gut, 2001. **48**(1): p. 41-6.

195. Hua, G., et al., *Crypt base columnar stem cells in small intestines of mice are radioresistant.* Gastroenterology, 2012. **143**(5): p. 1266-1276.

196. Withers, H.R., et al., *Response of mouse intestine to neutrons and gamma rays in relation to dose fractionation and division cycle.* Cancer, 1974. **34**(1): p. 39-47.

197. Metcalfe, C., et al., *Lgr5+ stem cells are indispensable for radiation-induced intestinal regeneration.* Cell Stem Cell, 2014. **14**(2): p. 149-59.

198. Yui, S., et al., *YAP/TAZ-Dependent Reprogramming of Colonic Epithelium Links ECM Remodeling to Tissue Regeneration.* Cell Stem Cell, 2018. **22**(1): p. 35-49.e7.

199. Ohara, T.E., M. Colonna, and T.S. Stappenbeck, *Adaptive differentiation promotes intestinal villus recovery.* Dev Cell, 2022. **57**(2): p. 166-179.e6.

200. Yan, K.S., et al., *Intestinal Enteroendocrine Lineage Cells Possess Homeostatic and Injury-Inducible Stem Cell Activity.* Cell Stem Cell, 2017. **21**(1): p. 78-90.e6.

201. Tomic, G., et al., *Phospho-regulation of ATOH1 Is Required for Plasticity of Secretory Progenitors and Tissue Regeneration.* Cell Stem Cell, 2018. **23**(3): p. 436-443.e7.

202. Tetteh, P.W., et al., *Replacement of Lost Lgr5-Positive Stem Cells through Plasticity of Their Enterocyte-Lineage Daughters.* Cell Stem Cell, 2016. **18**(2): p. 203-13.

203. van Es, J.H., et al., *Dll1+ secretory progenitor cells revert to stem cells upon crypt damage.* Nat Cell Biol, 2012. **14**(10): p. 1099-1104.

204. Liu, Y. and Y.G. Chen, *Intestinal epithelial plasticity and regeneration via cell dedifferentiation.* Cell Regen, 2020. **9**(1): p. 14.

205. Murata, K., et al., *Ascl2-Dependent Cell Dedifferentiation Drives Regeneration of Ablated Intestinal Stem Cells.* Cell Stem Cell, 2020. **26**(3): p. 377-390 e6.

206. Becker, C., et al., *CLPP deficiency protects against metabolic syndrome but hinders adaptive thermogenesis.* EMBO Rep, 2018. **19**(5).

207. Rumyantseva, A., M. Popovic, and A. Trifunovic, *CLPP deficiency ameliorates neurodegeneration caused by impaired mitochondrial protein synthesis.* Brain, 2022. **145**(1): p. 92-104.

208. Choi, S.E., et al., *Mitochondrial protease ClpP supplementation ameliorates diet-induced NASH in mice.* J Hepatol, 2022. **77**(3): p. 735-747.

209. Wang, P., et al., *Aberrant human ClpP activation disturbs mitochondrial proteome homeostasis to suppress pancreatic ductal adenocarcinoma.* Cell Chem Biol, 2022.

210. Deepa, S.S., et al., *Down-regulation of the mitochondrial matrix peptidase ClpP in muscle cells causes mitochondrial dysfunction and decreases cell proliferation.* Free Radic Biol Med, 2016. **91**: p. 281-92.

211. Torres-Odio, S., et al., *Loss of Mitochondrial Protease CLPP Activates Type I IFN Responses through the Mitochondrial DNA-cGAS-STING Signaling Axis.* J Immunol, 2021. **206**(8): p. 1890-1900.
212. Walter, R.J., et al., *Wnt signaling is boosted during intestinal regeneration by a CD44-positive feedback loop.* Cell Death & Disease, 2022. **13**(2): p. 168.
213. Goto, N., et al., *Lymphatics and fibroblasts support intestinal stem cells in homeostasis and injury.* Cell Stem Cell, 2022. **29**(8): p. 1246-1261.e6.
214. Miyoshi, H., et al., *Wnt5a potentiates TGF-β signaling to promote colonic crypt regeneration after tissue injury.* Science, 2012. **338**(6103): p. 108-13.
215. Jha, A.K., et al., *Network integration of parallel metabolic and transcriptional data reveals metabolic modules that regulate macrophage polarization.* Immunity, 2015. **42**(3): p. 419-30.
216. Heinrich, F., et al., *Morphologic, phenotypic, and transcriptomic characterization of classically and alternatively activated canine blood-derived macrophages in vitro.* PLoS One, 2017. **12**(8): p. e0183572.
217. Wynn, T.A. and K.M. Vannella, *Macrophages in Tissue Repair, Regeneration, and Fibrosis.* Immunity, 2016. **44**(3): p. 450-462.
218. Julier, Z., et al., *Promoting tissue regeneration by modulating the immune system.* Acta Biomater, 2017. **53**: p. 13-28.
219. Hu, M., et al., *Interleukin-22 restored mitochondrial damage and impaired glucose-stimulated insulin secretion through down-regulation of uncoupling protein-2 in INS-1 cells.* J Biochem, 2017. **161**(5): p. 433-439.
220. Zha, J.M., et al., *Interleukin 22 Expands Transit-Amplifying Cells While Depleting Lgr5(+) Stem Cells via Inhibition of Wnt and Notch Signaling.* Cell Mol Gastroenterol Hepatol, 2019. **7**(2): p. 255-274.
221. Morhardt, T.L., et al., *IL-10 produced by macrophages regulates epithelial integrity in the small intestine.* Scientific Reports, 2019. **9**(1): p. 1223.
222. Danne, C., et al., *CARD9 in neutrophils protects from colitis and controls mitochondrial metabolism and cell survival.* Gut, 2022: p. gutjnl-2022-326917.
223. Martinez, A., et al., *Association of the organic cation transporter OCTN genes with Crohn's disease in the Spanish population.* Eur J Hum Genet, 2006. **14**(2): p. 222-6.
224. Yu, X., et al., *Association of UCP2 -866 G/A polymorphism with chronic inflammatory diseases.* Genes Immun, 2009. **10**(6): p. 601-5.
225. Lin, Z., et al., *OCTN1 variant L503F is associated with familial and sporadic inflammatory bowel disease.* J Crohns Colitis, 2010. **4**(2): p. 132-8.
226. Hampe, J., et al., *A genome-wide association scan of nonsynonymous SNPs identifies a susceptibility variant for Crohn disease in ATG16L1.* Nat Genet, 2007. **39**(2): p. 207-11.
227. Barrett, J.C., et al., *Genome-wide association defines more than 30 distinct susceptibility loci for Crohn's disease.* Nat Genet, 2008. **40**(8): p. 955-62.
228. Rakoff-Nahoum, S., et al., *Recognition of commensal microflora by toll-like receptors is required for intestinal homeostasis.* Cell, 2004. **118**(2): p. 229-41.
229. Lloyd-Price, J., et al., *Multi-omics of the gut microbial ecosystem in inflammatory bowel diseases.* Nature, 2019. **569**(7758): p. 655-662.
230. Lopez, L.R., et al., *Microenvironmental Factors that Shape Bacterial Metabolites in Inflammatory Bowel Disease.* Front Cell Infect Microbiol, 2022. **12**: p. 934619.
231. Heinken, A., J. Hertel, and I. Thiele, *Metabolic modelling reveals broad changes in gut microbial metabolism in inflammatory bowel disease patients with dysbiosis.* npj Systems Biology and Applications, 2021. **7**(1): p. 19.
232. Keighley, M.R., et al., *Influence of inflammatory bowel disease on intestinal microflora.* Gut, 1978. **19**(12): p. 1099-104.
233. Ruseler-van Embden, J.G. and H.C. Both-Patoir, *Anaerobic gram-negative faecal flora in patients with Crohn's disease and healthy subjects.* Antonie Van Leeuwenhoek, 1983. **49**(2): p. 125-32.

234. Andoh, A., et al., *Comparison of the fecal microbiota profiles between ulcerative colitis and Crohn's disease using terminal restriction fragment length polymorphism analysis.* J Gastroenterol, 2011. **46**(4): p. 479-86.

235. Matsuda, H., et al., *Characterization of antibody responses against rectal mucosa-associated bacterial flora in patients with ulcerative colitis.* J Gastroenterol Hepatol, 2000. **15**(1): p. 61-8.

236. Pisani, A., et al., *Dysbiosis in the Gut Microbiota in Patients with Inflammatory Bowel Disease during Remission.* Microbiology Spectrum, 2022. **10**(3): p. e00616-22.

237. Singhal, R. and Y.M. Shah, *Oxygen battle in the gut: Hypoxia and hypoxia-inducible factors in metabolic and inflammatory responses in the intestine.* J Biol Chem, 2020. **295**(30): p. 10493-10505.

238. Albenberg, L., et al., *Correlation between intraluminal oxygen gradient and radial partitioning of intestinal microbiota.* Gastroenterology, 2014. **147**(5): p. 1055-63 e8.

239. Gevers, D., et al., *The treatment-naive microbiome in new-onset Crohn's disease.* Cell Host Microbe, 2014. **15**(3): p. 382-392.

240. Friedman, E.S., et al., *Microbes vs. chemistry in the origin of the anaerobic gut lumen.* Proc Natl Acad Sci U S A, 2018. **115**(16): p. 4170-4175.

241. Araki, K., et al., *Comparison of mucosal microvasculature between the proximal and distal human colon.* J Electron Microsc (Tokyo), 1996. **45**(3): p. 202-6.

242. Cader, M.Z., et al., *FAMIN Is a Multifunctional Purine Enzyme Enabling the Purine Nucleotide Cycle.* Cell, 2020. **180**(2): p. 278-295 e23.

243. Cook, S.I. and J.H. Sellin, *Review article: short chain fatty acids in health and disease.* Aliment Pharmacol Ther, 1998. **12**(6): p. 499-507.

244. Donohoe, D.R., et al., *The microbiome and butyrate regulate energy metabolism and autophagy in the mammalian colon.* Cell Metab, 2011. **13**(5): p. 517-26.

245. Parada Venegas, D., et al., *Short Chain Fatty Acids (SCFAs)-Mediated Gut Epithelial and Immune Regulation and Its Relevance for Inflammatory Bowel Diseases.* Front Immunol, 2019. **10**: p. 277.

246. Park, J.H., et al., *Promotion of Intestinal Epithelial Cell Turnover by Commensal Bacteria: Role of Short-Chain Fatty Acids.* PLoS One, 2016. **11**(5): p. e0156334.

247. Taleb, S., *Tryptophan Dietary Impacts Gut Barrier and Metabolic Diseases.* Frontiers in Immunology, 2019. **10**.

248. Yanofsky, C., V. Horn, and P. Gollnick, *Physiological studies of tryptophan transport and tryptophanase operon induction in Escherichia coli.* J Bacteriol, 1991. **173**(19): p. 6009-17.

249. Williams, B.B., et al., *Discovery and characterization of gut microbiota decarboxylases that can produce the neurotransmitter tryptamine.* Cell Host Microbe, 2014. **16**(4): p. 495-503.

250. Scott, S.A., J. Fu, and P.V. Chang, *Microbial tryptophan metabolites regulate gut barrier function via the aryl hydrocarbon receptor.* Proceedings of the National Academy of Sciences, 2020. **117**(32): p. 19376-19387.

251. Alexeev, E.E., et al., *Microbiota-Derived Indole Metabolites Promote Human and Murine Intestinal Homeostasis through Regulation of Interleukin-10 Receptor.* Am J Pathol, 2018. **188**(5): p. 1183-1194.

252. Michaudel, C., et al., *Rewiring the altered tryptophan metabolism as a novel therapeutic strategy in inflammatory bowel diseases.* Gut, 2022.

253. Sofia, M.A., et al., *Tryptophan Metabolism through the Kynurenine Pathway is Associated with Endoscopic Inflammation in Ulcerative Colitis.* Inflamm Bowel Dis, 2018. **24**(7): p. 1471-1480.

254. Wnorowski, A., et al., *Alterations in Kynurenine and NAD(+) Salvage Pathways during the Successful Treatment of Inflammatory Bowel Disease Suggest HCAR3 and NNMT as Potential Drug Targets.* Int J Mol Sci, 2021. **22**(24).

255. Jagt, J.Z., et al., *Fecal Amino Acid Analysis in Newly Diagnosed Pediatric Inflammatory Bowel Disease: A Multicenter Case-Control Study.* Inflammatory Bowel Diseases, 2021. **28**(5): p. 755-763.

256. Martin-Gallausiaux, C., et al., *Butyrate Produced by Commensal Bacteria Down-Regulates Indolamine 2,3-Dioxygenase 1 (IDO-1) Expression via a Dual Mechanism in Human Intestinal Epithelial Cells.* Front Immunol, 2018. **9**: p. 2838.

257. Clarke, G., et al., *The microbiome-gut-brain axis during early life regulates the hippocampal serotonergic system in a sex-dependent manner.* Molecular Psychiatry, 2013. **18**(6): p. 666-673.

258. Rath, H.C., et al., *Different subsets of enteric bacteria induce and perpetuate experimental colitis in rats and mice.* Infect Immun, 2001. **69**(4): p. 2277-85.

259. Osaka, T., et al., *Meta-Analysis of Fecal Microbiota and Metabolites in Experimental Colitic Mice during the Inflammatory and Healing Phases.* Nutrients, 2017. **9**(12).

260. Bloom, S.M., et al., *Commensal Bacteroides species induce colitis in host-genotype-specific fashion in a mouse model of inflammatory bowel disease.* Cell Host Microbe, 2011. **9**(5): p. 390-403.

261. Curtis, M.M., et al., *The gut commensal Bacteroides thetaiotaomicron exacerbates enteric infection through modification of the metabolic landscape.* Cell Host Microbe, 2014. **16**(6): p. 759-69.

262. Debedat, J., et al., *The human gut microbiota contributes to type-2 diabetes non-resolution 5-years after Roux-en-Y gastric bypass.* Gut Microbes, 2022. **14**(1): p. 2050635.

263. Weiss, A.S., et al., *In vitro interaction network of a synthetic gut bacterial community.* Isme j, 2022. **16**(4): p. 1095-1109.

264. Lai, Y., et al., *Serum Metabolomics Identifies Altered Bioenergetics, Signaling Cascades in Parallel with Exposome Markers in Crohn's Disease.* Molecules, 2019. **24**(3).

265. Busbee, P.B., et al., *Indole-3-carbinol prevents colitis and associated microbial dysbiosis in an IL-22-dependent manner.* JCI Insight, 2020. **5**(1).

266. Ihekweazu, F.D., et al., *Bacteroides ovatus Promotes IL-22 Production and Reduces Trinitrobenzene Sulfonic Acid-Driven Colonic Inflammation.* Am J Pathol, 2021. **191**(4): p. 704-719.

267. Shen, J., et al., *Indole-3-Acetic Acid Alters Intestinal Microbiota and Alleviates Ankylosing Spondylitis in Mice.* Frontiers in Immunology, 2022. **13**.

268. Gundu, C., et al., *Indole-3-propionic acid attenuates high glucose induced ER stress response and augments mitochondrial function by modulating PERK-IRE1-ATF4-CHOP signalling in experimental diabetic neuropathy.* Arch Physiol Biochem, 2022: p. 1-14.

269. Chen, L., et al., *Indolepropionic acid reduces obesity-induced metabolic dysfunction through colonic barrier restoration mediated via tuft cell-derived IL-25.* FEBS J, 2022. **289**(19): p. 5985-6004.

270. Zhang, B., et al., *The Mechanism Underlying the Influence of Indole-3-Propionic Acid: A Relevance to Metabolic Disorders.* Front Endocrinol (Lausanne), 2022. **13**: p. 841703.

271. Gesper, M., et al., *Gut-Derived Metabolite Indole-3-Propionic Acid Modulates Mitochondrial Function in Cardiomyocytes and Alters Cardiac Function.* Front Med (Lausanne), 2021. **8**: p. 648259.

272. Sári, Z., et al., *Indolepropionic Acid, a Metabolite of the Microbiome, Has Cytostatic Properties in Breast Cancer by Activating AHR and PXR Receptors and Inducing Oxidative Stress.* Cancers, 2020. **12**(9): p. 2411.

273. Lundberg, J.O. and E. Weitzberg, *Nitric oxide signaling in health and disease.* Cell, 2022. **185**(16): p. 2853-2878.

274. Laurans, L., et al., *Genetic deficiency of indoleamine 2,3-dioxygenase promotes gut microbiota-mediated metabolic health.* Nat Med, 2018. **24**(8): p. 1113-1120.

275. Png, C.W., et al., *Mucolytic Bacteria With Increased Prevalence in IBD Mucosa AugmentIn VitroUtilization of Mucin by Other Bacteria.* Official journal of the American College of Gastroenterology | ACG, 2010. **105**(11): p. 2420-2428.

276.   Zhang, T., et al., *Alterations of Akkermansia muciniphila in the inflammatory bowel disease patients with washed microbiota transplantation.* Appl Microbiol Biotechnol, 2020. **104**(23): p. 10203-10215.
277.   Zhai, R., et al., *Strain-Specific Anti-inflammatory Properties of Two Akkermansia muciniphila Strains on Chronic Colitis in Mice.* Front Cell Infect Microbiol, 2019. **9**: p. 239.
278.   Chang, C.C., et al., *Functional Plasmon-Activated Water Increases Akkermansia muciniphila Abundance in Gut Microbiota to Ameliorate Inflammatory Bowel Disease.* Int J Mol Sci, 2022. **23**(19).
279.   Rao, Y., et al., *Gut Akkermansia muciniphila ameliorates metabolic dysfunction-associated fatty liver disease by regulating the metabolism of L-aspartate via gut-liver axis.* Gut Microbes, 2021. **13**(1): p. 1-19.
280.   Wang, D., et al., *Aspartate Alleviates Colonic Epithelial Damage by Regulating Intestinal Stem Cell Proliferation and Differentiation via Mitochondrial Dynamics.* Mol Nutr Food Res, 2022: p. e2200168.

Acknowledgements

DANKE !

Nora Mindermann · Patricija Kotovika · Amira Metwaly
Hélène Omer · Deborah Püngel · Sigrid Kiessling
Sevana Khaloian
Sandra Bierwirth · Pati Richter · Niu Yunhui
Christina Reim
Kaelin Smith · Brita Sturm · Silke Kießling
Sabine Kervan · Janine Kövilein · Uli
Marjolein Heddes · Lun Li · Emanuel Berger
Nico Gebhard · Klaus Peter Janssen
Tina Krammel · Mama und Papa
Lena · Sandra Reitmeier

Guojing Qu · Stephanie Kuhls
Beate Honold · Marianne Reiser · Sabine Schwamberger · Annie Naujoks · Nadja Rupprich
Aline Lucaks · Helene Heimes
Collaborators · Katja Steiger
Marie Kröger · Doriane Aguanno
Valentina Schüppel · Jacqui Wiethaler · Ingrid Schmöller · Martina Müller
Matthieu Allez · Team
Baraa Altaha · Saskia · Steffi Ewald · Karin Kleigrewe
Katharina Jäger · Lydi · Dirk Haller · My Family
Isabella Lengfelder · Olivia Coleman · Omas und Opas · Nina Heppner · Eva Rath
Anna-Maria · Miriam Ecker · Aline Potrack
Friends · Silvia Pitariu

It was a great journey !

Publications and Presentations

(Urbauer E maiden name: Gleisinger E)

Original manuscripts and reviews

Urbauer E***,** Aguanno D*, Mindermann N, Omer H, Metwaly A, Khaloian S, Reitmeier S, Remke M, Jarosch S, Huber S, Busch D, Stecher B, Allez M, Steiger K, Rath E, Haller D
Mitochondrial perturbation of the epithelium causes microbial dysbiosis and unresolved tissue injury in intestinal inflammation
bioRxiv. 2023.2007.2027.549844. doi:10.1101/2023.07.27.549844 (2023).
Submitted to *Nat Microbiol.*

Urbauer E*, Rath E*, Haller D
Mitochondrial metabolism in the intestinal stem cell niche – sensing and signaling in health and disease
Front. Cell Dev Biol. 2021 Jan 5;8:602814. doi:10.3389/fcell.2020.602814.

Zietek T, Giesbertz P, Ewers M, Reichart F, Weinmüller M, **Urbauer E**, Haller D, Demir I E, Ceyhan G O, Kessler H, Rath E
Organoids to study intestinal nutrient transport, drug uptake and metabolism – update to the human model and expansion of applications
Front. Bioeng. Biotechnol. 2020 Sep 11. doi:10.3389/fbioe.2020.577656.

Khaloian S, Rath E, Hammoudi N, **Gleisinger E**, Blutke A, Giesbertz P, Berger E, Metwaly A, Waldschmitt N, Allez M ,Haller D
Mitochondrial impairment drives intestinal stem cell transition into dysfunctional Paneth cells predicting Crohn's disease recurrence
Gut. 2020 Nov;69(11):1939-1951. doi:10.1136/gutjnl-2019-319514.

*These authors contributed equally to the manuscript

Published abstract

Urbauer E, Rath E, Aguanno D, Omer H, Metwaly A, Khaloian S, Steiger K, Allez M, Haller D
Mitochondrial perturbation of the epithelium causes microbial dysbiosis and unresolved tissue injury in intestinal inflammation
Gastroenterology, Volume 162, Issue 7, S-1-1-1395.

Khaloian S, Rath E, **Gleisinger E,** Berger E, Metwaly A, Waldschmitt N, Hammoudi N, Allez M, Haller D
Mitochondrial impairment in Crohn's disease-like inflammation drives intestinal stem cell transition towards dysfunctional Paneth cells
Gastroenterology, Volume 156, Issue 6, S-32.

Oral presentations

Urbauer E, Aguanno D, Mindermann N, Rath E, Omer H, Metwaly A, Khaloian S, Steiger K, Allez M, Haller D
Metabolic injury of the intestinal epithelium triggers dysbiotic expansion of *Bacteroides* spp. driving chronic inflammation
Digestive Disease Week (DDW). May 6-9, 2023, Chicago, USA

Urbauer E, Aguanno D, Rath E, Omer H, Metwaly A, Khaloian S, Steiger K, Allez M, Haller D
Microbial signals and host sensing control metabolic injury in the intestinal epithelium
30th United European Gastroenterology Week. Oct 08-11, 2022, Vienna, Austria

Urbauer E, Rath E, Aguanno D, Omer H, Metwaly A, Khaloian S, Steiger K, Allez M, Haller D
Mitochondrial perturbation of the epithelium causes microbial dysbiosis and unresolved tissue injury in intestinal inflammation
Digestive Disease Week (DDW). May 20-24, 2022, San Diego, USA

Rath E, **Urbauer E,** Berger E, Haller D
Mucosal healing upon metabolic injury is orchestrated by a complex regulation of intestinal epithelial cell metabolism
Online NuGo week 2021 – Mitochondria, nutrition and health. Sep 06-08, 2021, Online

Gleisinger E, Rath E, Khaloian S, Berger E, Metwaly A, Hammoudi N, Allez M, Haller D
Mitochondrial impairment drives intestinal stem cell transition into dysfunctional Paneth cells predicting Crohn's disease recurrence
Keystone Symposia: Tissue Organoids as Models of Host Physiology and Pathophysiology of Disease. Jan 19-23, 2020, Vancouver, Canada

Khaloian S, Rath E, **Gleisinger E,** Berger E, Metwaly A, Waldschmitt N, Hammoudi N, Allez M, Haller D
Mitochondrial impairment in Crohn's disease-like inflammation drives intestinal stem cell transition towards dysfunctional Paneth cells
Digestive Disease Week (DDW). May 18-21, 2019, San Diego, USA

Poster presentations

Urbauer E, Aguanno D, Schüppel V, Haller D, Rath E
Dietary fatty acids increase intestinal L cell numbers independent of the development of obesity
NuGO week 2022: Food bioactives for disease prevention - from mechanisms to chrononutrition. Aug 29 - Nov 01, 2022, Tarragona, Spain

Urbauer E, Aguanno D, Rath E, Omer H, Metwaly A, Khaloian S, Steiger K, Allez M, Haller D
Microbial signals and host sensing control metabolic injury in the intestinal epithelium
14th Seeon Conference (German Society for Hygiene and Microbiology, DGHM). Jun 30 - Jul 02, 2022, Seeon, Germany

Gleisinger E, Rath E, Khaloian S, Berger E, Metwaly A, Hammoudi N, Allez M, Haller D
Mitochondrial impairment drives intestinal stem cell transition into dysfunctional Paneth cells predicting Crohn's disease recurrence
Keystone Symposia: Tissue Organoids as Models of Host Physiology and Pathophysiology of Disease. Jan 19-23, 2020, Vancouver, Canada

Gleisinger E, Khaloian S, Waldschmitt N, Ham S K, Yoon H, Rath E, Haller D
Mitochondrial dysfunction in intestinal epithelial cells influences regenerative and neoplastic processes
EMBO|FEBS Lecture Course: Mitochondria in life, death and disease. Sep 24-28, 2019, Herceg Novi, Montenegro

Gleisinger E, Khaloian S, Waldschmitt N, Ham S K, Yoon H, Rath E, Haller D
Mitochondrial dysfunction in intestinal epithelial cells influences regenerative and neoplastic processes
11th Seeon Conference (German Society for Hygiene and Microbiology, DGHM). Jul 06-08, 2018, Seeon, Germany

Gleisinger E, Khaloian S, Gosch S, Zietek T, Rath E, Haller D
Tamoxifen confounds experimental outcomes in murine intestinal organoids highlighting the use of proper controls
EMBO|EMBL Symposia: Organoids: Modelling Organ Development and Disease in 3D Culture. Sep 10-13, 2018, Heidelberg, Germany

Khaloian S, Rath E, **Gleisinger E,** Berger E, Metwaly A,, Waldschmitt N, Haller D
Intestinal inflammation and impaired mitochondrial function correlate with reduced Lgr5$^+$ crypt-based columnar stem cells stem cell numbers and occurrence of dysfunctional Paneth cells
NuGO week 2018 – Mitochondria, nutrition and health. Sep 03-06, 2018, Newcastle, UK

Grants

Travel Grant, Keystone Symposia Future of Science Fund scholarship
(Keystone Symposia, Jan 19-23, 2020, Vancouver, Canada)

Travel Grant, Global Young Scientist Summit
(GYSS, Jan 17-20, Singapore)

List of cited publications

Urbauer, E., et al. Mitochondrial perturbation of the epithelium causes microbial dysbiosis and unresolved tissue injury in intestinal inflammation. *bioRxiv*, 2023.2007.2027.549844, doi:10.1101/2023.07.27.549844 (2023).

Urbauer, E., Rath, E., and Haller, D. Mitochondrial Metabolism in the Intestinal Stem Cell Niche - Sensing and Signaling in Health and Disease. *Front Cell Dev Biol* **8**, 602814, doi:10.3389/fcell.2020.602814 (2020).

Hiermit erkläre ich an Eides statt, dass ich alleiniger, federführender Hauptautor der oben genannten Publikation bin, die in dieser Arbeit wörtlich zitiert wurden. Die betreffenden Passagen wurden ausschließlich von mir verfasst.

Curriculum vitae

M.Sc. Elisabeth Urbauer

formerly Elisabeth Gleisinger

Professional experience:

10/2017 – 07/2023	**PhD student**: ZIEL-Institute for Food and Health, Technical University of Munich, Germany
	Topic: Mitochondrial function in the regulation of epithelial cell homeostasis – impact on intestinal pathologies
09/2016 – 12/2016:	**Research Internship**: Department of Molecular Biosciences, Stockholm University, Sweden
09/2014 – 12/2014:	**Research Internship:** Bavarian Health and Food Safety Authority, Research & Development Molecular Biology, Munich, Germany

Education:

04/2015 – 08/2017:	**Molecular Biotechnology (M.Sc.),** Technical University of Munich, Germany
	Master thesis: Investigation of the mechanism underlying the observed impairment of barrier and immune response by V/M-increased intestinal protease activity in the large intestine of IL10$^{-/-}$ mice
10/2011 – 07/2014:	**Nutritional Science (B.Sc.),** Technical University of Munich, Germany
	Bachelor thesis: Characterization of *Escherichia coli* double mutants with defects in biotin biosynthesis and transport
09/2002 – 04/2011:	**Hertzhaimer Gymnasium, Trostberg, Germany**
08/2008 – 06/2009:	Creekview High School, Texas, USA